Separation of particles from liquids

by the solid core cyclone.

by

Michael David Slack

A thesis submitted for the degree of

Doctor of Philosophy.

Dept. Mechanical, Materials

& Manufacturing Engineering

Materials Division

University of Newcastle Upon Tyne

Newcastle Upon Tyne

1997

Abstract

A computational and physical modelling study is made of the removal of inclusions from liquid steel by use of a novel form of hydrocyclone in which a solid conical core that replaces the conventional vortex finder acts as a guide to the spiralling liquid flow and acts also as a capture surface for disentrained inclusions.

In preliminary investigations, an inviscid computational model is derived that is found to be effective in outlining the general behaviour of specific hydrocyclone flows when tested against published experimental results. The more generally applicable commercial CFD code Fluent is likewise tested, from which it is shown that, among the turbulence models available, the anisotropic turbulence typical of spiralling hydrocyclone flows requires a form of Reynolds stress model for effective computation. The conventional k-ε model is found to be misleading.

On this basis, mathematical modelling and optimal computational design of hydrocyclones containing an axial conical solid core show that the separation efficiency of the cyclone is profoundly enhanced by the presence of a core, and that by use of a particle tracking model effective centripetal migration of inclusion particles in steel will occur towards the core.

Experiments with a water model of computed optimal cyclone designs provided effective validation of the numerical study. Photographically active particles of neutral density were tracked by a novel stroboscopic technique which permitted bi-directional observation revealing instantaneous velocity, spatial position and spiral angle. Using populations of low density particles having the same spectrum of Stokes velocity as inclusions in the size range 35 to 150 microns found typically in liquid steel, sampling by Coulter counter showed that effective

separation to the core surface of particles down to an equivalent size of 30 microns was achieved.

In a final step, a pilot cyclone design for use with steel was established and water model tests at full scale showed that stable cyclone flow and discharge are achievable with gravity feed to the cyclone.

Acknowledgements

I would like to thank EPSRC for financial support and the funding of my Canadian excursion. I would also like to thank British Steel Technical for their financial support, technical advice and the great time that I had in their laboratories.

To Bert for his supervision, guidance and conversation. I must thank the Materials Division as a whole for repairing my interest in Engineering and opening my horizons beyond mechanical engineering. The great friends and good times that I have had.

Contents

List of Plates

List of Symbols

z, θ, r	cylindrical co-ordinates	[-]
x	displacement	[m]
W	constant tangential velocity	[m/s]
v_z, v_r, v_θ	cylindrical velocity components	[m/s]
v_s, v_λ, v_θ	spherical velocity components	[m/s]
$v_{r.particle}$	radial velocity of the particle	[m/s]
vol_{cel}	volume of build up per mesh cell on core	[m^3]
vol_{band}	mean volume of sphericalparticals in band	[m^3]
v_θ	tangential velocity	[m/s]
v	velocity	[m/s]
V	constant axial velocity	[m/s]
u	diameter of underflow apex	[m]
t_{ij}	deformation tensor	[m^3/s^3]
t_0	average length of time	[s]
t	time	[s]
T	modulus	[-]
S_d	Interval width	[-]
s, λ, θ	spherical co-ordinate directions	[-]
r_p	radial position of particle	[m]
R_o	outer radius of cyclone	[m]
R_f	ratio of core flow to total flow	[-]
r_{cell}	ratio of number of particles landing in cell	[-]
R_1	Radius of vortex finder	[m]
r	radius	[m]
R	rate of strain	[-]
Q	volume flow rate	[m^3/s]
p	pressure	[Pa]
n_p	mean number of particles in band	[-]
n	number of samples or empirical exponent	[-]
L_1	length of cylindrical section	[m]
L	length of cyclone	[m]
l	length of vortex finder inside body of cyclone	[m]
l	turbulent length scale	[m]
k	kinematic energy of turbulence	[J]
$Int_{average}$	representative average of number of particles in each 1μm sub-band.	[-]
i, i, k subscripts	denote co-ordinate directions	[-]
h, δλ	node displacement interval, 2-dimesional spherical grid	[-]
H	Bernoulli's constant	[-]
G'(d)	corrected grade efficiency	[-]
G(d)	grade efficiency	[-]
e	diameter of vortex finder	[m]
d_p	equivalent spherical diameter of the particle	[m]
d_n	particle diameter of index n	[m]
D	cylindrical diameter of cyclone	[m]
C, C_1, C_2, C_3, C_4	constants	[-]
C_μ	empirical constant	[-]
b	diameter of inlet	[m]
a	centripetal acceleration	[m/s^2]

$\eta_z,\eta_r,\eta_\theta$	vorticity components	[1/s]
ν_t	Turbulent kinematic viscosity	[m^2/s]
μ_t	turbulent dynamic viscosity	[Pa·s]
Δt	time interval	[s]
Δp	change in pressure	[Pa]
θ_p	angular component of particle posistion	[rad]
ϕ_o	constant associated to RNG model	[-]
δ_{ij}	kronecker delta; i=j:δ_{ij}=1, i≠j:δ_{ij}≠1	[-]
θ_H	helix angle	[rad]
β, ϕ_o, α, α_o	empirical constants associated with RNG model	[-]
$\Delta\rho$	density difference	[kg/m^3]
ρ	density	[kg/m^3]
θ	polar angular co-ordinate	[rad]
μ	dynamic viscosity	[Pa·s]
η	vorticity	[1/s]
ψ	Stokes steam function	[m^3/s]
Ω	Angular velocity	[rad/s]
Λ	Flow split ratio	[-]
ε	dissipation rate of turbulence	[m^2/s^3]
α	Reynolds number dependent parameter	[-]
β	constant	[-]
ω	angular velocity of particle	[rad/s]
σ	standard deviation	[-]
α	Included angle of cyclone	[rad]
$\overline{v_i}$	mean velocity component	[m/s]
v_i'	Fuctuating velocity component	[m/s]
$-\rho\overline{v_i'v_j'}$	Reynolds stress component	[$kg/m\cdot s^2$]
$\bar{x}$	arithmetic mean value	[-]

Chapter I

Introduction

1.1 Clean Steel

As the metallurgical industries strive for position in a highly competitive world market the need for a cost effective quality product becomes paramount. This has meant that organisations like the Steel industries look to maximise the use of efficient production operations, with better engineered operations and practices. This study was driven by the need to produce a cheap clean steel.

Steel contains a low volume of particulate inclusions, of < 1 μm up to 200 μm in size, which cause quality problems in the finished product. They originate during steel manufacture and from the different secondary processing treatments employed [C3, H4, N1]. This study is about the removal of alumina Al_2O_3 inclusions from the melt. Alumina is associated with aluminium treated steels. According to Kiessling [K4], the cleanness of steel is relative; a steel of a given cleanness may be sufficient for one product and not for another. Ideally it should be possible to predict the effect of inclusions on the product, for example mechanical fatigue or ductile fracture, based on the probability of inclusions larger than a critical size. The problem is that the exact size at which a given inclusion becomes harmful is at present not known though there are many theories [G3, K3, N1].

Present techniques for inclusion control and removal from steel focus upon disentrainment under gravity or in circulation systems that can be induced by gas injection or directed flows. Alumina is highly interactive and a capture surface of slag or refractory is essential. Tundish designs have been developed to produce flow patterns that promote inclusion movement to a surface slag layer or refractory surface. However,

there is a limit to the power and the effectiveness of directed tundish flows that can be achieved within the available gravity head. Inclusion removal becomes increasingly uncertain with diminishing target particle sizes [J1]. It is with these considerations in mind that a new approach to inclusion control for bulk steels is sought. The following section discusses the principal build-up mechanisms associated with the flow in nozzles. This then introduces the idea of using centripetal acceleration induced by curved flows for the purpose of directing particulate inclusions to a refractory surface.

1.1.1 Alumina Build-up

Alumina inclusions are known to adhere to one another [K7, K9] or to refractory surfaces at steel making temperatures [N1, W1]. Needless to say, alumina deposits are seen as a problem and production methods have been developed to alleviate the problem. Flow patterns in liquid steel at slide gates and stopper nozzles can contribute to excessive clogging in the continuous casting of steel and may therefore result in severe disruptions to the casting process [H4]. Design modifications to nozzles and methods such as gas injection have been developed to reduce the chance of inclusions adhering.

The problem of alumina build-up in nozzles has been examined by Wilson [W4], who has offered explanations for the deposition mechanism and the location of build-up deposits. Centripetal forces are known to contribute to particulate movement [K1]. Small alumina inclusions in steel have a density that is approximately half that of the melt and in a curving flow they will move to the centre of rotation. Wilson [W4] first modelled the fluid flow into a nozzle using a computational fluid dynamics (CFD) technique. Particle trajectories were then imposed on the calculated velocity field to predict the location at which particle sizes contacted the nozzle surface. This was done for different nozzle entry types and helped to explain the observed build-up patterns in

the actual nozzles. The centripetal force generated in the curved flow as the liquid entered the nozzle caused the 90 μm equivalent spherical diameter inclusions and larger to travel to the walls of the nozzle were they subsequently adhered. The deposition of smaller particle sizes was attributed to the turbulent eddies in the fluid. Assuming an impurity of equivalent spherical diameter d_p follows a fluid moving through a curved path of radius r, with the same tangential velocity v_θ as that of the fluid, then a force is imposed on it due to the density difference $\Delta\rho$. The radial velocity $v_{r.particle}$ of the inclusion based on the Stokes law is given as

$$v_{r.particle} = \frac{d_p^2 \cdot \Delta\rho \cdot v_\theta^2}{18 \cdot \mu \cdot r} \qquad 1.1$$

This may not always be the case in rotating flows and deviations from Stokes's law occur with particle size and fluid velocity. It should be emphasised that the centripetal force acting on an alumina particle in a rotating flow increases with fluid velocity, particle size and with reducing radial curvature.

Although the centripetal transport of particulate inclusions can be damaging [H4] it may also be exploited for inclusion removal (disentrainment) [W4]. If smaller diameter particles than those associated with directed tundish flows are to be separated out of the flow, a larger, more consistent centripetal force is required. A process tool that induces spiral rotation in a liquid and therefore imposes an enhanced radial acceleration on a particulate suspension for the purpose of separation is the hydrocyclone.

1.2 The solid core hydrocyclone

This thesis presents a study of a novel technique for the removal of particulate inclusions from liquid steel in which the principal of the hydrocyclone is adapted for steel treatment to enable the cyclone to act as a filter. This idea was initially proposed in an

EPSRC CASE Award application† submitted in 1993 for which British Steel Technical, (now the British Steel Technology Centre) became the collaborating company. In this modified form of the hydrocyclone, the liquid phase is injected tangentially into a tapered annulus formed by inserting a tapered conical solid core into the cyclone body, thereby inducing a confined spiral fluid rotation. The solid inclusions have a lower density than the liquid and therefore are caused to migrate towards the centre of rotation due to the centripetal force imposed on them by the swirling motion. The central solid refractory candle along its length acts as a capture surface for the particulate inclusions. The flow is unidirectional and discharges at the hydrocyclone apex. The new idea is shown schematically in figure 1.1. As steel can not be pumped easily it was recognised that the driving head for this device would probably have to be provided by gravity heads within the limits available to the steel making process and the study is therefore based upon possible driving heads that could be achieved within existing plant. If for example, the device were placed at the teeming nozzle, a maximum melt driving head of up to 3 m could be available. On a smaller scale, the required driving head might be achieved using a vertical pouring tube. Possible arrangements are suggested schematically in figure 1.2.

---

† A.E.Wraith, "Inclusion removal by rotating fields" Dept. Mechanical, Materials and Manufacturing Engineering, University of Newcastle Upon Tyne, July 1992.

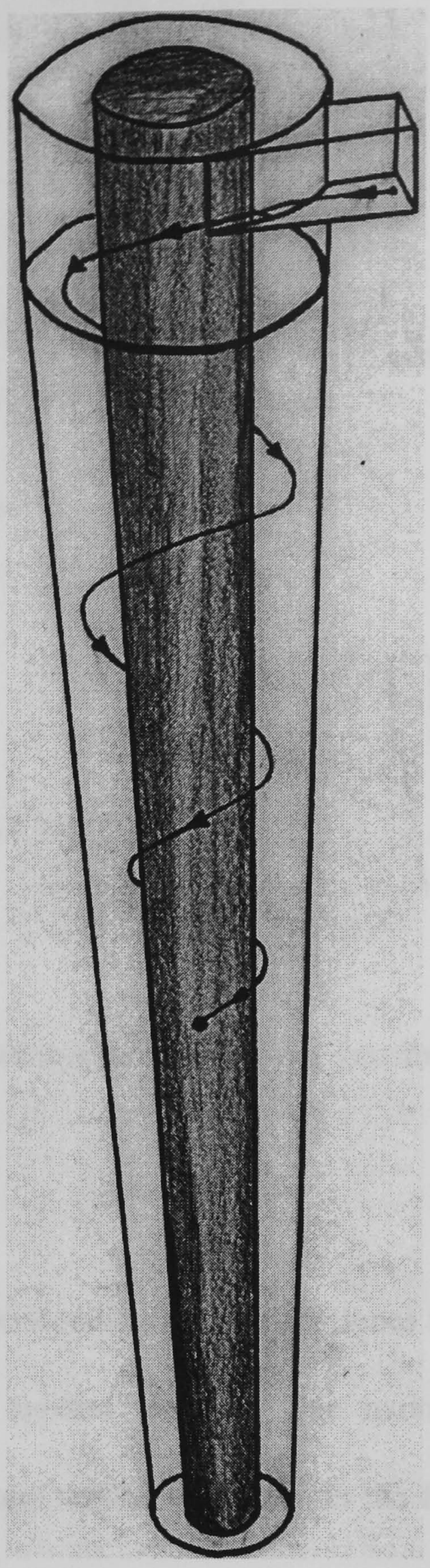

Figure 1.1. Schematic diagram of the solid core cyclone showing a possible particle trajectory.

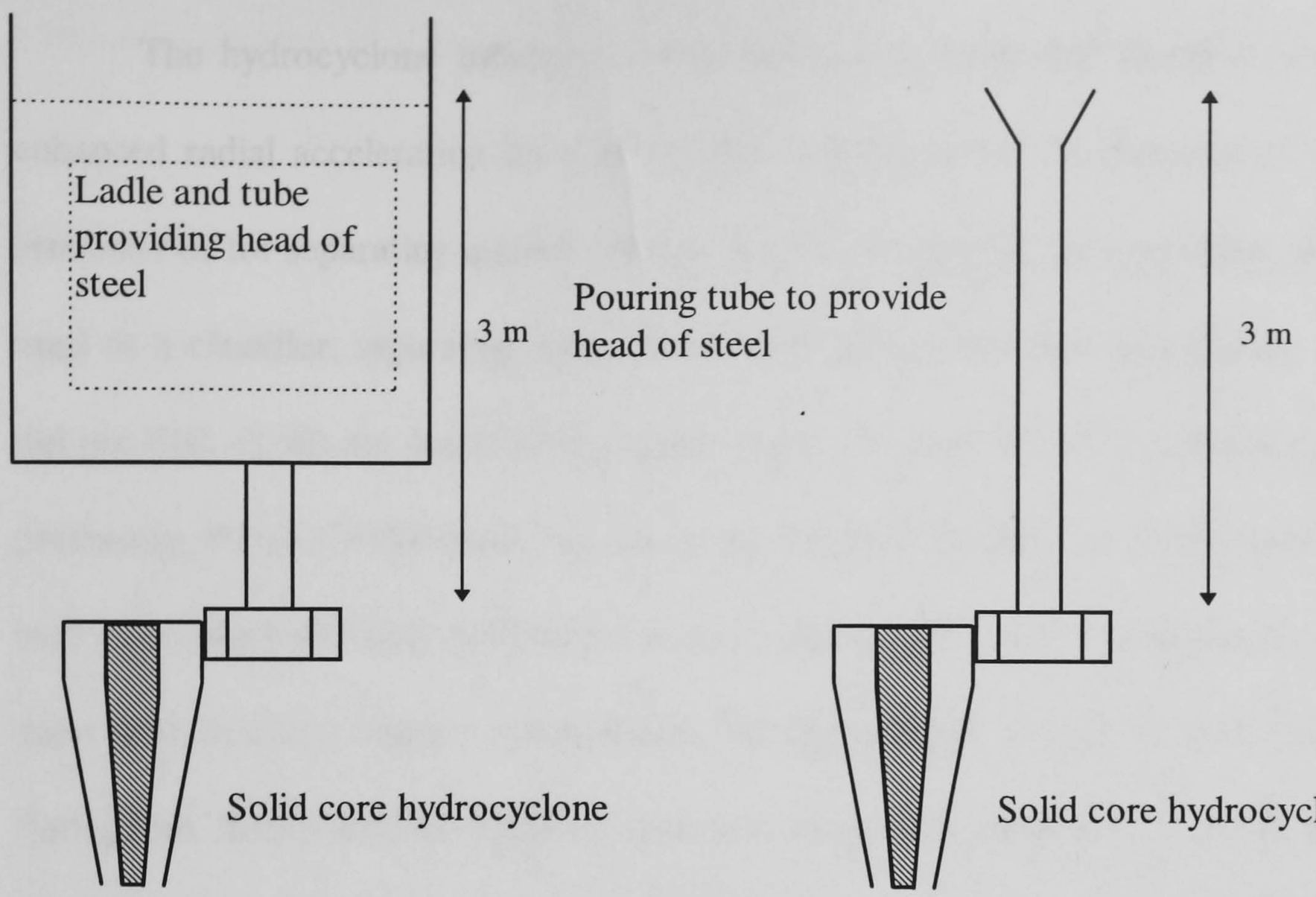

Figure 1.2. Schematic arrangements showing possible ways of providing the driving head

The present understanding of hydrocyclones forms a basis from which to analyse the new technique as applied to steel. The main features and characteristics of a conventional hydrocyclone will be discussed in the following section as an introduction to the special case of the solid core modification. In the end , the study showed the idea of the solid core cyclone at 3m working head was feasible and at that point the industrial collaborator British Steel proposed a pilot trial.

1.3 An introduction to the hydrocyclone

The hydrocyclone induces spiral rotation in a liquid and therefore imposes an enhanced radial acceleration on a particulate suspension for the purpose of separating size and / or for separating mineral species. In minerals processing operations, it is mainly used as a classifier, separating sizes. The hydrocyclone was first patented in 1891, but did not find significant practical application until the early 1950's in mineral and mining processing industries and more recently in the chemical industry. Hydrocyclones are now well established and their application is still widening [B8, S7]. The absence of moving parts and simple compact construction, combined with a high volume of material throughput means that the hydrocyclone is a more convenient and practical phase and size classifier than other, slower sedimentary devices. Unfortunately their potential has yet to be fully realised since the wide range of possible design and operating variables mean that their operation is not fully understood and still being researched.

The conventional hydrocyclone design is shown schematically in figure 1.3. It normally consists of a conical vessel attached to a cylindrical top. There are two outlets, both on the axis of symmetry, the underflow, which is situated at the apex of the cone and the overflow which is an inner tube descending from the top of the cyclone, usually referred to as the vortex finder because of its stabilising effect on the vortex flow around it. A tangential inlet that can be either circular or rectangular in cross section is located as close to the top of the cylindrical top section as possible. The liquid containing the suspended material is injected tangentially into the stationary vessel. This causes a swirling vortex motion, see figure 1.4, that exerts a radial acceleration on any suspended material. Particles of different sizes have different Stokes velocities, and separation occurs because the larger move more quickly and therefore further than the small across the cyclone radius in the residence time of the spiral flow. The direction and extent of

this radial acceleration, for a given hydrocyclone design is dependent on the density difference between the suspended material and the liquid carrier phase.

A hydrocyclone in which the density of the particulate phase is greater than the liquid carrier phase is the most common type in the minerals processing industry. In hydrocyclones of this type the larger particles migrate outwards to the cone wall where they assume a downwards spiral and exit at the underflow. The smaller particles have a low Stokes velocity, which means they migrate more slowly and therefore their distribution across the flow changes little. Those in the centre are captured in the upward flow and spiral upward and out through the vortex finder see figure 1.4. The rest are discharged with the coarse fraction at the underflow. The main use of the hydrocyclone in mineral processing is as a classifier where it has proven extremely efficient at fine separation sizes. In grinding circuits the underflow discharge is normally recycled and the overflow moves on to the next stage in the processing [A2, B8, S7]. The vortex finder controls the separation and the flow leaving the cyclone. Figures 1.5.1 and 1.5.2 show some typical radial parallel hydrocyclone arrangements used by the minerals processing industry, figure 1.5.1 is typical of the type used for ore processing, while figure 1.5.2 shows smaller hydrocyclones used for dealing with slimes. The effectiveness of separation depends on cyclone dimensions and operating conditions, which tend to become specific factors in design. Smaller diameter hydrocyclones give better separation efficiency for the same pressure drop [B8, S7]. Therefore, banks of small diameter hydrocyclones are used in parallel to treat large flow rates.

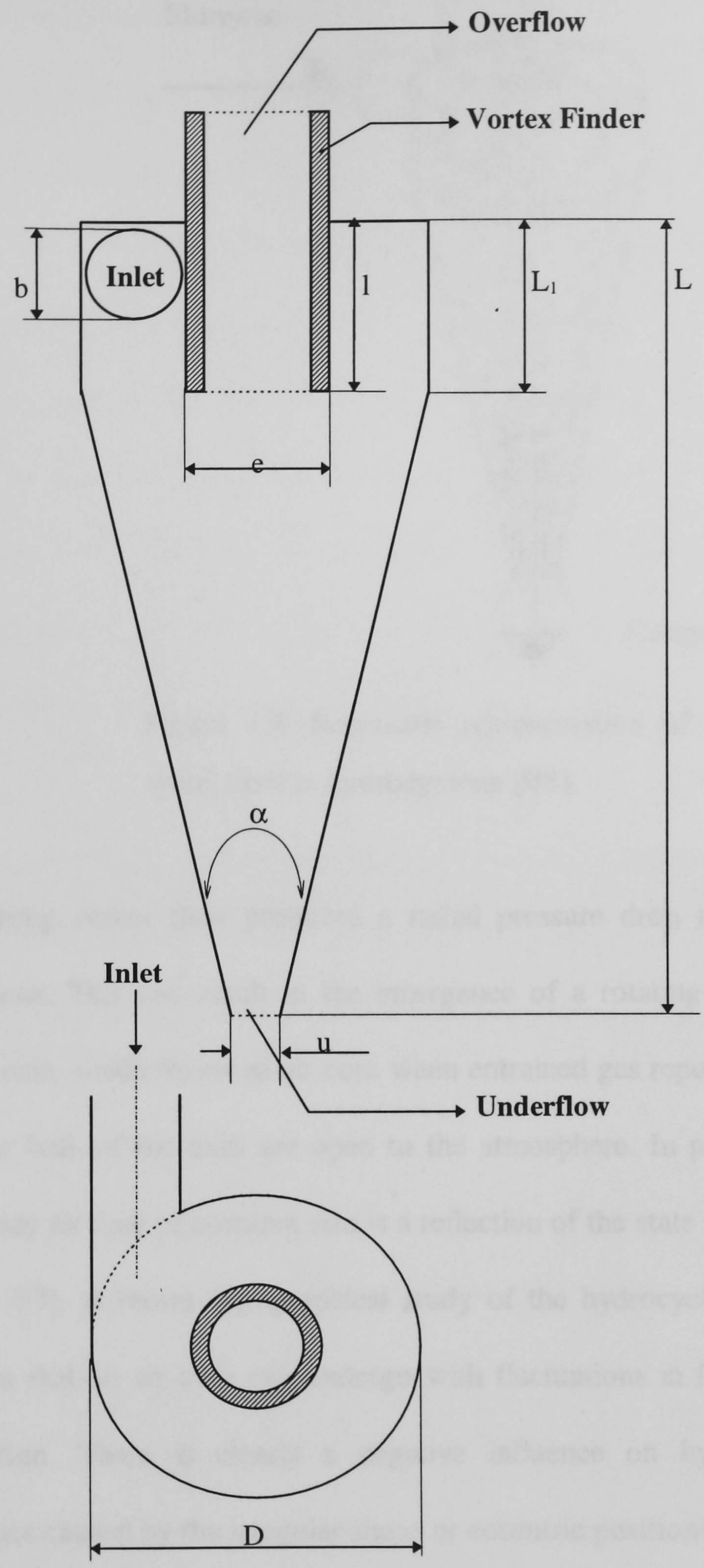

Figure 1.3. Showing principle features of a hydrocyclone.

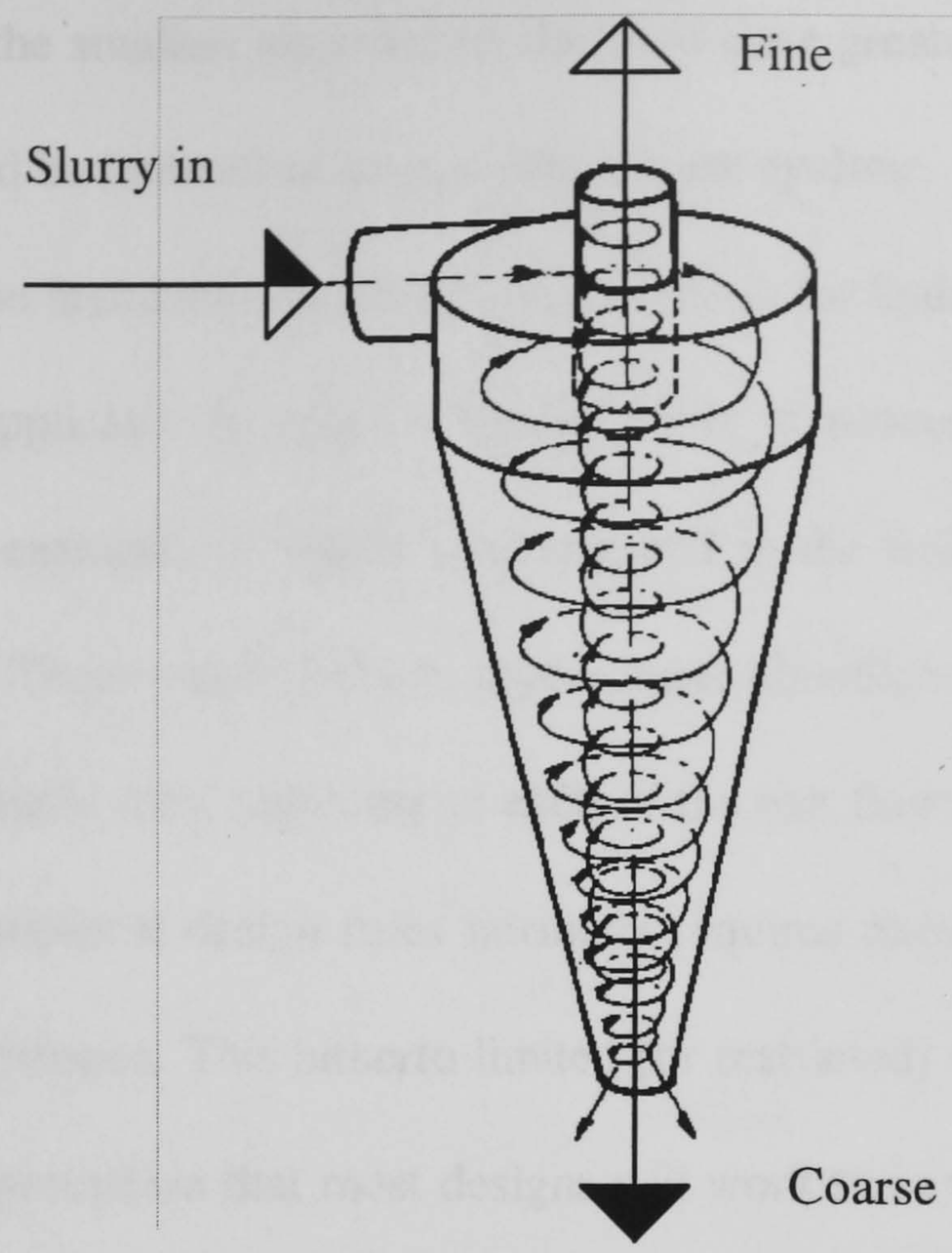

Figure 1.4. Schematic representation of the spiral flow in hydrocyclone [B8].

Strong vortex flow produces a radial pressure drop towards the axis of the hydrocyclone. This can result in the emergence of a rotating cylindrical free surface about the axis, which forms an air core when entrained gas reports to the central axis or if either or both of the exits are open to the atmosphere. In practice, stable operation with a steady air core of constant size is a reflection of the state and stability of the spiral flow [B8, S7]. A recent topographical study of the hydrocyclone showed the violent instabilities that an air core can undergo with fluctuations in flow rate and particulate concentration. There is clearly a negative influence on hydrocyclones processing performance caused by the irregular shape or eccentric positioning of an air core [W2].

This aspect of the flow will be discussed in relation to the stabilised flow in the solid core hydrocyclone design, which aims to suppress the formation of an air core. The pressure on the solid core is never less than that of the surroundings. Which can be

arranged by making the smallest diameter of the solid core greater than the diameter of any air core that could be induced in an equivalent open cyclone.

The bulk of the literature describing design criteria for hydrocyclones is limited to empirical formulae applicable to specific special cases in processes which have many significant variables, examples of which can be found in the following references [A2, B8, D4, R3, R4, S7]. These can be used to approximate classification efficiency, which is the distribution of particle sizes reporting to each of the exit flows. Normally, the design optimisation under empirical design rules normally requires experiment or trial for the confirmation of performance. This hitherto limited (or restricted) view of design analysis may stem from an appreciation that most designs will work to some limited extent given a realistic pressure drop. To quote Bradley [B8]

> "It speaks highly of the versatility of the cyclone that notwithstanding our lack of knowledge of its basic principles, it has proved satisfactory in so many varied applications".

Figure 1.5.1.

Figure 1.5.2.

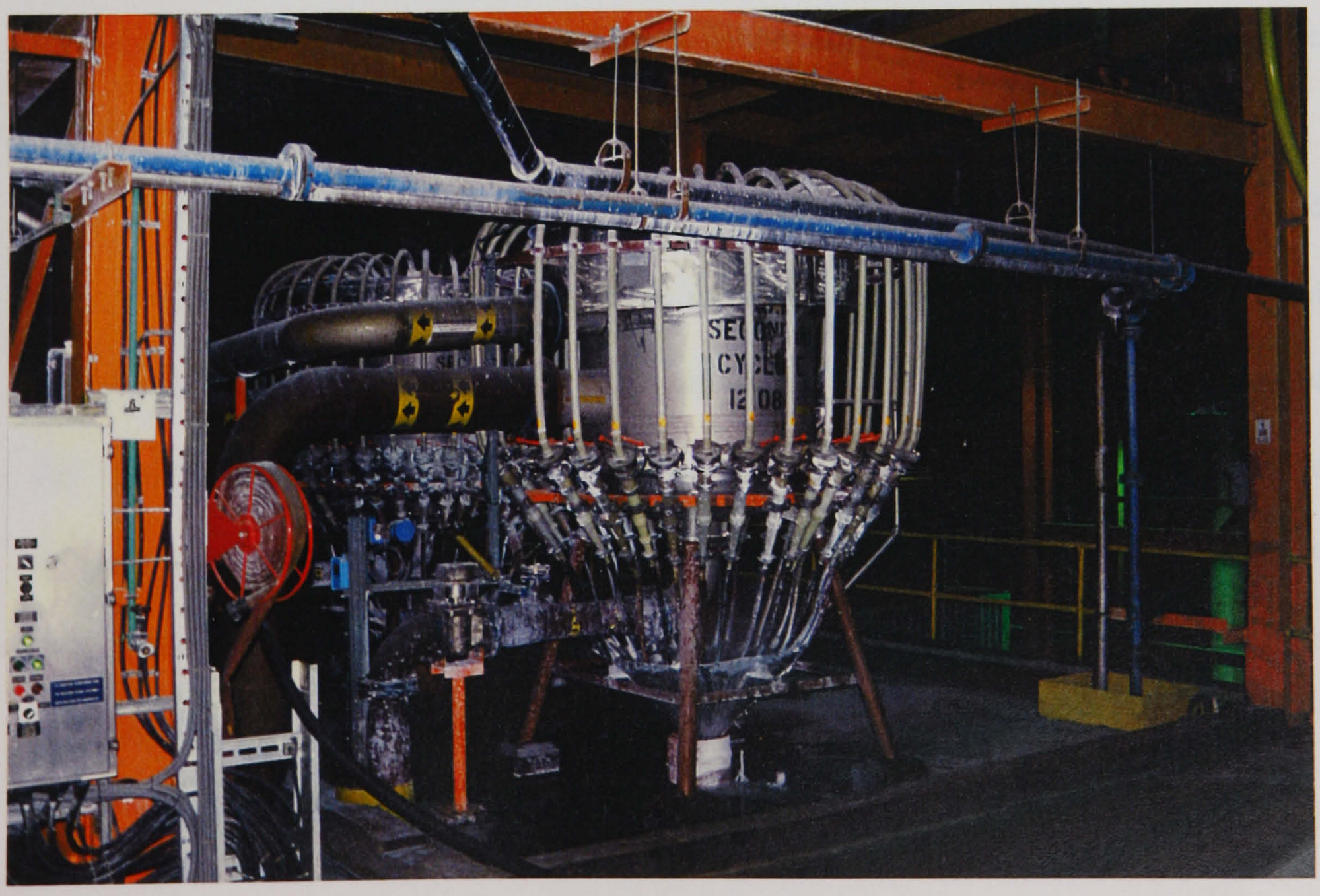

Figure 1.5.1 and 1.5.2. Show radial parallel hydrocyclone arrangements. Figure 1.5.1 is typical of the type of hydrocyclone used in ore processing, while figure 1.5.2 shows small radius cyclones for dealing with slimes.

1.3.1 Flow patterns in a hydrocyclone

One of the earliest and most notable experimental studies of the flow patterns in the hydrocyclone is described in the classic paper by Kelsall of 1952 [K2]. Before then, investigations had been limited to basic operational classification experiments and theoretical approaches that lacked experimental understanding. Kelsall's work was aimed at determining the exact mechanics of separation in the hydrocyclone. Understanding the velocity distribution within the flow field is important in setting up a theoretical model of the separation process, and ultimately for simulating particle trajectories from which theoretical performance can then be predicted. The technique employed by Kelsall was the first published non-intrusive flow measurement of the conventional hydrocyclone, unlike previous disruptive hot wire anemometry and pitot pressure measurements which are described in Bradley [B8]. Fine aluminium particles that followed the motion of the fluid were observed through a microscope that had rotating objectives, effectively cancelling the tangential motion of the particles and giving a direct measurement of their components. This approach and other visual methods form the basis of one aspect of the current study and are discussed in more detail in Chapter VI.

Kelsall resolved the fluid velocity into three components, tangential, radial and axial. The flow field can generally be taken as axisymetric except for the region in and just around the tangential inlet section. Figures 1.6.1, 1.6.2 and 1.7 show the shape of the experimentally determined axial and tangential velocity flow profiles plotted at different axial positions as they changed with radius, and the flow patterns that can exist in a hydrocyclone. It can be seen from Kelsall's data that the radial velocity of the flow is so small when compared with the axial and tangential velocities in the body of the

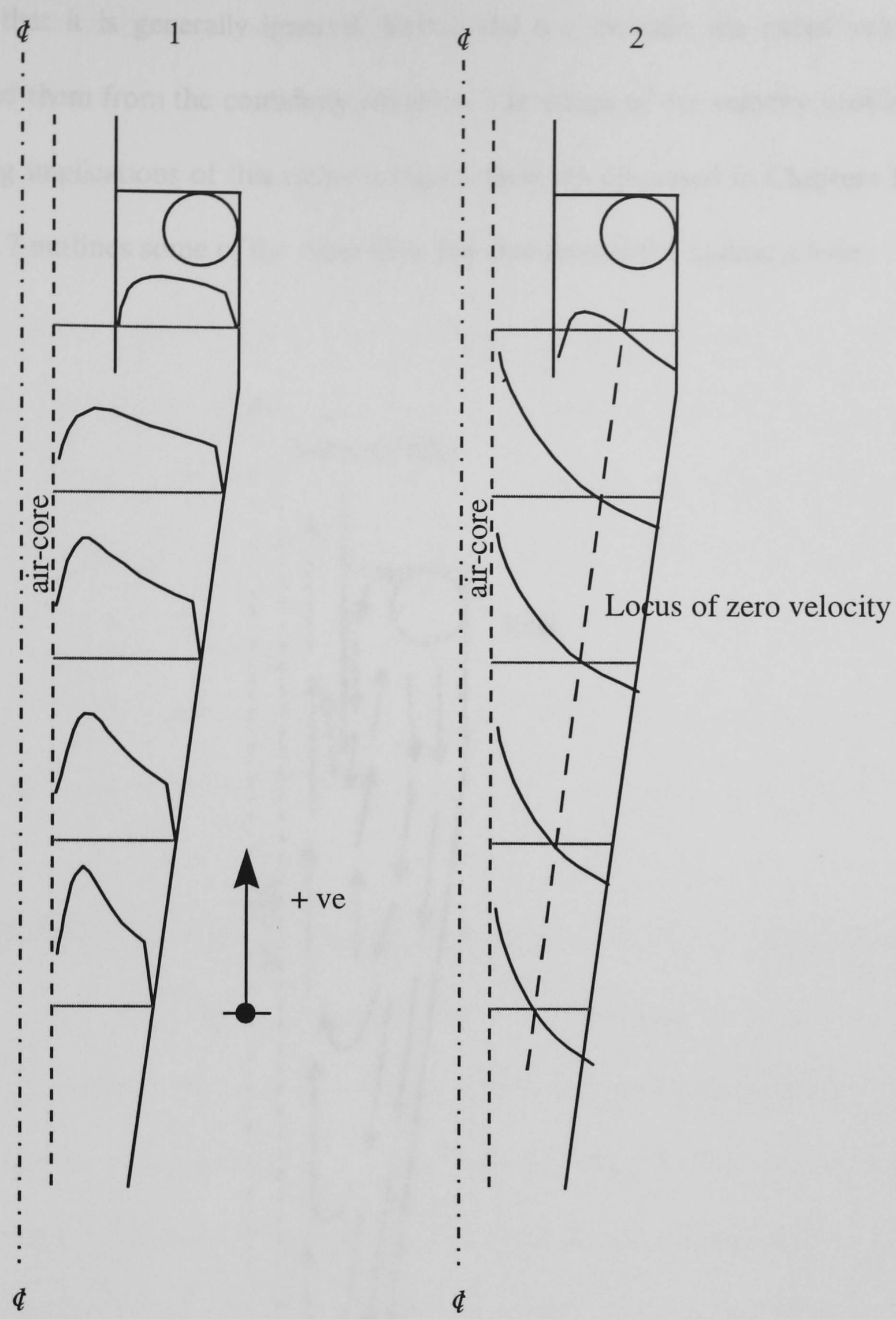

Figure 1.6.1 and 1.6.2. Showing the tangential and axial velocity distributions in a hydrocyclone based on the observations of Kelsall [K2].

cyclone that it is generally ignored. Kelsall did not measure the radial velocities but calculated them from the continuity equation. The shape of the velocity profiles and the modelling implications of this rather complex flow are discussed in Chapters II and III. Figure 1.7 outlines some of the other flow features seen in the hydrocyclone:

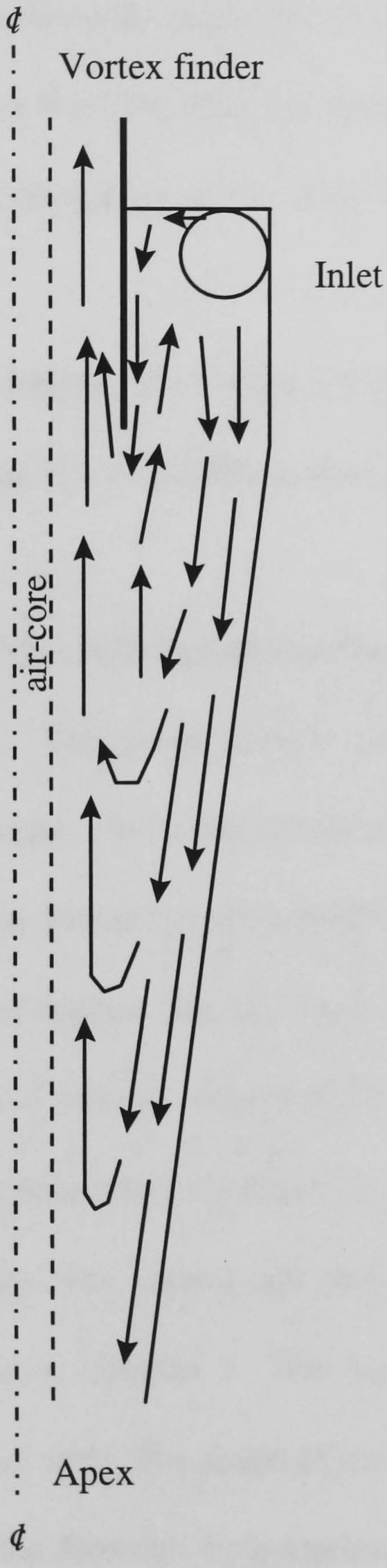

Figure 1.7. Showing a simplified account of the flow patterns in a hydrocyclone.

- The existence of an outer region of downward flow and an inner region of upward flow necessitates a position at which there is no vertical velocity, known as the *locus of zero vertical velocity* [B8, S7].

- The pressure gradient along the top of the hydrocyclone drives the fluid radially inward. This fluid moves down the vortex finder exiting in the overflow stream and is known as *short circuiting*. Particles that find their way into this short circuiting flow are not subject to the full separating action of the hydrocyclone [B4, B8, S7].

- In some hydrocyclone designs the natural up flow of the vortex is in excess of overflow stream, resulting in a recirculation zone or*toriodal vortex* [B8, S7].

Kelsall's work has been criticised because he used a longer than average vortex finder to stabilise the flow. This eased particle visualisation by reducing noise from turbulent fluctuations. However, the results advanced understanding and have been used in the validation of countless theoretical models [B5, B8, R3, S7], making it one of the most definitive hydrocyclone studies. Kelsall's work for the minerals processing industry made the hydrocyclone one of its most elegant, functional and versatile tools.

A later flow visualisation study by Knowles et al [K5] of a hydrocyclone with a normal length vortex finder was carried out using high speed cinematography, the technique is discussed later in Chapter 5. This hydrocyclone was operated in closed circuit and ran without an air core. The shape of the measured velocity profiles matched those of Kelsall. Because the Knowles hydrocyclone ran without an entrained air core has made it a much simpler case to model theoretically. The results of the Knowles work have therefore been used for the validation of a number of both analytical and numerical

models [B3, D3, S2]. Knowles velocity data has been used to validate the modelling work in Chapters 2 and 3.

1.3.2 Hydrocyclone development

The early sixties saw the first experimental optimisation study by Rietema [R3] who investigated and suggested some design parameters, building on the work of Kelsall. From these two works resulted the next stage in the understanding of hydrocyclones, enabling the specification of a set of relations between the hydrocyclone dimensions (ref. table 1.1 and figure 1.2 for notation). The cylindrical section is assumed to be at least as long as the vortex finder. The included or cone angle (though not specified) is suggested from the ratio of L/D to be less than 30°. Fontein [F2], in a further optimisation study, found that the best practical angle for recovering mixed suspensions was around 10° in small cyclones. A correct choice of cone angle helps maintain the swirl velocity, which would decay along the central axis in a purely cylindrical tube as a result of frictional losses [C1].

When Svarovsky published the book titled "Hydrocyclones" in 1984 [S7], the idea of using an adapted hydrocyclone to separate two immisible liquids and produce a highly concentrated yet small volume sample of a lighter phase was novel. The work carried out under the supervision of Thew [H2] dealt with the dewatering of oils, aimed at the off-shore industry. The new dewatering application required new thinking, and an extensive development program was undertaken. This was helped at the time by recent advances in computers, and the numerical representation of fluids flows that is now changing the approach to hydrocyclone design. Hargreaves [H2], who carried out the

work, developed an effective 2-dimensional computer flow model which was then used in one of the first computational optimisation studies of the hydrocyclone.

Table 1.1. Suggested relations between the hydrocyclone dimensions determined by Rietema, see figure 1.2 for symbol definitions.

Components	Ratio
L/D	5
l/D	0.4
e/D	0.34
b/D	0.28

1.4 The solid core hydrocyclone investigation

The solid core cyclone described previously is a simple design based on the conventional hydrocyclone. Since an inclusion laden overflow would be inappropriate for steel, the solid core replaces the conventional vortex finder and extends over the length of the cyclone, see figure 1.1. The need to establish the validity of the solid core cyclone as a method of cleaning melts prompted the present study. The new design has many variables and consequently quite an extensive study is needed but the present understanding of conventional hydrocyclones forms a basis from which start. The strategy for the present study was therefore to elucidate the mechanics of the flow system in a conventional hydrocyclone before applying the theories to the new hydrocyclone concept.

In the thesis each aspect of the work is dealt with in sections or chapters. The associated literature and its implications to the work are dealt with at the beginning of each section. Briefly, classical analytical approaches to the complex swirling flow in a conventional hydrocyclone have been considered. A comparison of different turbulence modelling techniques have made it possible to predict the flow in a hydrocyclone by numerical methods. This has been done using a commercially available computational fluid dynamics (CFD) package. The CFD package was then used to establish the feasibility of the solid core cyclone idea and thereby gave initial direction to a physical modelling study.

Chapter II

Fluid dynamics of the hydrocyclone

2.1 Introduction

This chapter deals with the application of fluid dynamics in the hydrocyclone. The description of the velocity field is essential to effective hydrocyclone design. However, effective modelling techniques have been both limited in scope and difficult to apply. The limitations of analytical modelling techniques for the description of the complex flow patterns in a hydrocyclone is discussed. A simple 2-dimensional model is developed by applying a finite difference method to the Batchelor formulation for steady axisymmetric flow with swirl [B2].

Industrial hydrocyclones are used in many cases with slurries of different concentration and particle sizes. These flows have a complex behaviour, with varying density and viscosity and are therefore difficult to describe mathematically. When dealing with concentrated slurries, empirical models may be the best method of approach. For lower particulate concentrations theoretical studies of the flow in hydrocyclones, based on the fundamental Navier-Stokes equation, have included both numerical models [D3, D8, H2, H5, P1, P2, R1, R2] and analytical studies, the most notable and extensive being those by Bloor and Ingham [B3, B4, B5]. Analytical analysis, although not as versatile as numerical modelling, offers a clear insight into the underlying physical mechanisms of fluid flow in the hydrocyclone. The full Navier-Stokes equations [Appendix I] are a set of non-linear, coupled, parabolic partial differential equations [K10]. The analytical approach makes simplifying assumptions (leading to the linearising of the equations)

aimed at establishing a solvable mathematical model that describes the fluid motion. These assumptions may be quite drastic. However, the complexity of the flow in a hydrocyclone has made it very difficult to form assumptions that would result in a solvable analytical model and this has been one of the key aspects slowing the understanding of how the hydrocyclone actually works. The following section discusses some of the standard simplifying assumptions that may be used to modify the Navier-Stokes equations applied to the description of the fluid motion in the hydrocyclone.

2.1.1 Describing cyclonic flows

The "ideal fluid" assumption is purely hypothetical, describing a fluid with no viscosity and no compressibility, and it is a key simplification applied to the Navier-Stokes equations. This assumption is based upon Prandtl's observations [P4, P5] of the nature of turbulent flows. At high Reynolds numbers ($\rho Lv/\mu$), mixing has such a massive effect velocity profiles may be regarded as being independent of the viscous drag at the walls and therefore reflect only the kinetic effects of the flow. The flow outside the wall region is consequently assumed independent of molecular viscosity and may be treated as inviscid.

A second classification applied to ideal flow is the distinction between rotational and irrotational flow. An element of fluid may suffer rotation or distortion, or both, in the course of its motion. It is possible for a particle to distort without rotating. In irrotational flow the average of the angular velocities of two mutually perpendicular sides of a fluid element must equal zero [V2]. The velocity distribution of an irrotational fluid can be determined by a linear equation derived from the mass conservation equation [D6]. The velocity of the fluid may therefore be described in terms of velocity potential ϕ, hence this type of flow is also known as potential flow. Linearity is the distinctive property of

irrotational flow which allows the employment of many mathematical techniques [K10]. It is not possible to analyse rotational flow in the same depth as irrotational flow, since the governing equation is no longer linear. However, the flow in a hydrocyclone consists of both rotational and irrotational parts and also may not be assumed inviscid across the whole flow. The following discussion considers difficulties and identifies the significant aspects of the fluid dynamics applied to the hydrocyclone.

2.1.2 Observations of swirl in the hydrocyclone

The experimental work of Kelsall [K2] showed that the tangential velocity increases sharply with radius in the central core region under the vortex finder and that thereafter it decreases with radius. By identifying the radial position at which the maximum tangential velocity occurs, the tangential velocity profile can be divided into two regions. Figure 2.1 based on Kellsals results shows that the central region is characterised as a forced vortex following the "constant v/r law", while the outer annulus away from the wall has a free vortex velocity distribution and obeys the "constant vr law" [R3]. A free vortex, like sink water draining down a plug hole is irrotational, whereas in the forced vortex of a centrifuge for example, the fluid rotates as a solid body having constant angular velocity and is rotational.

Flows in the cyclone do not conform exactly to the vortex laws because the velocity profile is affected by internal friction caused by viscosity and turbulence. The inviscid assumption does not therefore apply to the whole flow region. Turbulence intensities in swirling flows are increased due to the destabilising effects of the added angular momentum, a matter which is discussed in more detail in Chapter III. Figure 2.1 illustrates how the tangential velocity profile conforms fully neither to the free nor to

forced vortex conditions. It is therefore convenient to describe it by an empirical expression

$$v_\theta r^n = \text{const} \qquad 2.1$$

The empirical exponent n is dependent on the cyclone and its operation. For free vortex rotation, n = 1, a condition which represents complete conservation of angular momentum. When n = -1, the equation represents fluid rotating as a solid body with constant angular velocity.

In the free vortex flow of the hydrocyclone there is a high shearing action. Movement of concentric layers of fluid at increasing tangential velocity as radius decreases produces shear forces. In the forced vortex flow the fluid rotates as a solid body and there is consequently no shearing. From Bradley [B8] the value of n used for hydrocyclones based on empirical measurements is usually around 0.5 to 1.0. This indicates that in the hydrocyclone, the condition tends to that of the free vortex in which conservation of angular momentum is implied. The next section moves on from their empirical representation, elucidates the fluid dynamics involved and presents a simple model based on the assumptions of inviscid flow and free vortex motion.

2.2 Solving the flow in a free vortex

The following investigation of the free vortex motion of an inviscid fluid is based on the assumptions in the previous section that the hydrocyclone tends towards free vortex behaviour. The description of the flow field varies in complexity in the

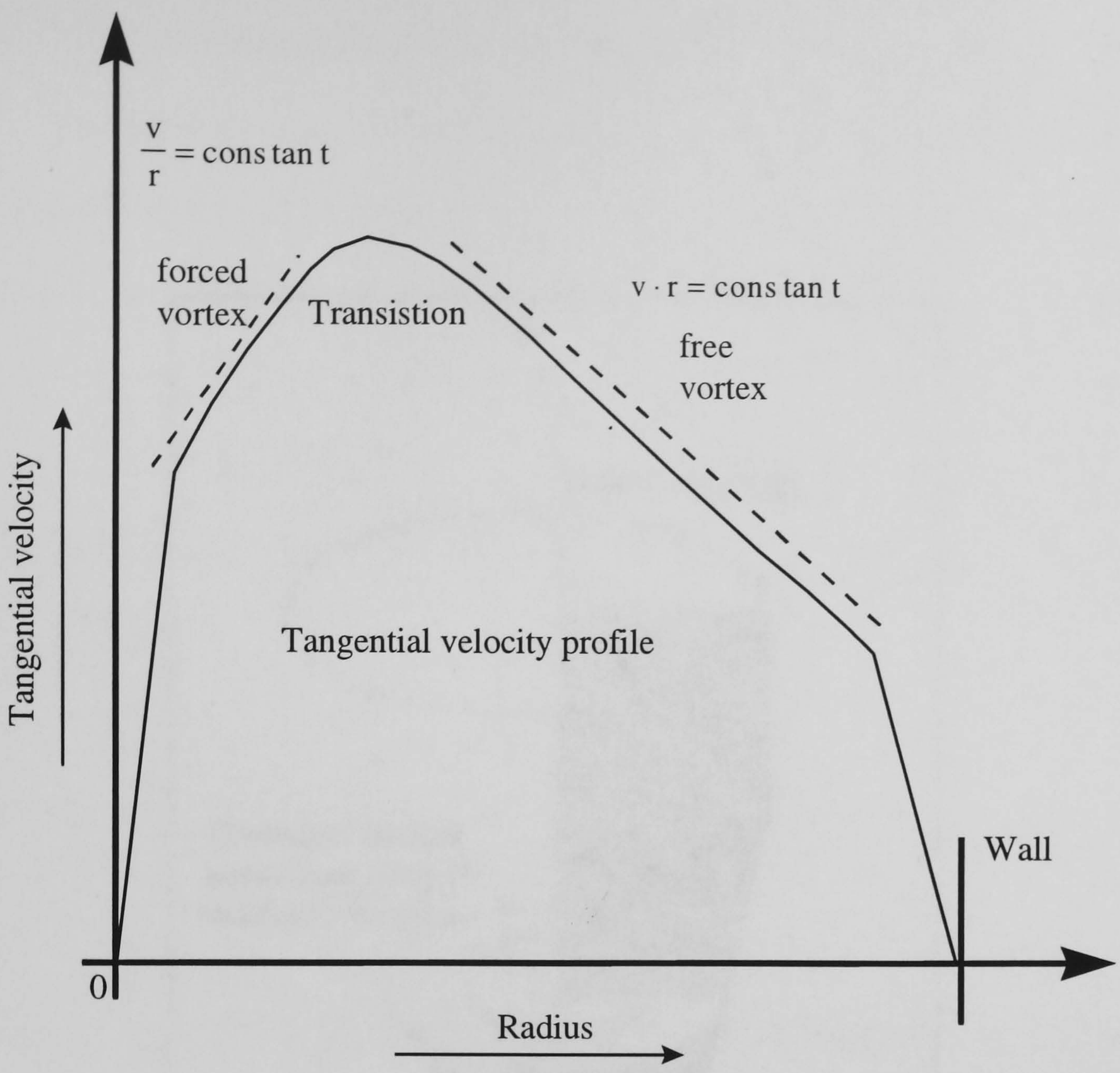

Figure 2.1. Illustrates how the tangential velocity profile conforms fully neither to the free nor to forced vortex conditions.

hydrocyclone depending on which plane is considered. For simplicity and consistency cylindrical polar co-ordinates (z,r,θ) are used, with corresponding velocity (v_z,v_r,v_θ) and vorticity $(\eta_z,\eta_r,\eta_\theta)$ components. The flow is considered in two ways, shown in figure 2.2, by taking a slice perpendicular along the axis of symmetry and by taking a horizontal 2-dimensional slice to the axis of symmetry.

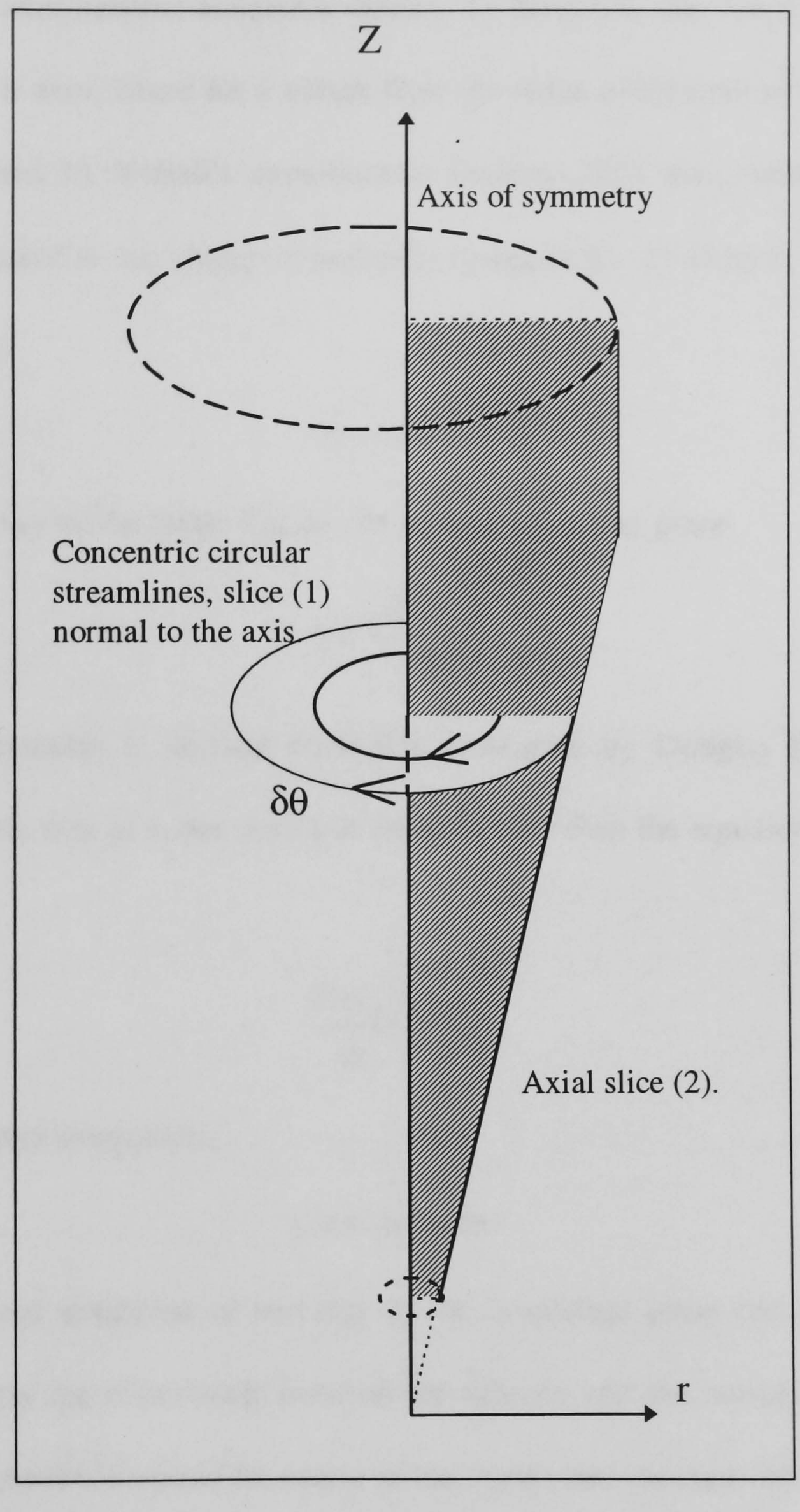

Figure 2.2. Showing cylindrical co-ordinate system with 2-dimensional slices.

2.2.1 Proof of irrotational flow in a free vortex

The following observation has not previously been noted in the literature. Referring to figure 2.2, consider first the horizontal plane slice (1) in which the streamlines are axisymmetric concentric circles. By definition, the velocity perpendicular to a streamline is zero, hence for a vortex flow the radial component of velocity $v_r = 0$. This is supported by Kelsall's experimental findings [K2] that radial velocities are negligible compared to the tangential and axial components. Vorticity η, from Batchelor [B2], is given as

$$\eta = \text{curl } v, \tag{2.2}$$

whence neglecting all the terms that do not correspond to this plane,

$$\eta = \frac{1}{r}\frac{\partial(rv_\theta)}{\partial r} \tag{2.3}$$

This same expression is derived from first principles by Douglas [D6]. Since, by definition the vorticity in a free vortex is equal to zero then the equation can be written as

$$\frac{d(rv_\theta)}{dr} = 0, \tag{2.3}$$

which given, upon integration,

$$v_\theta \cdot r = \text{constant}. \tag{2.4}$$

Thus, the derived definition of vorticity in the horizontal plane can be expanded to describe correctly the relationship between the velocity and the radius in a free vortex. The velocity increases towards the centre of the vortex and theoretically tends to infinity as the radius tends to zero. Since the free vortex is irrotational, the Bernoulli constant remains the same for all the streamlines.

2.2.2 Derivation of the radial pressure distribution due to swirl

The radial pressure distribution due to the swirling fluid motion in a hydrocyclone, first introduced in Chapter I, is now explained on the basis of fluid dynamics principles. When fluid flows in a curved path, the velocity of the fluid along any streamline will undergo a change in direction and there is an acceleration towards the centre of curvature. The consequent rate of change of momentum of the fluid must, according to Newton's second law, result from a force acting radially across the streamlines and thus produce an increase in radial pressure. This is shown by taking the momentum equation for steady state flow in terms of vorticity η, see Batchelor [B2]. Neglecting body forces, the vector form is

$$v \times \eta = \nabla\left(\frac{1}{2}v^2 + \frac{p}{\rho}\right). \qquad 2.5$$

Following Batchelor [B2], we introduce the quantity H defined by

$$H = \frac{p}{\rho} + \frac{1}{2}v^2, \qquad 2.6$$

which represents the total head of fluid. Now for axisymetric vortex motion in the horizontal plane, the only velocity component of consequence is v_θ. Combining equation 2.5 with the definition for vorticity η in this plane, equation 2.2, and neglecting all the derivatives in the axial direction, it follows that

$$\frac{dH}{dr} = v_\theta\left(\frac{v_\theta}{r} + \frac{dv_\theta}{dr}\right). \qquad 2.7$$

Which gives the radial pressure gradient as

$$\frac{1}{\rho}\frac{dp}{dr} = \frac{v_\theta^{\,2}}{r}. \qquad 2.8$$

This derivation of the radial pressure distribution or centrifugal head helps to characterise the flow in the hydrocyclone. Centrifugal head accounts for the largest consumption of the total driving head in the hydrocyclone [R3]. The radial pressure distribution determines the position and dimensions of the internal air-core. Driesen [D7] first derived this expression relating the tangential velocity v_θ to the radial pressure distribution by applying similar assumptions to the full Navier-Stokes equations. In the literature this radial pressure relationship has also been derived geometrically from first principles by both Bradley and Douglas [B8, D7].

These solutions considered so far are axisymmetric and independent of z and therefore essentially 1-dimensional. Although this approach improves comprehension of the mechanics of the flow in a hydrocyclone, it has only a limited application. Developed next is an axisymmetric model that describes the flow in 2-dimensions in the axial plane, i.e. a treatment for slice (2) of figure 2.2, using Stokes stream function.

2.2.3 Axisymetric flow with swirl applied to the hydrocyclone

Attempts to model the hydrocyclone processes theoretically in this particular plane have met with limited success owing to the added complexity in this flow direction. The initial theoretical work of Bloor and Ingham [B3] showed that the velocity values derived from an irrotational treatment of the flow in the axial plane using velocity potential ϕ did not compare well with experimentally measured values. In Chapter I it was shown that there are circulation's and flow reversals in the axial plane signifying finite vorticity. It is therefore not reasonable to solve the flow in terms of velocity potential.

An analytical approach which describes the flow curvature in the axial plane of a hydrocyclone and incorporates the swirling component of the vortex is based on a derivation by Batchelor for steady axisymmetric flow with swirl [B2]. This describes steady axisymetric flow with swirl in terms of Stokes stream function, or vorticity stream function as it is sometimes known drawing on my own observations of section 2.2.1 and 2.2.2 to simplify the derivation. The problem is treated as 2-dimensional, axisymmetric and steady permitting a Stokes streamline to represent a (Bernoulli surface) of constant Bernoulli head formed by rotating the curve of constant Stokes stream function about the axis of revolution. This allows the azimuthal components of velocity v_θ and vorticity η_θ to be expressed in terms of Bernoulli surfaces, eliminating the interaction of the swirling component v_θ with the motion in the axial plane.

The model is developed using cylindrical co-ordinates in keeping with the previous example. Working in terms of Stokes stream function, the equations of continuity can be automatically satisfied for inviscid, incompressible steady flow. The velocity components v_Z and v_r are defined in terms of Stokes stream function by

$$v_z = \frac{1}{r}\frac{\partial \psi}{\partial r}, \qquad 2.9\ a$$

$$v_r = -\frac{1}{r}\frac{\partial \psi}{\partial z}. \qquad 2.9\ b$$

The vorticity components for axisymmetric flow are given as

$$\eta_z = \frac{1}{r}\frac{\partial (r v_\theta)}{\partial r}, \qquad 2.10\ a$$

$$\eta_r = -\frac{\partial v_\theta}{\partial z}, \qquad 2.10\ b$$

$$\eta_\theta = \frac{\partial v_r}{\partial z} - \frac{\partial v_z}{\partial r}. \qquad 2.10\ c$$

Stokes stream function is axisymmetric and may be described in terms of (z, r) co-ordinates, whence the azimuthal component of vorticity can be written

$$\eta_\theta = -\frac{1}{r}\left(\frac{\partial^2\psi}{\partial z^2} + \frac{\partial^2\psi}{\partial r^2} - \frac{1}{r}\frac{\partial\psi}{\partial r}\right) \qquad 2.11$$

Assuming steady flow, the following equations of motion follow from the momentum equation 2.5:

$$v_r\eta_\theta - v_\theta\eta_r - \frac{\partial v_z}{\partial t} = \frac{\partial H}{\partial z}, \qquad 2.11\ a$$

$$v_\theta\eta_z - v_z\eta_\theta - \frac{\partial v_r}{\partial t} = \frac{\partial H}{\partial r}, \qquad 2.11\ b$$

$$v_z\eta_r - v_r\eta_z - \frac{\partial v_\theta}{\partial t} = 0. \qquad 2.11\ c$$

H is a function only of z and r in axisymetric flow.

Equation 2.11 c may be written as

$$\frac{D(rv_\theta)}{Dt} = 0, \qquad 2.12$$

which represents uniform circulation round a material curve in the form of a circle centred on the axis of symmetry and normal to it (axisymmetric free vortex flow, see section 2.2.1).

In the steady state case the Stokes's streamline on which ψ is constant represents a stream surface formed by rotating the streamline curve about the axis of symmetry. The argument of Bernoulli's equation remains constant on the stream surface, from equation 2.6 it can be stated that

$$\tfrac{1}{2}\left(v_z^2 + v_r^2 + v_\theta^2\right) + \frac{p}{\rho} = H(\psi) \qquad 2.13$$

From equation 2.4 or 2.12 it is therefore possible to write as a function of ψ

$$rv_\theta = C(\psi). \tag{2.14}$$

Rearranging the vorticity equations gives

$$\eta_z = v_z \frac{dC}{d\psi}, \tag{2.15}$$

$$\eta_r = v_r \frac{dC}{d\psi}, \tag{2.16}$$

An equation describing η_θ in terms of H and C can be derived from either of the dynamical equations in the z or r directions

$$\frac{\eta_\theta}{r} = \frac{v_\theta \eta_\theta}{rv_r} + \frac{1}{rv_r}\frac{dH}{d\psi} = \frac{C}{r^2}\frac{dC}{d\psi} - \frac{dH}{d\psi}, \tag{2.17}$$

Combining the azimuthal component of the vorticity equation in terms of stream function gives

$$\frac{\partial^2\psi}{\partial z^2} + \frac{\partial^2\psi}{\partial r^2} - \frac{1}{r}\frac{\partial\psi}{\partial r} = r^2\frac{dH}{d\psi} - C\frac{dC}{d\psi} \tag{2.18}$$

From equations 2.8 and 2.14 it is possible to write

$$\frac{1}{\rho}\frac{\delta p}{\delta r} = \frac{v_\theta^{\,2}}{r} = \frac{C^2}{r^3} \tag{2.19}$$

so that

$$\begin{aligned} H &= \tfrac{1}{2}\left(v_z^2 + v_\theta^2\right) + \int \frac{C^2}{r^3}\,dr \\ &= \tfrac{1}{2}v_z^2 + \int \frac{C}{r^2}\,dC. \end{aligned} \tag{2.20}$$

In order to proceed with this equation it is necessary to impose some up-stream boundary conditions so that H and C can be described. Then ψ can be determined as a function of z and r over the whole field. H and C are only capable of being described by very simple functions of ψ. Batchelor therefore assumes the fluid up-stream has uniform

axial velocity U and rotates as a rigid body with angular velocity Ω. Since the stream function ψ is axisymetric the stream conditions are defined as

$$\psi = \tfrac{1}{2} U r^2 \text{ and } C = \Omega r^2 \qquad 2.21$$

and since the flow is cylindrical in the upstream condition

$$H = \tfrac{1}{2} U^2 + \Omega^2 r^2 . \qquad 2.22$$

Rewriting these upstream conditions as

$$C = \frac{2\Omega}{U}\psi \text{ and } H = \tfrac{1}{2} U^2 + \frac{2\Omega^2}{U}\psi , \qquad 2.23$$

indicates dependence of C and H on ψ over the whole field. The governing equation describing the flow therefore takes the form of a linear elliptic partial differential equation

$$\frac{\partial^2 \psi}{\partial z^2} + \frac{\partial^2 \psi}{\partial r^2} - \frac{1}{r}\frac{\partial \psi}{\partial r} = \frac{2\Omega^2 r^2}{U} - \frac{4\Omega^2 \psi}{U^2} . \qquad 2.24$$

Which until now has only ever been solved analytically.

In a flow that is described by an elliptical equation, influences at a point spread in all directions and therefore must be solved in terms of two co-ordinate directions. Examples of elliptical flows include recirculating (or separated) flows. The flow in a hydrocyclone behaves like an elliptical flow with flow separation in which high streamline curvature occurs. Elliptic equations are solved using a boundary value approach. That is, all points within the flow domain are determined from the conditions specified on the perimeter boundary.

[The literature revealed that] the equation above in spherical polar co-ordinates has been applied to the hydrocyclone in an investigation by Bloor and Ingham [B5]. They solved the equation analytically for a simple cone but treated it as closed system ignoring the effect of the underflow. A further analytical study was carried out by Hwang et al

[H8], modelling the underflow by incorporating a flow split ratio to describe the underflow and overflow boundary conditions. These two complicated analytical approaches involved using Bessel functions and non-dimesionalising the equation, obtaining answers for only the simplest of geometries.

The equation treats the axisymetric flow as a free vortex but, because of the use of Stokes stream function, it is possible to describe the rotational flow in the axial plane. This approach gives the best model to-date for a description of the flow in a hydrocyclone in two dimensions where turbulence is not considered. It is unfortunate that the development of this model for the hydrocyclone came so late. The publication of this approach coincided with new advances in computers and the representation of fluid flows with which more detailed analysis can be carried out, consequently its contribution to the literature has become more an exercise in understanding than an advance in design methods. Nevertheless, it was decided that solving equation 2.24 numerically instead of analytically could allow more realistic and versatile boundary conditions to be applied and deserved further investigation. As a general conclusion the use of an analytical approach to solution is illuminating, but the application of computational methods offers far greater scope for boundary conditions. A simple fast model was therefore developed to describe the swirling flow in a hydrocyclone. This proved to be a good exercise in numerical modelling and in understanding the hydrocyclone. The details are presented in the next section.

2.3 An inviscid numerical model for predicting axisymetric flow with swirl in a hydrocyclone

The previous section introduced an equation describing swirling flow for an axisymetric geometry, that could be used to describe the flow in a hydrocyclone. As a

preliminary to the more far-reaching computational study of the solid core cyclone discussed in later chapters, it was considered useful to attempt a solution of equation 2.24 by using a numerical method which would compliment the analytical approach of Bloor and Ingham [B5]. Although there are more complex equations which can be used to describe the flow field of a hydrocyclone it was thought that the initial development of a model based upon equation 2.24 would provide:

- a fuller understanding of cyclonic flows,
- first hand experience in using computational fluid dynamics [CFD],
- a possible rapid solution design tool for swirling flow systems,
- a basis for an initial feasibility investigation into swirling flows for cleaning molten metal.

The velocity data of Knowles flow visualisation experiment [K5] was adopted as a basis for model validation, in which the hydrocyclone operated without an air core. Other than the work of Kelsall [K2] who used a long vortex finder to stabilise the flow, it appears to be the best documented velocity data for a hydrocyclone and the most appropriate for this application.

Equation 2.24 can be expressed in either cylindrical or spherical co-ordinates. The literature favours spherical co-ordinates (s, λ, θ), see figure 2.3, as an approach that best suits the conical shape of the cyclone. In the previous section 2.2.3 cylindrical co-ordinates were used to maintain continuity with sections 2.2.1 and 2.2.2, though for modelling purposes spherical co-ordinates are preferable. The final spherical polar form of equation 2.24 used in the model is given as

$$\frac{\partial^2\psi}{\partial s^2} + \frac{1}{s^2}\frac{\partial^2\psi}{\partial\lambda^2} - \frac{1}{s^2}\cot\lambda\frac{\partial\psi}{\partial\lambda} = -\frac{W^2}{U}. \qquad 2.25$$

The nature of the equation in spherical polar co-ordinates dictates that fluid enters the cyclone with uniform axial and tangential velocities U and W respectively. The velocity components in terms of Stokes stream function satisfying the mass conservation equation in spherical co-ordinates are given as

$$v_s = \frac{1}{s^2 \sin\lambda} \frac{\partial \psi}{\partial \lambda}, \qquad 2.26\ a$$

$$v_\lambda = -\frac{1}{s \cdot \sin\lambda} \frac{\partial \psi}{\partial s}. \qquad 2.26\ b$$

The following section describes how approximation methods are applied to the differential equation 2.25 so that it may be solved numerically over an entire flow field within given boundary conditions.

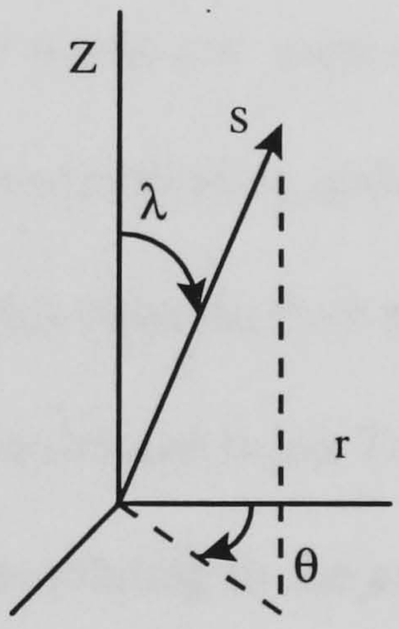

Figure 2.3. Spherical co-ordinate system.

2.3.1 Numerical modelling

Computational fluid dynamics [CFD] is the name given to the numerical representation of fluid flows. The mathematical formulation of fluid flows usually leads, as in this case, to a partial differential equation or a set of such equations. Partial differential equations have been solved analytically, offering accurate solutions, but they are restricted to problems involving shapes for which the boundary conditions can be satisfied, and are not useful for most practical systems. This eliminates all problems with

boundary curves that are not defined in terms of equations. It also excludes many for which the boundary conditions are too difficult to satisfy, even though the equations for the boundary curves are known. In such cases approximation methods, whether analytical or numerical in character, are the only means of solution. This type of solution is being increasingly sought since it offers much wider scope for the application of realistic boundary conditions. The solutions are as accurate as the data warrants or as accurate as is necessary for the required technical purposes.

2.3.2 Finite difference approximation

Finite difference is a numerical approximation method widely used in CFD. The flow region is first discretised into a grid (or mesh); the intersections of the mesh are termed nodes. The influence that corresponding nodes have on each other between the mesh intervals is approximated. In this case the flow parameter is stream function ψ. The derivatives in the equation are approximated using Taylor's theorem (see Smith [S3] for a full explanation). Those derivatives relating to the axisymmetric swirling flow equation, derived using Taylor's theorem, are:

$$\frac{\partial^2 \psi}{\partial s^2} = \frac{\psi_{i+1,j} - 2\psi_{i,j} - \psi_{i-1,j}}{h^2} \qquad 2.27\ a$$

$$\frac{\partial^2 \psi}{\partial \lambda^2} = \frac{\psi_{i,j+1} - 2\psi_{i,j} + \psi_{i,j-1}}{(\delta\lambda)^2} \qquad 2.27\ b$$

$$\frac{\partial \psi}{\partial \lambda} = \frac{\psi_{i,j+1} - \psi_{i,j-1}}{2(\delta\lambda)} \qquad 2.27\ c$$

$$\frac{\partial \psi}{\partial s} = \frac{\psi_{i+1,j} - \psi_{i-1,j}}{2h} \qquad 2.27\ d$$

The i,j subscript gives the mesh node location in the two co-ordinate directions r and θ, while h and $\delta\lambda$ are the small distances between nodes about s and λ respectively. The derivatives are substituted into the equation and rearranged to give the influence of the surrounding node points on the [i,j] node. This is known as a template, see figure 2.4. An iterative method is then used to solve the equation for every point on the grid within the flow domain. Since the direction of influence at a particular point is not known, an iterative solution is required, based on repeated guess and correct cycles. The procedure is said to be convergent when the difference between the exact solution and successive approximations tends to zero.

2.3.3 Solution method of the flow equation

The solution method used was the successive over relaxation method, the algorithm was obtained from Numerical Recipes [V1]. The relaxation coefficient was set to one reverting the solution algorithm to the Gaus-Siedel method, see Smith [S3], this increased stability but slowed convergence. The number of grid cells were small by today's computing standards and convergence speeds were almost instantaneous. The advantage of this type of solution method is that it uses the newly updated values as it progresses through the interpolation of the grid, see figure 2.4.

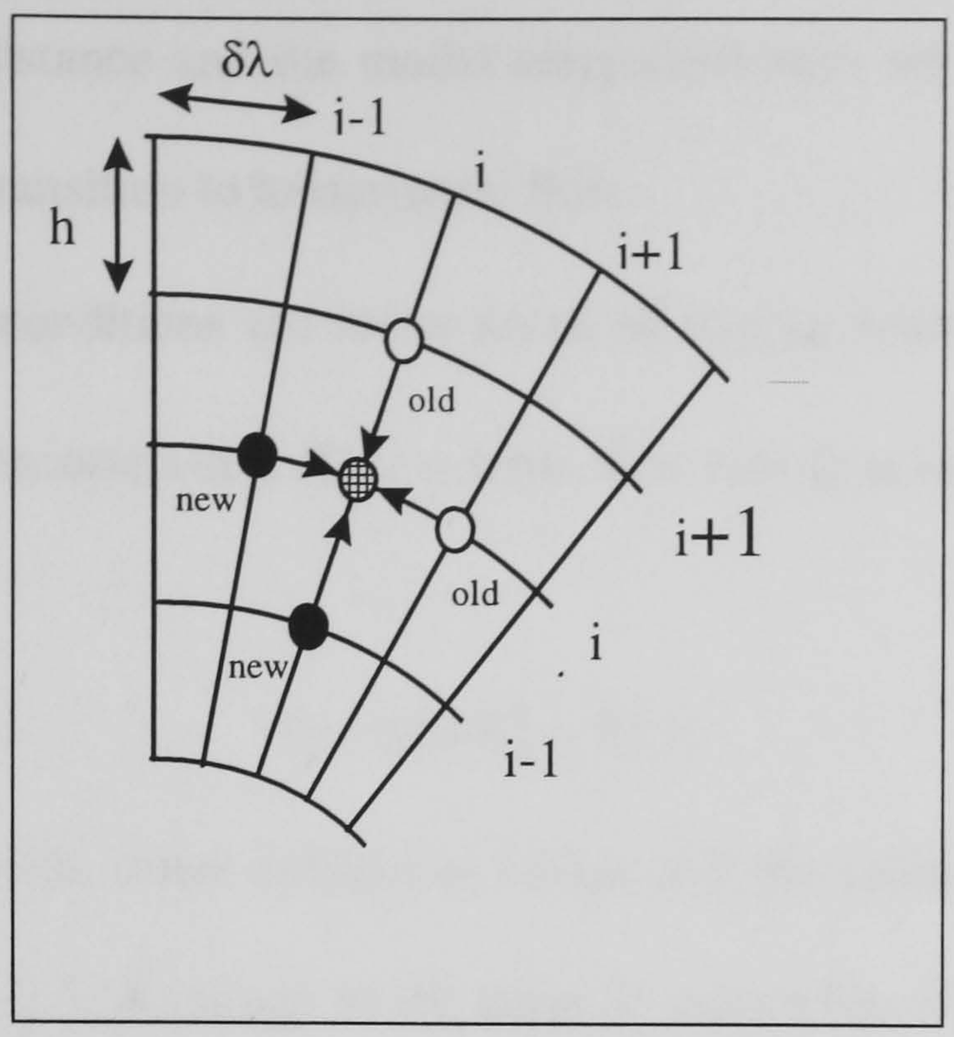

Figure 2.4. Showing the template used in the Gauss-Siedel interpolation procedure, O's represent nodes in the template.

A poor choice of grid spacing can lead to approximation errors in the solution, known as the discretisation errors. Improvement to the accuracy of the solution is generally assumed to occur as the mesh lengths decrease. The idea is to use a sequence of solutions obtained from finer and finer meshes. This will eventually give a solution that differs from the previous by less than some assigned amount. The problem is that the matrix increases rapidly in size, particularly with an increase in co-ordinate directions. After a number of refinements, it may become too large for storage in the immediate access store of the computer.

2.3.4 Boundary conditions

Equation 2.25 requires a linear uniform distribution of constant tangential and axial velocity at the entry, described by Bloor and Ingham [B5] as a "top hat profile". It is assumed that the 3-dimensional flow entering a hydrocyclone becomes axisymetric

after travelling some distance and the model entry conditions are therefore the velocity components after the transition to axisymetric flow.

The boundary conditions are set in terms of stream function ψ. The computed area must be entirely encompassed. The volume flow rate Q across the entry is defined by

$$Q = \pi U(R_0^2 - R_1^2), \qquad 2.28$$

where R_o and R_1 are the outer cylindrical radius and the radius of the vortex finder respectively, see figure 2.5. A change in the value of stream function along this boundary represents an inflow or outflow. The stream function ψ is such that it is not the absolute value of stream function that matters but how it changes with position. The Stokes stream function ψ is consequently defined from equation 2.28 at each radial node position r across the entry section as

$$\psi = \frac{1}{2} U(R_0^2 - s^2 \sin^2 \lambda). \qquad 2.29$$

In a similar way to that described in the paper by Hwang *et al* [H8], both the underflow and overflow are described respectively, for a specified flow split ratioΛ as

$$\psi = \frac{Q}{2\pi(1+\Lambda)} \qquad 2.30\ a$$

$$\psi = \frac{Q\Lambda}{2\pi(1+\Lambda)} \qquad 2.30\ b$$

Though the problem can be formulated in either cylindrical or spherical co-ordinates, the model has been successfully coded using a spherical co-ordinate system, for the full code see [Appendix II]. Figure 2.5 shows a course grid of the uniform mesh used, with the boundary conditions imposed on it. Due to symmetry the grid only represents one half of the hydrocyclone. A uniform mesh is used for simplicity, where a boundary did not lie exactly on a node and impinged upon the grid, ghost points were

used. These are nodes that remain unchanged during the iteration but are then updated between iterations through the linear interpolation of the new value and the constant boundary value. Nodes outside the flow domain are deemed dead and no calculation is carried out on them.

The advantage of spherical polar co-ordinates are that they fit the conical section well the disadvantage is that the cylindrical section and vortex tube boundaries impinge on it requiring the use of many ghost points. In contrast a cylindrical grid can be made to fit in to most axisymetric geometries by adjusting node displacements and numbers, but at the expense of many unused cells. Also, the narrower sections are only sparsely represented, which possibly leads to higher discretisation errors.

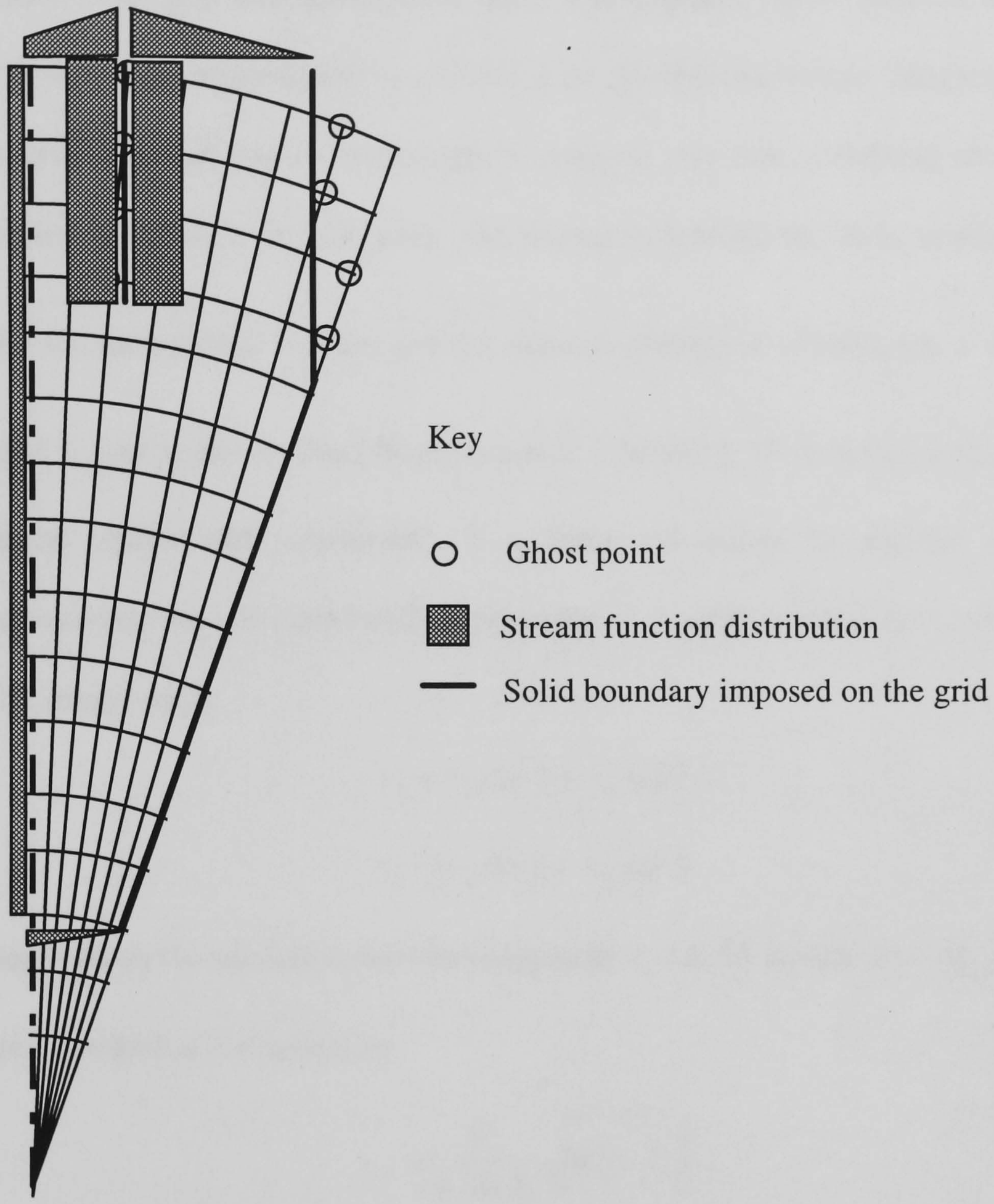

Figure 2.5. An example course grid of the uniform mesh used, with the boundary conditions imposed on it.

2.3.5 Results

The code was compiled using Turbo Pascal V6 [H1, W5] and proved to be simple and quick to set up, on an IBM format personal computer. A 30 by 30 node 2-dimensional mesh easily within the memory constraints of the computer was used for the calculation. The grid also produced a stable convergence. Approximation errors can occur in skew or elongated meshes resulting in an unstable calculation. The program then writes two data files when convergence is achieved, the first containing the value of Stokes stream function at each node, the second containing the three components of velocity for each spatial location and the induced centripetal acceleration $a = \frac{v_\theta^2}{r}$. The values of v_s and v_λ are obtained from equations 2.26 and 2.27. In order to compare the theoretical results with experiment, it is more convenient to resolve these two components into the axial and radial components of velocity denoted by v_z and v_r. Thus v_z and v_r are given by

$$v_z = v_s \cos\lambda + v_\lambda \sin\lambda \qquad 2.32$$

$$v_r = v_s \sin\lambda - v_\lambda \cos\lambda \qquad 2.33$$

For steady flow, the azimuthal velocity component v_λ can be evaluated along Bernoulli's surfaces on which ψ is constant by

$$v_\theta = \frac{W}{s \cdot \sin\lambda} \cdot \sqrt{R_0^2 - 2\frac{\psi}{U}}\,. \qquad 2.34$$

This type of analysis yields a mass of information describing the whole flow field and can not be solely viewed using conventional x-y graphics. The data in essence needs to be viewed in 3-dimensions to appreciate the whole flow field described by the model. The data therefore required an amount of post processing for which a simple graphics routine was developed alongside the code to draw streamline contour plots, giving drawings of

lines of constant, evenly spaced stream function value. This was used in the development of the original code to check for discontinuities and later to display the calculated hydrocyclone flow patterns.

Figure 2.6 shows the predicted streamline contour plot in the Knowles hydrocyclone and the non-dimensionalised predicted and measured velocity data used to validate the model. It is difficult to relate a three-dimensional inlet condition to a two-dimensional linear profile and it is for this reason that velocity comparison is non dimensionalised. The reference values are the mean axial and tangential velocities from the first profile location presented in the Knowles paper [K5] at an equivalent position in the inviscid model. A second graphics program was also written to display velocity and centripetal acceleration profiles throughout the cyclone. These two programs provided quick and easy access to the data calculated by means of the ideal model.

2.3.6 Discussion of Ideal Model Results

The Knowles hydrocyclone [K5] operated without an air core and this source of validation is therefore particularly appropriate to the present study since the model was unsuitable to predict the location of a free surface. In the stream function contour plot, the flow pattern at entry appears distorted due to the doubtful assumption of the initial linear velocity distributions at the entry. However, the model is based on the assumptions of free vortex motion and consequently the flow field corrects itself within a short distance, see figure 2.6. The stream function contours in the Knowles hydrocyclone show clearly that the inner streamline reverses direction and passes to the overflow, while the streamlines closest to the cone wall continue directly to the underflow. The model is therefore able to describe the correct flow patterns in a hydrocyclone and to

calculate high curvature streamlines, a problem that encounters difficulty in more complicated numerical models.

Insertion of the vortex finder into the flow and the change from cylindrical to conical section is described well by the model, which would not have been possible using an analytical approach. The dimensionless velocity analysis compares well with the results of work carried out by Knowles [K5]. It predicts well the location of the locus of zero velocity shown in both the contour plot and the non-dimensionalised velocity profiles. Because the model is inviscid and assumes free vortex rotation, the central viscous core becomes incalculable, and the calculated tangential velocity tends to infinity on the axis. In a practical cyclone, there are often regions of toroidal circulation which lead to short circuiting flows in the upper region of the cyclone and are well documented in the literature. The model predicts the location of these regions but is unable to calculate their values as they consist of closed streamlines and hence provide no reference Bernoulli surface value.

These toroidal circulation's are discussed by Bloor and Ingham [B4, B5]. The complexity of analysing this region is enormous suggesting that the more efficient approach would be to solve the complete Navier-Stokes equations numerically. It is therefore fortunate that the theoretical model agrees adequately with experimental results and that the effects of this region on the main flow may be neglected in this case. The literature revealed a similar approach was taken by Brayshaw [B10] modelling a conventional hydrocyclone using a 2-dimensional inviscid numerical model using a cylindrical co-ordinate system but based on a different equation derived previously by Bloor and Ingham [B3]. In their later publication Bloor and Ingham [B5] apply Batchelor's derivation of axisymetric flow with swirl [B2] in spherical co-ordinates, equation 2.25, to describe the hydrocyclone in favour of their own original model.

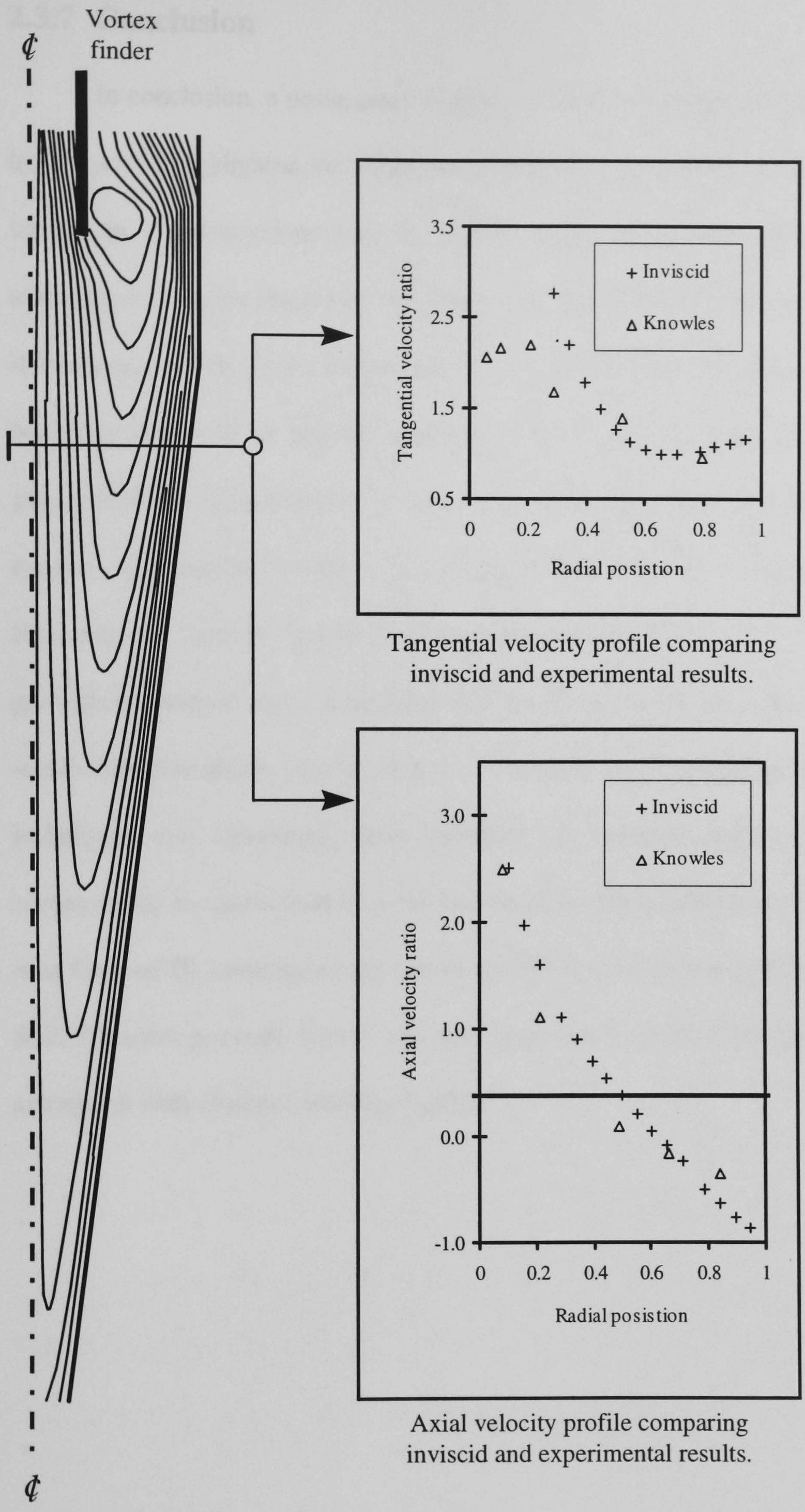

Tangential velocity profile comparing inviscid and experimental results.

Axial velocity profile comparing inviscid and experimental results.

Figure 2.6. Computer generated stream function contour plot of a hydrocyclone with axial and tangential velocity profiles calculated using the inviscid model compared to experimental results.

2.3.7 Conclusion

In conclusion, a preliminary analysis of the flow patterns in the swirling flow of a hydrocyclone highlighted the difficulties involved in its analytical description. The fluid motion in a hydrocyclone may be treated in this simplified case as inviscid and by assuming free vortex behaviour. As an exercise the analytical approach and the numerical development of the simple 2-dimensional swirling flow model enabled more complicated boundary shapes to be applied, providing a fuller understanding of cyclonic flows and gave a first hand experience of using computational fluid dynamics [CFD]. The model is capable of describing the basic flow patterns that occur in axisymetric swirling flows. However, the model is limited in its application to the hydrocyclone by the difficulty of prescribing realistic entry conditions and its failure to incorporate some of the more subtle fluid phenomena that occur in the swirling flows. Advances in numerical modelling techniques and computers, have provided the engineer with a wide selection of commercially available fluid flow models based on the full Navier-Stokes equations. The next Chapter III investigates the use of the different models available to the commercial fluid dynamics package Fluent and their description of the complicated turbulent flow associated with confined swirling liquids.

Chapter III

Turbulent flow and its representation

3.1 Introduction

In the previous section analytical modelling approaches were considered for the modelling of swirling flows with specific reference to the hydrocyclone. These involved assumptions that simplified the constitutive equations describing fluid flow, thus allowing them to be solved by conventional analytical means. Fluid flow is however not at all simple and although this type of approach can substantially complement our understanding of the flow mechanism, it fails to incorporate a multitude of fluid phenomenon that occur in both natural and engineering flows.

It was decided to investigate using a commercially available computational fluid dynamics code Fluent, to model the fluid motion in the solid core hydrocyclone. In Fluent V4.31 there is the possibility of using three different fluid flow models to represent turbulent fluid motion. In the previous chapter it has been shown that the fluid motion in a hydrocyclone is not straight forward as the turbulence has a pronounced affect. It is therefore necessary to investigate the application of these models to the swirling motion in the solid core hydrocyclone and determine which is the best suited. This chapter discusses the different models and compares them with the published experimental results for a conventional hydrocyclone operating without an air-core.

3.2 Turbulence modelling

The flow within the hydrocyclone is essentially very complicated and even with the most advanced fluid dynamics equations and powerful computers there are still many aspects of the flow that can not be described adequately. It is therefore necessary to appreciate what limitations are involved in the mathematical prediction of turbulent flows and how best to model the complex swirling flow of the hydrocyclone. Turbulent flow is encountered in the majority of fluid flow systems and is unfortunately one of the most complicated to solve. Tritton [T4] puts the problem as follows:

> "There is a reason to suppose that the loss of predictability occurs as a property of the Navier-Stokes and continuity equations, although these equations contain the determinism of classical mechanics. It is the onset of turbulence representing in some sense the breakdown of these equations".

The mechanism of turbulence is not fully understood so it is the responsibility of the flow analyst to appreciate the effects of turbulence and use the most effective method to predict its influence on the velocity field and on the transport of secondary phases such as particle suspensions.

Turbulence occurs in pipes of simple circular cross section where the Reynolds number of the flow exceeds 2000, in a hydrocyclone it will conceivable occur at much less. The unsteady turbulent nature of the fluid in a hydrocyclone flow system brings with it a multitude of influences that affect all transport mechanisms within the fluid phase. This shows as a non-regular motion in which the velocity at any point varies with time in both direction and magnitude. With this fluid motion comes eddy formation, a rapid interchange of momentum in the fluid and, consequently, substantial mixing. The mean

flow field may be steady or unsteady but the turbulent motion is always unsteady. Turbulent systems are more complex than laminar flows and unlike them, can not be described in terms of the velocity gradients and Newtonian viscosity. It is therefore necessary to rely upon less specific relationships which relate the rate of diffusion of momentum to the velocity field [Y1].

An essential feature of turbulent flow is the existence of fluid elements in which local, rapidly circulating flows occur. These are continually being formed and destroyed, and are termed eddies. Among the different types of eddy, large and medium sized eddies exist in the main section of the flow where the bulk of the kinetic energy of the fluid is associated. In the motion of the larger eddies, viscous dissipation is negligible, thus energy degradation occurs by the larger eddies transferring their energy to smaller ones which consume kinetic energy by viscous dissipation. In one of the first recorded observations of turbulence, Leonardo da Vinci describes the mechanics of turbulence generation in notes accompanying a sketch titled "Swirling water", He writes in translation [P3]:

> "Observe the motion of the surface of the water which resembles that of hair, which has two motions, of which one depends on the weight of the hair, the other on the direction of the curls; thus the water forms eddying whirlpools, one part of which is due to the impetus of the principal current and the other to the incidental motion and return flow".

The application of numerical procedures to the solution of the Navier-Stokes equation can in theory produce a description of turbulent flows, but in reality it is not yet practical. To solve the relevant equations would require a three-dimensional mesh large

enough to cover the region of interest, but with a spacing smaller than the smallest turbulent motion (eddy), which could be as small as 0.1 mm. In addition to incorporate the unsteady nature of the flow would require a time step smaller than that associated with the fastest eddy, Younis [Y1]. However, in the majority of cases the mean properties of the flow are of greatest importance, rather than the individual turbulent motions. Therefore, from an engineering point of view, the aim is to (be able to) describe the overall effect that the turbulence phenomena have on the statistically averaged flow properties.

3.2.1 Concepts in the statistical theory of turbulent flow

To represent turbulence a statistical approach is taken, in order to provide an averaged representation of the flow. Each variable e.g. velocity v_i is separated into its mean and fluctuating components. The mean velocity of a point in the flow can be defined by time averaging over a sufficient length of time t_o, giving the mean velocity component as

$$\overline{v_i} = \frac{1}{t_0}\int_0^{t_0} v_i(t)dt\,. \qquad 3.1$$

Thereby making it possible to define the instantaneous velocity v_i as the sum of the mean and fluctuating velocity components

$$v_i = \overline{v_i} + v_i'\,. \qquad 3.2$$

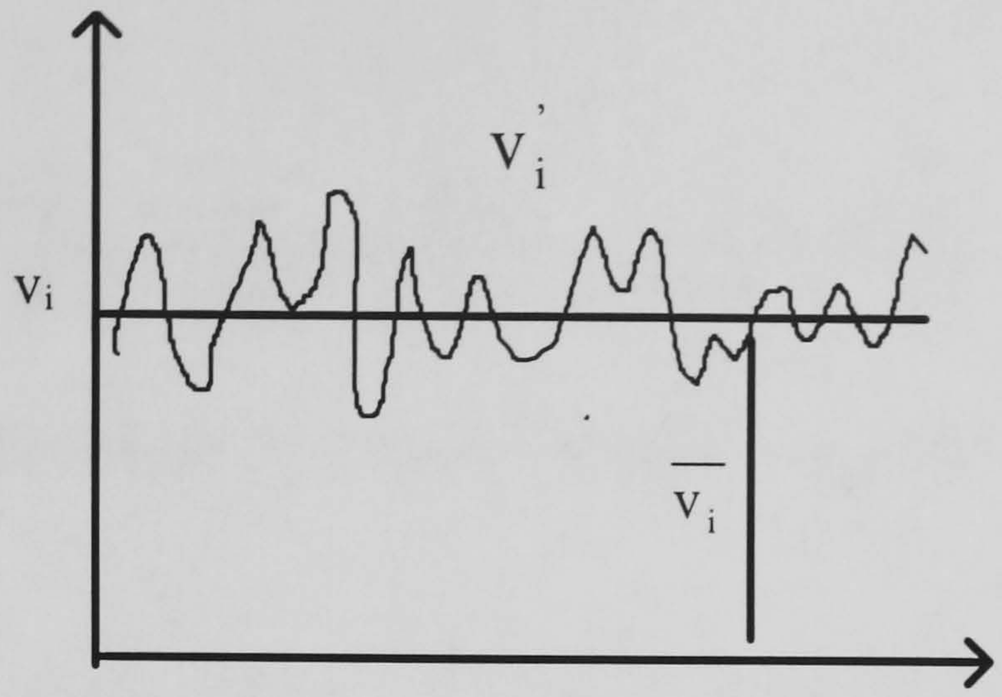

Figure 3.1. Illustrating the time averaged and fluctuating velocity components in turbulent flow.

Consequently, the time averaged value of the fluctuating component must be equal to zero, i.e.

$$\overline{v_i'} = \frac{1}{t_0}\int_0^{t_0} v_i'(t)dt \equiv 0. \qquad 3.3$$

Dividing the velocity into its mean and fluctuating parts, the continuity equation can now be written

$$\frac{\partial\left(\overline{v_i} + v_i'\right)}{\partial x_i} = 0 \qquad 3.4$$

Averaging equation 3.4, then

$$\frac{\partial \overline{v_i}}{\partial x_i} = 0 \qquad 3.5$$

and subtracting this result from the original equation 3.4

$$\frac{\partial v_i'}{\partial x_i} = 0. \qquad 3.6$$

Introducing the mean and fluctuating components into the instantaneous Navier-Stokes equations for Newtonian flow, see [Appendix I], time averaging and neglecting body forces gives

$$\frac{\partial \overline{v_i}}{\partial t} + \overline{v_j}\frac{\partial \overline{v_i}}{\partial x_j} + \overline{v_i'}\frac{\partial \overline{v_i'}}{\partial x_j} = -\frac{1}{\rho}\frac{\partial p}{\partial x_j} + \nu\frac{\partial^2 \overline{v_i}}{\partial x_j^2} \qquad 3.7$$

Applying the averaged results of the continuity equation [Appendix I], means that it can be written as

$$\overline{v_j}\frac{\partial \overline{v_i}}{\partial x_j} = -\frac{1}{\rho}\frac{\partial p}{\partial x_j} + \nu\frac{\partial^2 \overline{v_i}}{\partial x_j^2} + \frac{1}{\rho}\frac{\partial\left(-\rho\overline{v_i' v_j'}\right)}{\partial x_j}. \qquad 3.8$$

In this way the Navier-Stokes equations are no longer expressed in terms of instantaneous values but are time averaged, and the new term $-\rho\overline{v_i' v_j'}$ is introduced. This term has the dimensions of stress and represents the rate at which momentum is transferred by the turbulent fluctuations. This new stress component is the Reynolds stress, a result of the interchange between the two fluctuating velocity components at the same point. In there original form the Navier-Stokes equations were a closed set of equations. The new form has more unknowns than equations and is therefore unsolvable. This is known as the closure problem [S4, S8, G4, Y1] which clearly needs to be resolved if successful solutions for turbulent flows are to be achieved.

3.2.2 Turbulence Models of Closure

The purpose of a turbulence model is to provide a numerical value for $-\rho\overline{v_i' v_j'}$ at each point in the flow and therefore make it possible to close the time averaged Navier-Stokes equation. The objective is to represent the Reynolds stresses as realistically as possible while maintaining a low level of complexity. The choice of turbulence model is

an important consideration and it should be the one best suited to the particular flow problem. Understanding the chosen model's limitations and advantages is essential to get the best answer without lengthy unnecessary computation times.

There are two main approaches for closure:

1. By relating $-\rho v_i' v_j'$ to the mean velocity $\bar{v}$ and some other known or knowable quantities, for instance the effective turbulent or eddy viscosity. The eddy viscosity varies with position in the flow depending on the local level of turbulent activity and may be derived in a number of different ways. This modelling approach is referred to as eddy viscosity modelling. Generally the lowest acceptable levels of model in this category that produce adequate results within the current levels of acceptability are the two equation eddy viscosity models, of which the most widely used is the kε model.

2. By constructing differential transport equations for $-\rho\overline{v_i' v_j'}$ and solving these in the same way as the Navier-Stokes equations, a method known as second moment closure modelling. This is a much more complicated method which increases the computational time but provides a more complete description of turbulence.

3.2.3 Eddy viscosity modelling

The gradient of the Reynolds stresses across the flow causes an acceleration of the fluid in the same way as the viscous stress. However, the Reynolds stress term can be very large compared to the viscous term, hence the difference in velocity profiles between turbulent and laminar flow. Boussinesq [B6] recognised a possible analogy between the effect of turbulent fluctuations on a flow, and the molecular fluctuations which produce dynamic viscosity. The proportionality between stress and rate of strain in laminar flow is applied by modelling Reynolds stresses proportional to the mean rate of strain in turbulent flow. This introduces an equivalent turbulent viscosity proportional to the extent of turbulence which is known as the eddy viscosityν_t

$$\overline{v_i' v_j'} = \nu_t \left[\frac{\partial \overline{v_i}}{\partial x_j} + \frac{\partial \overline{v_j}}{\partial x_i} \right] - \frac{2}{3} \delta_{ij} k \,. \tag{3.9}$$

It should be noted that ν_t is an action of the turbulence and not a property of the fluid. This equation should therefore be regarded as defining ν_t rather than $\overline{v_i' v_j'}$. The next step is to define a relationship for the eddy viscosity which is used to evaluate the turbulent stresses and thus close the time averaged Navier-Stokes equations.

Prandtl [P5] implied in the definition of eddy viscosity to be the square of the kinetic energy k of the turbulent motion, k being given as

$$k \equiv \frac{1}{2} \left(\overline{v_i'}^2 + \overline{v_j'}^2 + \overline{v_k'}^2 \right), \tag{3.10}$$

where for isotropic turbulent conditions,

$$(\overline{v_i'} = \overline{v_j'} = \overline{v_k'}). \tag{3.11}$$

In the CFD code used for this work, Fluent, a linear k-ε model is used. The Reynolds stresses are related to the mean flow by the Boussinesq analogy. The velocity scale and length scale are characterised by

$$v_i \propto k^{1/2} \tag{3.12}$$

and

$$l \propto \frac{k^{3/2}}{\varepsilon} \tag{3.13}$$

respectfully. An extension of this reasoning leads to an expression for ν_t in terms of the characteristic length scales, l, of turbulent eddies

$$\nu_t \propto v_i \cdot l. \tag{3.14}$$

The effective or turbulent viscosity ν_t is therefore defined in terms of kinetic energy k and dissipation rate ε by the expression

$$\nu_t = C_\mu \frac{k^2}{\varepsilon} \tag{3.15}$$

where C_μ is an empirical constant.

An exact equation for the kinetic energy k can be formed by multiplying the instantaneous momentum equation by the instantaneous velocity components and taking an average. After suitable manipulation of the exact, instantaneous and time averaged forms of the Navier-Stokes equation (momentum equation), the equation for k assuming isotropic conditions takes the form

$$\frac{\partial k}{\partial t} + \overline{v_i} \frac{\partial k}{\partial x_i} = \frac{\partial}{\partial x_i}\left[v_i' \left(\frac{v_j' v_j'}{2} + \frac{p}{\rho} \right) \right] - \overline{v_i' v_j'} \frac{\partial \overline{v_i}}{\partial x_j} - \nu \frac{\partial v_i' \partial v_i'}{\partial x_j \partial x_j}. \tag{3.16}$$

rate of generation + convection = diffusion + generation + destruction

The terms on the right of equation 3.16 introduce unknown correlation's which must be approximated in terms of known quantities. The eddy viscosity is evaluated from the solution of two differential equations, one for k and the other for the length scale l. However, in the most commonly used k-ε model, the rate of dissipation of turbulence ε is taken instead of l as the second equation, mainly because it is proportional to both the length scale l and the kinetic energy k.

k and ε are predicted respectively at each point in the flow using the following modelling equations. The exact equation for ε is derived from the Navier-Stokes equations (Tennekes and Lumley [T1]) and is highly complicated since it contains many unknown terms which are not amenable to direct measurement. The actual modelled equations assuming isotropic conditions are given as

$$\frac{\partial k}{\partial t} + \overline{v_i}\frac{\partial k}{\partial x_i} = \frac{\partial}{\partial x_i}\left[\frac{\nu_t}{\sigma_k}\frac{\partial k}{\partial x_i}\right] - \nu_t\left(\frac{\partial \overline{v_i}}{\partial x_j} + \frac{\partial \overline{v_j}}{\partial x_i}\right)\frac{\partial \overline{v_i}}{\partial x_j} - \varepsilon \qquad 3.17$$

rate of generation + convection = diffusion + generation + destruction

and

$$\frac{\partial \varepsilon}{\partial t} + \overline{v_i}\frac{\partial \varepsilon}{\partial x_i} = \frac{\partial}{\partial x_i}\left[\frac{\nu_t}{\sigma_\varepsilon}\frac{\partial k}{\partial x_i}\right] + C_1\frac{\varepsilon}{k}\nu_t\left(\frac{\partial \overline{v_i}}{\partial x_j} + \frac{\partial \overline{v_j}}{\partial x_i}\right)\frac{\partial \overline{v_i}}{\partial x_j} + C_2\frac{\varepsilon^2}{k}. \qquad 3.18$$

rate of generation + convection = diffusion + generation + destruction

The k-ε model describes the turbulent stresses only in terms of the kinetic energy due to fluctuating components and the viscous dissipation rate of the turbulent kinetic energy. Because of the linear isotropic limitation of ν_t in the approximated terms, the model is unable to relate to flows with anisotropic turbulent stresses. Though the same simple isotropic coefficient, equation 3.15, that links the two equations 3.17 and 3.18 does produce a very stable set of transport equations. The constants in the equations have been calculated empirically and may be found in publications by Avérous, Fluent and Guthrie [A3, F1, G4]

The k-ε model has become the most popular used and tested turbulence model used by engineers and scientists for predicting the Reynolds stresses, but its limitations are becoming clearer as more complicated flow problems are being tackled. Spezial [S4] writes

"The standard k-ε model of turbulence can give rise to highly inaccurate predictions for the normal Reynolds stresses which make it impossible to describe such effects as secondary flows in for instance non-circular ducts".

Flows where the Reynolds stresses play an important part may not be represented properly.

Among these are flows which involve curvature such as those in the hydrocyclone. Turbulence is known to be very sensitive to streamline curvature which destabilises the flow and leads to enhanced turbulent mixing. Pereclious and Rodes [L2, P1], have shown how wrong the k-ε model can be when predicting swirling flows analogous to the rotating flows within the hydrocyclone. It overestimated turbulent stress to the point of completely misshapen predictions of both axial and tangential velocity profiles for simple swirling flows.

There have been many attempts to improve the performance of the k-ε model by introducing curvature coefficients and correction terms. However, these do not fully account for the consequences of the interactions between the mean-flow periodicity and random turbulent fluctuations. Varying coefficients and (or) introducing correction terms is very specific method of solution and therefore difficult to apply to new simulations.

3.2.4 Turbulence and curvature

It is well established that turbulence is known to be very sensitive to curvature in the plane of main shear. In a boundary layer developing over a convex surface, for example, the sense of curvature is stabilising, which leads to the suppression of turbulent activity and the collapse of turbulent shear stresses in regions of finite shear. The reverse

applies on convex surfaces, where the curvature destabilises the flow leading therefore to enhanced mixing, Hoffmann and Muck [H3, M2].

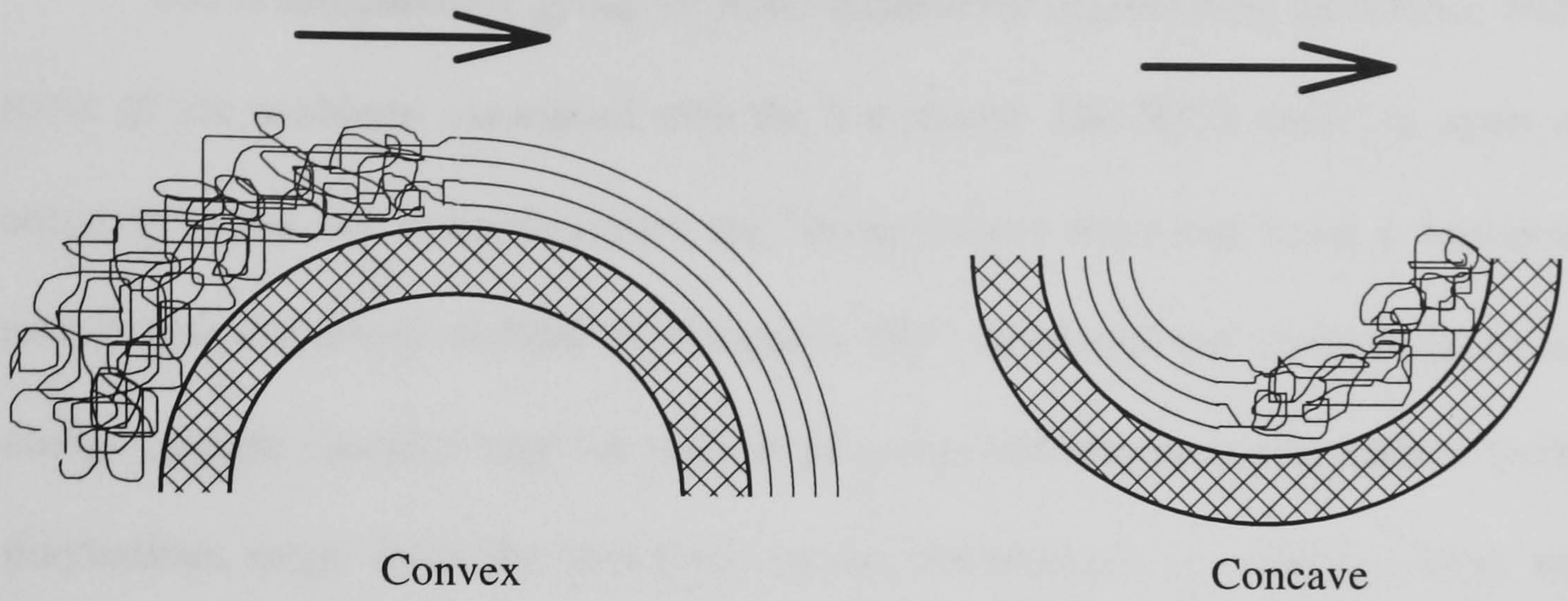

Figure 3.2. Schematic diagram showing the stabilising and destabilising effects of convex and concave surfaces on the turbulent nature within a fluid boundary layer.

The hydrocyclone is made up of concave and convex parts, the body of the cyclone is a concave surface while the protruding vortex finder is convex. Kelsalls work [K2] was criticised for his use of an unusually long vortex finder, which was used to stabilise the flow for visualisation purposes. The flow in a solid core hydrocyclone is stabilised by the presence of the central cylindrical core. This may be beneficial to the overall stability of the physical system and its application, but the theoretical representation of turbulence across the section of flow becomes difficult. The turbulence model must deal with a flow region in which there is both turbulence generation and suppression. A model other than the k-ε model is required, this takes us on to discuss the applicability of two other turbulence models, first the renomalisation group model and then the Reynolds stress model.

3.2.5 The RNG model for turbulence

The renormalisation group or RNG method for representing turbulence remedies some of the problems associated with the k-ε model. The RNG model is again a two equation model but is derived from the Navier-Stokes equations using a mathematical renormalisation group method. Kolmogorov [K8] developed the spectral theory of the energy cascade characterising the transfer of energy between turbulent eddies. Turbulent fluctuations range from the molecular to the macroscopic i.e. small to large eddies. Energy fed into turbulence from the main flow goes primarily into the larger eddies. From these, smaller eddies are generated and then still smaller ones. The process continues until the length scale is so small that viscous action becomes dominant and dissipation occurs.

Renormalisation group methods involve scaling away the contribution of the smaller eddies while maintaining their effect in an averaged form as a contribution to a transport coefficient [M1]. This is done by considering the energy spectrum and removing the modes where the wave number (of the normalised eddy frequency) is high enough for the eddy to be sufficiently small due to viscous dissipation, that its energy is negligible. These small eddies are termed Kolmogorov micro-eddies. The theory gives an expression for the effective viscosity which also accounts for low Reynolds number flows by incorporating molecular viscosity [A3]

$$\nu_t = \nu\left[1+\sqrt{\frac{C_\mu}{\nu}}\frac{k}{\sqrt{\varepsilon}}\right]^2 . \qquad 3.19$$

Two transport equations are deduced from the theory for k and ε :

$$\frac{\partial k}{\partial t} + \overline{v}_i \frac{\partial k}{\partial x_i} = \frac{\partial}{\partial x_i}\left[\alpha \nu_t \frac{\partial k}{\partial x_i}\right] - \nu_t T^2 - \varepsilon \qquad 3.20$$

$$\frac{\partial \varepsilon}{\partial t} + \overline{v}_i \frac{\partial \varepsilon}{\partial x_i} = \frac{\partial}{\partial x_i}\left[\alpha \nu_t \frac{\partial k}{\partial x_i}\right] - C_1 \frac{\varepsilon}{k} \nu_t T^2 - C_2 \frac{\varepsilon^2}{k}. \qquad 3.21$$

where T is the modulus for the mean flow deformation tensor t_{ij}, R is a rate-of-strain term which was neglected in equation 3.18 where the Reynolds number was supposed high, equal to

$$R = 2\nu_t \frac{\partial \overline{v}_i}{\partial x_j} \frac{\partial \overline{v_k'}}{\partial x_i} \frac{\partial \overline{v_k'}}{\partial x_j}, \qquad 3.22$$

this is represented in the renormalisation group model as

$$R = \frac{C_\mu T^3 \left(1 - \frac{Tk}{\varepsilon \phi_0}\right)}{1 + \beta \frac{T^3 k^3}{\varepsilon^3}} \frac{k^2}{\varepsilon}, \qquad 3.23$$

α is a Reynolds number dependent parameter given by the following law

$$\frac{\nu}{\nu_t} = \left|\frac{\alpha - 1.3929}{\alpha_0 - 1.3929}\right|^{0.6321} \left|\frac{\alpha + 2.3929}{\alpha + 2.3929}\right|^{0.3679}. \qquad 3.24$$

The constants are determined theoretically.

Swirl or high streamline curvature effects can be taken more accurately into effect by modifying C_μ as a function of curvature. The renormalisation group model has given good results for weakly to mild swirling flows. The principal advantage of the RNG model is that the constants used in it are determined theoretically and that the model includes correction for low-Reynolds number effects. RNG is not much more expensive than the standard k-ε model to run because there are still only two equations. The renormalisation group approach provides a nice alternative to the far more complex Reynolds stress model in a wide number of cases, which will be discussed in the next

section. It should not escape our attention that the RNG procedure is a systematic way of reducing the number of degrees of freedom and consequently the number of descriptive terms necessary for the representation of turbulence.

3.2.6 Second Moment Closure (Reynolds Stress Model, RSM)

In a second moment closure model, the Boussinesq eddy viscosity hypothesis is abandoned and the unknown Reynolds stresses are obtained directly from the solution of differential transport equations in which they are the dependent variables. This type of turbulence model, known as the Reynolds stress model [RSM]. is a much more recent development than the simpler 2-equation k-ε model, it is therefore not as well documented and is much less widely used. The RSM describes the turbulent nature of fluid flow by use of more explicit realistic expressions than the k-ε model. It consists of differential or algebraic equations each governing the balance between the generation, redistribution and transport of a related Reynolds stress. The advantage of this type of model is that it can capture many of the complex effects encounted in nature and in engineering applications without having to incorporate ad-hoc modifications necessary in lower order closure models. The RSM is an important advance in turbulence modelling which gives accurate accounts of streamline curvature, rotation and swirl.

The exact transport equation for the Reynolds stress tensor is obtained from the Navier-Stokes equation by multiplying the equation for the instantaneous components by its opposing instantaneous velocity component and time averaging the result. The resulting equation illustrates the conceptual simplicity of the Reynolds stress equations

$$\frac{\partial}{\partial t}\left(\overline{v_i' v_j'}\right) + \overline{v_k} \frac{\partial}{\partial x_k}\left(\overline{v_i' v_j'}\right) =$$

$$-\frac{\partial}{\partial x_k}\left[\overline{\left(v_i' v_j' v_k'\right)}+\overline{\frac{p}{\rho}\left(\delta_{kj} v_i'+\delta_{ik} v_j'\right)}-\nu\frac{\partial}{\partial x_k}\left(\overline{v_i' v_j'}\right)\right] \qquad 3.25$$

$$-\left[\overline{v_i' v_k'}\frac{\partial \overline{v_j}}{\partial x_k}+\overline{v_j' v_k'}\frac{\partial \overline{v_i}}{\partial x_k}\right]$$

$$+\overline{\frac{p}{\rho}\left[\frac{\partial v_i'}{\partial x_j}+\frac{\partial v_j'}{\partial x_i}\right]}-2\nu\overline{\left[\frac{\partial v_i'}{\partial x_k}\frac{\partial v_j'}{\partial x_k}\right]}-2\Omega\left(\overline{v_i' v_j'}\varepsilon_{ikm}+\overline{v_i' v_m'}\varepsilon_{jkm}\right)$$

Connective transport $\left(-\rho\overline{v_i v_j}\right)$ = Diffusive Transport $\left(-\rho\overline{v_i v_j}\right) T_{ij}$ + Production $\left(-\rho\overline{v_i v_j}\right) P_{ij}$ +

Pressure strain $\left(-\rho\overline{v_i' v_j'}\right)\ \phi_{ij}$ + Dissipation $\left(-\rho\overline{v_i' v_j'}\right)\varepsilon_{ij}$ + Rotation R_{ij}

However, in order to close this equation set, it is necessary with the exception of the production term P_{ij} to approximate the terms on the right hand side of the equation as follows

$$T_{ij}=\frac{\partial}{\partial x_k}\left(\frac{\nu_t}{\sigma_k}\frac{\partial\left(\overline{v_i' v_j'}\right)}{\partial x_k}\right) \qquad 3.25\ a$$

$$\phi_{ij}=-C_3\frac{\varepsilon}{k}\left[\overline{v_i' v_j'}-\frac{2}{3}\delta_{ij}k\right]-C_4\left[P_{ij}-\frac{2}{3}\delta_{ij}P\right] \qquad 3.25\ b$$

$$\varepsilon_{ij}=\frac{2}{3}\delta_{ij}\varepsilon\,. \qquad 3.25\ c$$

An important property of second moment closure is that the generation rates or production P_{ij} of stresses arising from the interaction between stresses and strains do not need to be approximated therefore P_{ij} remains

$$P_{ij}=-\overline{v_i' v_k'}\frac{\partial \overline{v_j}}{\partial x_k}-\overline{v_j' v_k'}\frac{\partial \overline{v_i}}{\partial x_k}\,. \qquad 3.25\ d$$

Leschziner.[L3] has shown the levels of the turbulent stresses (or stress anisotropy) in a turbulent flow are principally governed by their respective generation or production

rates. The diffusive term is the contribution of the viscous diffusion term to the total rate of transport of $\overline{v_i' v_j'}$. The dissipation term represents the conversion of turbulent kinetic energy to heat due to molecular viscosity this is approximated from the molecular shear stresses, which are assumed to be isotropic. The turbulent kinetic energy dissipation rate ε is determined in exactly the same way as for the k-ε model using equation 3.18. As the Reynolds stresses have been solved individually the kinetic turbulent energy can therefore be solved simply as

$$k = \frac{1}{2}\left(\overline{v_i'}\right)^2 . \qquad 3.26$$

The Reynolds stress model represents the maximum acceptable level of complexity for all practical flow calculations. The method provides a more complete description of turbulence than mean field closure methods. It also accounts for the anisotropy of macro-turbulence and gives good results for swirling of curved flows. It has been shown that the Reynolds stress model is generally better in flow curvature calculations, [G1, G2, S1] Its principle disadvantage is its complexity, since it is necessary to solve six additional equations for the Reynolds stress compared to only two for the k-ε model. It is also less computationally stable. This limits its use to cases that the two equation models cannot solve where the flow geometry is particularly complicated or where the flow is governed by processes other than turbulence.

The next section is a discussion on how conventional hydrocyclones have been numerically modelled in the literature. This is then followed by a discussion of the modelling set up using Fluent V4.31. The three different turbulence models in Fluent are validated against existing published experimental data for a conventional hydrocyclone this is done to confirm their application to the solid-core cyclone design.

3.3 Numerical analysis of the hydrocyclone

In an article in Chemical Engineering Progress, Knowlton.[K6] called for a reliable computer design model for cyclones that is capable of predicting the effect of geometry changes and system parameters on cyclone efficiency. The way forward is described as the capability to develop "designer cyclones" optimised for the specific operating conditions of a particular process. There are two types of computer design packages that may be capable of meeting the Knowlton requirements:

- Those based on established empirical rules for specific materials handling, for example the geometry independent computer design program AEA-cyclone cited by Bahu [B1]. Although this type may be adequate for many conventional cyclone applications they do not cater for unusual cyclone geometries or processes. Essentially they are used to predict an initial design which then undergo operational trials to confirm effectiveness.
- The alternative is to use a computational fluid dynamics package with specifically written numerical codes. This type of model has just recently come to the forefront in cyclone design providing a computer test bed to investigate new ideas quickly and cheaply.

The numerical treatment of the Navier-Stokes equations gradually crept into the analysis of the hydrocyclone in the early 1980's. This resulted from the rapid improvement in computers and a better understanding of the numerical treatment of turbulence. The first notable work was the application of a zero equation turbulence model by Pericleaus and Rodes [P2], which was used to reproduce the findings of the experimental work of Kelsall [K2]. A zero equation turbulence model is essentially a step

backwards, as the k-ε model was fore fronting CFD modelling during this period. Pericleaus et al [P1] had demonstrated in a previous paper that the k-ε model in its standard form inadequately predicts both axial and tangential velocity trends for the hydrocyclone, thus making the zero-equation model the only realistic alternative at that stage. Pericleaus and Rhodes treat the Navier-Stokes equations as laminar but solve them simply for the modified turbulent viscosity μ_t given by the tangential and axial velocity components using a modified Prandtl mixing length model [P4] of the type

$$\mu_t = \rho l^2 \left| \frac{\partial \overline{v_i}}{\partial x_j} \right|. \qquad 3.27$$

The model agrees well with experiment, though it assumes that the turbulence is in local equilibrium. This means that at each point in the flow the turbulent energy is dissipated at the same rate. The overall simplicity of this model makes for a stable and quick, if rather crude, result. An empirically based mixing length is specific to each individual cyclone. The individual nature of the mixing length model used to describe the turbulent viscosity means it is not transferable to other geometries and operating conditions. For design applications a versatile turbulence model that does not need constants to be changed, is required.

Even so, other workers in the field have taken up this approach. Davidson [D3] adequately reproduced the velocity measurements of Knowles et al [K5] for a hydrocyclone operating without an air core. Further modifications by Rajamani [H5, M3, R1, R2], adapted the turbulent viscosity to account for the presence of solid particles, and assumed a slurry density dependent on the solids concentration. Simple turbulence models come into there own when incorporating a secondary phase calculation, as the incorporation of further equations in the more comprehensive models can mean a substantial increase in computation time.

Hargreaves and Silvester (1990) [H2] performed a CFD analysis on a hydrocyclone using the full Reynolds stress model (RSM) for closure. This simulation was performed in 2-dimensions, taking an axisymmetric slice through the hydrocyclone the predicted results gave a good account of the flow patterns in a hydrocyclone. This showed that the RSM could be used to account for the hydrocyclone's anisotropic turbulent flow.

Dyakowski and Williams [D8] reiterate the need for an anisotropic model of turbulence to solve the flow within a hydrocyclone. Their modelling approach used an algebraic Reynolds stress model specifically developed for the analysis of small diameter hydrocyclones. The model solves a set of six algebraically determined equations, each representing an individual stress which reduces computation time while still incorporating a non homogeneous model of turbulence.

Considering the analysis of the literature and the previous discussion of the various turbulence models available, it appears that the more comprehensive Reynolds stress model for closure is the one best suited to the complex anisotropic turbulent flow found in the hydrocyclone. Inevitable the Reynolds stress model will also be the best option to tackle the more severely swirling flow in the annular solid core cyclone. The following section discusses the use of the commercially available fluid dynamics code Fluent and compares the three turbulence models.

3.4 Fluent V 3.41

The commercial computational fluid dynamics package, Fluent V 3.41, was used for the next stage in the present modelling work. The program was already mounted on the Newcastle University computing network and available under an academic licence. It incorporated a number of different models for describing fluid flow and also, the

capability to predict the trajectory of a low volume concentrations of a particulate phase. For these reasons it was decided to asses the feasibility of using Fluent to model the fluid motion in a solid core cyclone.

Fluent V 3.4.1 incorporates all the components that the inviscid model had, such as grid discretisation, solvers for the constitutive fluid flow equations and a graphical output for post processing data. In the past all the various components in commercial packages were incorporated into a single comprehensive program. As technology and the demand for more advanced versatility advance, programs are being split into their individual components. CFD software companies are finding it more difficult to cater to all the areas, and we are seeing a move now to individually packages and the need for more standalone versatile formats.

The Fluent V 3.41 package can perform calculations of fluid flow in 3-dimensions using a finite volume method to solve the constitutive equations describing fluid flow. The finite volume method is similar to the finite difference method outlined in Chapter II, section 2.3.2, but instead stores the flow field data at the cell centres and is able to solve the flow in about the three co-ordinate directions. Fluent V 3.41, academic licensed version, consists of two parts, a pre-processor (grid generation) and a solver (flow calculation). The pre-processor sets up grids with body fitted co-ordinates that is, it distorts cells to fit the geometry. Much more data describing the location of each individual node is required, which must then be accessed during processing. Distorted cells therefore increases convergence time and can reduce the stability of the solution. The continuing improvement in the speed and memory storage of computers renders this now a viable method, and allows more realistic flow modelling.

3.4.1 The pre-processor, Pre-BFC

The grid technique used by the pre-processor Pre-BFC is termed "single block". A three dimensional cubic grid is first assigned to memory, the size of which is limited by the immediate access store of your computer. This grid is then distorted by assigning the node locations to positions within the geometry. Because the cyclone is being modelled in three dimensions and requires a suitable long tangential inlet, the single block method leaves a lot of cells outside the geometry in order to incorporate the tangential inlet pipe. These cells are then assigned as dead and are not used in the computation, but unfortunately they still take up memory in the computer and so reduce the number of active cells that can be applied to the problem.

A second limitation of Pre-BFC is that it does not readily allow the attachment of two cylinders at right angles to each other. Therefore, any optimisation study of hydrocyclones would have to be carried out using square inlets. This may not be a disadvantage since square inlets are in fact known to improve the performance of a hydrocyclone for the principle reason that they reduce expansion losses and smooth the introduction of flow into the cylindrical section Bradley [B6]. Square cross sections may however not be viable in practice when dealing with the molten metal flows which are the ultimate objective of the present work. But, as will be discussed later, their effect on the optimisation study was found not to be damaging.

Pre-bfc has since been replaced by a far more sophisticated post-processor Geo-mesh, which is sold under licence by Fluent. A late launch of this product and then problems regarding an educational licence meant that Geomesh was not available for this work.

3.4.2 Validation of Fluent and turbulence models

No published experimental data are available to compare with the computational analysis of the solid core cyclone. Nevertheless, it was considered necessary to establish the suitability of the computational models available in Fluent for this application. The same conventional hydrocyclone example used for the inviscid model, (Knowles [K5]) was taken for validation. The velocity distribution data from this work has been used by other workers to validate their numerical models, see for example Davidson [D3]. The same cyclone design was later analysed by Dabir [D1] using laser Doppler anemometry techniques, whose data further confirms that of Knowles. The Knowles hydrocyclone was operated without an air-core, which likens it further to the solid core cyclone. The computational grid shown in figure 3.3, was set-up in cylindrical co-ordinates using Pre-BFC. Because of the difficulty of representing the tangential inlet conditions in 2-dimensions, as in the inviscid model, Chapter II, the study was therefore carried out in 3-dimensions. Although the original hydrocyclone had a straight circular inlet it had to be modelled using an equal area square inlet. Pressure boundary conditions were then applied at the three entries, with a turbulence intensity level of 11% and the characteristic length equal to the major dimension of each entry. The physical constants of the liquid phase were set to those of water.

Fluent V4.2 incorporates a number of turbulence models describing the averaged affects of turbulence on the fluid flow. In addition, it is capable of simulating the dissipation of a low volume concentration of particles, for when, once the velocity field is accurately predicted, a dispersed phase model may be used to investigate the classifying action of the hydrocyclone. As discussed in Chapter II, the turbulence in a hydrocyclone

is anisotropic and the anisotropic nature of the swirling flow requires a model best suited to calculating this type of system.

The Fluent package offers three turbulence models, the k-ε model, the renormalisation group model and the anisotropic Reynolds stress model. The manual suggests the RNG model as that best suited to swirling flows. Each of the models available was tested in a validation study based upon the data of Knowles [K7], which is discussed in more detail below. The objective was to establish which would be best for the ultimate design optimisation study of the solid core cyclone. The earlier discussion of turbulence modelling advocated the RSM but because the RSM is a higher order closure model, it can be inherently unstable and slow. It is therefore better to obtain a solution using the k-ε model before activating the RSM calculation. Without pre-calculated boundary layer conditions, the RSM solution is extremely slow and for the complicated hydrocyclone flow system would be prone to collapse.

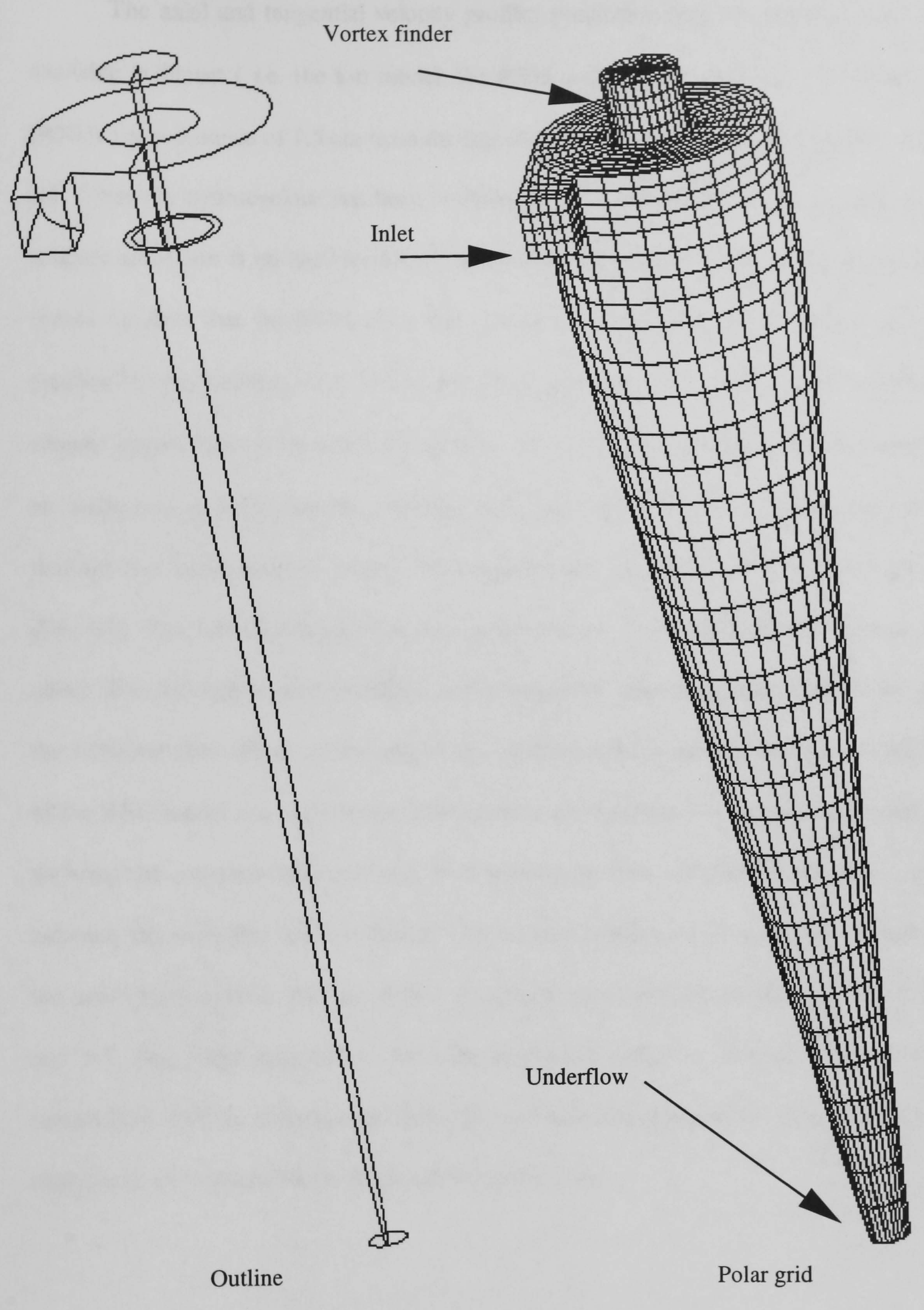

Figure 3.3. Outline of Knowles hydrocyclone geometry and the structured polar grid used in the calculation

3.4.3 Discussion of results

The axial and tangential velocity profiles predicted using the turbulence models available in Fluent (i.e. the k-ε model, the RSM and the renormalisation group model (RNG)) at a distance of 7.5 cm from the top of the cyclone are shown in Figures 3.4 and 3.5. Since the hydrocyclone has been modelled in 3-dimensions the entry conditions are realistic and there is no need to non-dimensionalise the results for the comparison. The results confirm that the RSM gives the best approximation of the measured velocity profiles for the Knowles data. This was a good indication of its suitability to model the simpler unsplit flow of the solid core cyclone. The k-ε model and RNG model proved to be ineffective in predicting the swirling flow field of the cyclone, reinforcing earlier findings that eddy viscosity models are unsuitable for predicting anisotropic turbulence [D8, S1]. The RNG model gave a very good picture of the axial velocity though the effect of turbulence is underpredicted in the tangential velocity profile. This shows that the turbulent flow affects in this and similar swirling systems are beyond the capabilities of the RNG model. In contrast, the RSM gives a good representation of a hydrocyclone showing the expected tangential and axial velocity profiles, with flow reversal (or split) between the underflow and overflows. The velocity profiles are as expected throughout the entire hydrocyclone and are shown in the post-processed Fluent pictures, figure 3.6 and 3.7. The RSM approach is the only turbulence model to produce a satisfactory comparison with the experimental data, this was therefore adopted for all computational analysis of the velocity fields in the solid core cyclone.

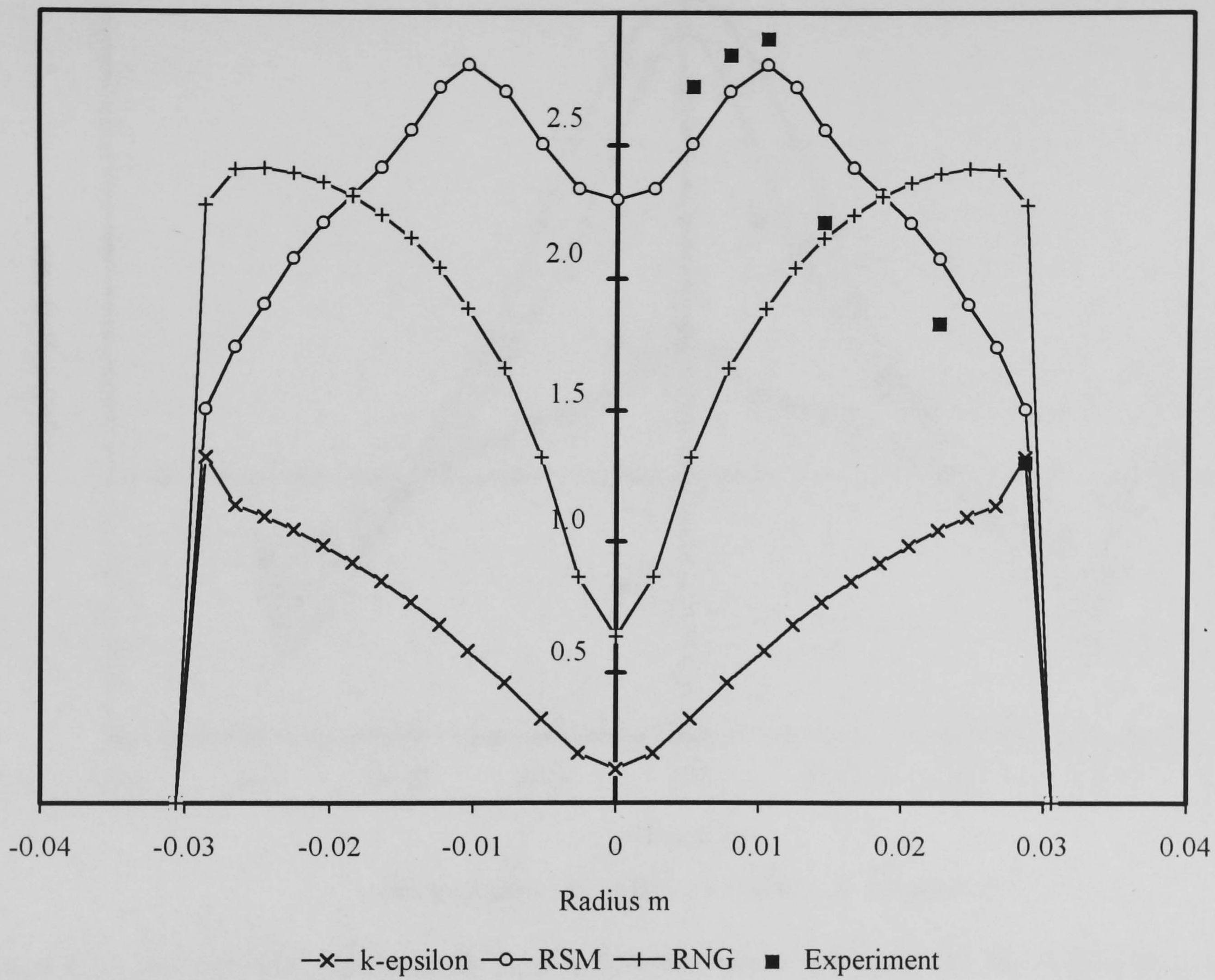

Figure 3.4. Tangential velocity predictions for three turbulence models used to model the swirling flow in a 72 mm diameter hydrocyclone the k-ε, Reynolds stress and the renormalisation group models compared to the experimental data of Knowles [K8].

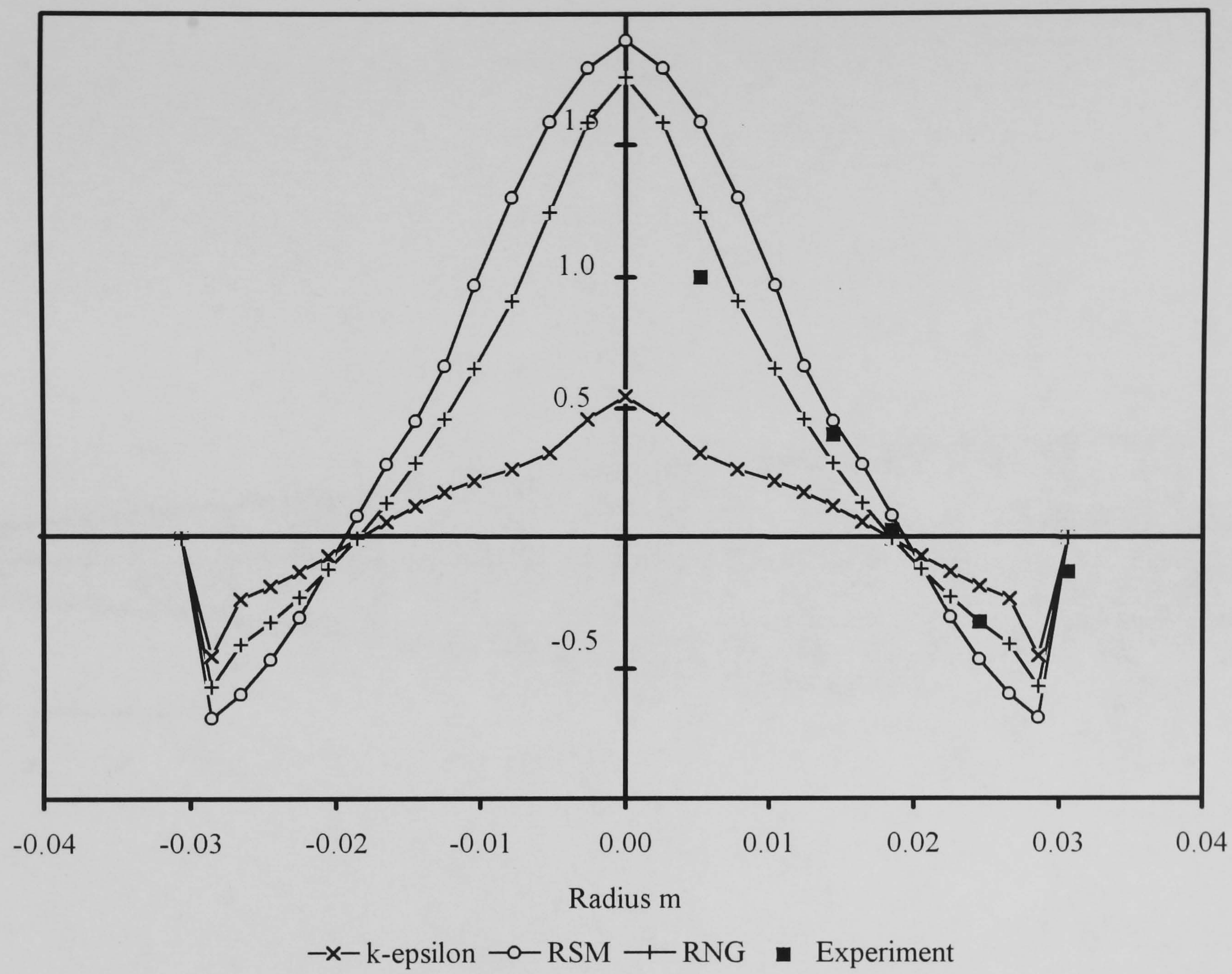

Fi

gure 3.5. Axial velocity predictions for three turbulence models used to model the swirling flow in a 72 mm diameter hydrocyclone the k-ε, Reynolds stress and the renormalisation group models compared to the experimental data of Knowles [K8].

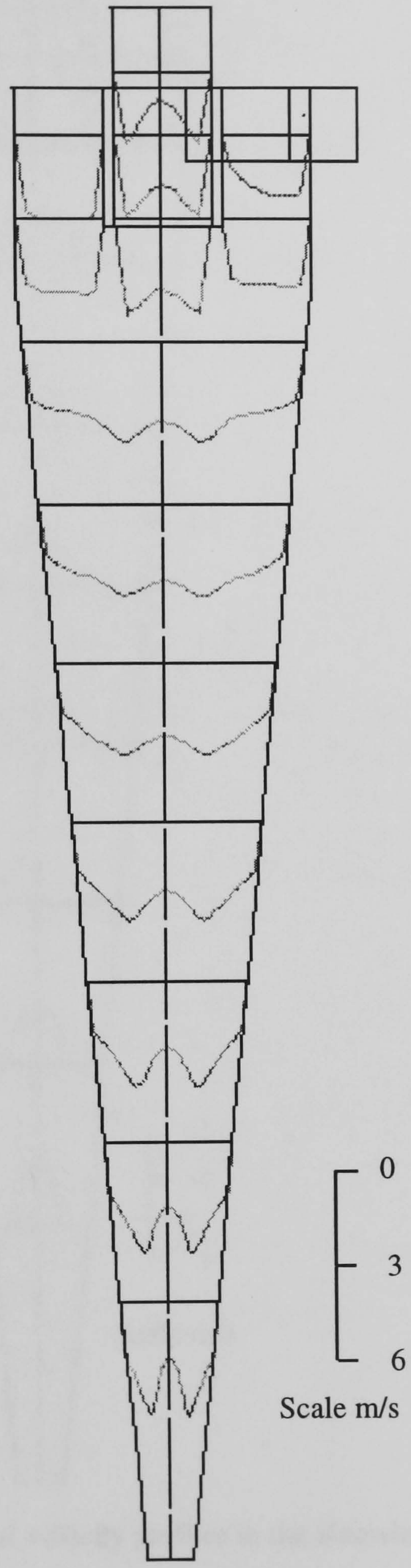

Figure 3.6. Tangential velocity profiles in Knowles hydrocyclone calculated using RSM.

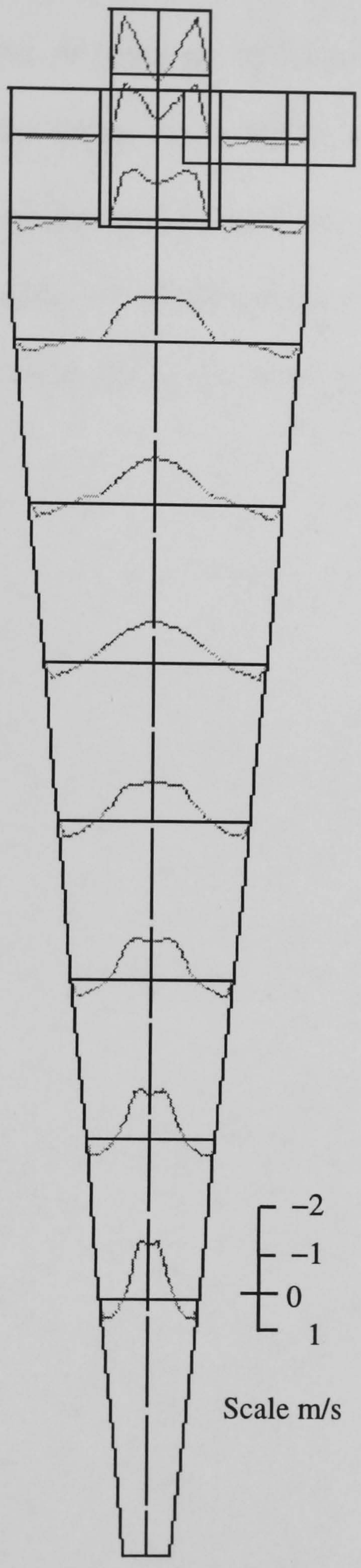

Figure 3.7. Axial velocity profiles in the Knowles hydrocyclone predicted using RSM.

The next chapter deals with the computational analysis and design of the solid core cyclone using Fluent. The solid core cyclone will be meshed in 3-dimensions for a number of varying geometries using a cylindrical polar grid similar to the one used in the validation exercise. At this stage, following the discoveries of the Fluent validation study the renormalisation group model can be discarded. Even though the k-ε model did not predict the correct flow characteristics in the conventional hydrocyclone it will still be used to pre-calculate the boundary layer on to the grid before the RSM is run. The design approach taken will be discussed in the next section.

Chapter IV

Development of the solid core hydrocyclone using computational fluid dynamics [CFD]

4.1 Introduction

Following on from the validation and discussion of the different turbulence models that may be used to simulate the fluid motion in a hydrocyclone. In the Chapter III it was shown that the Reynolds stress model produced the best comparison to published experimental results for a conventional hydrocyclone operating without an air-core. The Reynolds stress model is therefore adopted for the computational analysis of the velocity field in the solid core cyclone. This chapter deals with the CFD design analysis of the solid core hydrocyclone application and its feasibility for the removal of alumina inclusions from liquid steel. The section begins with an outline of the different design parameters that may be employed in the conventional hydrocyclone.

4.1.1 Outline of hydrocyclone design

The ultimate measure of effectiveness in the design of a solid core cyclone for a metal melt is the fraction (%age) of the population of any particle size that is captured. Inclusions in steel lie in a range of sizes from in-excess of 100 μm equivalent spherical diameter to less than 1 μm, table 4.2. The criterion for effectiveness is; the smaller the particle removed from the steel flow, the better the apparent cyclone performance. A design approach to the solid core cyclone is no less complicated than that of the

traditional cyclone classifier; the design variables analysis outlined by Svarovsky [S7] and Bradley [B8] may provide a guide, as follows.

- Cyclone diameter:

  The smaller the cyclone the smaller the diameter of the particle (cut size) that is separated and the larger the pressure drop at a given flow rate. This is why multiple hydrocyclone units consisting of any number of cyclones manifolded in parallel are used to achieve effective throughputs at small particle sizes.

- Aperture sizes :

  The injection momentum rate has a peak value with feed (inlet) diameter and should be maximised i.e. there is an optimum entry diameter for every cyclone. Feed inlet geometry is also critical to cyclone performance. A rectangular section with the long side parallel to the cyclone axis is preferred.

- Body dimensions :

  It is debatable whether the familiar cylindrical section originated to ease construction and provide a simple feed opening, though this is advantageous. An increase in length gives an increase in capacity; separation efficiency also increases with length. The smaller the cone angle, the lower the cut size and the smaller the secondary circulation's. However, larger angles improve the sharpness of separation.

- Operating pressure :

  To maintain the same flow rate as the diameter of the cyclone decreases requires an increase in pressure energy. In the present application of the solid core cyclone pressure is limited to a maximum, therefore a smaller diameter cyclone means accepting a smaller flow rate.

Additional design aspects of the solid core cyclone are the effect of negative differential particle density and the shape and dimensions of the core. In work on oil recovery from water in a cyclone, where there is a weak negative density effect, Hargreaves et al [H2] found that for small diameter (30-60 mm) conventional hydrocyclones there was an optimum flow range which gave an acceptable clarification efficiency. Below this range, velocities were too low to promote separation, whereas at high flow rates a low pressure core formed which reduced performance by constraining the overflow. The presence of a solid core would obviously influence performance. In the present study, it is hoped to understand by modelling how the core affects the flow, to identify the positive and negative effects and respectively to exploit and to minimise them in progressing towards an effective design.

4.1.2 Computational analysis

The dimensions and operating conditions of the test simulations are detailed in Table 4.1. The physical constants used, for molten steel at a temperature of 1600 °C from Iida and Guthrie [I8] were, dynamic viscosity of 5.5×10^{-3} N/m^2 and a density of 7100 kg/m^3. The first productive dimensions were found by trial and error, based on the internal dimensions of a ladle shroud and the design criteria set down by Reitema [R3] for the conventional hydrocyclone, see Chapter I. The preliminary investigation indicated

a small diameter cyclone, case 1, see table 4.1 and figure 4.1 showing a schematic solid core cyclone and corresponding dimensions. This provided a starting point onto which subsequent modifications could then be implemented. In order to produce a high centripetal acceleration with the limited available head in melt processing, a small cyclone radius is necessary, but this would limit volume throughput. In these circumstances, large steel flows would require a group of small cyclones in parallel to exploit fully the capture effectiveness of the small cyclone.

To take account of entry conditions, it was necessary to model the solid core cyclone in 3 dimensions. Monredon et al [M3] showed that modelling an axisymmetric hydrocyclone was insufficiently accurate due to the inherent limitations of the axisymmetric assumption. The initial test of the RSM in 3 dimensions against the data of Knowles et al [K5] for flow field validation in the previous section, established that approximately 21000 cells were required for a solution, with a computation time of about 20 hours using the available computers, an example grid is shown in figure 4.2.

The small diameter cyclone, case 1 (0.06 m diameter), proved to have a reasonably effective escape curve. The results were obtained for a constant entry pressure and steady flow. In reality the head of melt providing the driving force is likely to decrease. The effect of changes in driving head was investigated in a series of tests at different entry pressures.

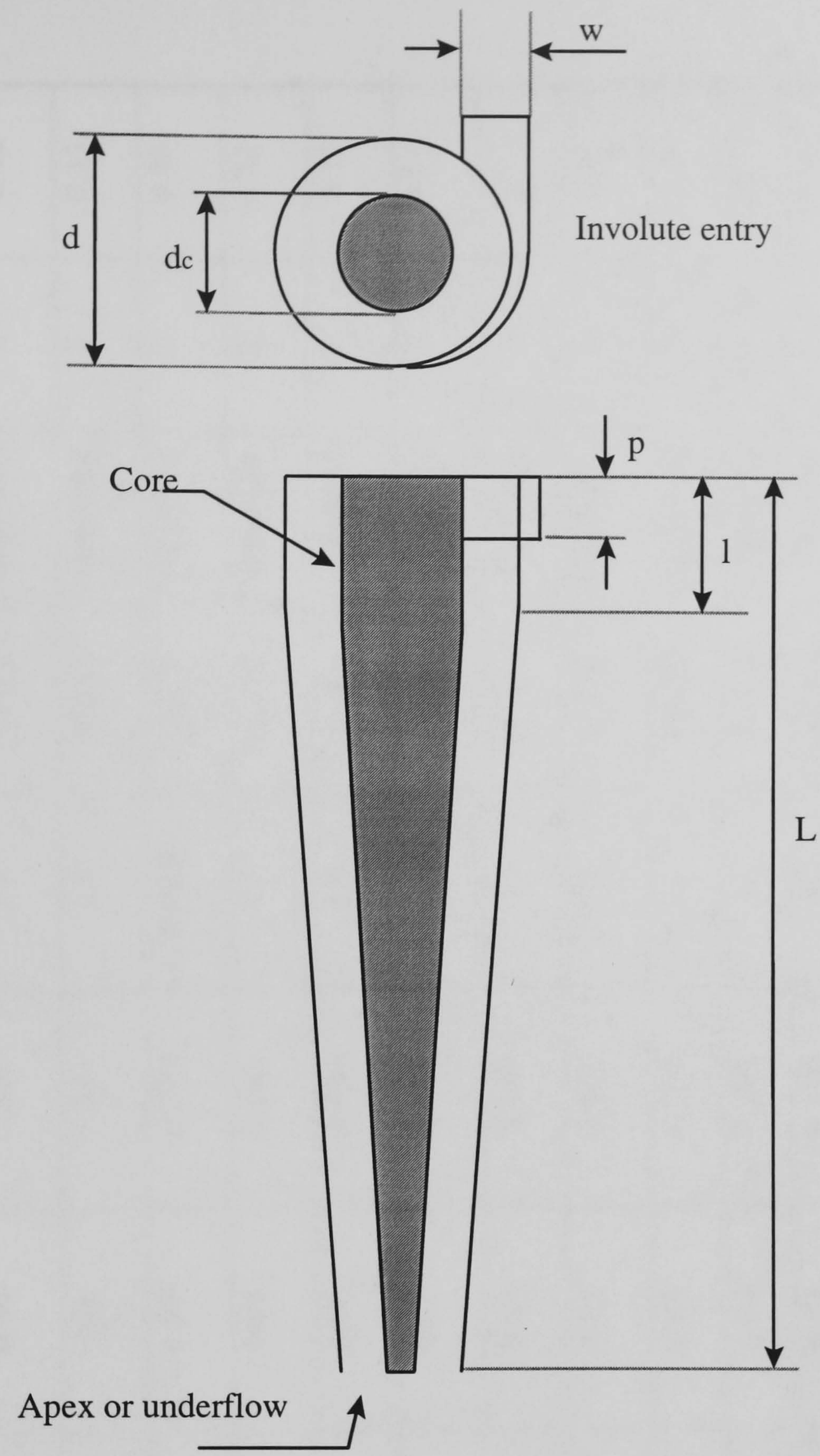

Figure 4.1. Sketch showing a schematic of the solid core

	Cyclone diameter d m	Core diameter, top d_c m	Cylindrical length l m	Conical length L m	Cone angle ° α	Inlet dimensions w×p mm	Inlet type	Operating pressure, bar g	Mass flow rate of steel tonnes/min
case 1	0.06	0.03	0.05	0.290	6	12×25	tangential	2	0.52
spigot dia 30 mm	0.06	0.03	0.05	0.290	4.7	12×25	tangential	2	0.42
spigot dia 40 mm	0.06	0.03	0.05	0.290	3.6	12×25	tangential	2	0.33
spigot dia 60 mm	0.06	0.03	0.05	0.290	Parallel	12×25	tangential	2	0.96
cone length 365 mm	0.06	0.03	0.05	0.365	4.7	12×25	tangential	2	0.52
cone length 440 mm	0.06	0.03	0.05	0.440	3.9	12×25	tangential	2	0.52
cone length 590 mm	0.06	0.03	0.05	0.590	3	12×25	tangential	2	0.51
core dia 45 mm	0.09	0.045	0.05	0.440	3	22.5×25	tangential	2	0.97
core dia 55 mm	0.12	0.06	0.05	0.440	7.8	30×25	tangential	2	1.36
1-bar	0.06	0.03	0.05	0.290	6	12×25	tangential	1	0.36
0.5-bar	0.06	0.03	0.05	0.290	6	12×25	tangential	0.5	0.23
Involute	0.06	0.03	0.05	0.290	6	12×25 by 45 °	involute	2	0.52

Table 4.1. Test case dimensions and operating pressures.

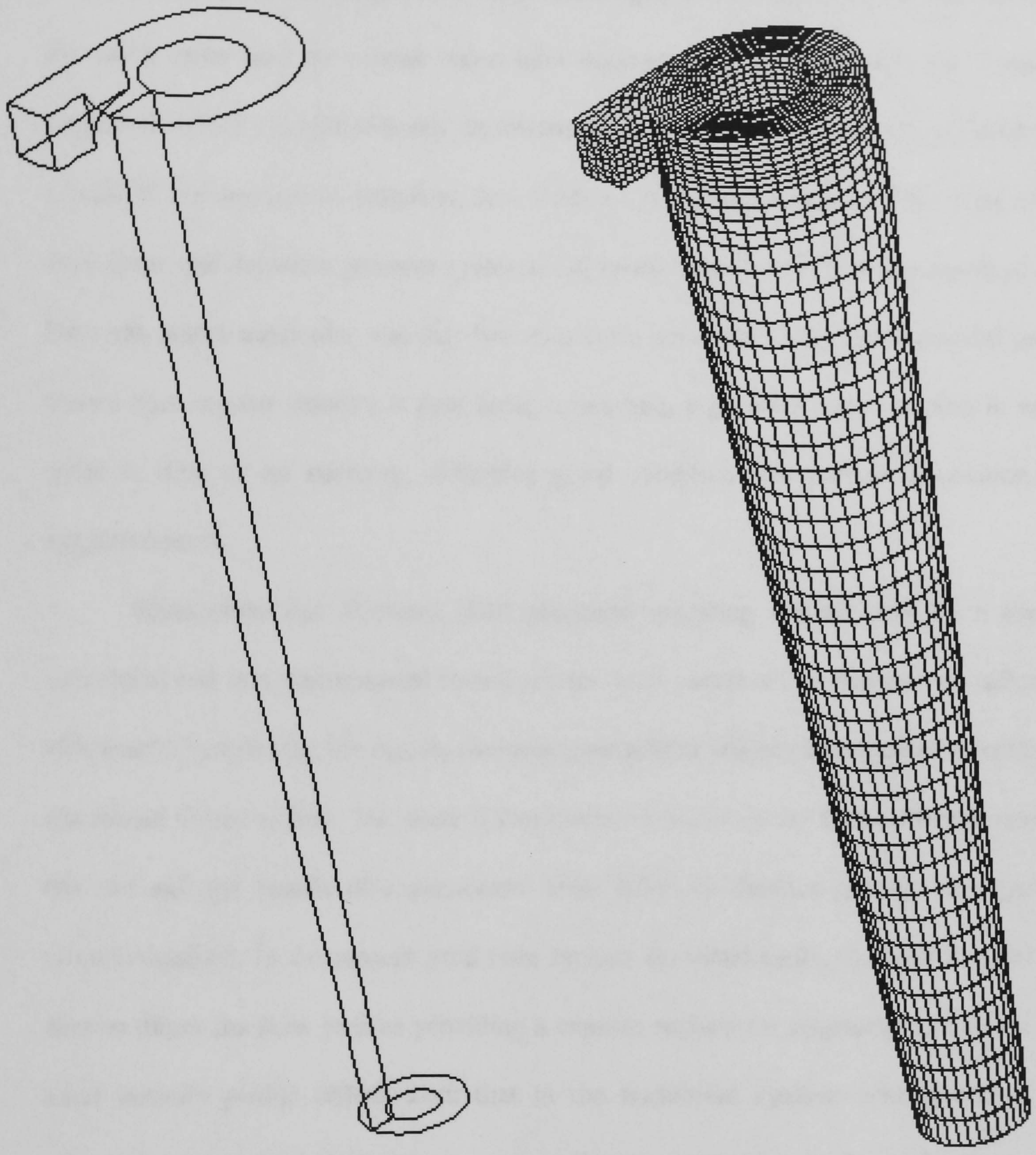

Outline Structed Polar grid

Figure 4.2. Cylindrical polar grid used to model the solid core hydrocyclone.

4.1.3 Velocity profiles

Using the RSM to predict velocity profiles, it can be seen in Figures 4.3 and 4,4 that the tangential and axial velocity profiles are believable, resembling closely those in a conventional hydrocyclone [B7, K2, K5]. The tangential velocity is seen to increase from the outer cone wall to a peak value then decrease towards the core. An increasing tangential velocity profile towards the centre supports the assumption of free vortex flow typical of the anisotropic turbulent flow field in hydrocyclones. Free vortex flow means flow shear and therefore promotes particle dispersion. The vortex flow changes type near the core, where molecular viscosity becomes more dominant. Also, the tangential profile shows that angular velocity is now being conserved, ergo solid body rotation in which there is little or no shearing, indicating good conditions for particle deposition and agglomeration.

Dyakowski and Williams [D8] proposed replacing the air core by a narrow cylindrical rod in a conventional hydrocyclone (with overflow) to improve classification efficiency by exploiting the rapidly decreasing tangential velocity in the radial direction of the forced vortex region. The need to incorporate a vortex finder limited the diameter of the rod and the results of experimental trials failed to displace the air core [private communication]. In the present solid core cyclone for metal melts, the core is wider and acts to direct the flow besides providing a capture surface for migrating inclusions. The axial velocity profile differs from that in the traditional cyclone with overflow: the pressure drop in the radial direction causes the expected decrease in axial velocity, but there appears to be a faster moving flow layer just off the core. in the forced vortex region. This fast axial moving layer corresponds to the position of peak tangential velocity in the flow. Particles entering this region will therefore be swept down and in

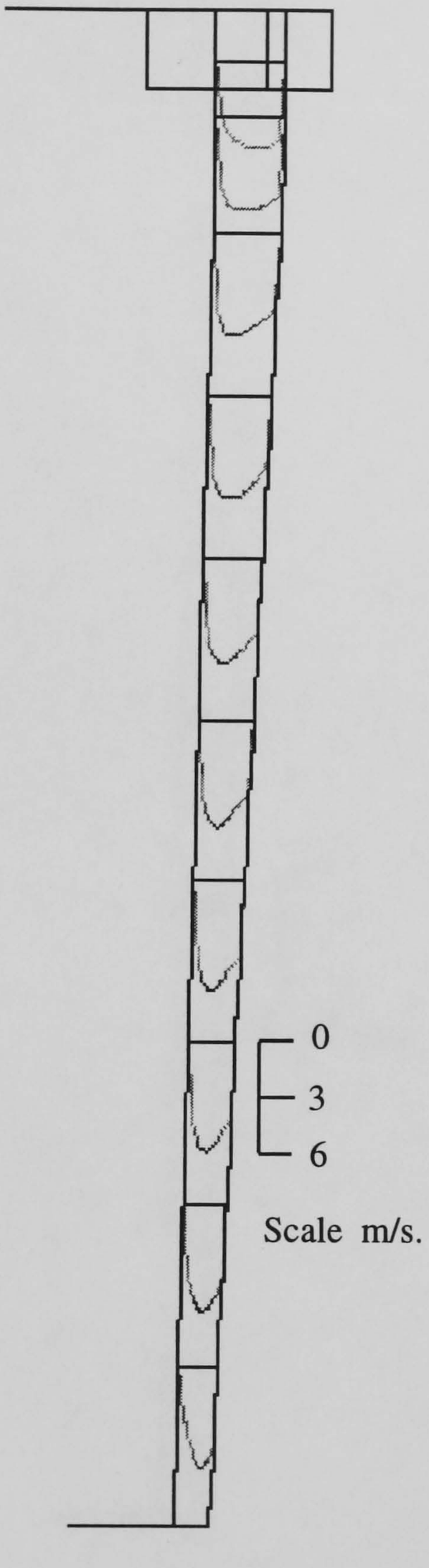

Figure 4.3. Tangential velocity profiles in solid core hydrocyclone calculated using RSM.

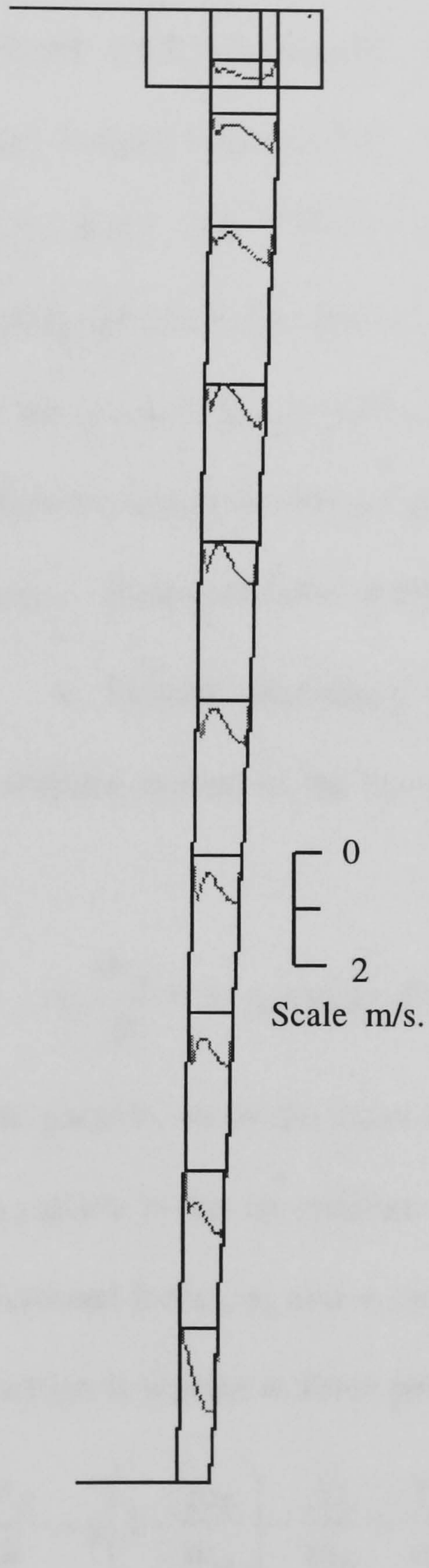

Figure 4.4. Axial velocity profiles in the solid core hydrocyclone predicted using RSM.

towards the core. Once the flow field is established particle trajectories are then predicted to establish the capture efficiency of each solid core cyclone design.

4.1.4 Particle tracking

The effectiveness of inclusion migration to the core was assessed on the basis of particle path predictions. Fluent V4.2.2 is capable of low volume dispersed phase simulation [F1]. The inclusion volume concentration in a steel melt is low enough to assume that inclusions have no direct effect on the carrier phase i.e. that there is no momentum exchange. It is further assumed that there are no chemical effects or particle-particle interactions and that the second phase particles are spherical. The force balance equation of motion for a particle travelling in a liquid takes the form

Particle mass × Acceleration = Resultant force on the body in the direction of motion.

= Gravity - Buoyancy - Drag - Additional forces.

Considering a cartesian co-ordinate system in the co-ordinate direction x, this can be written simply as

$$m_p \frac{dv_p}{dt} = m_p g - m_l g - D - F_x \qquad 4.1$$

Where m_p is the mass of the particle, m_l is the mass of the liquid displaced, g is the gravity force imposed on the particle in this co-ordinate direction, D is the drag force on the particle, F_x represents additional forces, v_p and v_l are the particle and fluid velocities respectively. If the above equation is written as force per unit particle mass it becomes

$$\frac{dv_p}{dt} = g\left(1 - \frac{m_l}{m_p}\right) - \frac{D}{m_p} - \frac{F_x}{m_p}. \qquad 4.2$$

Given that

$$\frac{m_l}{m_p} = \frac{\rho_l}{\rho_p} \quad \text{and} \quad m_p = \tfrac{1}{6}\pi d^3 \rho_p$$

where ρ_l and ρ_d are the liquid and particle densities and d_p is the particle diameter then the gravity and buoyancy term combined can be written as

$$g\left(1 - \frac{\rho_l}{\rho_p}\right). \qquad 4.3$$

The drag force component on a spherical particle in a 3-dimensional flow, see Douglas [D6] for a full derivation, is defined as

$$D = \tfrac{1}{8}\rho_l \pi d_p^2 \left(v_l - v_p\right) C_D \qquad 4.4$$

C_D is the drag coefficient which is a function of the relative Reynolds number defined as

$$Re = \frac{\rho_l d_p \left|v_l - v_p\right|}{\mu}. \qquad 4.5$$

Where μ is the fluid viscosity. From equation 4.4 for the drag force and the expression for Reynolds number it is possible to write the drag force per unit particle mass as

$$\frac{D}{m_p} = \frac{18\mu}{\rho_p d_p^2} \frac{C_D\, Re}{24} \left(v_l - v_p\right). \qquad 4.6$$

The force balance equating the particle inertia with the forces acting on the particle and following the Fluent manual [F1] can now be written as

$$\frac{dv_p}{dt} = \frac{18\mu}{\rho_p d_p^2} \frac{C_D\, Re}{24} \left(v_l - v_p\right) + g\left(1 - \frac{\rho_l}{\rho_p}\right) + \frac{F_x}{m_p} \qquad 4.7$$

In this investigation an additional force that is important because $\rho_l > \rho_p$ is the force required to accelerate the fluid surrounding the particle.

When a particle is set in motion it is given a kinetic energy but in addition the fluid that is displaced by its movement has to be given an amount of kinetic energy

$\frac{1}{2} m_l v_l^2$ where m_l is the mass of liquid displaced. Consequently, the work done is greater than if only the particle were moved. The result is as if the particle had added mass. The sum of the added mass and the actual particle mass is known as the virtual mass, "virtual mass" force is derived from the sum of the two kinetic energies. The "virtual mass" force expressed per unit particle mass $\frac{F_x}{m_p}$ is written as

$$\frac{F_x}{m_p} = \frac{1}{2}\frac{\rho_l}{\rho_p}\frac{d}{dt}\left(v_l - v_p\right). \qquad 4.8$$

Prediction of the dispersed phase trajectory in Fluent integrates the total force balance on the particle in a Lagrangian formulation.

In the cyclone, a particle moves through turbulent velocity fluctuations which vary with position in the flow. It is possible to represent these fluctuations on the steady state prediction of the carrier phase using statistical methods. Fluent uses the isotropic method similar to that described by Yuu [Y2], in which the rms of eddy fluctuating velocity components are obtained from the kinetic energy of turbulence as:

$$\sqrt{\overline{v_i'}} = \sqrt{2k/3}\,. \qquad 4.9$$

A normally distributed random number is applied to characterise the time spent in each eddy, after which time a new one is chosen. All values are updated when migration into another cell occurs. Small cell intervals are preferable for this type of simulation. There is a risk that incorporating a model of this type could produce deceptive results by over predicting the turbulent mixing in the hydrocyclone. A recent model proposed by Burry and Bergeles [B11] which incorporates the anisotropic nature of the flow would have been more suitable but was not developed in the study due to lack of time.

In order to obtain statistically reasonable results for particle migration, large numbers of particles have to be simulated or tracked. The length of time required to

carry out the turbulent eddy simulations needed to predict classification efficiency in this way for each chosen cyclone geometry would have been prohibitive. It was therefore thought acceptable for the present limited optimisation study to use only the mean steady state approximation of the anisotropic turbulent eddy behaviour. This avoided having to introduce the spatially dependent randomness required for turbulent particle tracking. Although not ideal, this approach would at least provide a standard case by which to compare cyclone geometries. As the particle changes its radial position in the swirling flow, the centripetal acceleration exerted on it varies and particles in the range of interest in steel, of order 20μm or larger, may therefore deviate between Stokesian and non-Stokesian behaviour. Fluent updates the drag coefficient in the equation of motion under these conditions as a function of the relative Reynolds number. Because of the variation in centripetal acceleration with position, this approach is essential to any particle trajectory prediction within a hydrocyclone. The ability to update the drag coefficient in the numerical particle tracking model is a clear advantage of the CFD approach. At the stage the particle modelling work was carried out there was no comparable experimental particle capture curves, which could be used to validate the particle tracking model.

4.1.5 Escape curves

The particle tracking study produced curves showing the percentage of particles within a defined size range that escape in the underflow. These percentage escape curves represent an approximation of the performance of the solid core hydrocyclone and offer a simple indication of efficiency. A curve for each test case was calculated by setting off an evenly distributed grid of identical particles at the inlet and recording the number of each set captured or escaped. This process was repeated for sets of particles of each size in a range 5 - 70 μm in intervals of 5 μm, the density of the alumina particles was taken

to be 3500 kg/m^3. Particles were assumed to stick to the core as soon as they contact with it. Figure 4.5 is an example of some 35 μm alumina particle tracks set off from different positions in the inlet as the migrate on to the central core, calculated using Fluents mean track particle tracking model. Figures 4.6 to figure 4.10 show the percentage of each size that escaped from the cyclones listed in Table 1. The most effective solid core cyclone is that producing a low particle size cut off point and having an escape curve with a small slope.

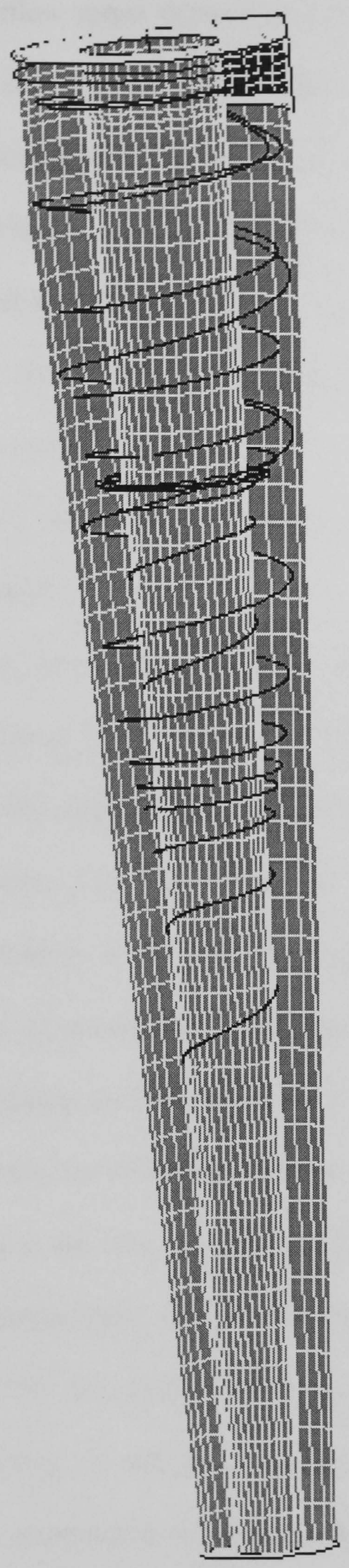

Figure 4.5. Possible, predicted particle tracks for 35 micron alumina inclusions migrating onto the solid core. The particles are set off at different locations in the inlet.

Figure 4.6 indicates the effect on particle capture of increasing the cyclone length while keeping the underflow spigot dimensions constant. This consequently adjusts the cone angle. The slope of the curve changes little but the cut off size decreases with increasing length. The driving head is a fixed condition for the model and is therefore not affected by this design change. Also, the underflow dimensions were kept the same and the volume throughput was unaffected. Although the mean tangential velocity is reduced due to the increase in friction losses with length, this is balanced by an increased residence time of the dispersed phase. Figure 4.7 shows the effect of changes in underflow size. As the underflow diameter is decreased, the volume flow rate and mean tangential velocity are reduced.

The fall in driving head as a ladle empties, for example, is an important factor in the design. Figure 4.8 shows that a reduction in pressure drop produces an increase in the cut off size and that the slope of the escape curve becomes steeper, but the change is not very significant between 2 bar and 1 bar head.

The size and geometry of the inlet affect separation performance as Figures 4.9 and 4.12 show. The inlet dimensions were increased in proportion to the increase in top diameter as was the capture surface of the core. Figure 4.10 shows the increase in capture efficiency caused by the smoothed shape of an involute entrance as a result of the decreased energy losses at the inlet. In conventional hydrocyclones involute entries are known to improve efficiency [B8], though they are not as easy to manufacture as the simple tangential inlet. The new solid core cyclone for molten steel processing is to be made in castable refractory. It will be much easier to produce a tangential inlet in castable refractory and preferable if it will mean a smoother introduction of the liquid steel into the cyclone body, which will reduce the chance of refractory wear. The optimum geometry for the design needs to consider more than just capture efficiency

curves, it also needs to be an operational possibility. Therefore, the larger the flow rate through the unit the better. A compromise between capture efficiency and volume flow rate was made and the optimum design geometry for further investigation was taken to be that of case (core diameter 45 mm) with an involute entry and a conical length of 440 mm. It should be stressed that these dimensions are in no-way to be seen as a final design, they provide a good initial starting point for a full investigation into the workings and validation of the solid core cyclone idea for the removal of alumina from steel.

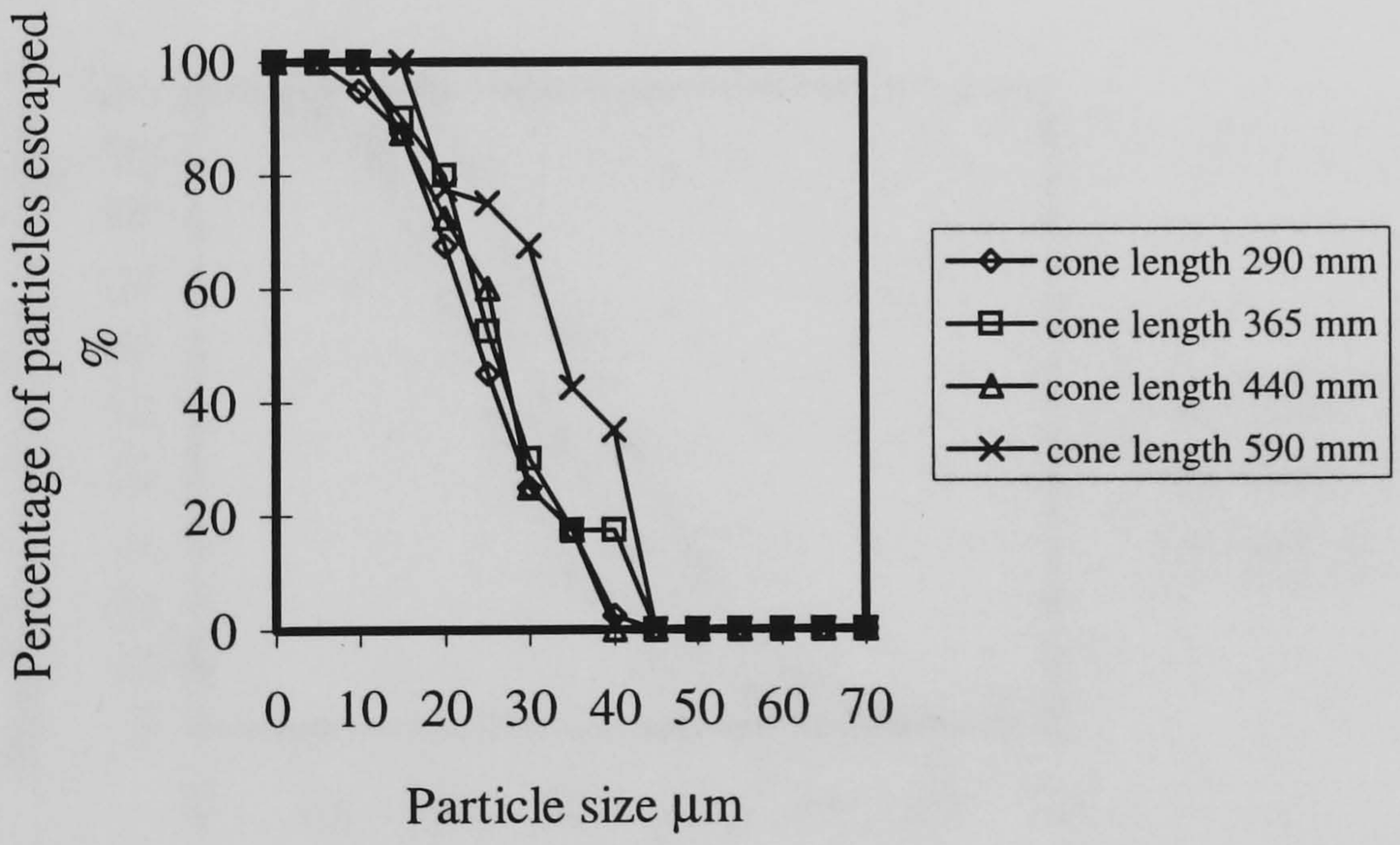

Figure 4.6. Percentage particle escape curves for different cone lengths.

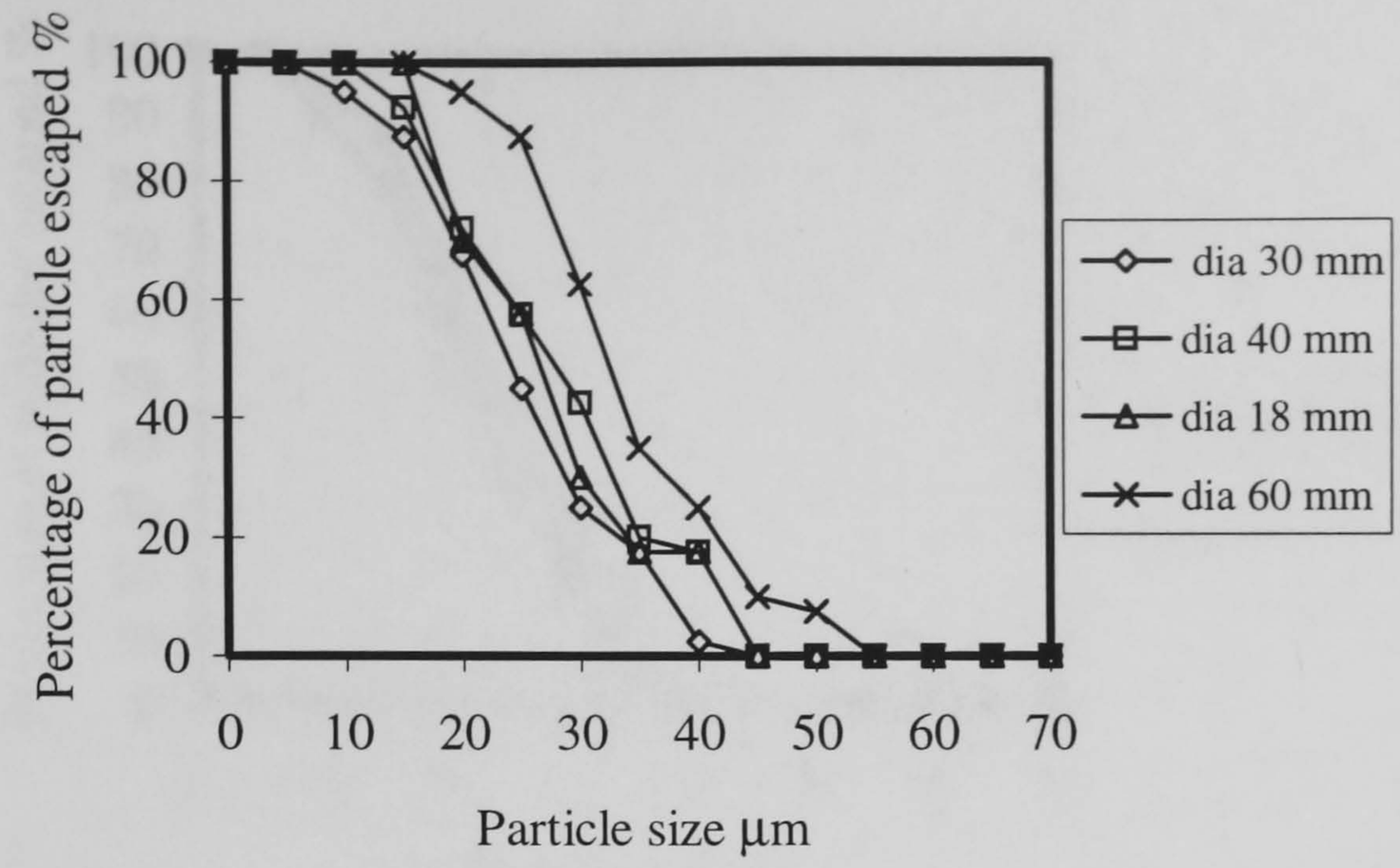

Figure 4.7. Percentage particle escape curves for different spigot diameters.

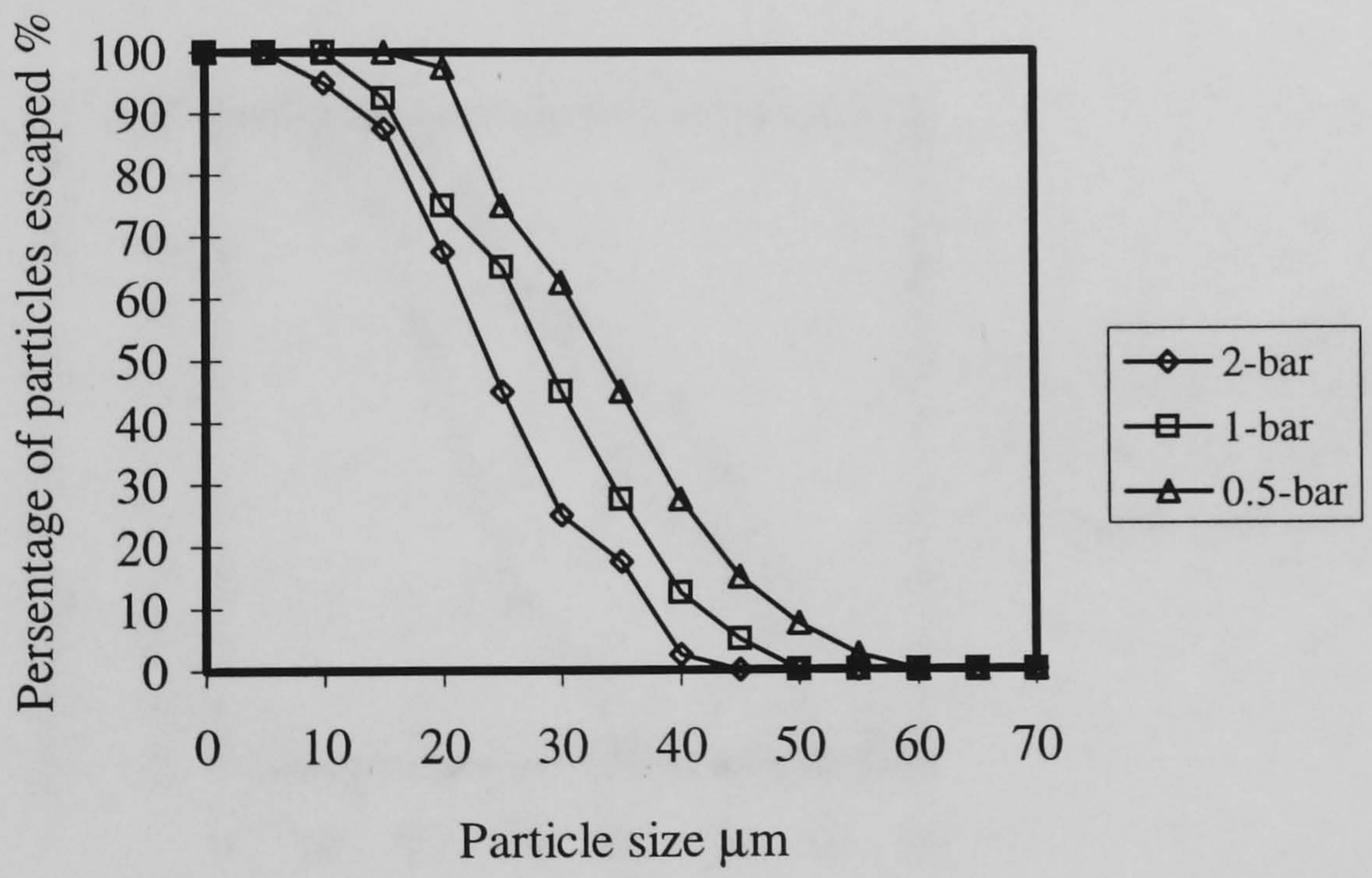

Figure 4.8. Percentage particle escape curves for different operating pressures.

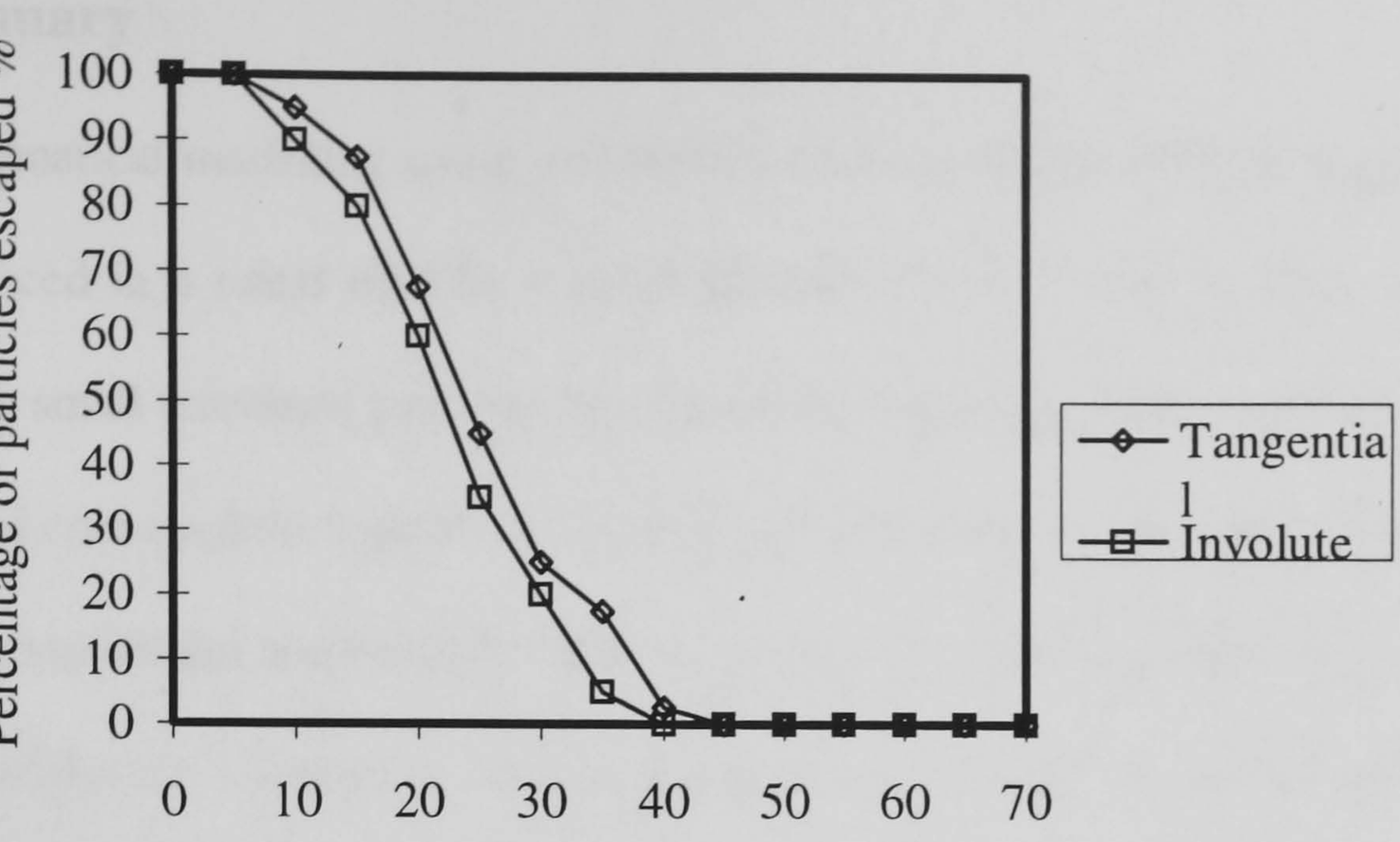

Figure 4.9. Percentage particle escape curves for a tangential and an involute entries

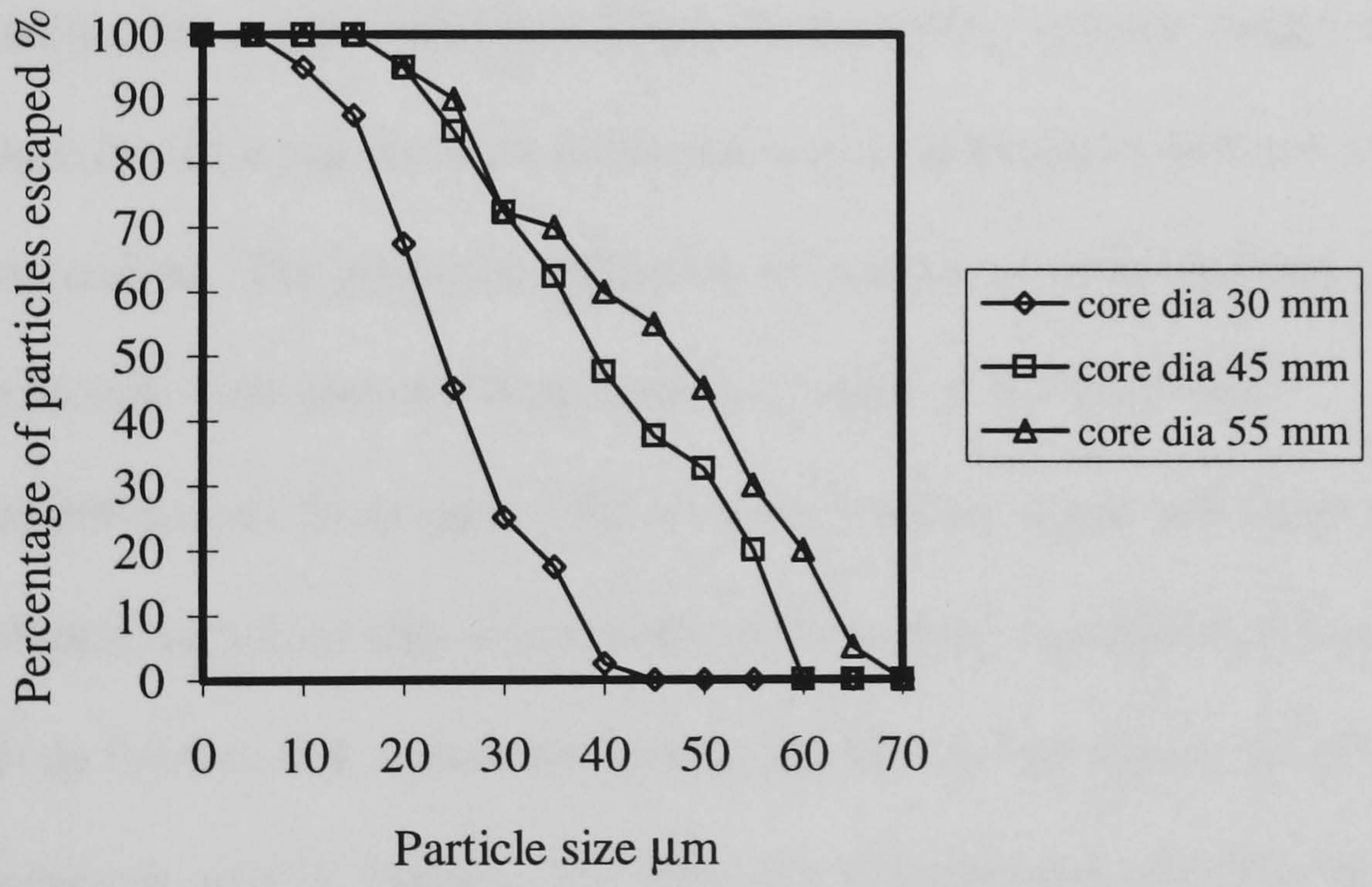

Figure 4.10. Percentage particle escape curves for scaled up diameter cyclones represented by core diameter.

4.1.6 Summary

Mathematical modelling using a three-dimensional model strongly suggests that the swirl induced in a metal melt by a small diameter cyclone with an axial solid core could remove small entrained particles by centripetal migration and attachment. In this sense the solid core cyclone appears to act as a high flow filter of alumina inclusions.

In computational trials on the removal of alumina particles from liquid steel, in which the particles are assumed to stick to the axial core surface on contact, design and test studies predicted the removal of all particles larger in size than 45 microns and a high proportion of those between 25 and 40 microns. Particle trajectories and contacts with the core capture surface were determined by a particle tracking method.

Assuming a maximum cyclone pressure drop of 2.0 bar gauge, which corresponds to a practical scale of melt gravity head, while still having a reasonable capture efficiency and consequently deemed the most effective cyclone design was (core diameter 45 mm) having a top diameter of 90 mm, a conical length of 440 mm and a flow rate of 1.0 tonnes/min. The predicted efficiency of particle removal did not appear to diminish dramatically with pressure drop down to a value of 0.5 bar gauge.

The benefit derived from using CFD is that it provided a test bed for designs that would not normally have been considered under the operating conditions of a steel plant. The results firmly indicate that a small diameter solid core cyclone design for the removal of alumina inclusions, may be feasible. The following Chapters describe how this finding was progressed and physically tested. Before this is done the next two sections of Chapter 4 extends the analysis of the computational work. Looking first at how the a particles entry position in the annular flow can influence its chance of chance of capture and then at a simple numerical approximation for the distribution of alumina build up on the central core.

4.2 Helix angles

Elements of fluid in a swirling annulus like those of the solid core cyclone describe a spiralling path. The helix angle θ_H about the horizontal position along the spiral is a function of the axial and tangential velocities, v_z and v_θ respectively, of the fluid at that point, given as

$$\theta_H = \tan^{-1} \frac{v_z}{v_\theta}. \qquad 4.10$$

Both the axial and tangential velocities vary radially and therefore also the helix angle, as for example is shown in figure 4.11.1 to 4.11.3. A lower density particle will not take the same spiral path that an element of the fluid would. Instead, it migrates radially across the flow and the helix angle of its track changes with its position. Following Stokes's law, the radial force acting on the particle results from the centrifugal acceleration a_r at that point, which is a function of its radial position and the tangential velocity i.e.

$$a_r = \frac{v_\theta^2}{r}. \qquad 4.11$$

The ideal condition for particle separation is a low axial velocity and a high tangential velocity corresponding to a low helix angle. Under these conditions the particle is more likely to travel the required radial distance to the core without exiting the cyclone. Take an example of a helix angle profile across the annulus shown in figure (4.11.3). The outer radial position at the cone wall has a high helix angle corresponding to a low tangential and high axial velocity. The helix angle then reduces towards the centre of the annular gap giving much better conditions for separation.

Computational studies of the steady state case show that the initial position of a particle in the inlet is an important factor in its chance of being captured. If a particle is to leave the inlet and enter along the outer wall, it is less likely to be captured due to the

higher helix angle than a particle which starts in the middle of the annular gap where the helix angle is low. Figure 4.12 shows the number of revolutions of the core before exiting that a neutral density particle would make at different starting positions. A small number means a loose spiral with a high helix angle and a therefore corresponds to a short residence time in the hydrocyclone. A large number indicates that the neutral particle will maintain a tight spiral with a low helix angle and remain longer in the hydrocyclone. Consequently, the number associated with the particle's position is proportional to the chance that a low density particle in the steel melt has of being captured.

A contributing factor to the paths taken by different particles in the inlet is the region of high radial velocity caused by the rotating flow in the top section recombining with the inlet flow. In conventional hydrocyclones, this radial flow across the top is described as a short circuiting flow, and every effort is made to avoid it. In the solid core hydrocyclone, the apparent short circuiting is beneficial because it draws inclusions in to the main flow and close to the core. Unfortunately those inclusions that avoid this region enter along the outer wall where there are high axial and low tangential velocities and is therefore less well positioned for migration to the centre, see figure 4.12.

These observations of helix angle and the particles position in the inlet are equally relevant to the conventional hydrocyclone. They emphasise that inlet and top design can have a pronounced effect on classification efficiency and their importance certainly merits further work.

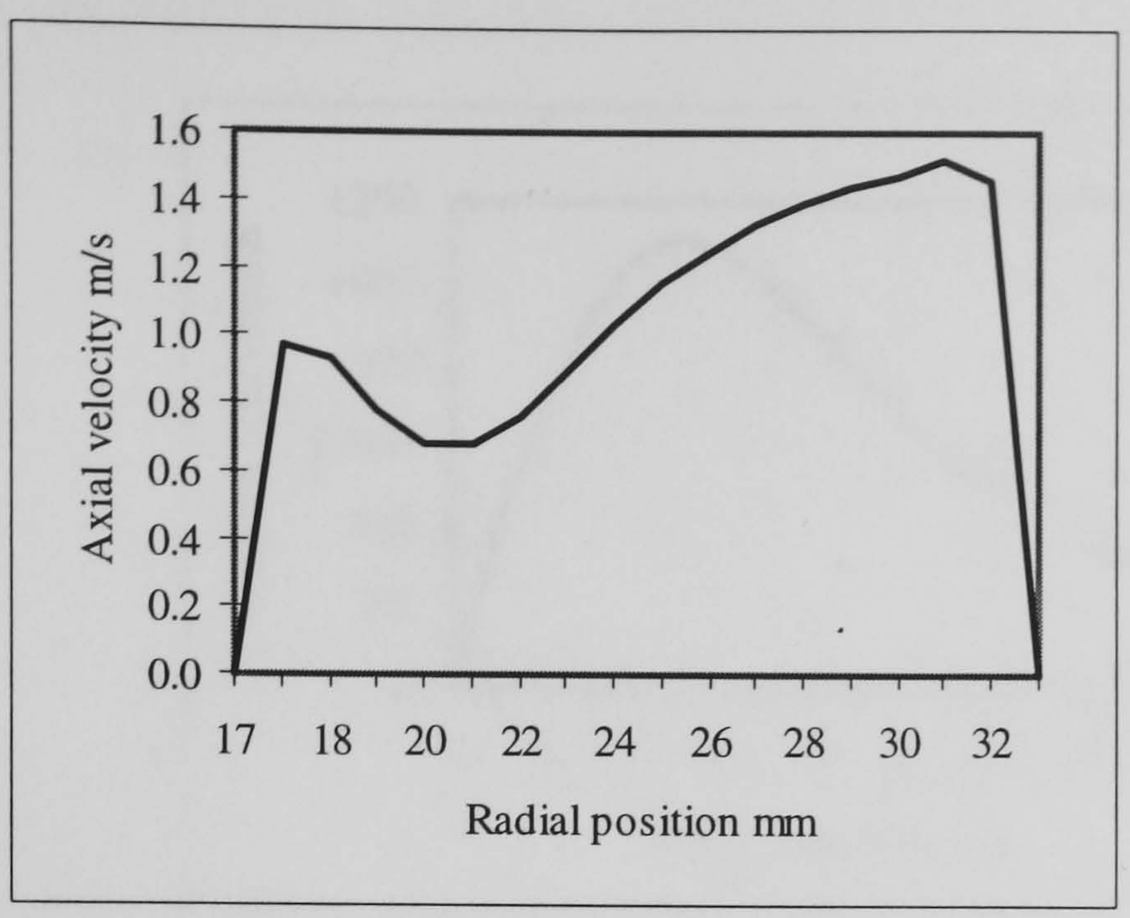

Figure 4.11.1. Axial velocity profile

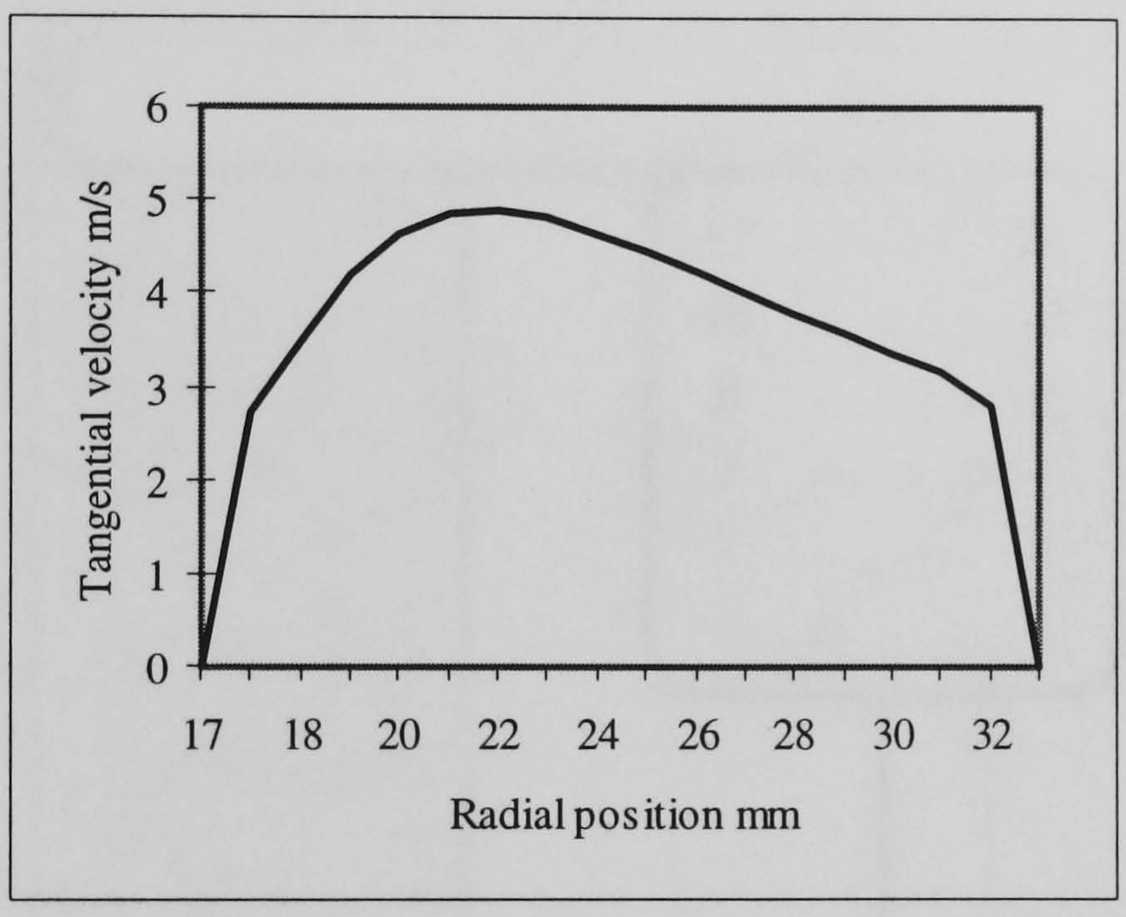

Figure 4.11.2. Tangential velocity profile

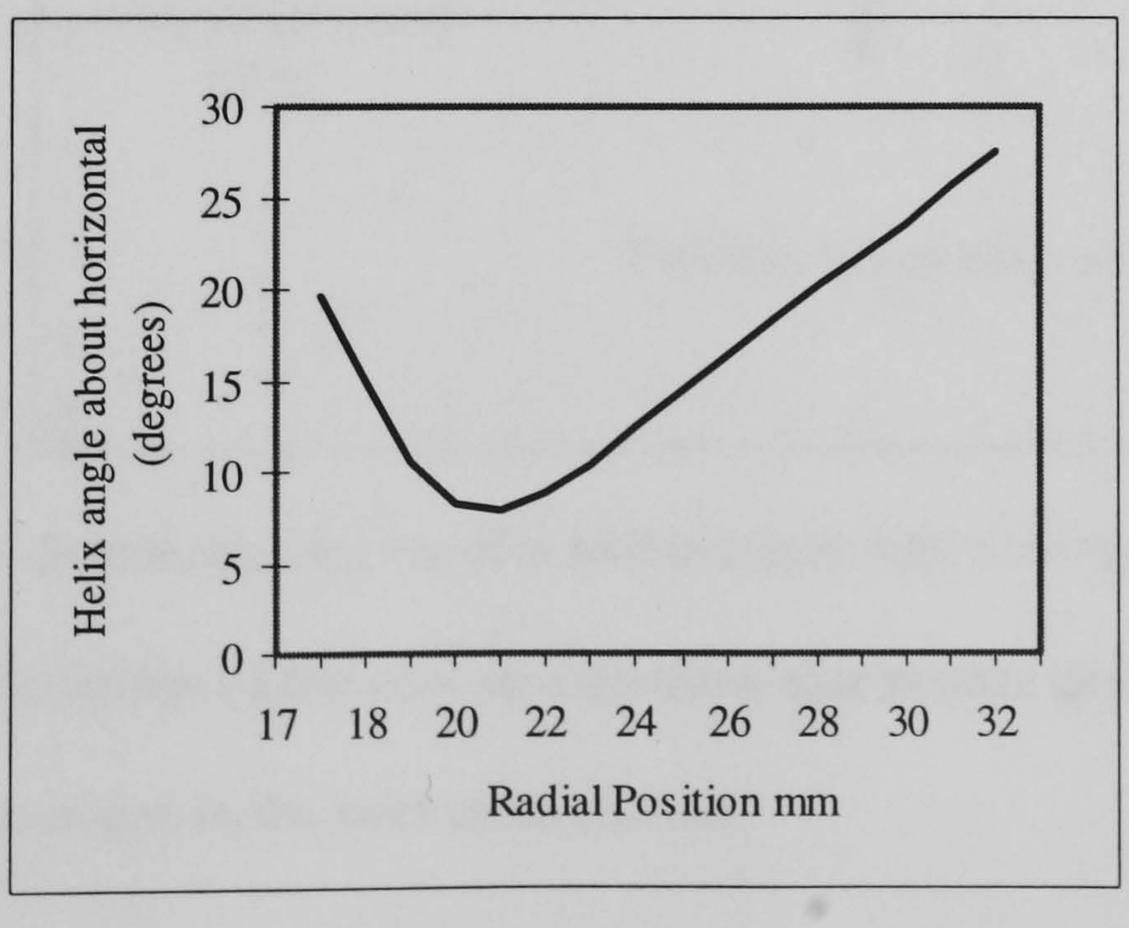

Figure 4.11.3. Profile of calculated helix angle.

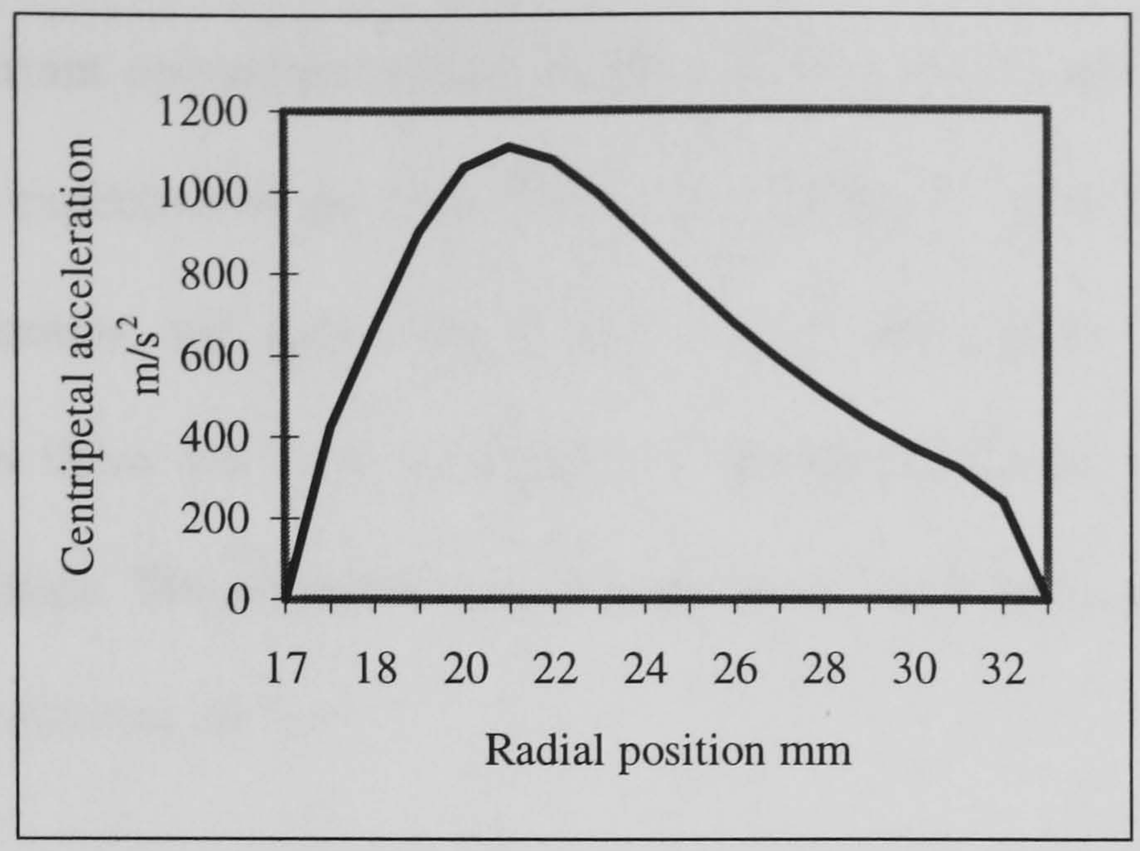

Figure 4.11.4. Centripetal acceleration profile

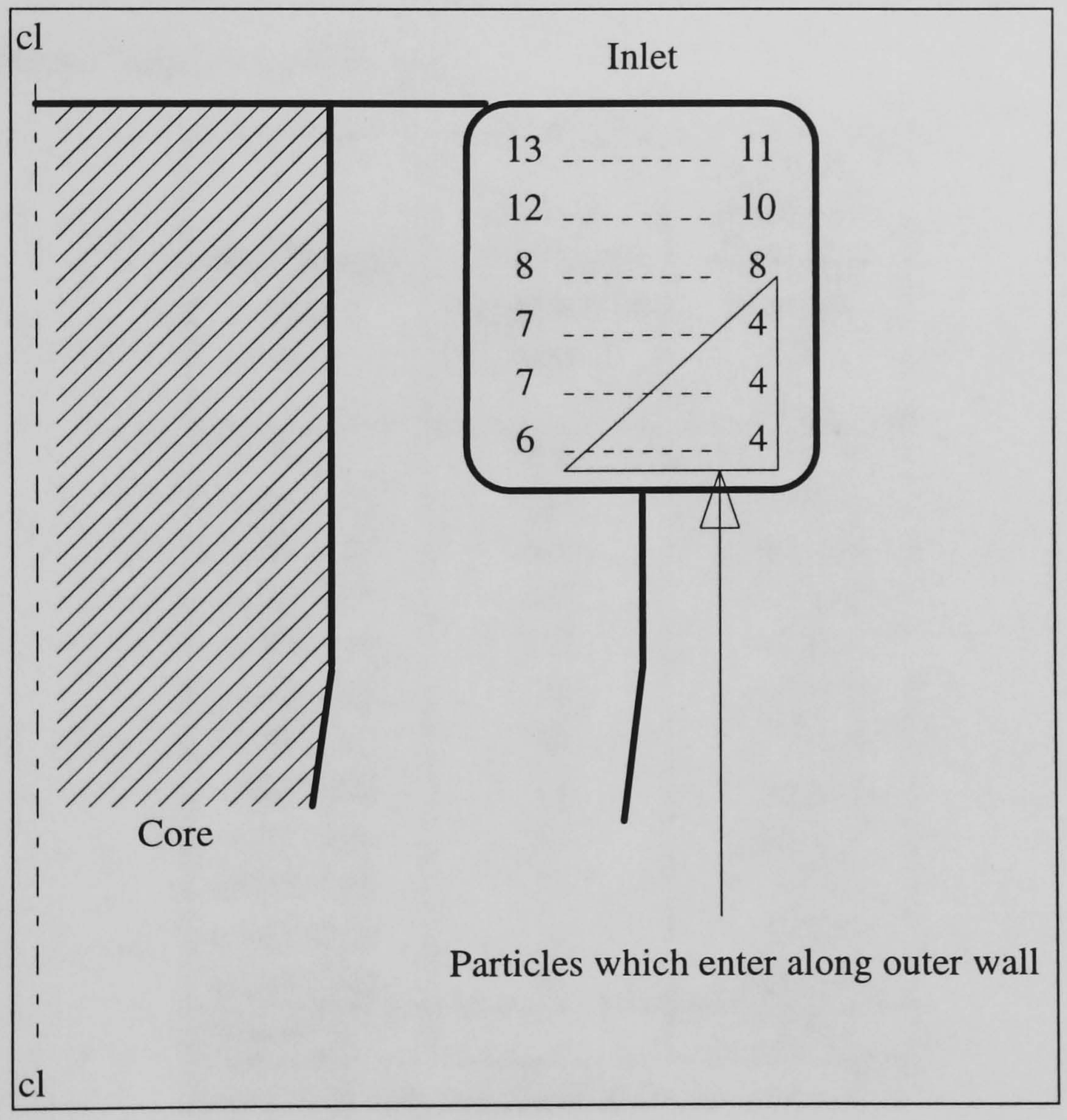

Figure 4.12. Schematic section of a half-involute inlet showing the computed number of complete revolutions of the core to underflow that neutral density particles will make as a function of position in the inlet cross section.

4.3 Deposition rate [alumina build up]

One important operational aspect of the design is the amount of inclusion build-up that would be expected on the core. The core provides a refractory surface to which the alumina inclusions will stick. The actual capture mechanism that takes place is uncertain, though there are many examples of alumina build up in submerged entry nozzles and tundishes. The computer model assumes an inclusion is captured if it comes into contact with the core surface.

Table 4.2. Size distribution of alumina inclusions in a steel melt, data provided by British Steel Technical, Teesside laboratories.

Size Range (μm)	**No. of Particles expected in 1 cm^3**	**Approx. volume of each size band in 1 m^3 (m^3)**
+10 -20	889	1.586E-6
+20 -30	747	5.988E-6
+30 -40	403	8.845E-6
+40 -50	195	9.110E-6
+50 -60	118	1.010E-5
+60 -70	70	9.890E-6
+70 -80	36	7.828E-6
+80 -90	18	5.710E-6
+90 -100	24	1.060E-5
+100 -150	34	3.570E-5
+150 -200	4	1.140E-5
+200 -250	0	0.000E+0
Total $\sum x$		1.170E-4

$\sum x$ sum of volume fraction for all sizes m^3/m^3

In table 4.2 each size band is broken up into 1 μm sub intervals and the volume of inclusion material in 1 cm^3 of liquid steel is calculated. This is done as a summation of

the spherical particle volumes for each 1μm sub interval within the size band, as shown in the following equation

$$Vol_{band} = \frac{Int_{average} \cdot \pi}{6} \cdot \sum_{n}^{n+9} d_n^3 \ . \qquad 4.13$$

The distribution of the particle sizes within each size band is assumed to be uniform and the number of particles in 1 cm^3 per 1 μm sub interval, $Int_{average}$, can be taken as an average of the number of particles in the second column of table 4.2. Multiplying the total volume of inclusion material in 1 cm^3 by 1e+6 indicates that the probable volume of inclusions in $1m^3$ or 7 tonnes of steel corresponds to a solid cube of side 49 mm. For simplicity this calculation has ignored voids.

4.3.1 Predicting build up

The amount and distribution of build up on the core per cubic meter of steel processed (assuming the above steel quality) has been predicted from the computer model. A data file was obtained from Fluent containing the final grid location of each of the identical 40 spherical particles set off across the inlet a core location corresponds to a particle being captured. This was done for particle diameters at 5 μm intervals. For each size band of inclusions in table 4.2 the band is split into intervals of 1 μm. It is assumed that the mean number ,n_p, of particles in each 1 μm interval present in 1 cm^3 of steel is equal to the total number in the original band from table 4.2 divided by the number of 1 μm intervals. A simple Pascal program was then used to read each data file and calculate the volume of build-up, vol_{cell}, per cubic meter at each grid cell location. This was done by multiplying the spherical volume of a single particle, the mean number and the ratio, r_{cell}, of particles that landed there to the original 40 particles released, i.e.

$$\mathrm{vol}_{cell} = \tfrac{1}{6}\pi d_p^3 \cdot n_p \cdot r_{cell} \cdot 10^6. \qquad 4.14$$

Each of the data files or matrices representing one particle size now contained the volume of build up at every cell location. To obtain the total volume of material deposited at each grid location on the core, a program was written that performed a 3-dimensional integration between equivalent grid cells using the trapezium rule taking a corresponding interval width S_d of 5 particles between the matrices. If n is the number of matrices to be overlaid then the volume build up in each cell v_{cell} is calculated by the trapezium rule as

$$\mathrm{vol}_{cell} = S_d \cdot \left[\frac{\mathrm{vol}_1}{2} + \frac{\mathrm{vol}_n}{2} + \mathrm{vol}_2 + \mathrm{vol}_3 + \ldots + \mathrm{vol}_{n-1} \right]. \qquad 4.15$$

A schematic diagram of the process is shown in figure 4.13. The height of the build up at each location could then be predicted by dividing this volume by the area of the cell. This was done for the solid core hydrocyclone case1 in the optimisation study.

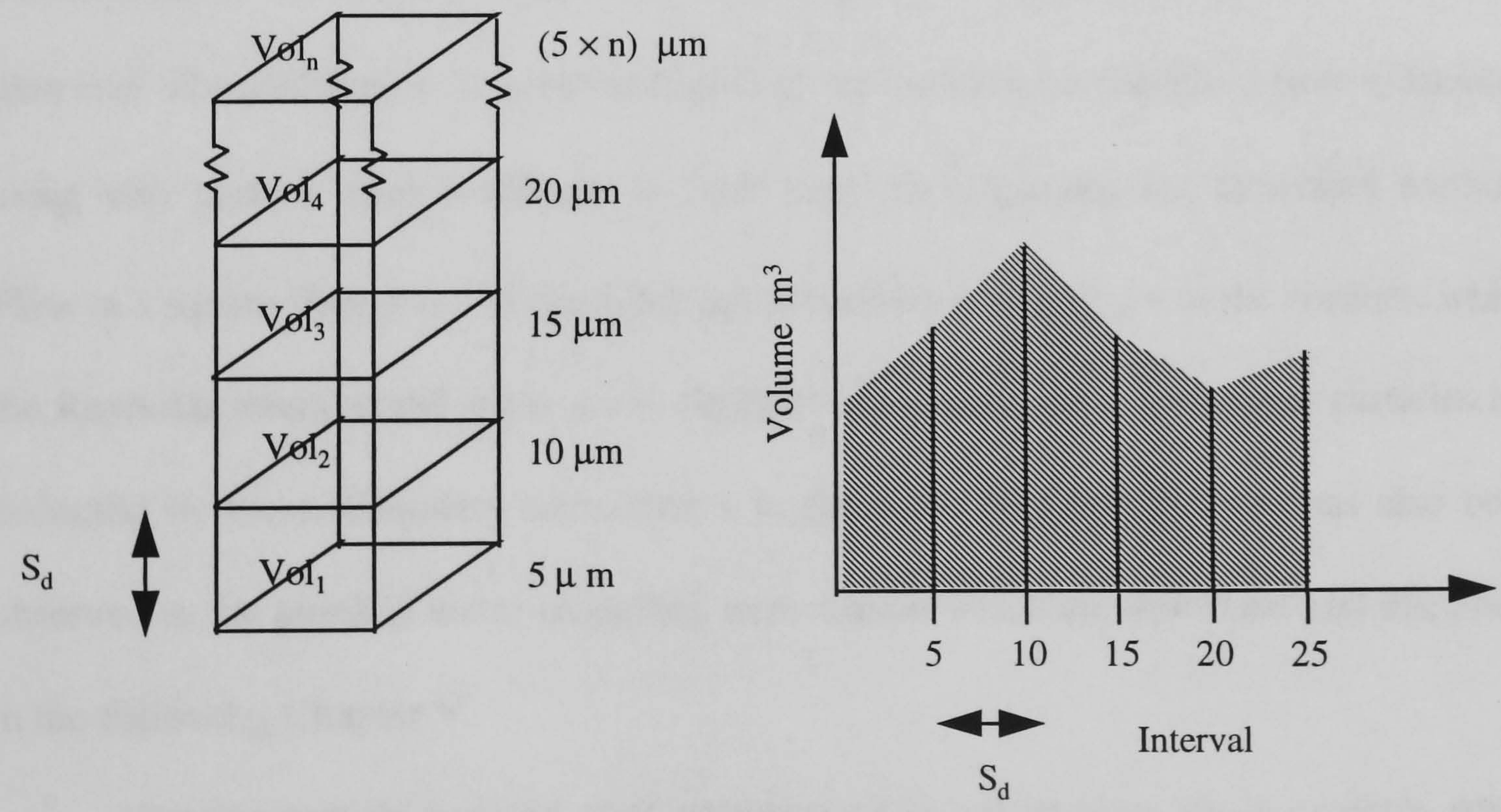

Figure 4.13. Schematic diagram outlining the use of the trapezium rule to calculate the total volume build up of alumina at each grid square on the core.

4.3.2 Numerically predicted build up distributions

In the design study, frequency distribution curves describe the escape of inclusions retained in the melt and an indication of the cleanness of the discharging steel with respect to alumina particles. The inclusions that constitute the material retained in the melt in the CFD modelling study are mostly small in size. It can be seen in the above table 4.2 that although numerous, the smaller sized inclusion make up only a small volume of the overall material present in the melt. Though many of the smaller inclusions are retained in the melt, the total volume of material left on the core based on the predicted escaped curves was calculated to be 1.106×10^{5} mm^3 per $1m^3$ of steel processed, which corresponds to a solid 48 mm sided cube. This predicted captured volume therefore accounts for 94 % of the total volume of inclusions in the melt.

It was discovered that larger particles introduced into the inlet of the cyclone model did not follow a straight line trajectory into the body of the cyclone. These particles curve towards the walls of the inlet where the computed track iteration would then end. The distribution of predicted build up on the core has therefore been calculated using only particle sizes 5-100 μm at 5μm intervals employing the described method. Flow in a square duct is not uniform but has secondary circulation's in the corners, which the Reynolds stress model is known to simulate adequately [H6]. The larger particles are deflected by these secondary circulation's in the inlet. This phenomenon has also been observed in the physical water modelling experiments which are described and discussed in the following Chapter V.

Fluent's particle tracking code performs all its calculations about a centre point. The outer dimensions of the particles are not considered during collision or as the particle passes into a boundary layer. This means that particles are not captured until their centre actually impinges on the surface.

Build up data was obtained for a 30 by 40 cell grid that lies on the core surface. The total amount of material captured on the core for the particle sizes between 5-100 μm was 58841 mm^3 from a maximum solids volume of 65332 mm^3 (per m^3 of molten steel passing through the cyclone). The number of particles representing each size band was quite small. When combined with the particle size interval, the build up prediction is consequently quite coarse. As a result, the build up patterns in figure 4.14 may appear to have a jagged (asperity) profile. Using more than 40 particles and smaller intervals may produce smoother profiles, but the model nevertheless indicates that there will not be uniform build-up on the core.

The larger particles that make up the bulk of the material have, due to their size, greater radial migratory forces acting on them and hence make contact with the core nearer to the top. The smaller material displaces more slowly and therefore travels further down the core and has a greater chance of escaping in the melt. The model implies that the bulk of the inclusions deposit in the same circumferential region of the core which gradually extends in a spiral around the core down its length. The steel enters with a uniform distribution of particles in the tangential inlet. The particles concentrate into an elongated cloud that stretches in a helix through the cyclone. The cloud spirals around the core, eventually depositing particles of about the same size at the same circumferential location.

The height of the accumulated deposit in the radial direction decreases down the core because the larger particles making up the bulk of the material quickly migrate to the core and therefore stick to it near the top. The smaller particle sizes travelling lower down deposit lower volumes of material. The model indicates that the build up height increases towards the narrower end of the core. Although the volume of material being deposited in the lower part of the cyclone is less than at higher levels, the increase in

build up height is enhanced because of the diminishing contact area of the core towards its apex.

The build-up model has several limitations; too few particles were used to produce a smooth build up profile; more intermediate particle size steps could be used to improve the accuracy of the integration method; the particle distribution data, though the best available, is only approximate. The model can therefore only give an idealised indication of what may occur. In reality, as the build up takes place, the core will change shape, thereby affecting the flow and consequently the particle trajectories and deposition pattern. The results show that the build up in the higher section could in practice almost bridge the annular gap for a solid core cyclone of these dimensions (case-1). The small size fractions only constitute a small percentage of the material that would be deposited.

Even the less efficient of the test cases in table 4.1 will capture a similar volume of material where the particles sizes below 50μm that are the most important to capture represent only a small volume of inclusion material. This build-up study has shown that the larger cyclone dimensions are preferred because they would process more steel before blocking. The performance curves indicated the design dimensions w1-5 were an effective compromise between capture performance and an increased flow rate. These dimensions would also allow for more build up of material. It is these dimensions which will be taken for the physical model validation of the solid core cyclone process in the

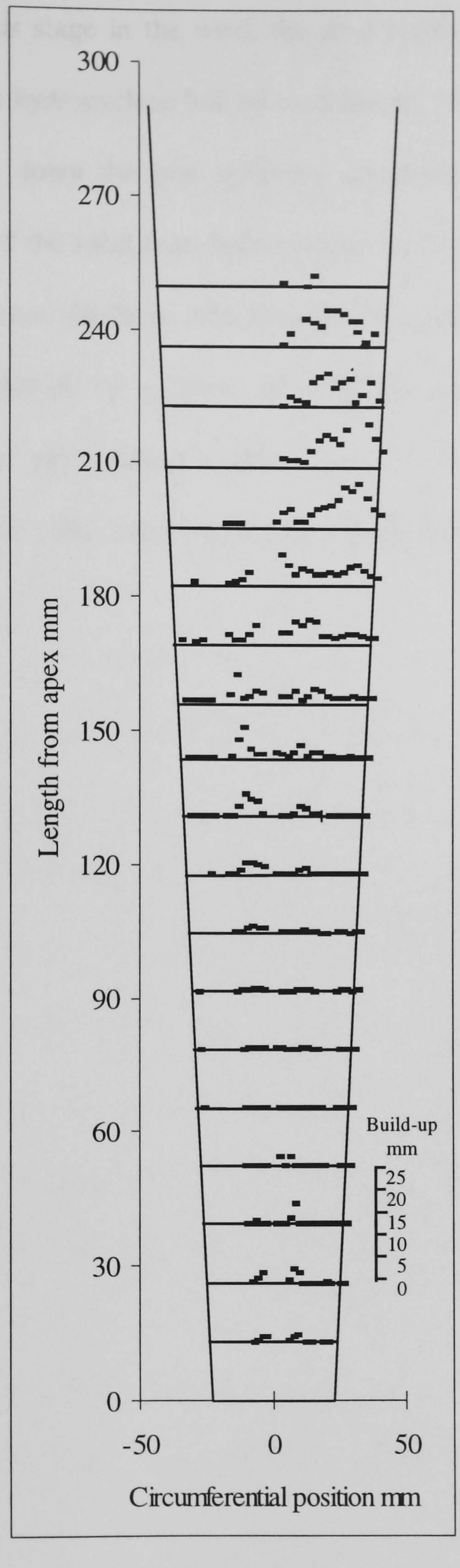

Figure 4.14. Showing the predicted build up patterns on the core at a series of projected circumferental positions, per m^3 of melt processed.

next chapter. At this stage in the work the final location or type of process route in which the solid core hydrocyclone will be used has not been specified. It is therefore not yet possible to pin down the best operating conditions and design dimensions. The computer analysis of the solid core hydrocyclone has shown that simply scaling up the dimensions to increase the flow rate through the system is not enough. A specific performance corresponds to a given set of dimensions and operating parameters. Therefore, like the conventional hydrocyclone, the best way to obtain a given performance for flow rates in-excess of a the single units capacity is to use a bank of them in parallel.

Chapter V

Experimental Approach

5.1 Introduction

In the previous Chapter IV computational design analysis yielded an optimised internal design based on capture efficiency. Volume flow rates as close as possible to steel plant operation and throughput were taken. It would be impractical to test the theory directly in molten steel. Water is considered an equivalent modelling medium, having approximately the same kinematic viscosity and therefore a similar physical behaviour. The size of the cyclone made it convenient to use a full scale model.

The proposed experimental rig dimensions set in the previous Chapter IV where computationally modelled using the physical constants for water $\rho = 1000$ kg/m^3 and $\mu = 1 \times 10^{-3}$ Pa·s. The velocity calculated at the inlet of the steel model was patched on to the inlet of the water simulation as an initial boundary condition. The velocity profile at this inlet corresponded to a flow rate of 150 l/min, equivalent to 1 tonne of liquid steel a minute. The predicted velocity profiles of the water model simulation agreed closely with the velocity profiles in the liquid steel modelling exercise, see figures 5.1 and 5.2 comparing the corresponding tangential and axial velocity profiles of the water and steel simulations. To fully validate the use of Fluent's Reynolds stress model of turbulence for the design optimisation study of Chapter IV it was necessary to compare the results of the solid core cyclone water simulation with physical modelling results obtained from the full scale water model. Once the velocity field was validated it would then be possible to investigate the validity of the particle tracking results.

5.2.1 The Physical Modelling Rig

The physical design for the solid core cyclone used in the flow visualisation study was constructed of a castable perspex for the main conical section which reduced the cost of machining and material wastage. The main taper was cast in two parts, a lower and an upper section. Casting made it possible to have a square outer profile at no extra cost which would minimise visual distortion for photographic measurements by providing flat viewing surfaces. Previous flow visualisation studies of tubular flow systems involved placing the whole arrangement in a square box and filling the section with either water or glycerol to minimise lens effects, see for example D1, D2, K2, K5.

Although fundamentally the cyclone curvature acts as a weak concave lens, the refractive index of the castable polymer is so similar to water that any lens effects are likely to be linearised. Distortion was checked by immersing sections of steel tape into the tapered annulus between cyclone wall and core and measuring them by travelling telescope. This was repeated at three locations throughout the section and no distortion was detected. The cylindrical top section was machined from a sandwich of squares of 25 mm thick sheet perspex. The whole arrangement was then bolted together using 10 mm diameter stainless steel studding. The separate sections were located axially by means of male-female turned grooves and key fittings that were friction sealed. The whole arrangement stood in a weir box to make sure that the underflow orifice ran submerged. This mimicked possible operational conditions and reduced the chance of entraining an air core. Figure 5.3 and 5.4 show side and top photographed views of the perspex model used in the visualisation experiment.

5.2.2 Particle injection for flow visualisation

In figure 5.3, a long copper tube with an elbow is shown which introduces the flow into the inlet. The elbow provides a junction to inject the particulate phase into the flow either for visualisation or classification measurements. A 3 mm bore injection tube was attached at the elbow passing through a modified ball valve, the ball valve provided the injector tube with directional orientation.

Particles were injected in two ways:

1. A modified syringe was attached to the injector tube which produced a single bursts of particles. It could not provide a continuous stream of particles.
2. A continuous, adjustable, concentration of particles was achieved by use of a variable speed peristaltic pump drawing off from a well-stirred reservoir of suspended particles as the injector source.

The apparatus was set up so that the cyclone discharge water from the weir box flowed back into a large reservoir 1 m^3 in volume. The reservoir maintained a steady temperature in the system. From it, two single phase Stuart Turner centrifugal pumps set in series with a constant head delivered the water feed to the cyclone entry. The pumping arrangement could quite adequately provide the 150 l/min required, equivalent to 1 tonne/min of molten steel. The flow was measured continuously using a calibrated flow meter. On return to the reservoir, the flow passed through a screen to remove any injected particulate matter. Figure 5.5 shows the schematic arrangement of the operational rig.

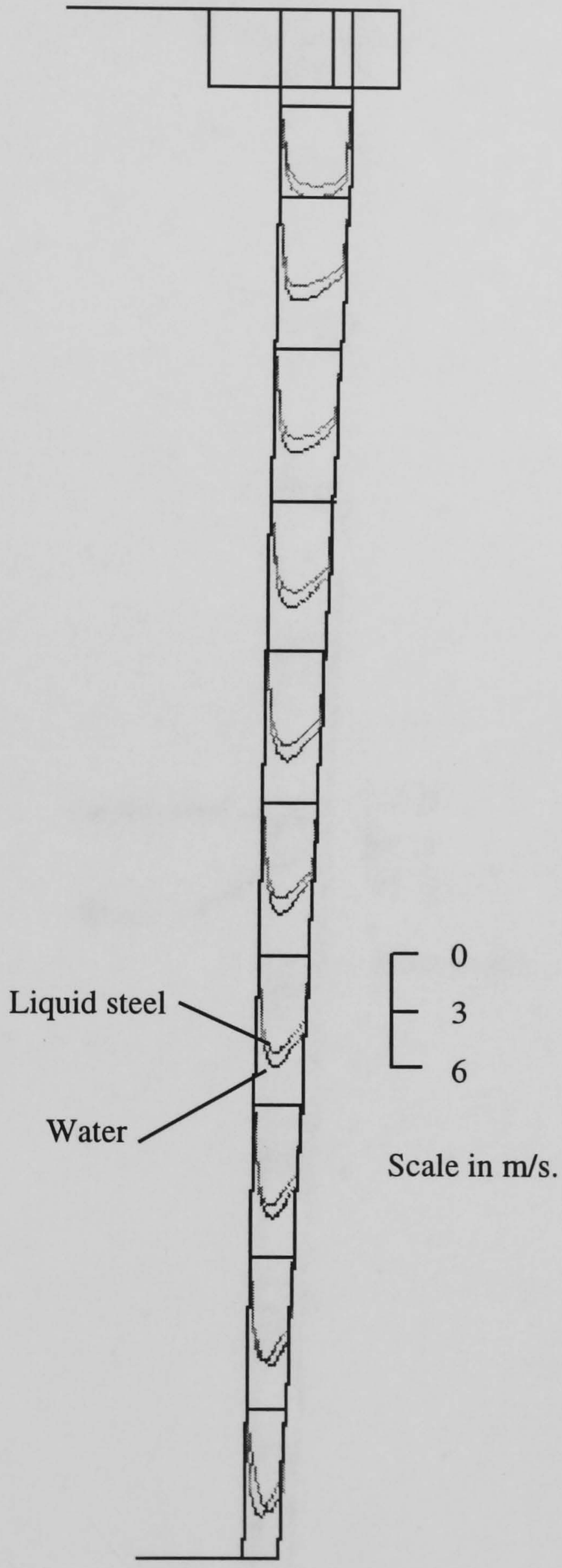

Figure 5.1. Showing the overlaid tangential velocity profiles for water and steel simulations using the same volume flow rate.

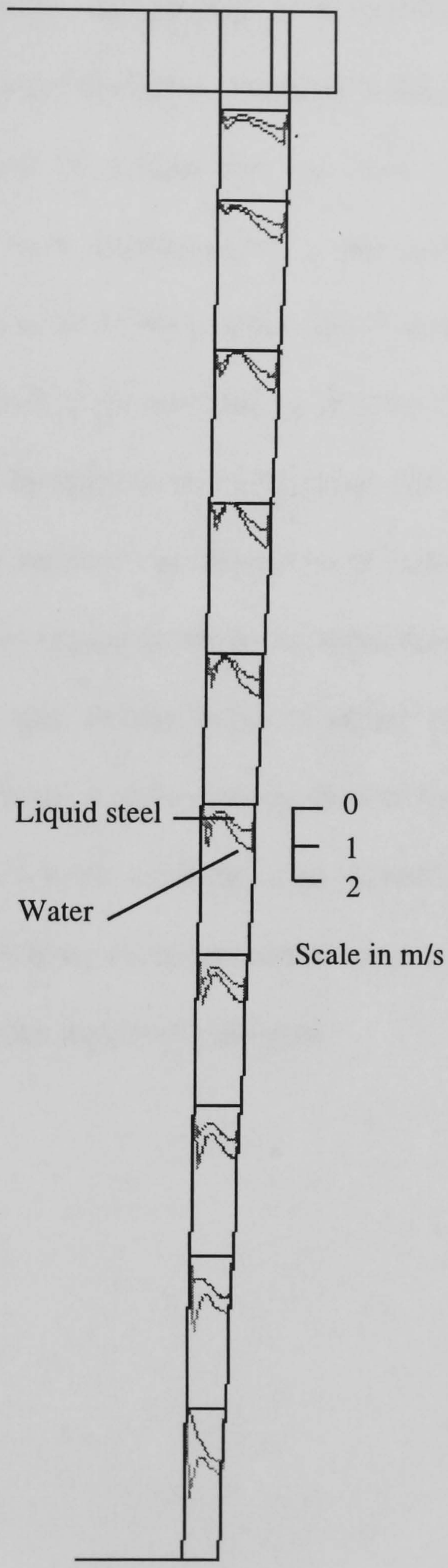

Figure 5.2. Showing the overlaid axial velocity profiles for water and steel simulations using the same volume flow rate.

5.2.3 Flow Visualisation

It was decided to use a non intrusive velocity measurement technique which was best suited to the study of the conical swirling flow of a hydrocyclone.

The technique which was adopted is a modified form of Particle Image Velocimetry (PIV). The general technique, described in detail by Adrian [A1], involved a double-exposure photograph of a flow that has been seeded with neutral buoyant particles. These particles were illuminated by a thin laser sheet and scattered light through an imaging system on to a photographic film. The light source was controlled to allow two exposures or more to be recorded on the film. The time between exposures was presumed known and therefore it was possible to obtain velocities by interpolating the measured displacement between two exposures of same the particle. The advantage over LDA is that it can give measured values instantaneously over the whole section of the flow being viewed. It was decided to use a similar particle imaging technique to measure the velocity field in the swirling annular flow of the solid core cyclone.

In reality, the LDA was not available as an alternative, but in any event it might not have been able to show some of the important features of the flow as clearly as the photographic technique which was finally adopted.

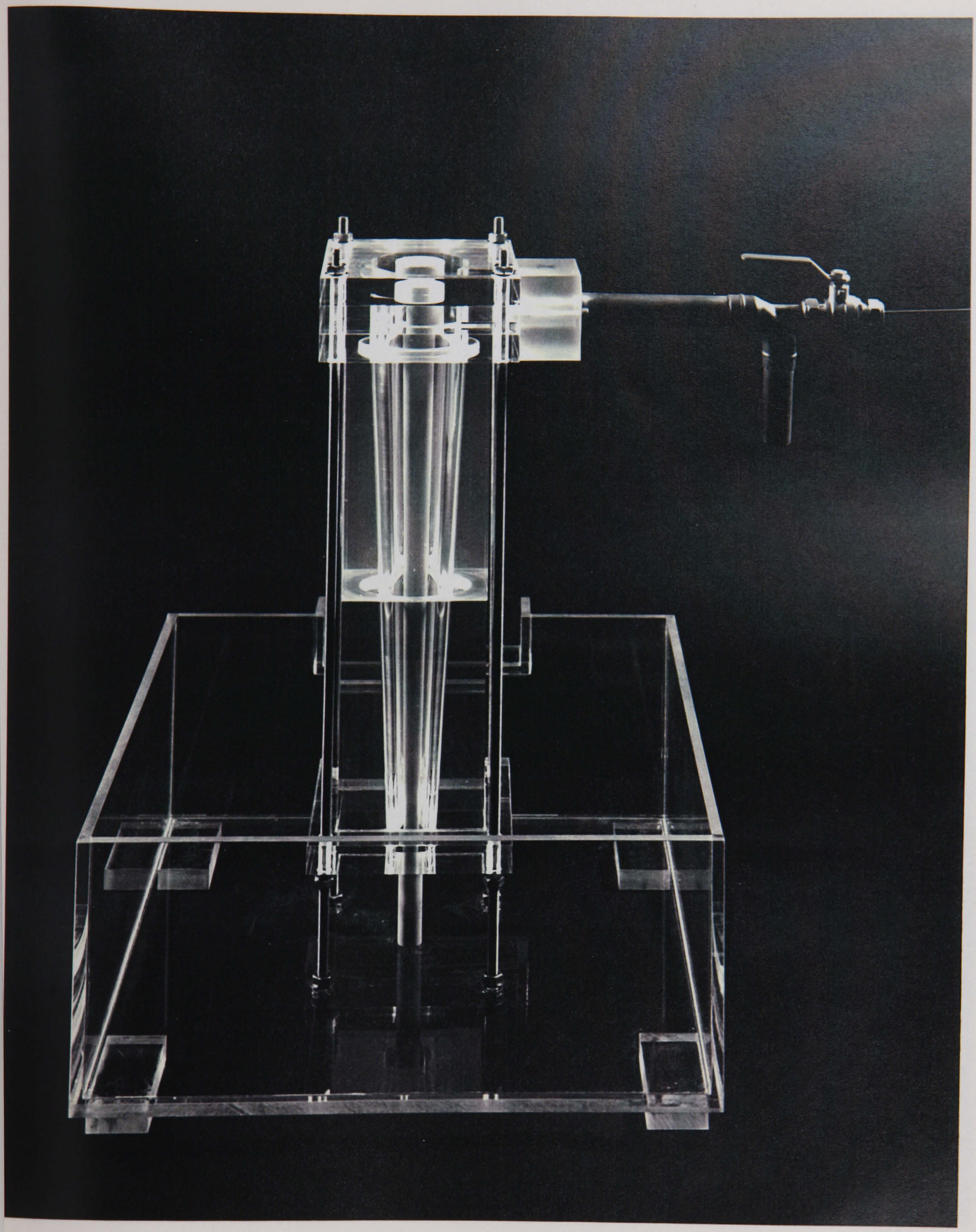

Figure 5.3. Photograph showing the side view of the perspex solid core hydrocyclone water model.

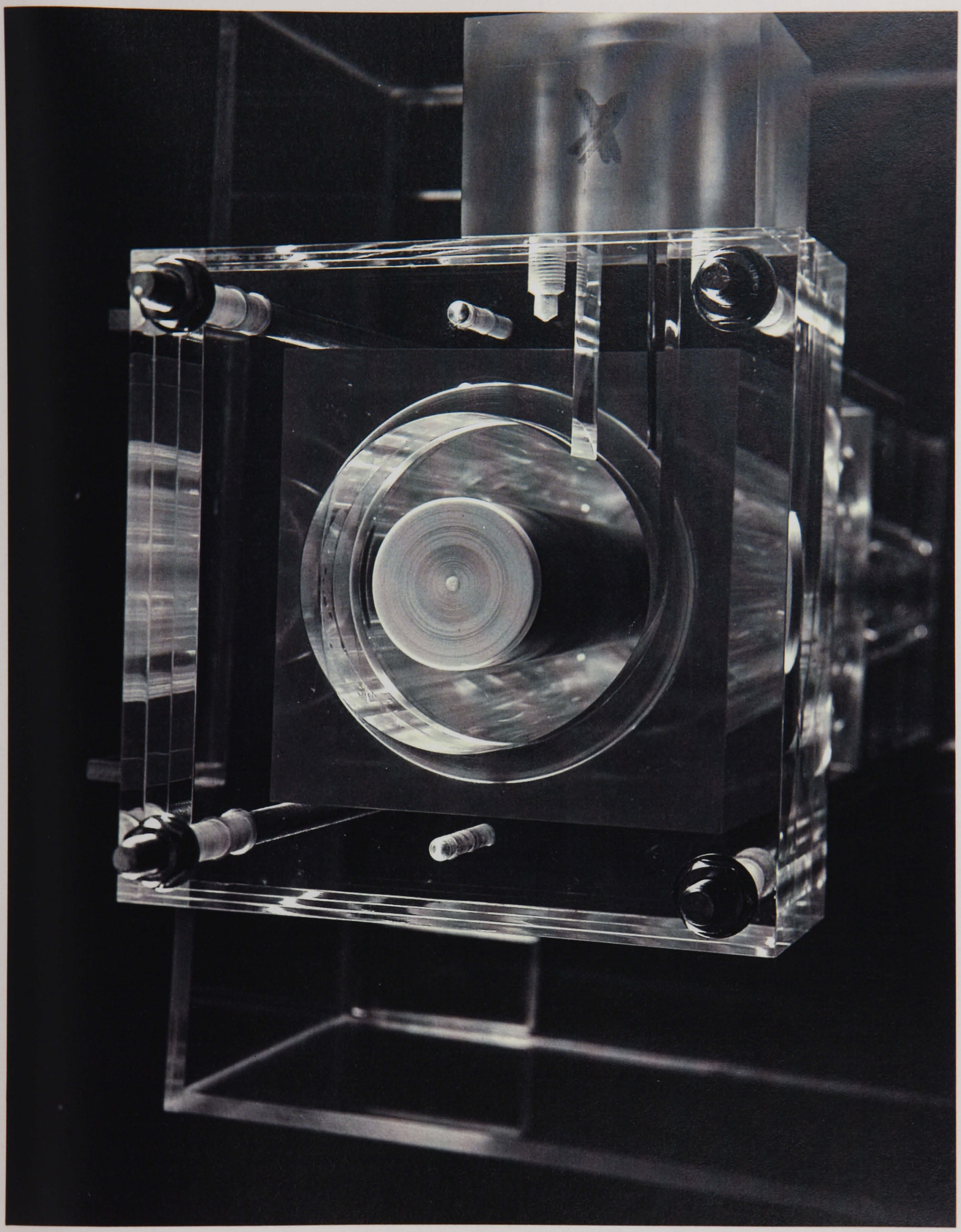

Figure 5.4. Photograph showing the top view of the perspex solid core hydrocyclone water model.

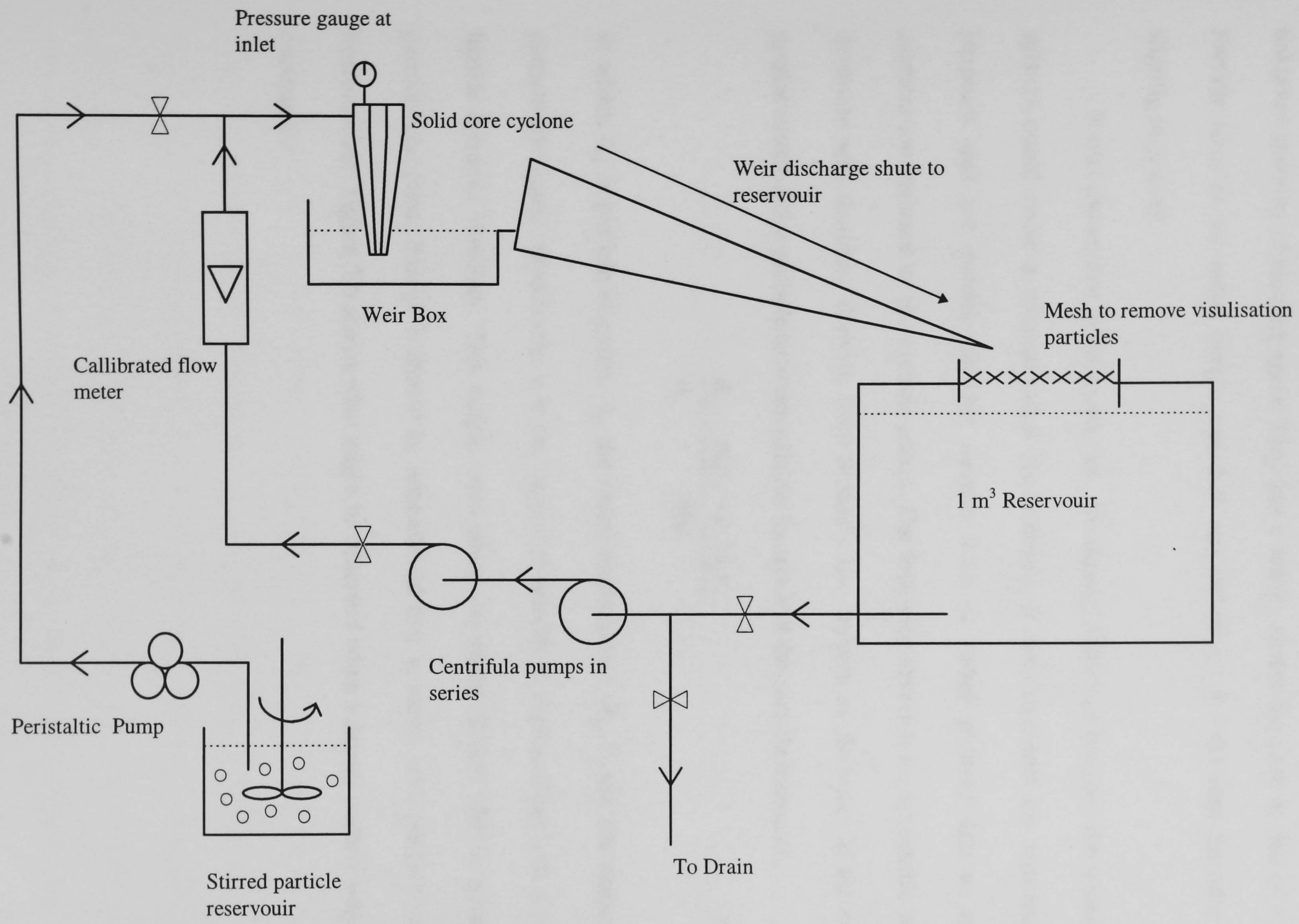

Figure 5.5. Overall diagram of apparatus used in the flow visulisation experiment.

5.2.4 Neutral density particles

Unexpanded polystyrene spheres were used as seed particles for observation. The particles were approximately spherical, made from a mixture of polystyrene and an unknown quantity of blowing agent. They had a density almost the same as that of water. Particle sizes in the initial sample varied in size between 1.4 - 0.7 mm diameter and slightly in density.

It was shown that in the worst case, the density difference between the water and spheres could cause a minimal radial displacement. It was important for visualisation purposes that the particle did not deviate from its radial position due to radial acceleration imposed by the cyclone action. The following criterion for acceptable radial deviation was therefore derived, from Stokes's law, written as the ratio of the radial displacement of the particle between particle images and the particle diameter,

$$\frac{d_D}{d_p} = \frac{\pi(\rho_p - \rho_l)d_p v_t}{36\mu}, \qquad 5.1$$

in which d_p is particle diameter, d_D the radial displacement, ρ_p, ρ_l are the density of particle and liquid respectively, v_t is the tangential velocity at a given point and μ is the liquids dynamic viscosity. This simple ratio gives the radial Stokes slip in terms of particle diameters, though it should be remembered that v_t varies with position in the hydrocyclone. Figure 5.6 shows what might be observed when a denser particle migrates outwards.

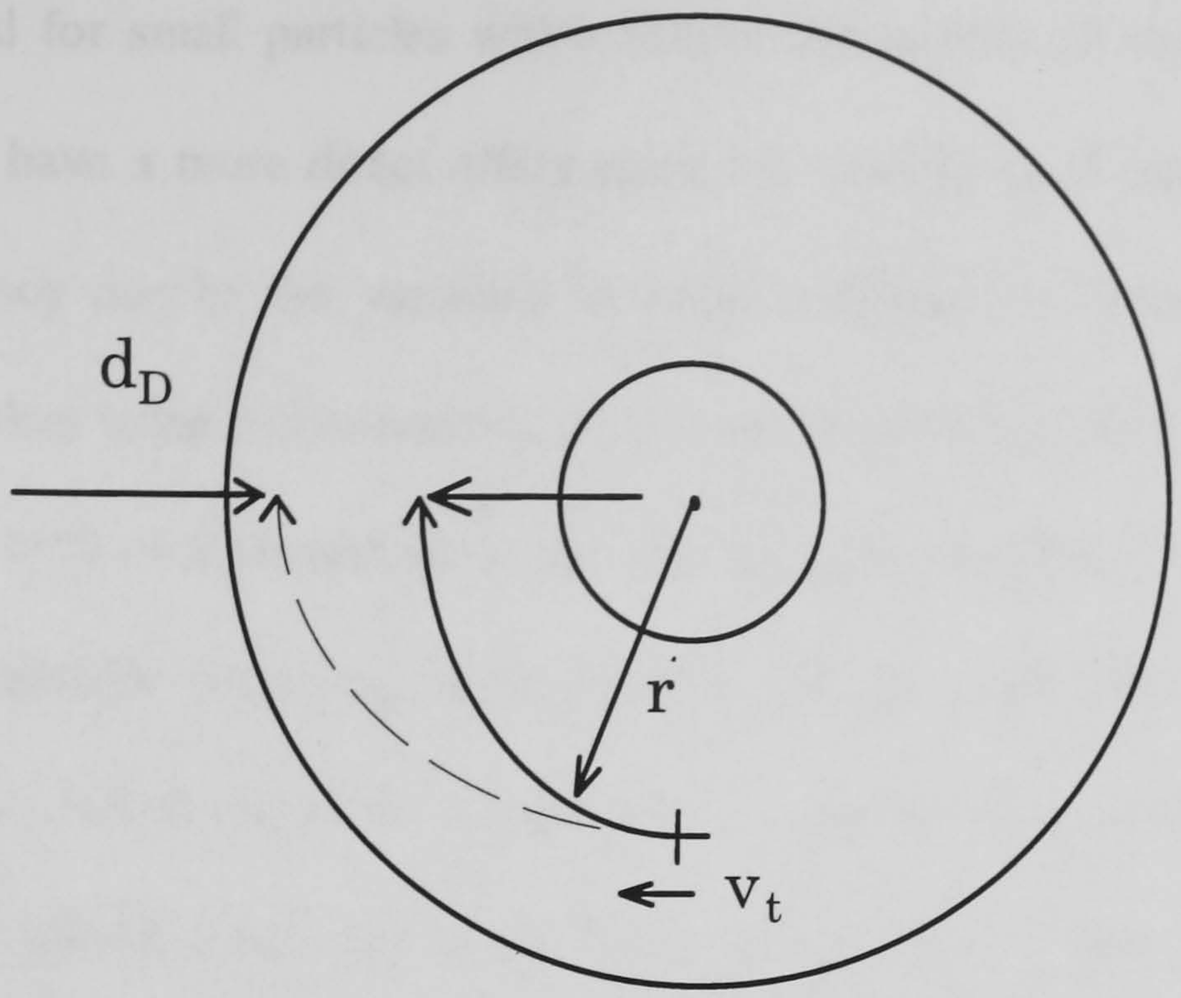

Figure 5.6. Schematic diagram showing plan view of cyclone,

with diverging particle track

An acceptable deviation from the neutral path was set at one particle diameter i.e. $\frac{d_D}{d_p} = 1$ in the fastest tangential velocity approximately 5 m/s. This corresponds to ± 3kg/m^3 density difference which was considered a minimum achievable density tolerance in separation experiments done using a floatation column. It was therefore necessary to recover those particles in the available size range that were of equivalent density to water for use in the visualisation study.

The mean diameter of the visualisation particles was 1mm. This was considered large enough not to be affected by small high frequency eddies, but also to be moved by the larger more energetic ones that have the greatest effect on the flow field as a whole. The individual small eddies have a high frequency and may induce an unsteady random track on very fine suspended particulates. The larger particles will to some extent smooth out the random nature of the flow at this scale, giving a more representative view of the overall flow patterns in the hydrocyclone and reducing the amount of averaging that

would be required for small particles which follow the motion of small eddies. Large scale fluctuations have a more direct effect upon the velocity field and hence upon the separation efficiency due to the variation in radial acceleration. Photographs, figures 5.7.1 and 5.7.2, taken using a conventional SLR camera on 35 mm ASA 400 film with an exposure time of 1/50 of a second show the visualisation particles in the annular flow. These pictures emphasise the speed of the particles and the three dimensional nature of the spiralling flow, which must be considered if consecutive particle images of the particles for PIV measurements are to be taken. The particle streak lines also clearly show the changing helix angle at different radial positions, this is discussed in the previous Chapter IV.

5.2.5 Velocity measurement in a spiralling flow

PIV techniques are mainly 2 dimensional and still not fully developed. In the case of swirling flows in the cyclone a 2 dimensional light sheet would not be suitable. 3 dimensional PIV involves using 2 or more views and has been carried out on a very simple flow system using a number of synchronised video cameras to capture different angles of the flow field [N2]. Two views of the same interrogation region are required; these should ideally be at right angles to each other to simplify data analysis. To obtain an exact particle location in space one view will shows the particle moving horizontally and vertically the other shows its radial and vertical position; this would provide confirmation of the particles identity in each view. Figure 5.8 shows a schematic representation of consecutive particle images following a helix track, that a visualisation particle would make if viewed from two perpendicular sides.

Figure 5.7.1

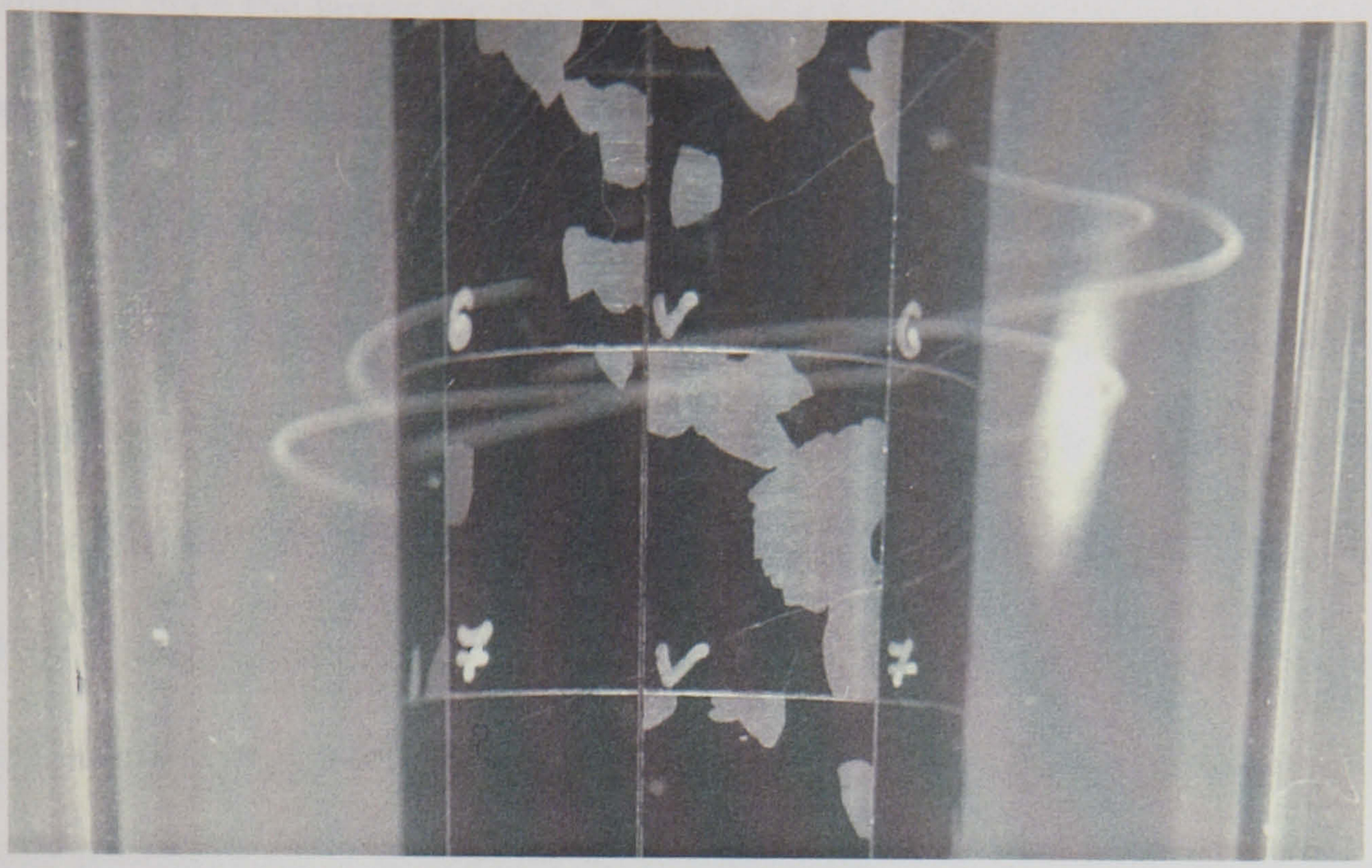

Figure 5.7.2.

Figure 5.7.1 and 5.7.2. Taken using a conventional SLR camera on 35 mm ASA 400 film with an exposure time of 1/50 of a second show streak photographs of the visualisation particles in the annular flow.

The size of the visualisation particles is important when considering the imaging technique since the larger the particle, the greater the viewing area. It seemed sensible to analyse a field of view which incorporated the full annular thickness between the core and the wall to give a better reference position and allow a reasonable mapping volume.

In the present study, two standard synchronised video cameras were used initially. The framing rate turned out to be too slow at 25 frames per second, since particle moved beyond the field of view in consecutive frames. The maximum shutter speeds available were 1/1000 sec and the particles produced a long streak in this time which could be measured to obtain an approximate velocity value. Although, as with any streak photography, it is difficult to determine the start and the finish of the streak and this approach was not therefore considered accurate enough. High speed video is available which would be capable of capturing several images of the same particle in consecutive frames but was not considered due to its high cost.

The use of a high speed cine camera was considered possible; this was the method employed by Knowles et al [K5]. This work focused two views at right angles to each other by prisms and mirrors on the same negative. The viewed region being interrogated was 2-3 mm^3 and therefore required a fast framing rate of 20000 quarter frames per second to capture a satisfactory image. When running at this speed a large particle population is required to ensure that each frame has at least one particle present. This consequently led to problems of identification due to having too many particles present. The seed particle size used was between 50-300 μm and the paper records difficulty in identifying identical particles and defining the radial location between the two views.

Viewing larger particles in a larger region would permit a slower time interval and therefore require fewer particles. Having few particles, the probability of images

overlapping in the same interrogation spot is reduced, though with a sparser particle distribution, the particles and hence the velocity measurements become randomly located in space and on the film images. It was decided to capture multiple particle images on the same photographic negative, using a stroboscopic technique to capture light reflected from the particles on to the film. Two perpendicular side views of the region described previously, would be directed on to the same negative using the mirror arrangement shown in figure 5.9. This led to the development of the high speed strobe camera, its design and operation were the result of a succession of trials, which is described below.

5.2.6 Strobe camera and photographic technique

A simple cardboard slotted disc spun by a stable adjustable speed electric motor produced the strobe effect. Figures 5.10.1 and 5.10.2. show two views of the strobe camera that was built. The spinning disc was placed in front of the camera lens producing a succession of exposures of the particle image on the negative as the slots passed the field of view. By incorporating the strobe disc into the camera itself meant that the rig could be illuminated with any amount of light and of any type. This is a much more versatile and simple method than trying to synchronise a number of strobed light sources. The camera was fitted with an iris leaf shutter. Conventional shutters on modern cameras slide a narrow slot across the film, exposing each section of the negative for the allotted length of time. In this case, a fluctuating light source would produce a striped effect on the negative. An Iris shutter opens and closes centrally thereby avoiding this effect because each part of the film is exposed for the same length of time at the same instant.

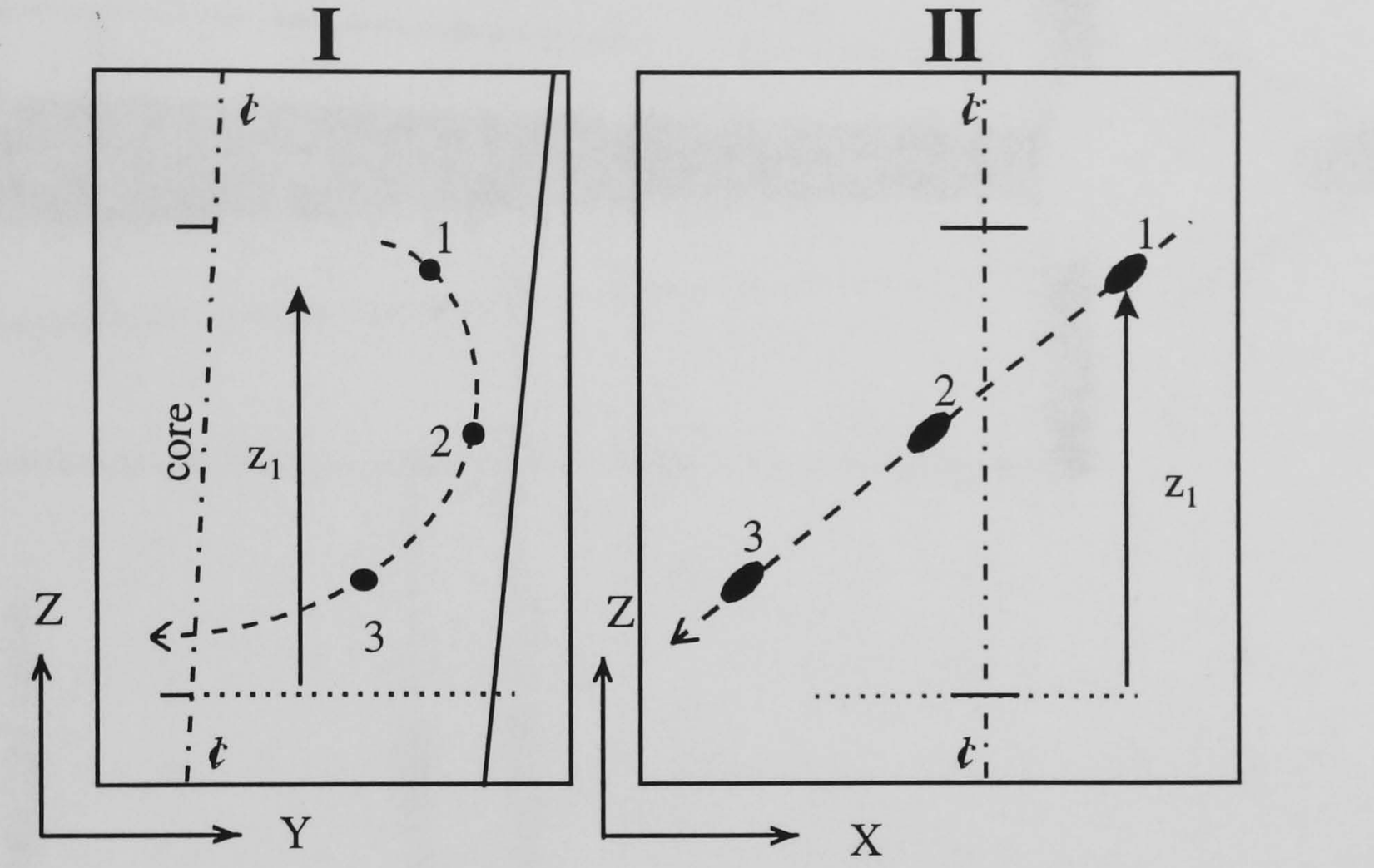

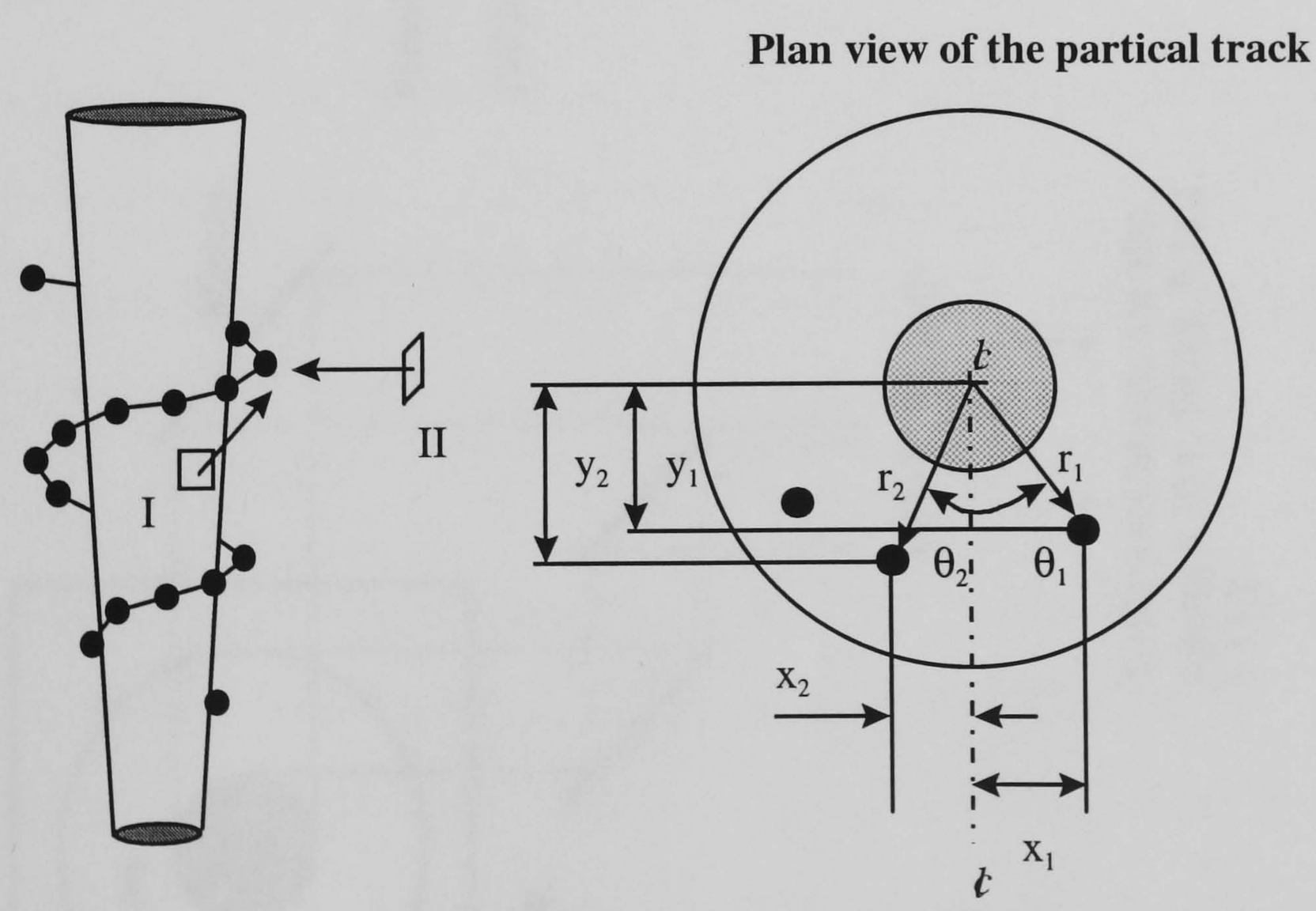

Figure 5.8. A schematic representation of consecutive particle images following a helix track, that a visualisation particle would make if viewed from two perpendicular sides.

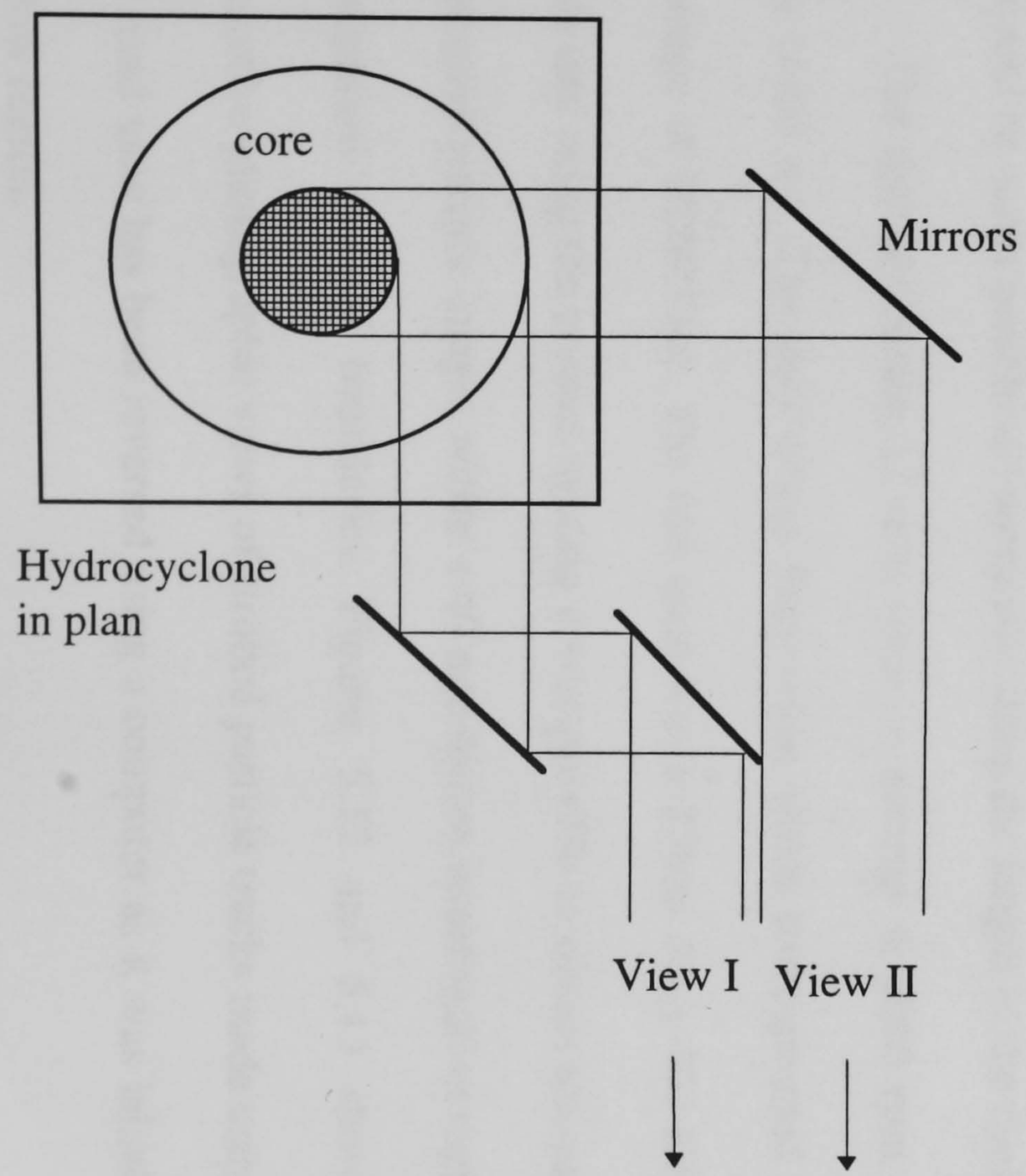

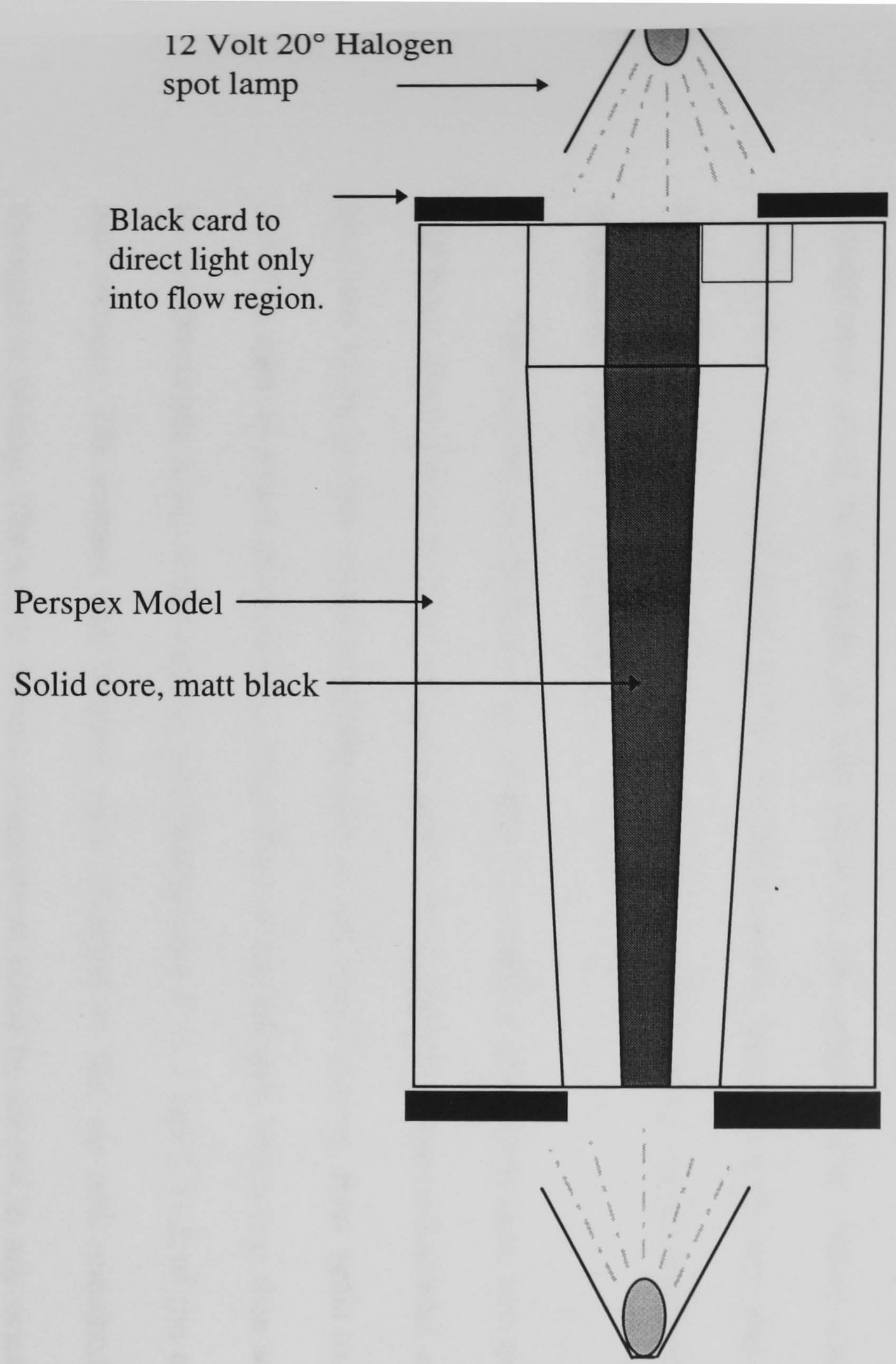

Figure 5.9. Mirror set up to obtain the two perpendicular views and the lighting arrangement used to impose a dark field lighting technique for the particle photography.

An iris shutter and lens obtained from an old plate camera were attached to a standard single lens reflex (SLR) camera body using a modified set of adjustable bellows. The SLR body merely held the film and enabled focusing. The bellows arrangement was identical to the set up used in macro photography, which meant that the whole arrangement could be brought in very close to the subject. The slotted disk was contained in a fixed matt black 12" dia film reel canister. into which the lens was sealed to exclude extraneous light. Focusing was achieved by moving the camera body and bellows on a carefully aligned track.

The camera arrangement was mounted on a ridged aluminium base. two and one half front silvered mirrors were used in a similar arrangement to that of Knowles *et al* to give two views at right angles simultaneously on the same negative, refer again to figure 5.9. The mirrors where mounted on a thick sheet of flat perspex which was then secured to the aluminium base of the camera, see photographs 5.11.1 and 5.11.2 of the camera and mirrors. The camera and mirrors were clamped to the rig and remained rigid throughout filming. The whole camera arrangement could be moved in any orientation and could be easily positioned vertically along the length of the cyclone

The disc containing 12 slots spun on average at 2000 rpm, producing an image every 1/400 sec. The slots where 5mm wide, which corresponded to an exposure time per image of 1/2000 sec. The film used was a 35mm ASA 400 Kodak Tmax. At these speeds and using the correct lighting it was possible to obtain adequate pictures showing consecutive particle images within a 40 mm square interrogation region in two views that encompassed marked boundaries. Figures 5.12 and 5.13 show two examples of consecutive photographic views of strobed particle tracks made using the technique. The right hand view has been reversed using a computer as it was initially a mirror image of the flow region.

A small photographic aperture was required to obtain a good depth of field and this reduced further the amount of available light falling on the negative beyond the reduction due to the strobe effect. Light intensity decreases with an increase in strobe frequency and care was therefore needed to obtain a satisfactory lighting arrangement. Knowles used shadow lighting, illuminating the particles from behind, but this method was of no use in the present work because of the shadow from the core. Kelsall preferred a dark field lighting method in which only the flow region was lit and this is the method that was eventually used here, see figure 5.9. The background is hardly illuminated and reflected light from the particles is therefore against a dark field. This method prevents stray light from the surrounding background fogging the earlier particle images in the sequence, while the overall exposure time is sufficient to make the background clearly visible. The light intensity of the particles was increased by colouring them with a yellow fluorescent paint. A concentrated light source was provided by 6 low voltage narrow angle halogen spot lights. These were small and gave off little heat so could be positioned easily and close to the rig, illuminating it from the top and bottom. In addition, the core was painted matt black to reduce the reflection of light and hence fogging of the particle images.

5.2.7 Scaling

Reference marks were scribed on to the core about its circumference at 20 mm intervals and along its length at 45° intervals. The camera was secured in place so that the two perpendicular views of the water filled region were visible and of identical size. The top of the hydrocyclone was then removed and into the flooded annular gap was placed a dart shaped 1mm square mesh. This filled both views between the core and outer walls and was used to align the mirrors, to focus and calibrate the picture and to check for distortion due to spurious lens effects. The focal length had to be the same for both views to ensure that both images were of the same scale. The top was then replaced, the strobe disc speed measured using a calibrated tachometer. The particle stream turned on and the photographs taken.

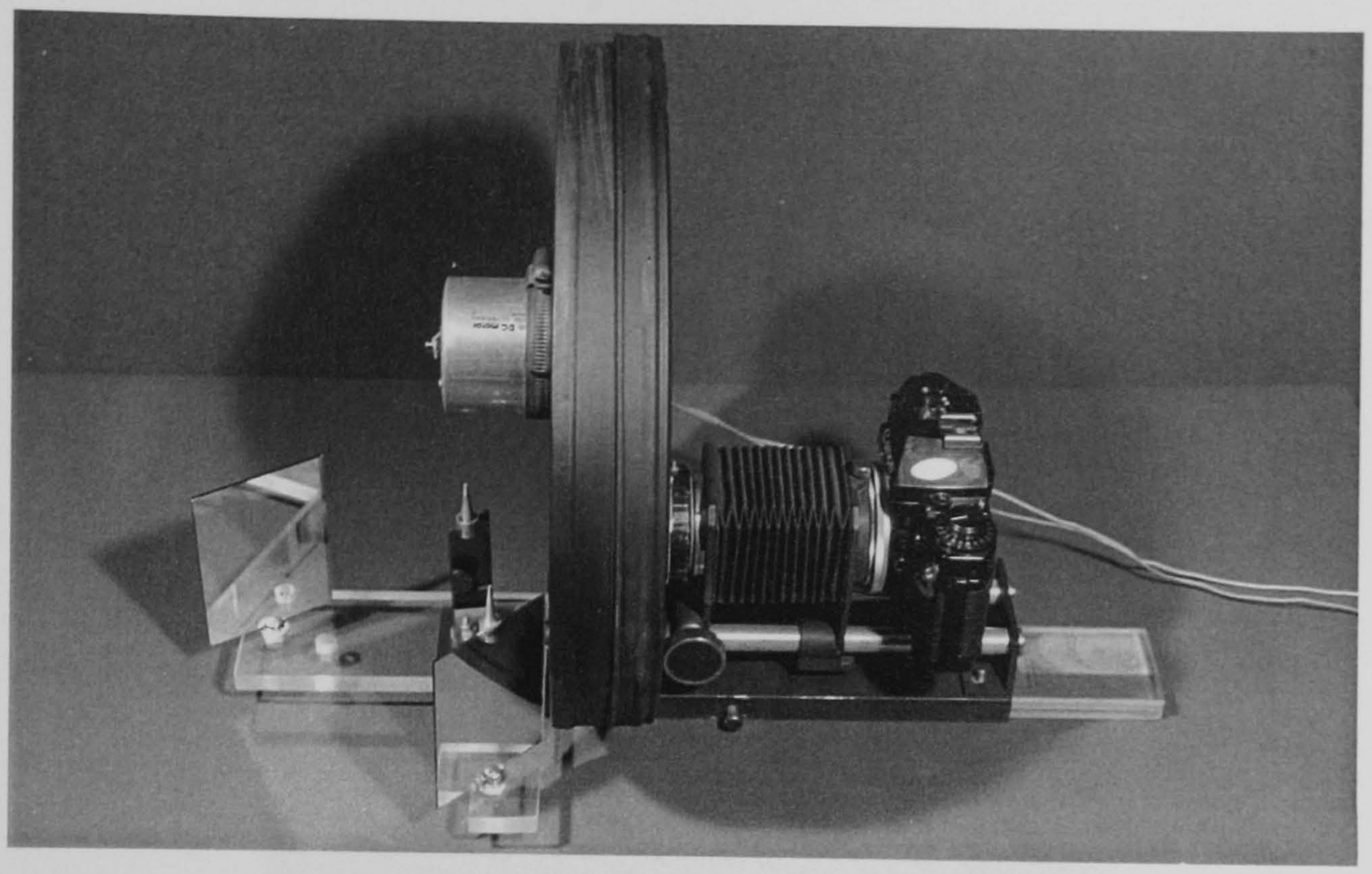

Figure 5.10.1.

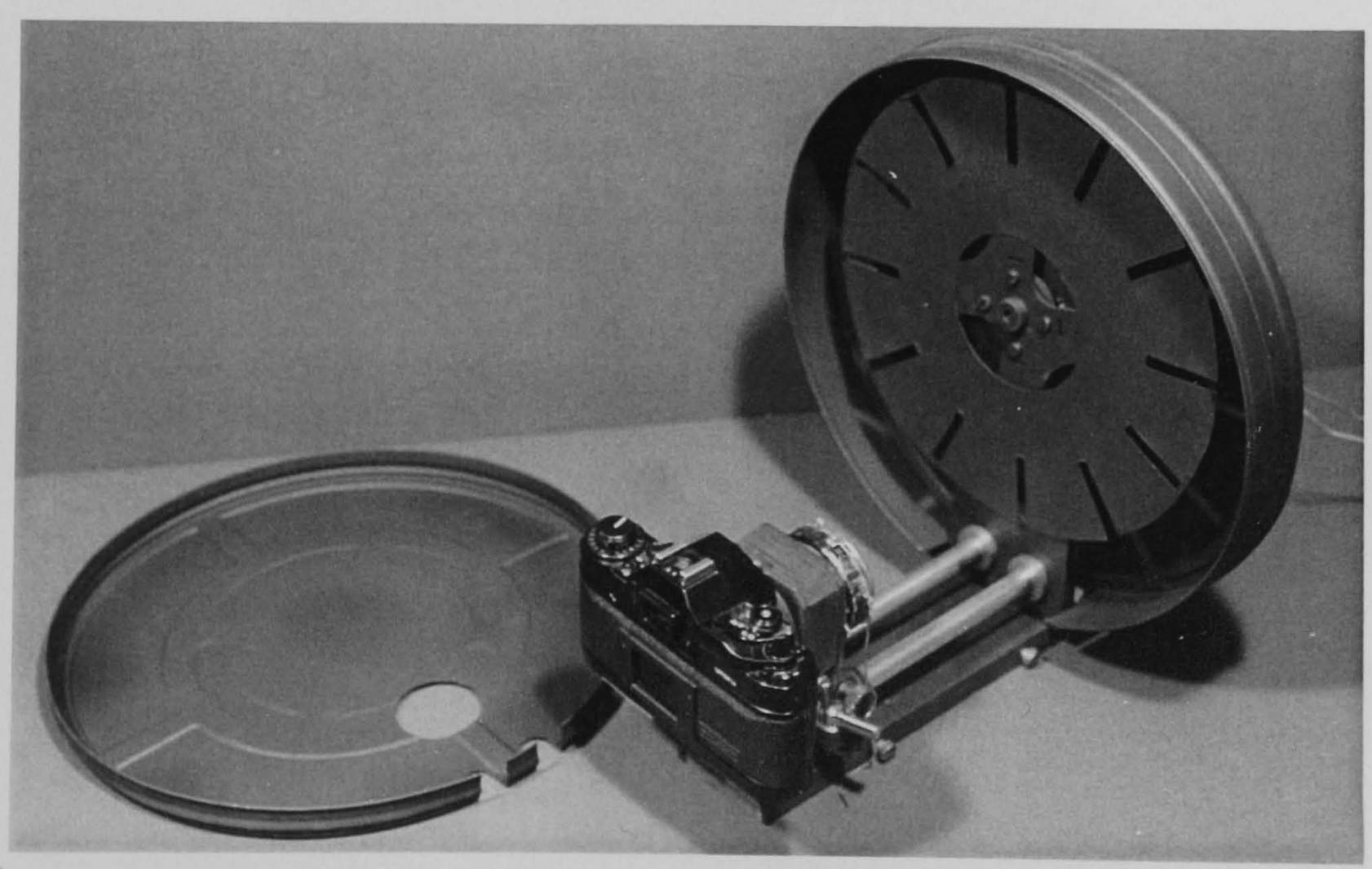

Figure 5.10.2.

Two photographic views of the strobe camera.

Figure 5.11.1.

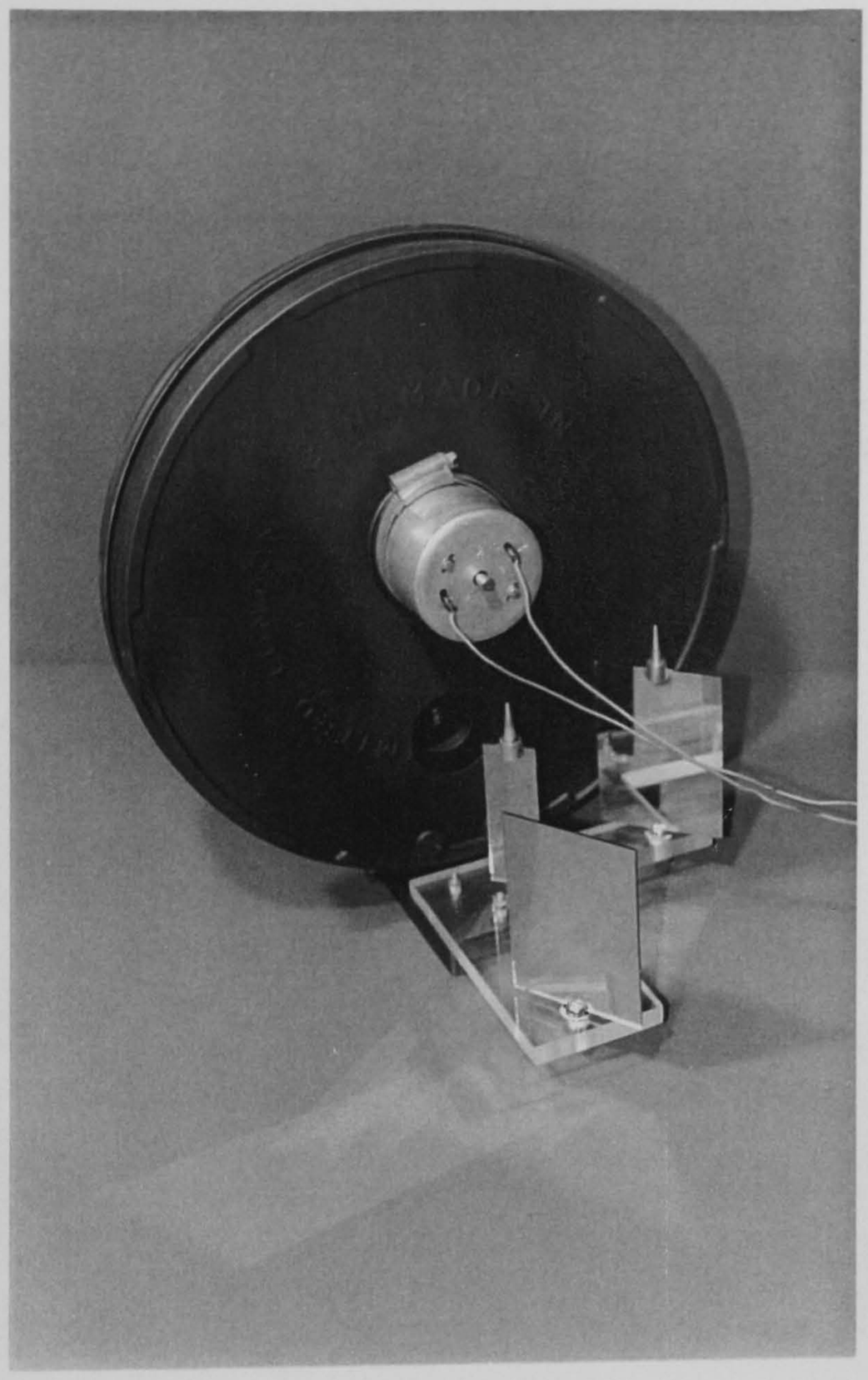

Figure 5.11.2.

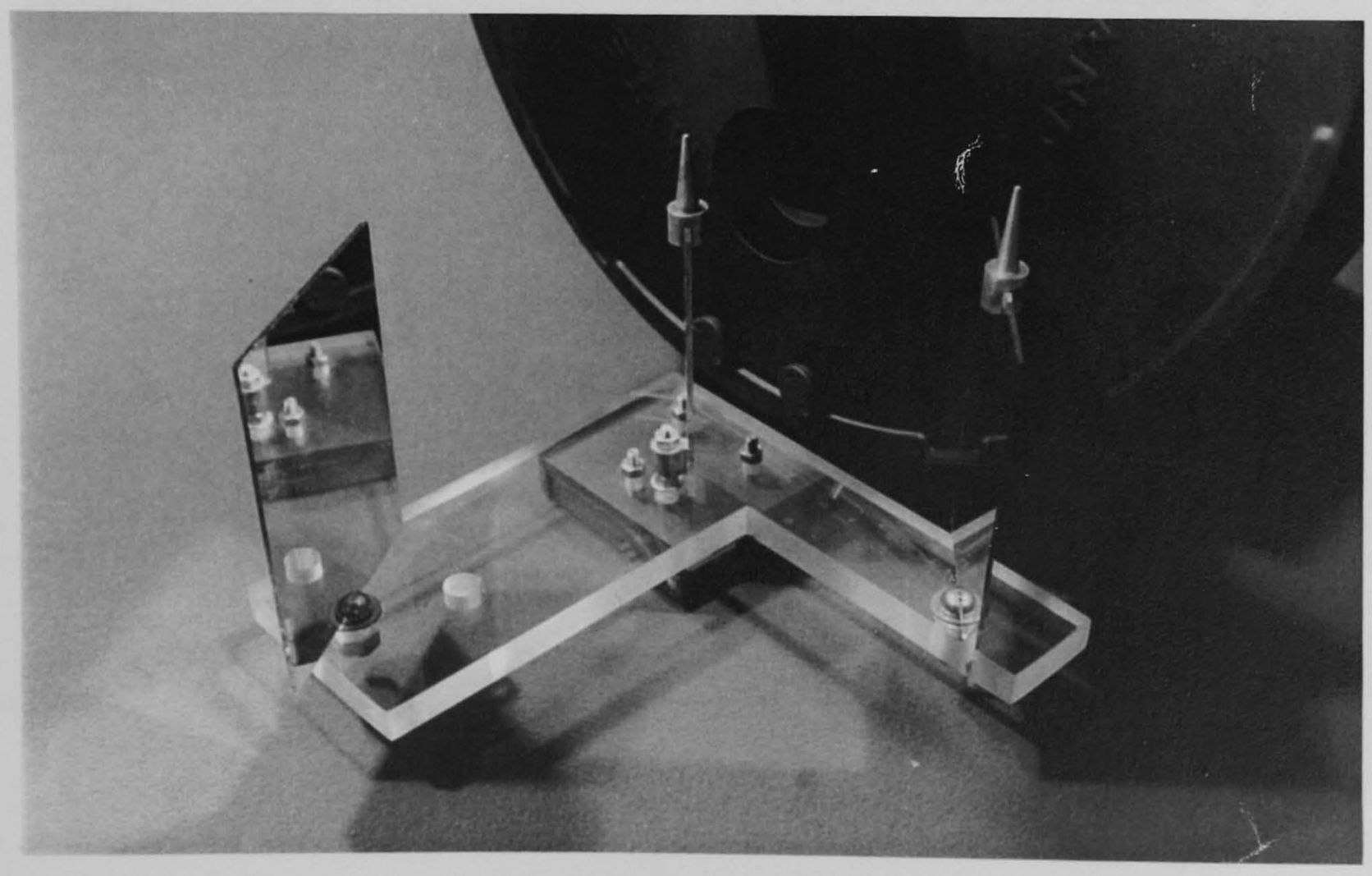

Two photographic views showing the mirror arrangement mounted on the strobe camera base.

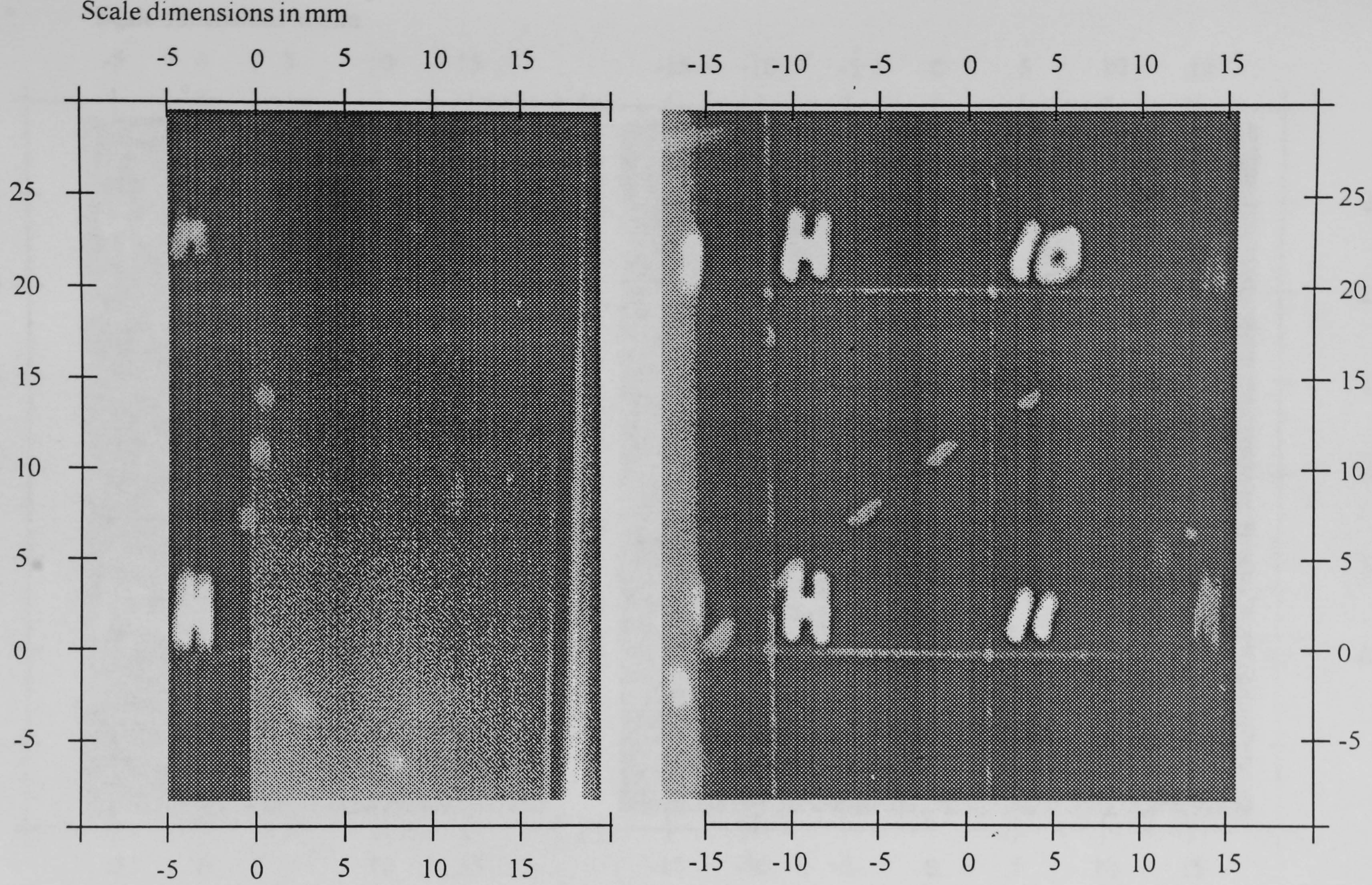

Figure 5.12. Photographic image of a strobed particle track showing two perpendicular views of the flow region. The consecutive images are 1/400 second apart with an exposure time for each image of 1/2000 second.

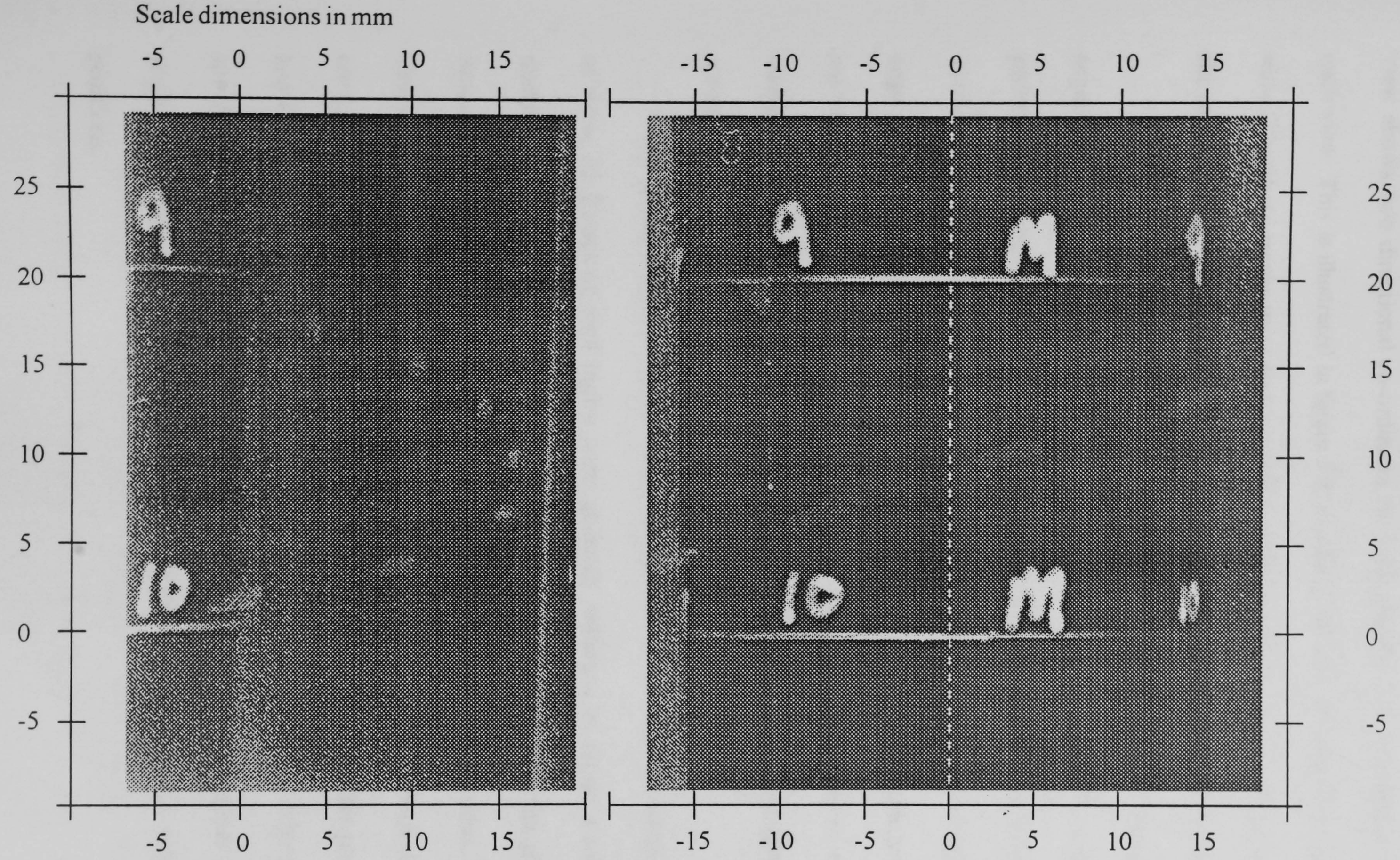

Figure 5.13. Photographic image of a strobed particle track showing two perpendicular views of the flow region. The consecutive images are 1/400 second apart with an exposure time for each image of 1/2000 second.

5.2.8 Interpretation of Strobe Pictures

The particle track was captured in two views perpendicular to one another. Each view shows two directional co-ordinates for each particle, one of which is the same in each view. This is illustrated in figure 5.8, in which the z-component is the same in each view. The photographs were developed at a consistent magnification of approximately 4x the actual scale of the region of view to minimise the inaccuracy of measurements.

The mirror arrangement in figure 5.9 directed two side views of the interrogation region onto the negative, producing photographs like those shown in the example strobe photographs figures 5.12 and 5.13. Measurements were taken about the most prominent circumferental mark and the vertical and horizontal positions corresponding to the core edge as shown schematically in view I, figure 5.8. The position in the horizontal plane of the vertical reference axis in view II is calculated from the diameter of the core at each circumferental mark and by scaling its position with respect to the photographic print and a core edge.

It was impossible to dictate where the particle track would be within the region of view. 35 frames of each region were generally sufficient to obtain a reliable radial distribution of velocity measurements. The measurements taken from flat photographic images essentially gave the particle image location in Cartesian co-ordinates. These were then converted to a more appropriate cylindrical co-ordinate system which describes the curved particles track rather better. The particle tracks are shown as flat plan views, as laid out in figure 5.8. Figures 5.12 and 5.13 show two examples of different types of spiralling particle tracks captured using the technique. Note the difference in the helix angle of the tracks and the consecutive image displacements at the two different radial positions.

The axial velocity component is calculated simply from:

$$v_z = \frac{(z_1 - z_2)}{\Delta t}, \qquad 5.1$$

where Δt is the time interval given by the speed of revolution of the slotted disc. The radial particle position about the reference is calculated as

$$r_p = \sqrt{x_p^2 + \dot{y}_p^2} \qquad 5.2$$

and

$$\theta_p = \tan^{-1} \frac{x_p}{y_{p1}}. \qquad 5.3$$

The radial velocity v_r is therefore

$$v_r = \frac{r_1 - r_2}{\Delta t} \qquad 5.4$$

The angular velocity ω is

$$\omega = \frac{(\theta_1 - \theta_2)}{\Delta t} \qquad 5.5$$

and hence the tangential velocity component v_t is

$$v_t = \omega r \qquad 5.6$$

The corresponding locations of these velocities was taken to be the mid point on the track between the two images.

5.2.9 Velocity data analysis

By enlarging the photographs, the errors associated with measurement were minimised and the particle image locations were determined with acceptable accuracy. It was possible to predict the central location of an image to within ± 0.125 mm. Calculated angular and radial positions were of a similar accuracy. Error bars have been calculated

for the velocity components taking into account the measurement accuracy from the photographs and the accuracy of the tachometer used to measure the strobe speed. The error bands did not vary with position or the measured velocity value and are displayed in figures 5.16 and 5.17.

Although the radial location of the centre of a particle image could be predicted accurately the displacement of the particle centre between images was too small to be distinguished from the possible radial displacement resulting from the radial acceleration imposed by the hydrocyclone swirl action. The hydrocyclone dimensions are optimised to produce radial accelerations $(\frac{v_t^2}{r}) > 60\times$gravity. An example of the calculated velocity data, which includes the radial displacements between images, is shown in Appendix III . If this radial discrepancy is due to a slight density difference between the particle and fluid, or turbulent eddy fluctuations, it is small enough to be negligible when compared to the axial and tangential velocity components. This observation further proves that the flow is in fact free vortex rotation.

185 different velocity measurements were analysed over a 260 mm length of the conical section of the hydrocyclone. The particle images and hence the velocity measurements were randomly located within a 3-dimensional segment of the hydrocyclone. Axisymetric flow is assumed, and for ease of data analysis the angular co-ordinate was dispensed with. This leaves all the velocity data distributed in one 2-dimensional vertical plane.

By comparing measured velocity profiles against those predicted for the water model by using Fluent, the numerical model's ability to describe the flow patterns that occur in the real flow system could be determined, and subsequently validated for use in the optimisation study. Since the data obtained by PIV rarely lay on a constant axial

plane, even 5mm axial spaced bands of velocity data were taken from those distributed throughout the plane and the values at these points plotted as the velocity. The profiles are generated by scaling the velocity value and adding it to its axial co-ordinate value taken from the cyclone apex this produces a sequence of velocity profiles throughout a cross-section of the solid core cyclone. Figure 5.14 and 5.15 show a range of tangential and axial velocity profiles plotted throughout the annular gap along an axial length of the tapering section of the solid core hydrocyclone. For comparison, the upper and lower velocity profiles either side of the 5mm band predicted by the numerical model are overlayed on to these profiles, a close up example of a tangential and axial velocity profile comparison are shown respectively in figures 5.16 and 5.17. Fluent uses a body fitted skew grid and, as a consequence, Fluent data files give only the flow variables at the cell centres. A small data post processing program was developed to enabled the user to choose any location (or set) in the flow region and then determine corresponding flow variable values by 2-dimensional linear interpolation between surrounding cell centres at that location. The code and a description are given in Appendix IV.

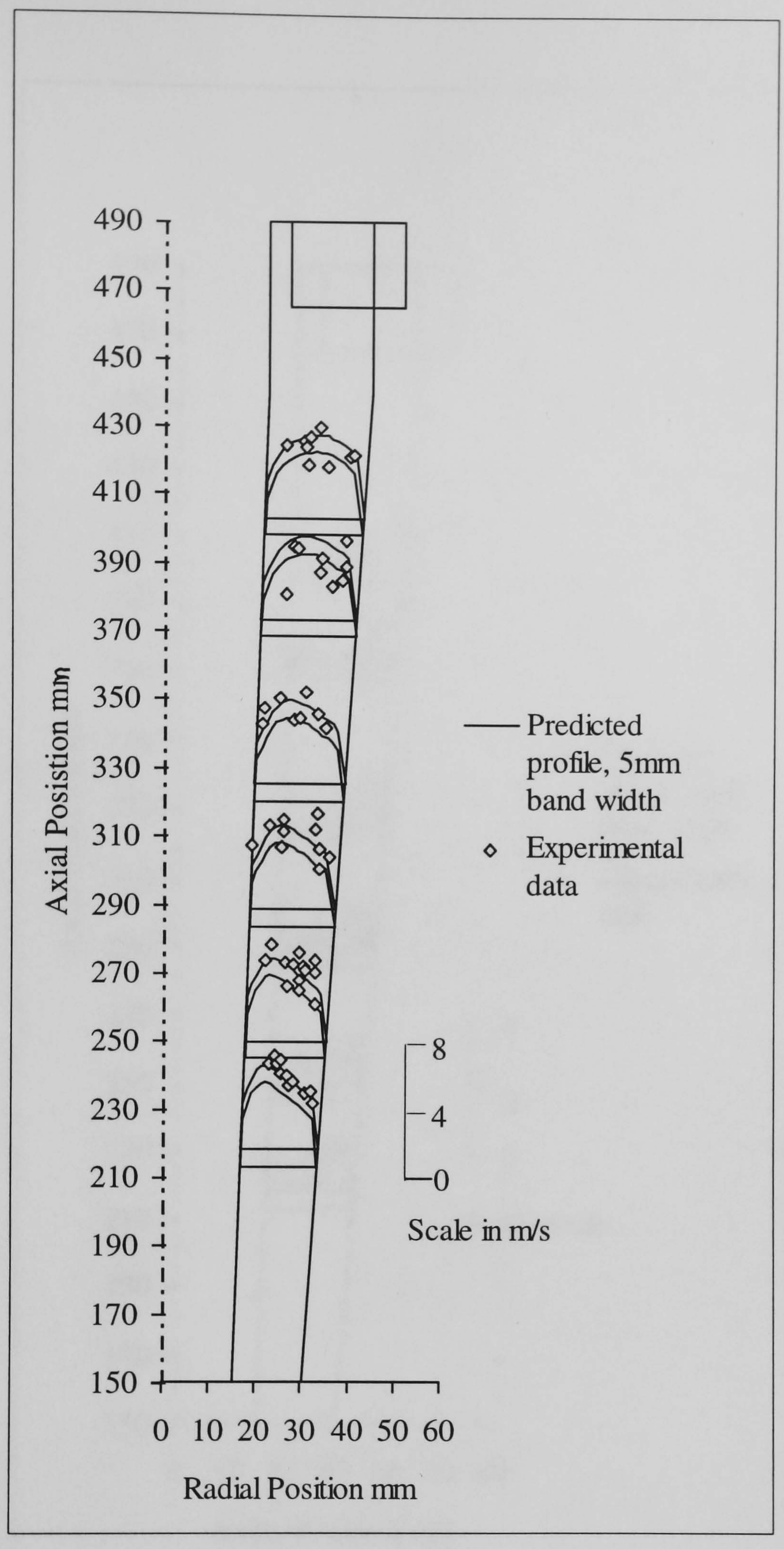

Figure 5.14. Shows range of tangential velocity profiles plotted throughout the annular gap along an axial length of the tapering section of the solid core hydrocyclone. The profiles compare experimental data points with those predicted numerically

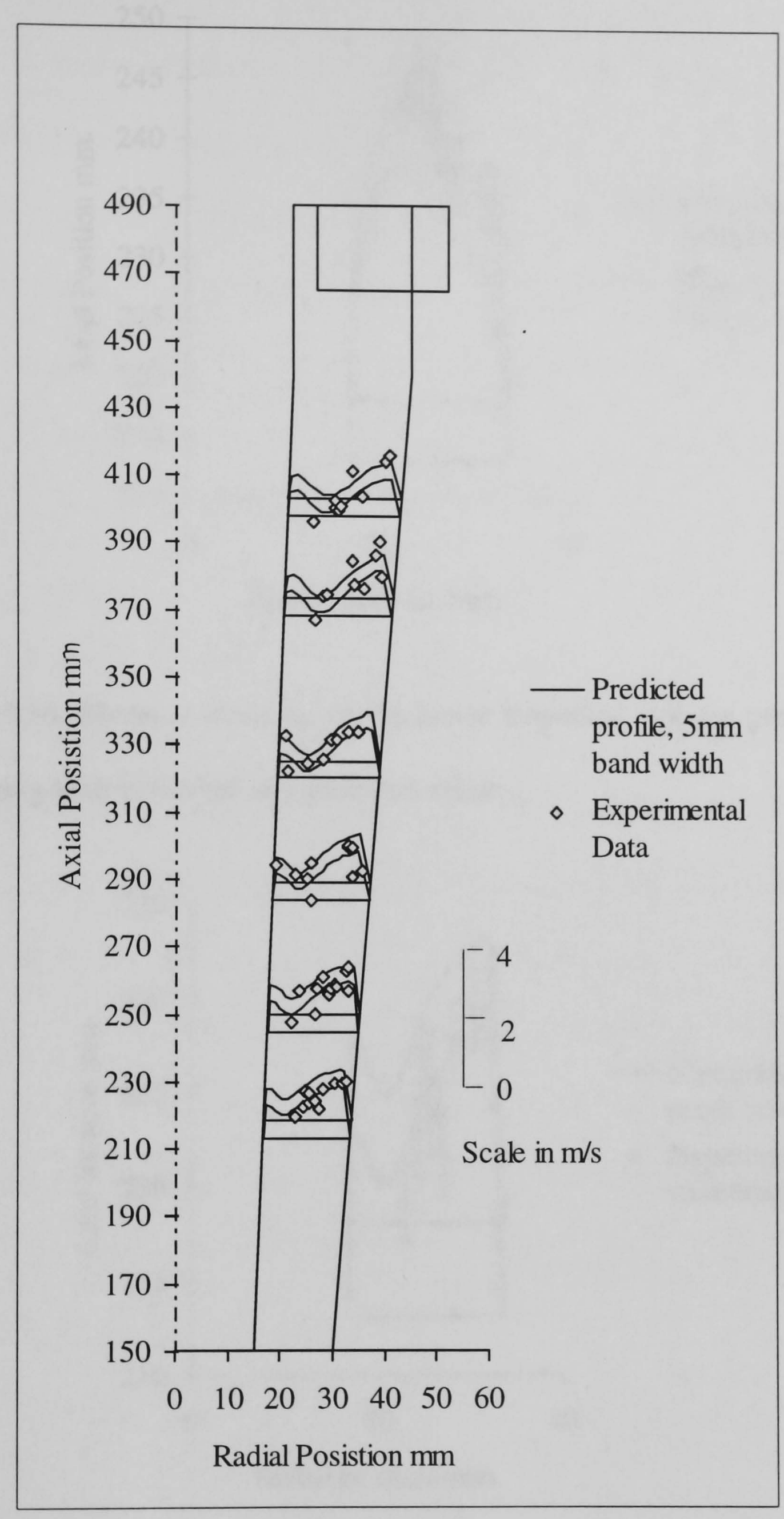

Figure 5.15. Shows range of axial velocity profiles plotted throughout the annular gap along an axial length of the tapering section of the solid core hydrocyclone. The profiles compare experimental data points with those predicted by Fluent.

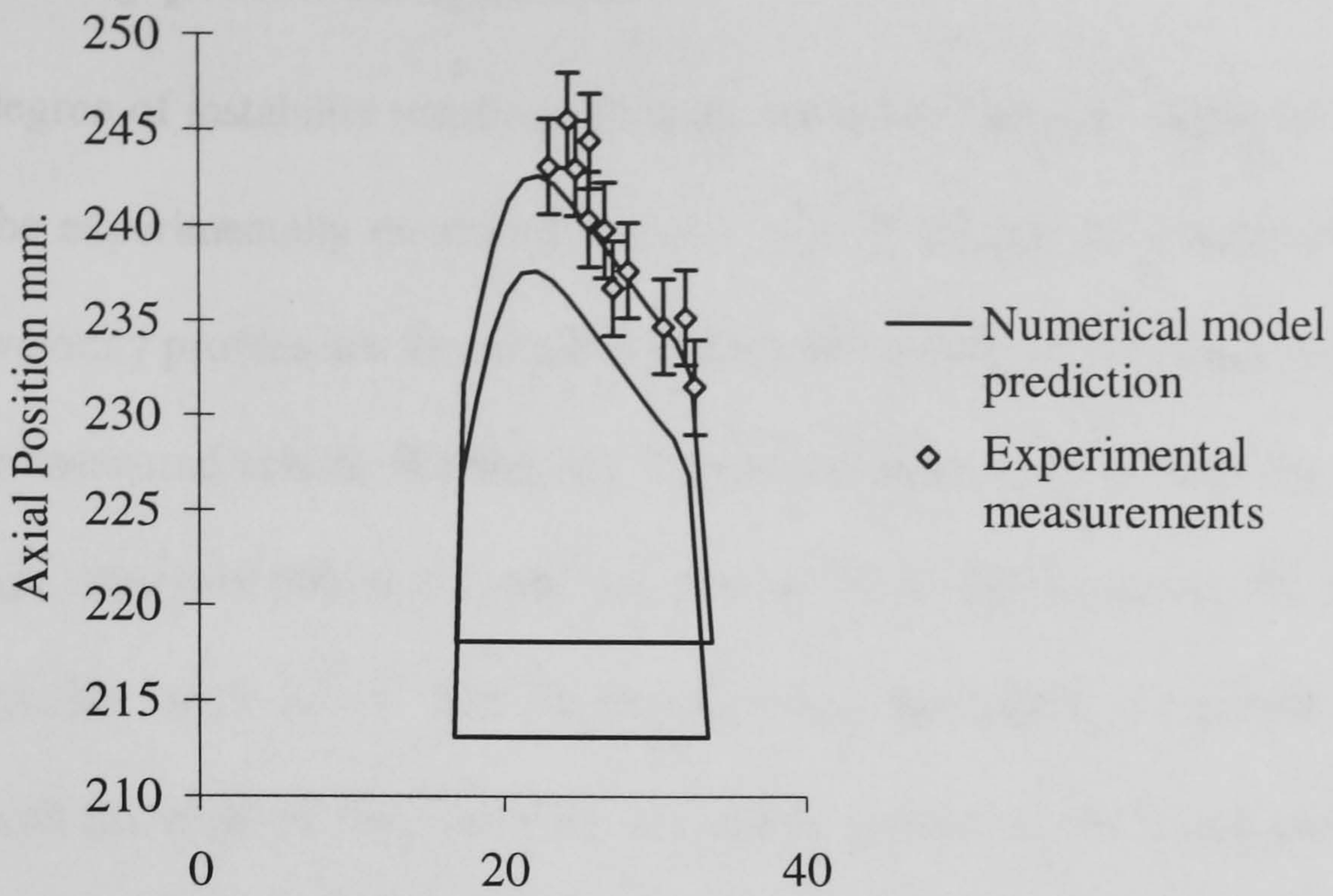

Figure 5.16. Shows a close up of the lower tangential velocity profile in figure 5.14, comparing both measured and predicted values.

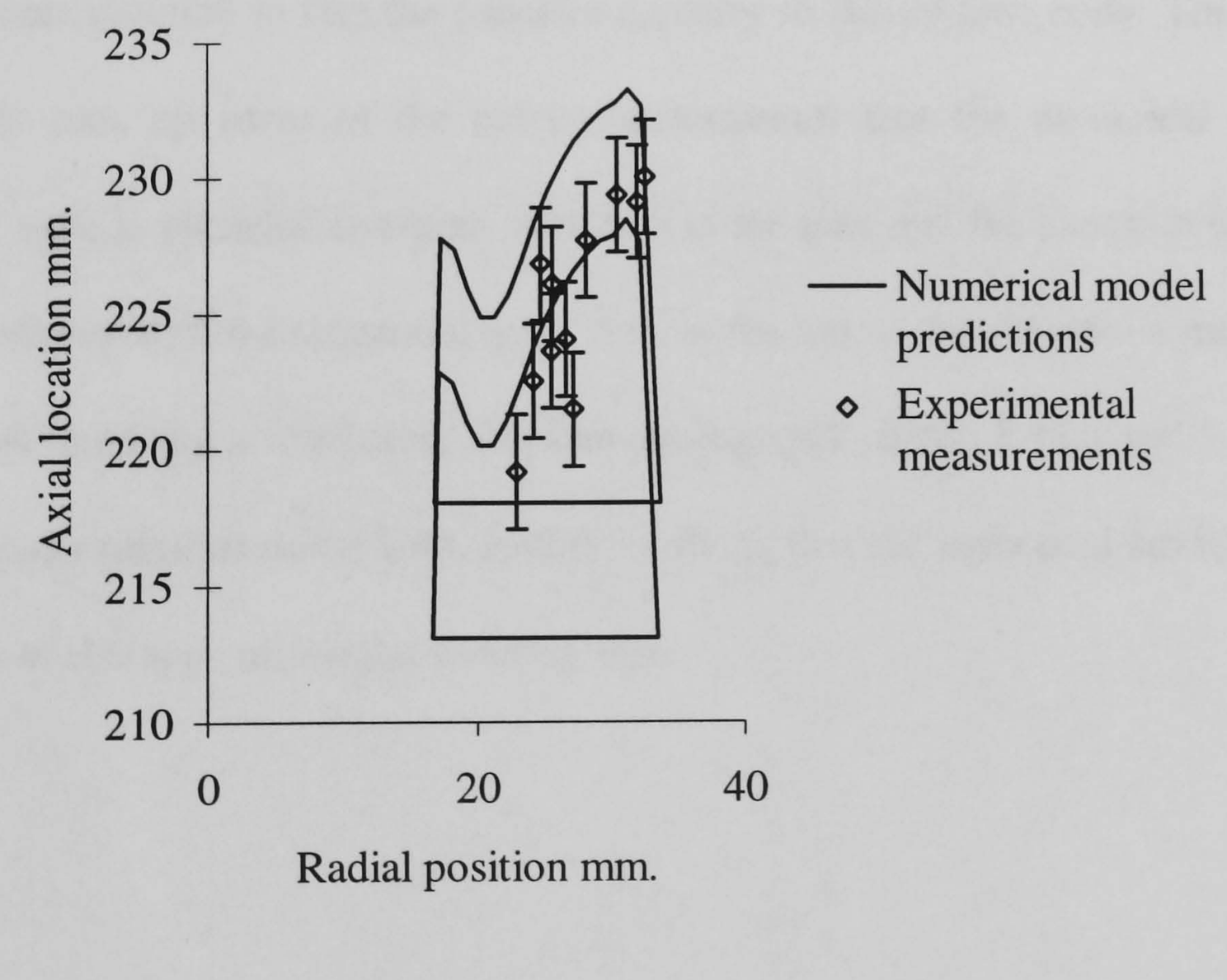

Figure 5.17. Shows a close up of the lower axial velocity profile in figure 5.15, comparing both measured and predicted values.

5.2.10 Velocity profile comparison

A degree of instability resulting from the turbulent unsteady nature of the flow is shown in the experimentally measured velocity data. It should be remembered that the calculated velocity profiles are the result of statistically averaged turbulence assumptions. Though the measured results displays the anisotropic nature of the turbulent flow field, the axial and tangential velocity bands that they form lie closely about the numerically modelled profile band limits. The Reynolds stress modelling equations appear to represent well the level of turbulence by accurately predicting the shape change of the velocity profiles over a 200 mm length of the hydrocyclone core.

The Fluent [RSM] turbulence code is therefore validated to model the swirling flows in this scale of solid core hydrocyclone. The results and assumptions of the optimisation study are also confirmed. Out of interest, the mirrors were removed and the strobe camera inverted to film the particles on entry to the cyclone body. This was done to possibly pick up some of the entry characteristics that the numerical model had predicted, such as particles diverging outwards in the inlet and the knock-in effect as the flow recombines with the tangential entry flow in the top of the cyclone, a mechanism to which short circuiting is attributed. The two photographs, figure 5.18.1 and 5.18.2, show neutral density particles doing both, further verifying that the numerical model represents the details of this type of annular swirling flow.

Figure 5.18.1.

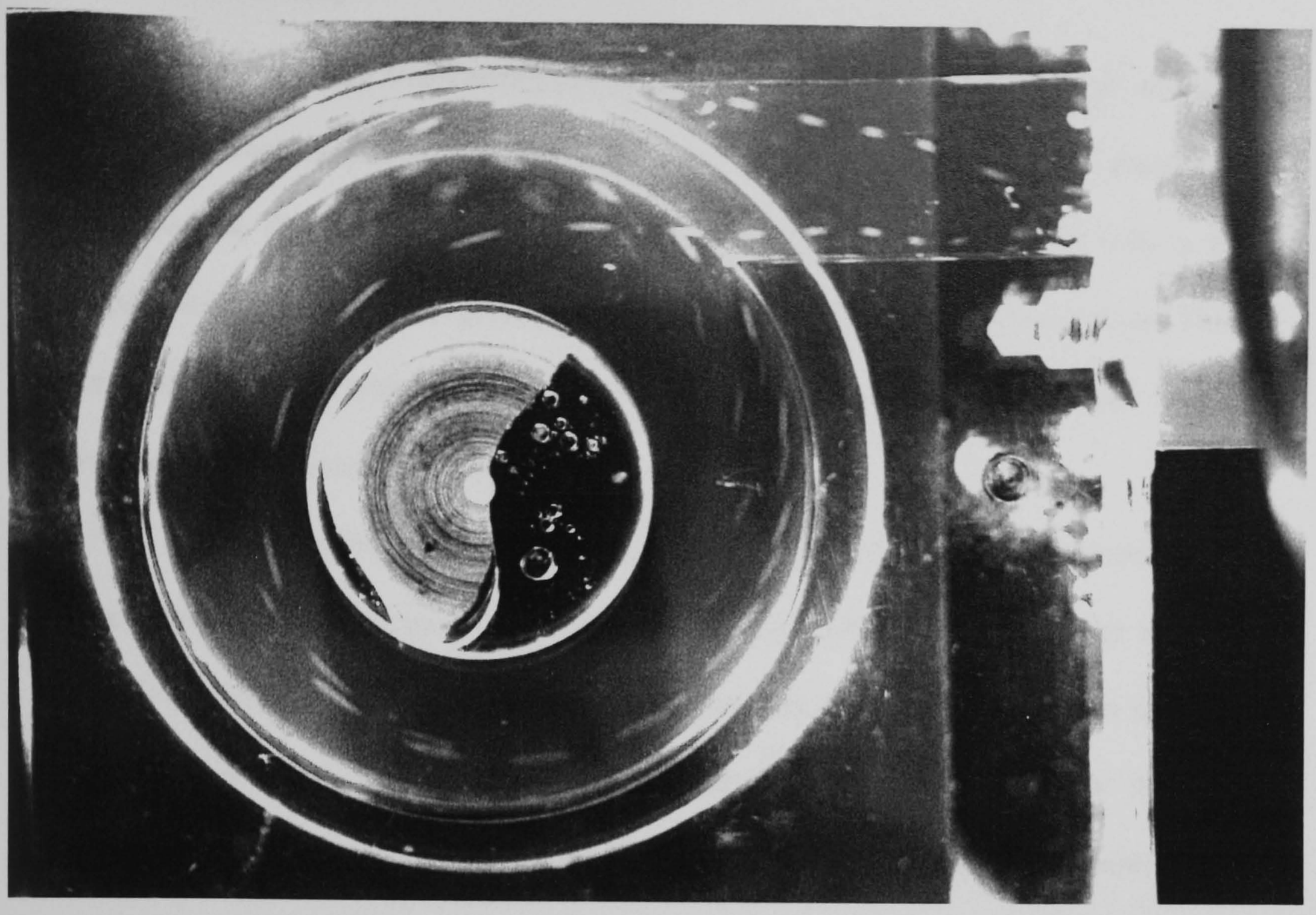

Figure 5.18.2.

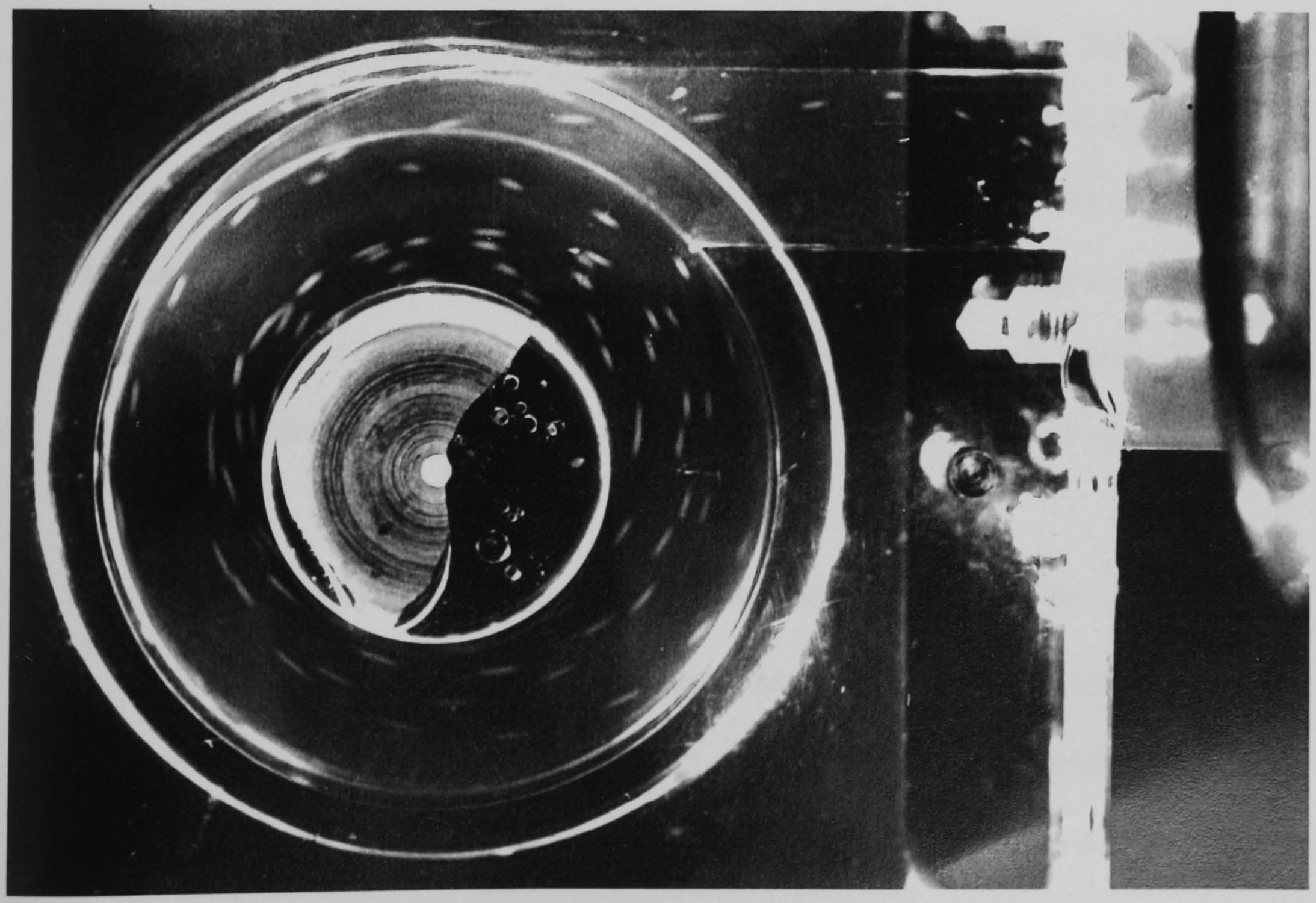

Strobe photographs of the top of the solid core cyclone showing neutral density particle trajectories in the square involute entry and the top of the cylindrical section.

5.2.11 Summary

Particle Image Velocimetry (PIV) techniques todate have made use of advanced techniques such as pulsed laser light sheets and computers to interpret the subsequent seed particle displacements in two dimensional slices of flow fields. Not only is this expensive but could not be applied to the spiralling flow field of the hydrocyclone. Three dimensional PIV is possible but has only been carried out hitherto using video for low velocity flow measurements < 1 m/s [N2].

A 3-dimensional photographic Particle tracking technique has been developed in this work which produces consecutive particle images 1/400 second apart by use of a simple strobe effect. The photographic equipment was built using only simple materials that were to hand. The strobe camera and mirrors, although simple, gave the three dimensional spatial location of consecutive particle images travelling at velocities in excess of 5 m/s while following a helix path within an annular hydrocyclone.

The velocity measurements in the full scale water model of a solid core hydrocyclone validate the predicted velocity profiles obtained by CFD. The velocity profile clearly shows that the annular swirl region exhibits both free and forced vortex motion as simulated using Fluent's Reynolds stress model of turbulence. The next stage is, therefore, to show that the velocity field induced in the annular flow will in fact cause alumina inclusions to migrate to the central core, leading into the next section of the experimental study, the modelling of the low density particle migration and capture.

5.3 Low density phase experiments: analysis and discussion

Following the velocity field measurements, the next stage in the investigation was the introduction of a lower density phase to the water model to represent alumina inclusions in molten steel. The objective of this series of experiments was to determine

the classifying action by predicting and confirming the amount of particles that could be made to migrate to the core surface. The lower density phase had therefore to behave comparably to fine alumina inclusions in molten steel. Equivalent particle properties were based on Stokes's law assuming the notion that two particles will separate at the same efficiency if their terminal settling velocity is the same. This assumption is of course subject to errors stemming from the validity of Stokes law, which never applies exactly due to its being based upon the approximation Re < 0.2. There are other uncertainties associated with the motion of irregular particles that may fall in a different orientation when settling under gravity. A representative model particle was taken to have a Stokes velocity in water equal to that of an alumina inclusion in molten steel where the representative particles dimension is the equivalent spherical diameter. Equivalent particle dimensions d are calculated after rearranging Stokes' law using equation 5.7, which is based on the free settling ratio in sedimentation [Wills W3] , where μ is dynamic viscosity

$$\frac{d_1}{d_2} = \sqrt{\frac{\mu_1 \cdot (\rho_{s2} - \rho_{f2})}{\mu_2 \cdot (\rho_{s1} - \rho_{f1})}} \qquad 5.7$$

The problem thus becomes a balancing act between density and size where the larger the particle, the smaller the required density difference between the liquid and solid phases. This introduces a potential for error. Small particles will tend to behave more like the finer alumina inclusions with respect to eddy motion in the turbulent flow. Large particles tend to disperse differently within the turbulent eddies. The period and direction of eddy fluctuations acting on different particle sizes can be very different. The particles that were eventually chosen had the same size range as the actual alumina inclusions.

The material found to have the best similarity with alumina inclusions in the steel melt based on both equivalent Stokes velocity and size were Eco-spheres. Eco-spheres

are hollow silica spheres with an average density of 700 kg/m^3 and ranging in size between 325 - 35 μm. These spheres are traditionally used as a light additive material to reduce density in the electronics industry and are also very tough. They therefore have a density ratio to water almost equivalent to that of alumina to steel. Their size range is close enough to the equivalent spherical dimensions of alumina inclusions to mimic their behaviour in the turbulent flow. Table 5.1 shows the comparative size of Eco-spheres in water to spherical alumina inclusions in liquid steel.

Table 5.1. Shows the corresponding spherical diameters of alumina inclusions in liquid steel based on the free settling rate of an Eco-sphere in water.

Eco-sphere diameter μm	Corresponding spherical alumina particle diameter μm
30	20
40	26
50	33
60	39
70	46
80	52
90	59
100	65
150	98
200	131
250	163

5.3.1 Particle Capture

Initial considerations

If a physical simulation of the inclusion attachment process were to be attempted, the initial problem was the development of a capture mechanism on the core for the model particles and the consequent analysis of the captured sample. Initial ideas for a sticky surface that the low density phase would stick to were unrealistic. Notwithstanding the difficulty of providing a sticky surface in the flow of water, subsequent removal of such fine particles for analysis presented a daunting prospect. 'Eco-spheres' do not stick to one another like alumina in hot metal, so once the notional sticky surface was saturated with the lower density phase, no more material would be captured.

Other ideas included photographic evidence of particle collisions with the core, and wax particle modelling. The difficulties of viewing a 360° surface using long exposure with small particles appeared to present insurmountable photographic problems. Alumina build up has been modelled by introducing wax particles into the flow [T3] and this could show the principal areas of build-up, but the capture mechanism was considered too uncertain to provide a quantifiable basis for study.

Figures 5.19.1 to 5.19.6, show screen grabs from video footage obtained during an initial visualisation test of low density Eco-spheres introduced into the cyclone flow. It is clear that the dust cloud initially disperses in the inlet due to the highly turbulent flow there. The dust is then seen to migrate to the centre forming a thin sleeve on the core. This layer of particles remains on the core until the flow slows at the exit of the underflow and the dust layer is subsequently shed from the core surface. From this observation came the idea of separating the underflow at the discharge from the solid .

Figure 5.19.1

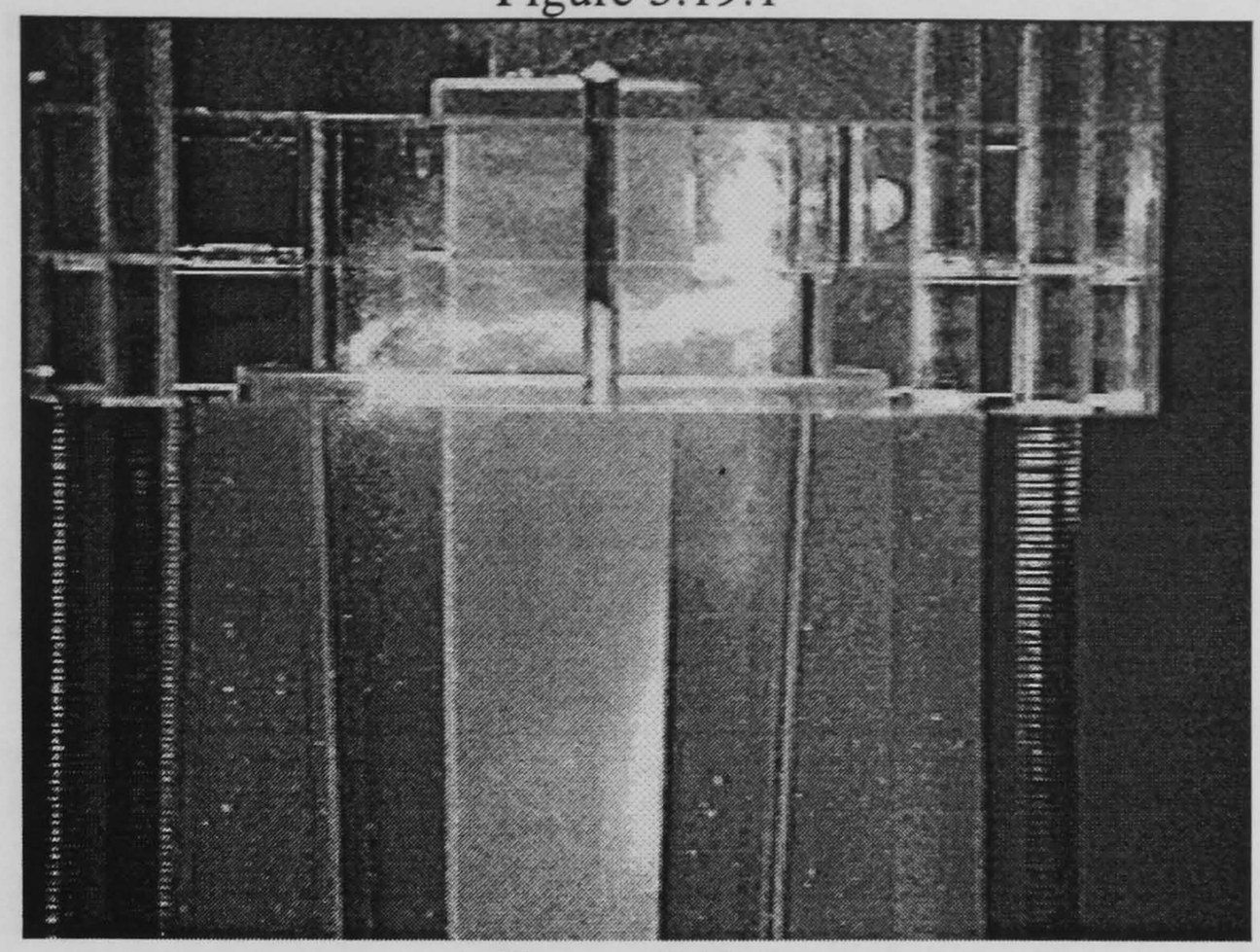

Figure 5.19.2

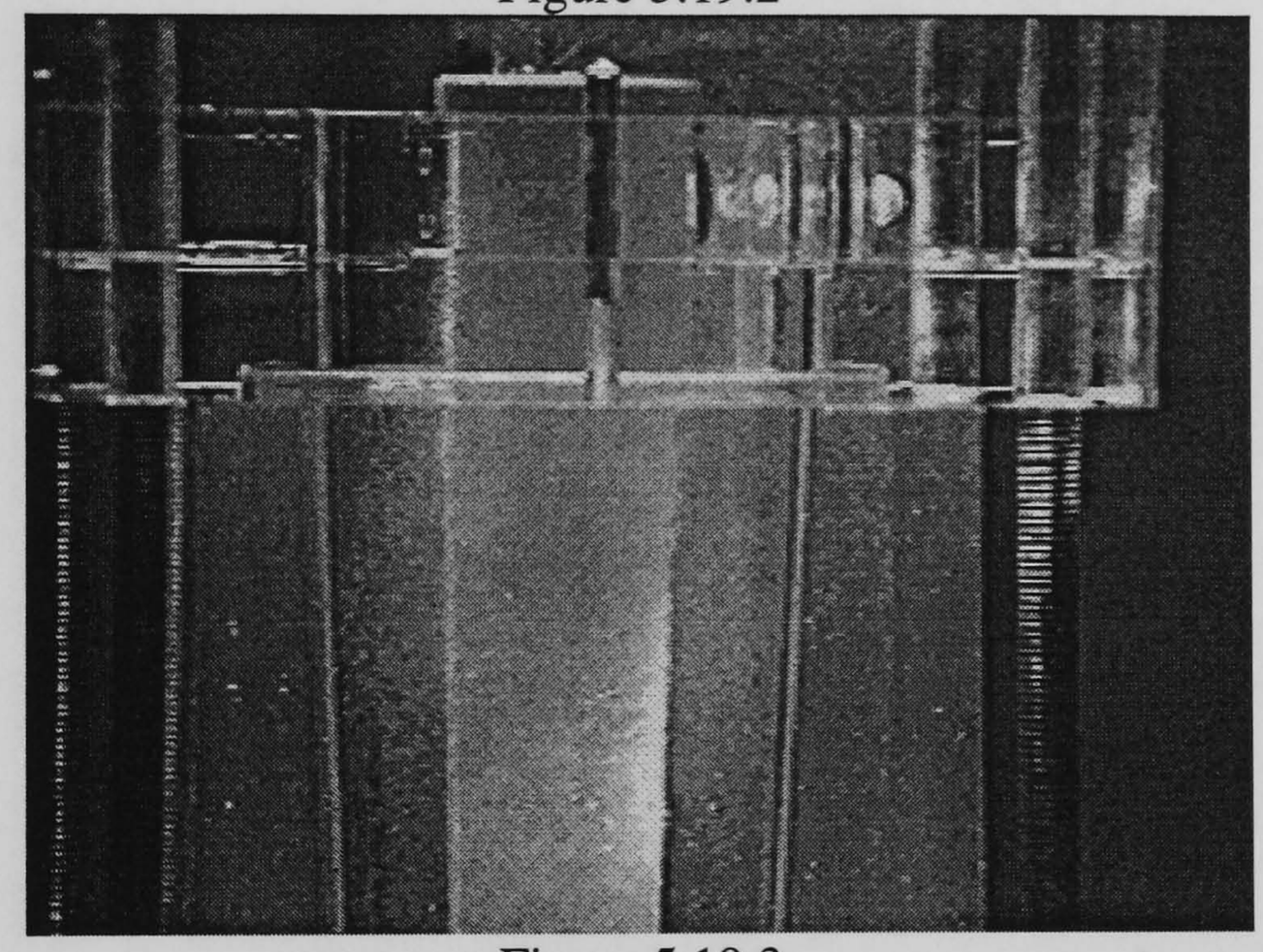

Figure 5.19.3

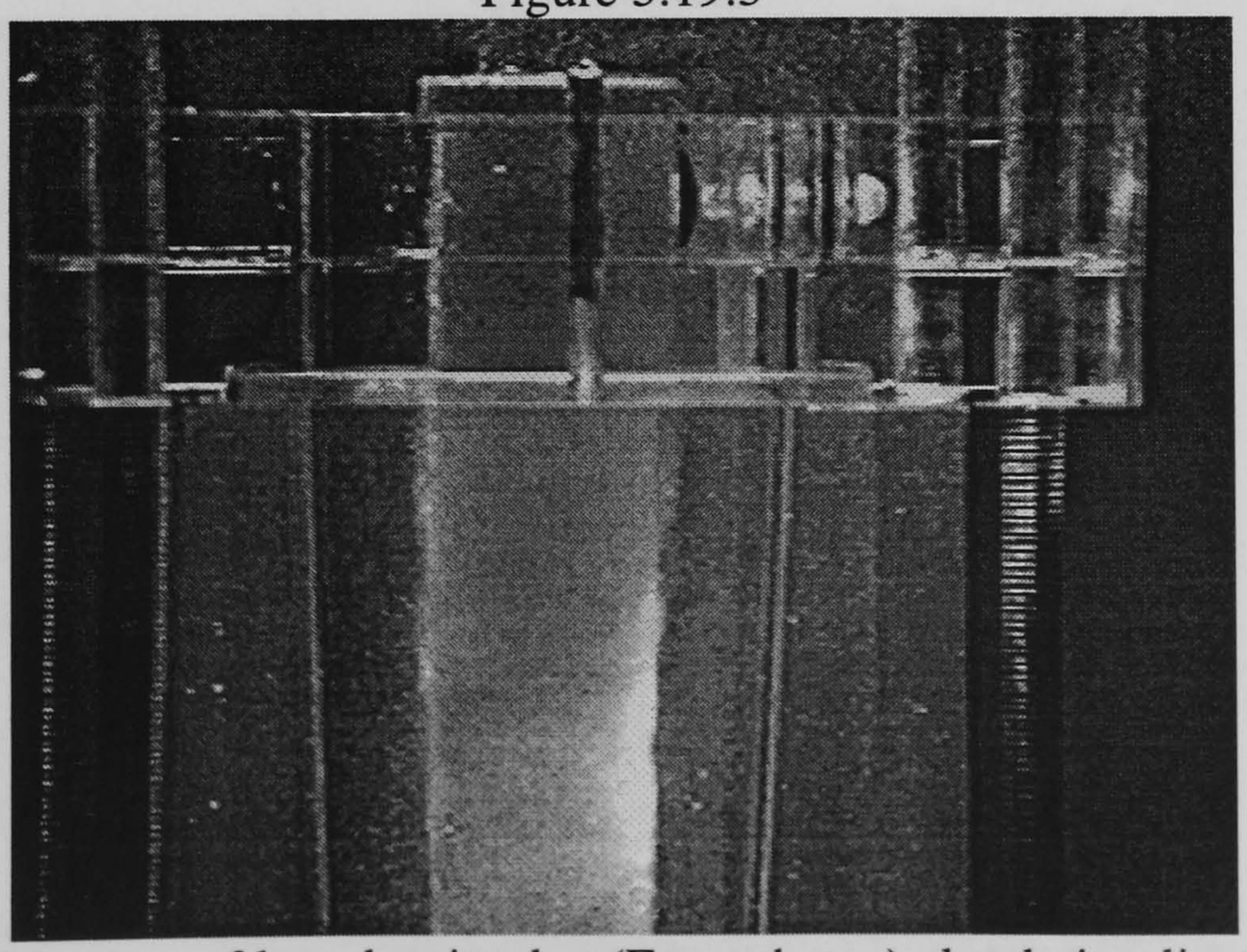

Screen grabbed images of low density dust(Eco-spheres) cloud visualisation filmed with a standard video camera.

Figure 5.19.4

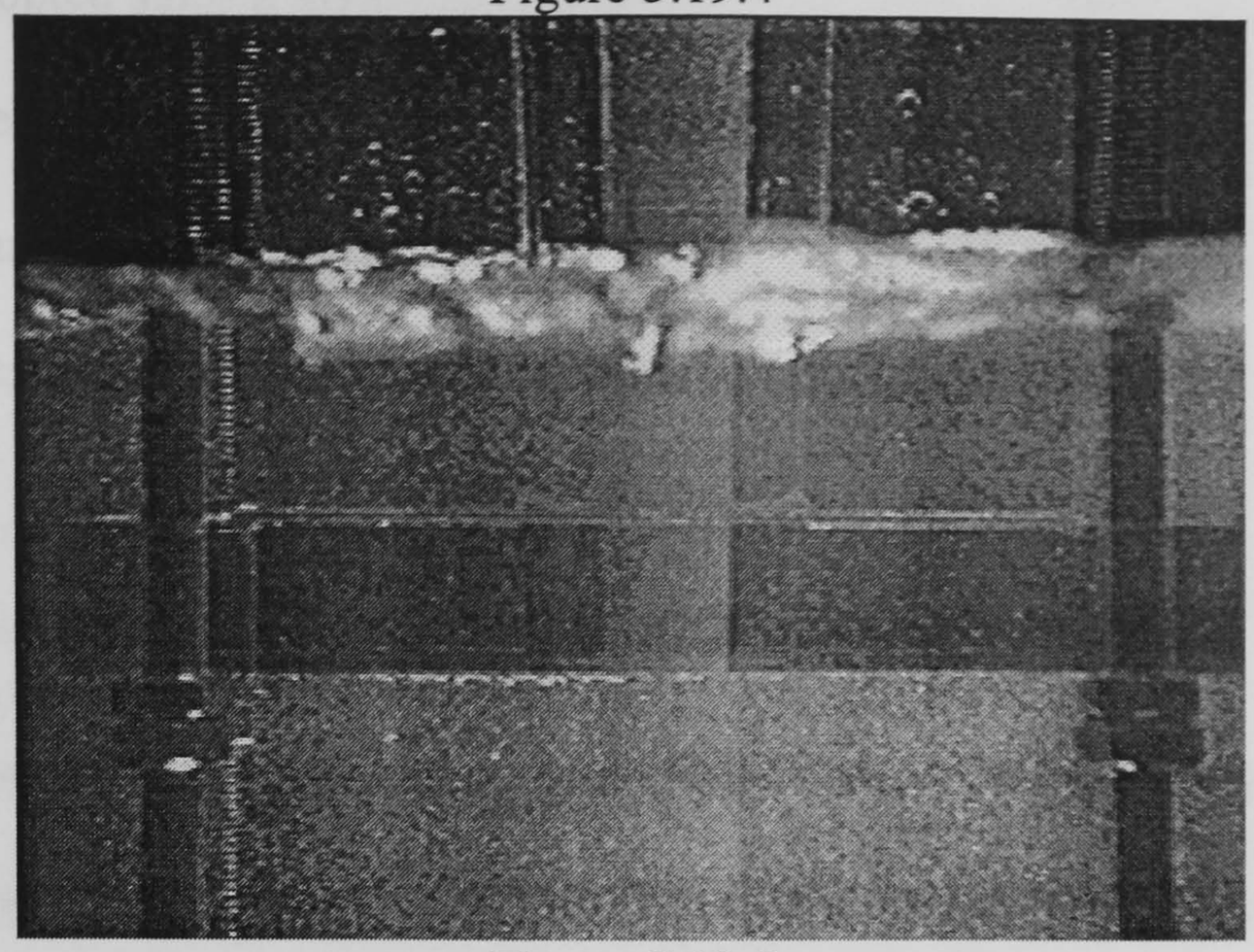

Figure 5.19.5

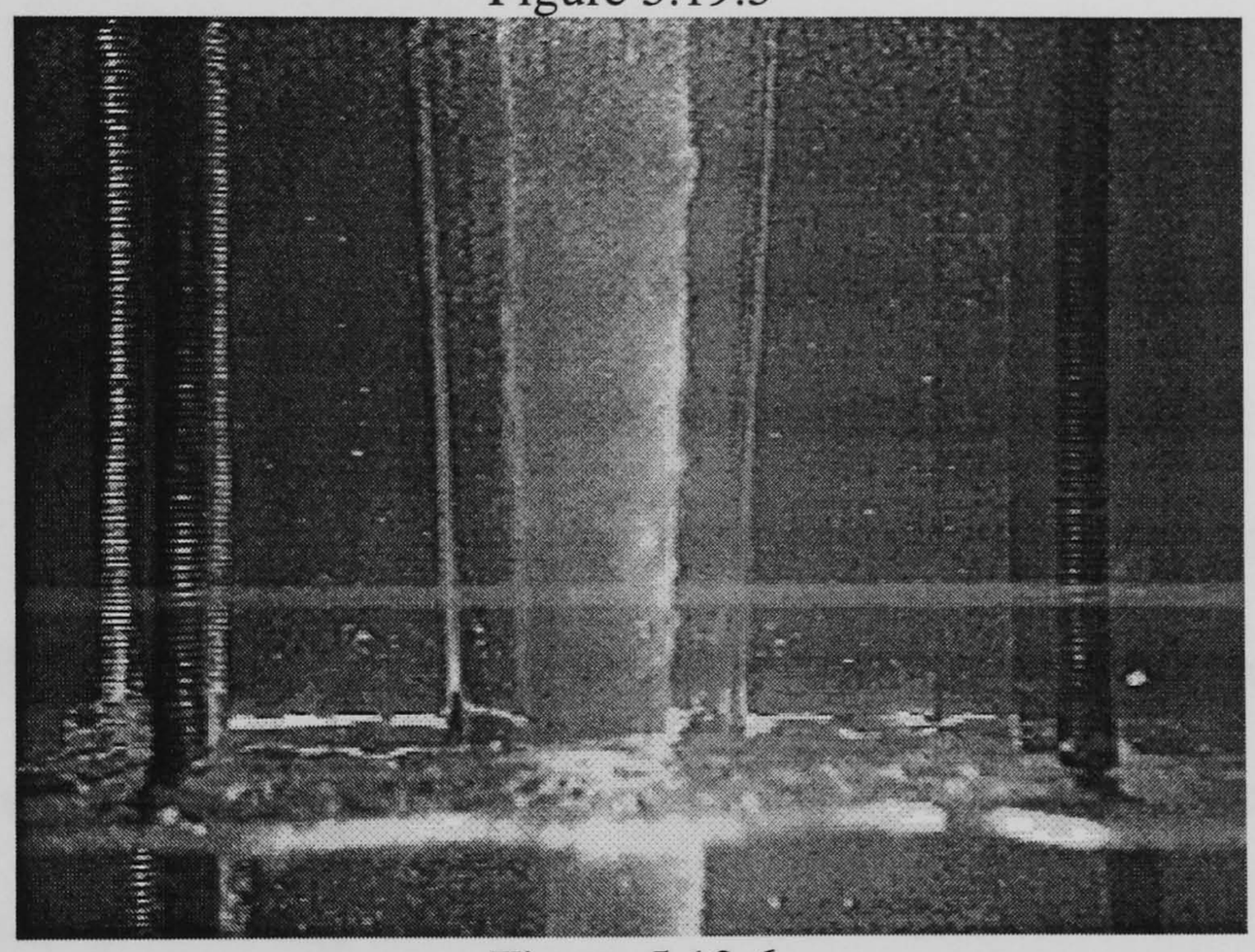

Figure 5.19.6

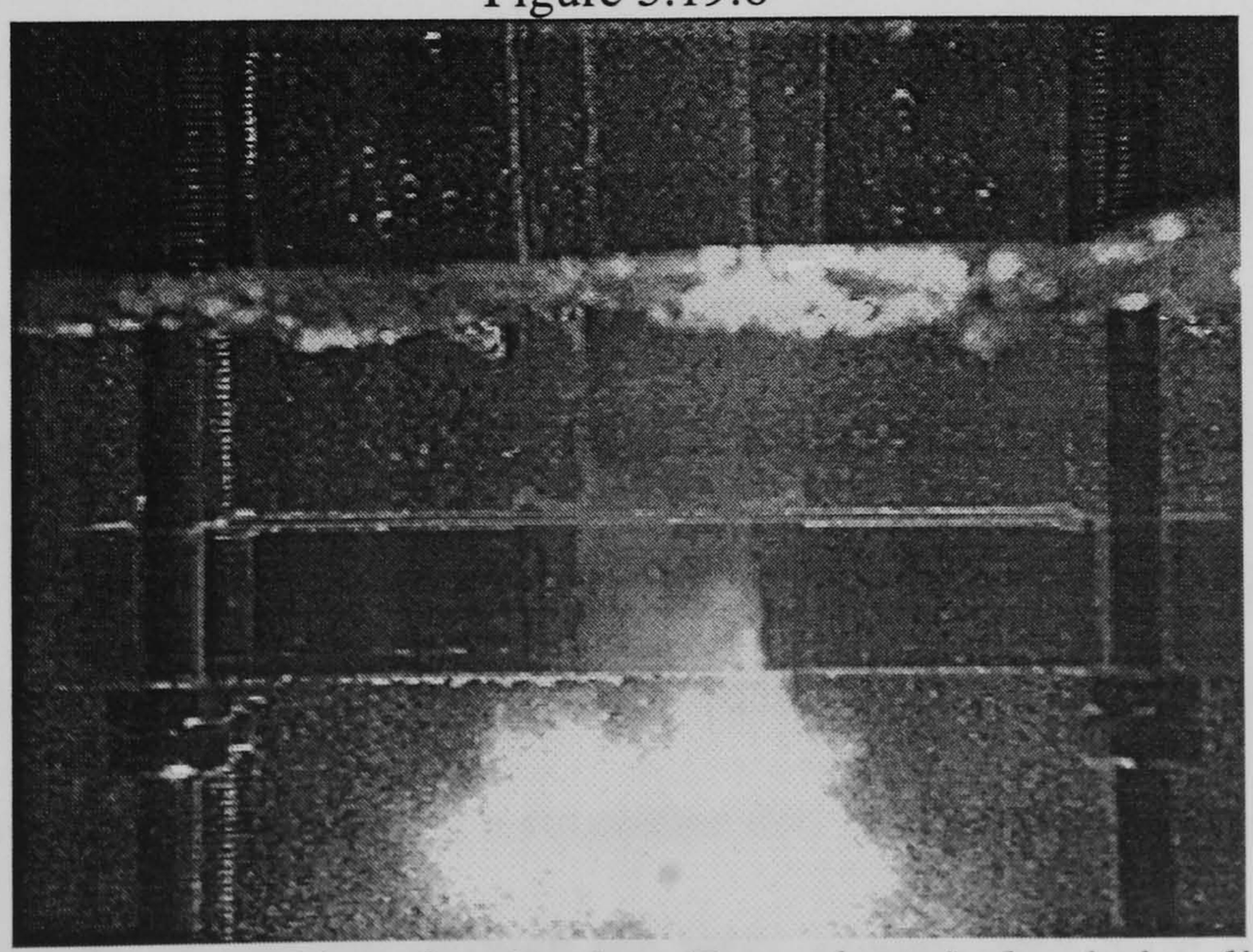

Screen grabbed images of low density dust (Eco-spheres) cloud visualisation study, filmed with a standard video camera.

core cyclone to recover the loaded layer at the core surface for analysis. This approach was finally adopted since it appeared capable of producing a quantified, classified output that would be a practical test of the migration process. Whether or not real alumina inclusions would in practice then stick to the core having reached it could be tested only at pilot plan scale under process conditions.

5.3.2 Solid Core Cyclone (With Divided Underflow)

The underflow discharge is divided into two streams by the introduction of a concentric pipe at the cyclone apex. This pipe is axial, with its upper edge concentric with the core, and extends upwards inside the cyclone to form an annular orifice around the conical surface of the core. The size of this annulus is adjusted by raising or lowering the pipe. By adjusting the annulus, a greater or smaller fraction of the spiralling downflow near the core surface can be separated from the underflow and discharged independently, a schematic of this arrangement is shown in figure 5.20. This form of divided underflow is not subject to the short-circuiting flows of the conventional cyclone. The particles should have sufficient time to migrate to their equilibrium position in the flow along the length of the cyclone.

The cyclone rig was modified to incorporate this annular pipe or 'splitter' A 1.5 mm gap was used so as not dilute the wall flow sample too much. The video footage of the Eco-sphere cloud, figure 5.19.6 showed that the cloud of particles travelling down the core sheds from the core surface just above the apex as the flow slows at the exit. The tube had to extend 25 mm inside the cyclone to be above this region at the apex where the dust cloud detached from the core surface. The wall or inner flow through the annular splitter was measured using a rotameter and drawn off at a flow rate equivalent to that which would be passing through the inner annulus area were it not there. This

flow rate was calculated using the Fluent CFD code model by integrating the velocity of liquid flow passing through the area taken up by the splitter. A pump provided the suction required to overcome the additional drag and energy losses due to the constriction at the entry to this annulus. Without the pump to draw the fluid through there is a chance that the constriction will cause the particles to shed from the core, this is shown in figure 5.21. The rig was run with filtered water in a steady state for a few minutes at the beginning of each test to ensure there were no particles remaining in the system and that the water filters were working. The Eco-spheres were then injected slowly into the flow, entering the cyclone through the elbow-bend using a syringe shown in the photograph of the rig, figure 5.22. A close up of the annular splitter during the models operation is shown in figure 5.23. The flow meters were observed throughout the experiment to establish that the flow conditions remained constant. The separated particles were then captured on a 38 μm mesh and washed off into a beaker of electrolyte solution for a size frequency analysis by resistivity measurement.

5.3.3 Samples and Measurement

A Coulter Counter was used to determine the numbers of each particle size in the samples. The Coulter Counter, described by Irani & Callis [I9], measures the particle size distribution suspended in an electrically conducting liquid. The suspension flows through a small aperture having an immersed electrode on either side. The particle concentration needs to be low enough so that the particles traverse the aperture one at a time. In most cases particle sizes distributions measured by this technique may have upto a 30% inaccuracy. The passage of a particle through the aperture displaces electrolyte, momentarily changing the resistance between the electrodes and producing a voltage pulse corresponding to the particle volume. The resulting series of pulses is amplified

then scaled and counted using pulse-height analysis. Particles should ideally have a chemically inert surface, a condition which is met by the Eco-sphere.

The test samples of Eco-spheres were taken from two different populations sieved to remove all the very fine and very large spheres. Each population contained a unique frequency distribution of particle sizes. The first contained higher quantities of the smaller spheres, frequency varying inversely with size, while the second population had fewer small spheres and a greater number of large ones. By using two different populations and making a comparison of the population "captured" (i.e. extracted from the core flow layer) with the initial sample in each case, it was possible to check whether the classification process was sample-dependent.

The size range of the silica Eco-spheres that were counted lay well within the limits of the technique. When working with populations of particles of this type everything must be averaged since every sample that is weighed out will have a slightly different frequency distribution. For these experiments, the average of ten test samples were taken as sufficiently representative of the population. Averaging of the flow effects is also necessary when working with inherently unstable turbulent flows so the particle capture experiments were also repeated ten times for each sample. Samples of Eco-spheres (0.2g) were weighed out injected into the cyclone (as discussed in section 5.1.2) and the inner annular fraction was recovered on a 38μm screen. The sample weight was limited to 0.2g because this was the maximum that could be sized without blocking the counter. The water supply from the mains was filtered down to 50μm, which therefore limited the useful size of Eco-spheres to +50 μm in the experiment. A 50 μm Eco-sphere corresponds to a 37μm alumina inclusion in molten steel, as outlined in table 5.1

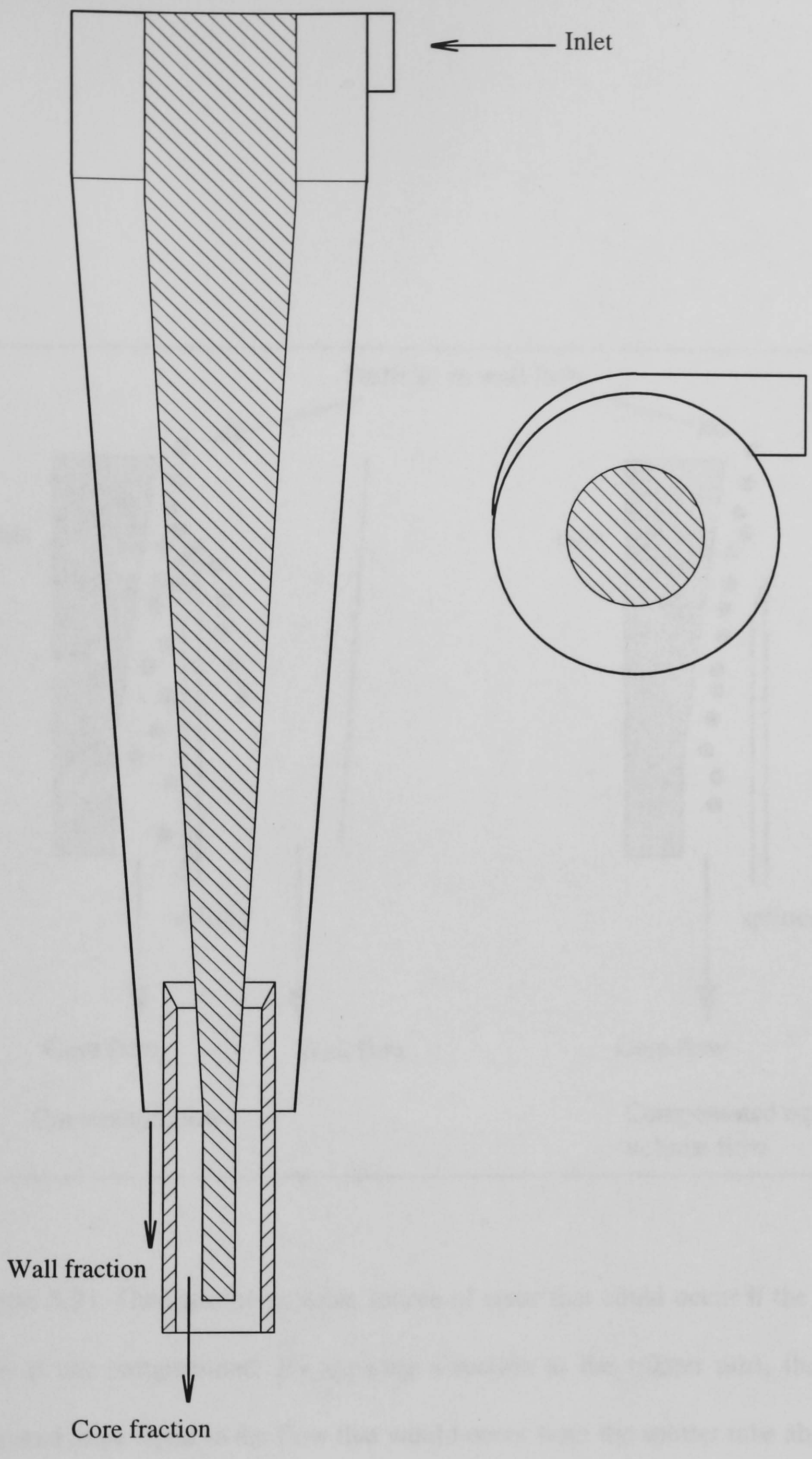

Figure 5.20. Schematic of the solid core cyclone with divided underflow.

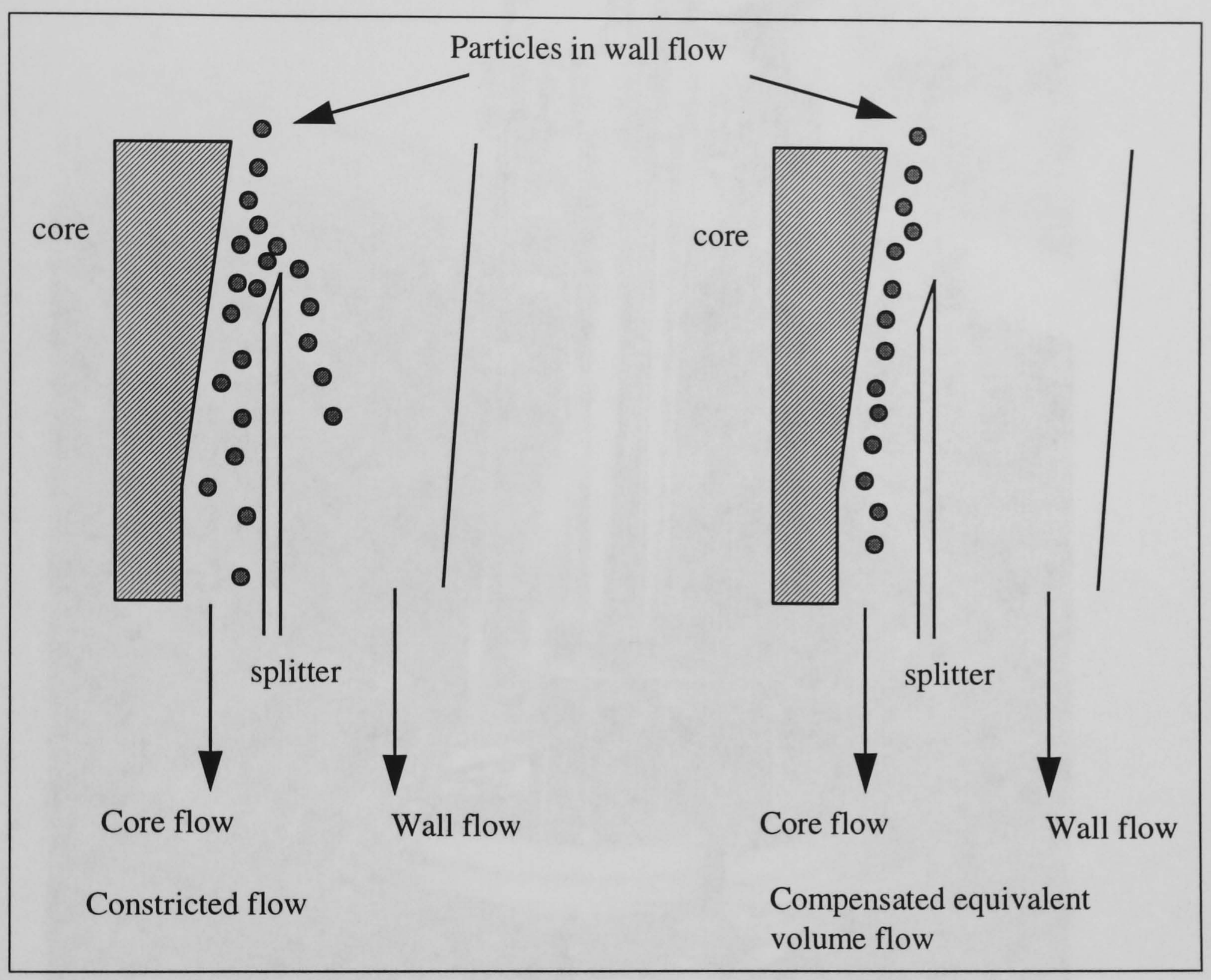

Figure 5.21. Outlines the possible source of error that could occur if the constricted wall flow is not compensated. By applying a suction to the splitter tube, the sample flow is adjusted to be equal to the flow that would occur were the splitter tube absent.

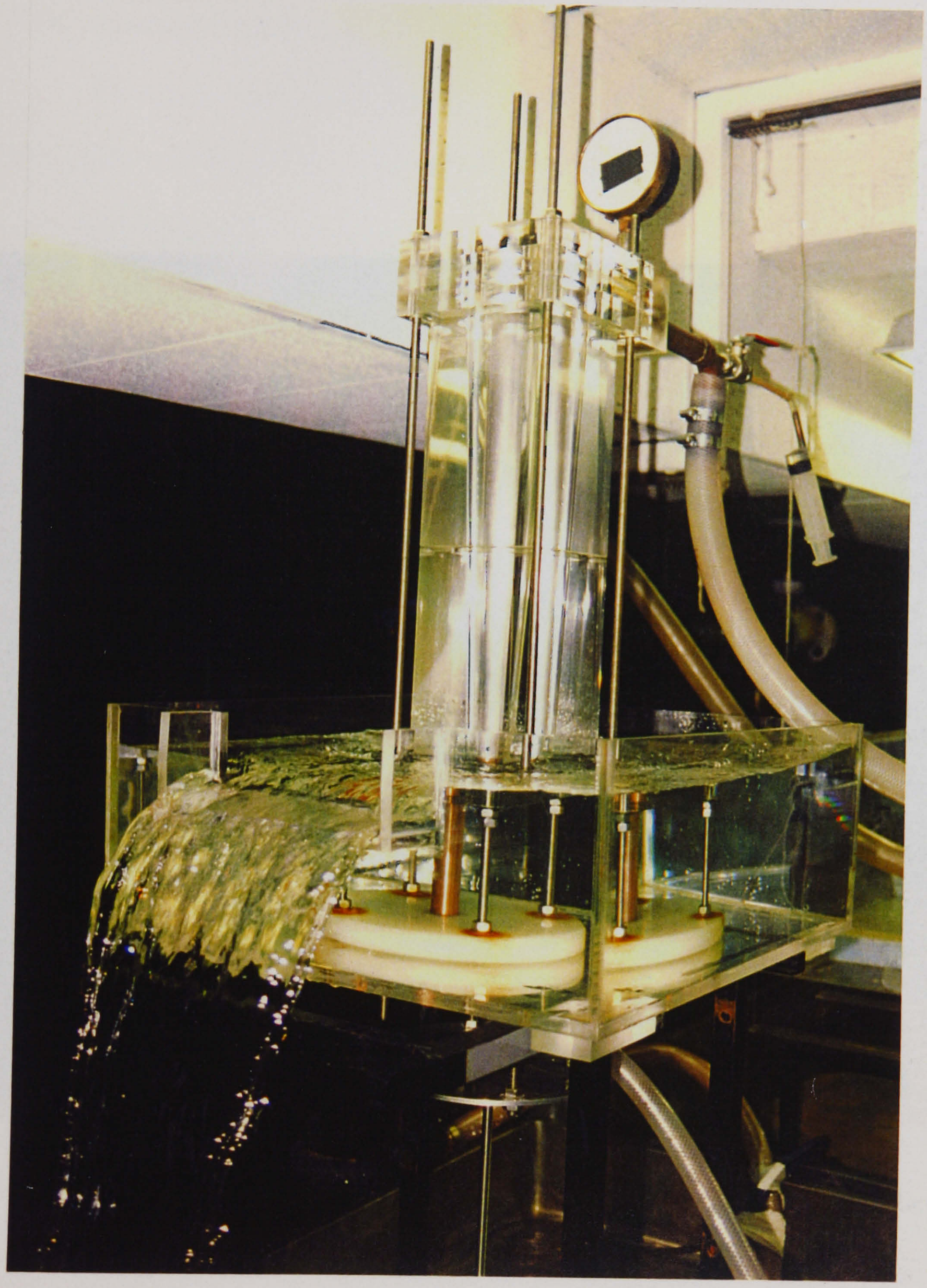

Figure 5.22. Photograph of the modified solid core hydrocyclone with annular slitter in operation.

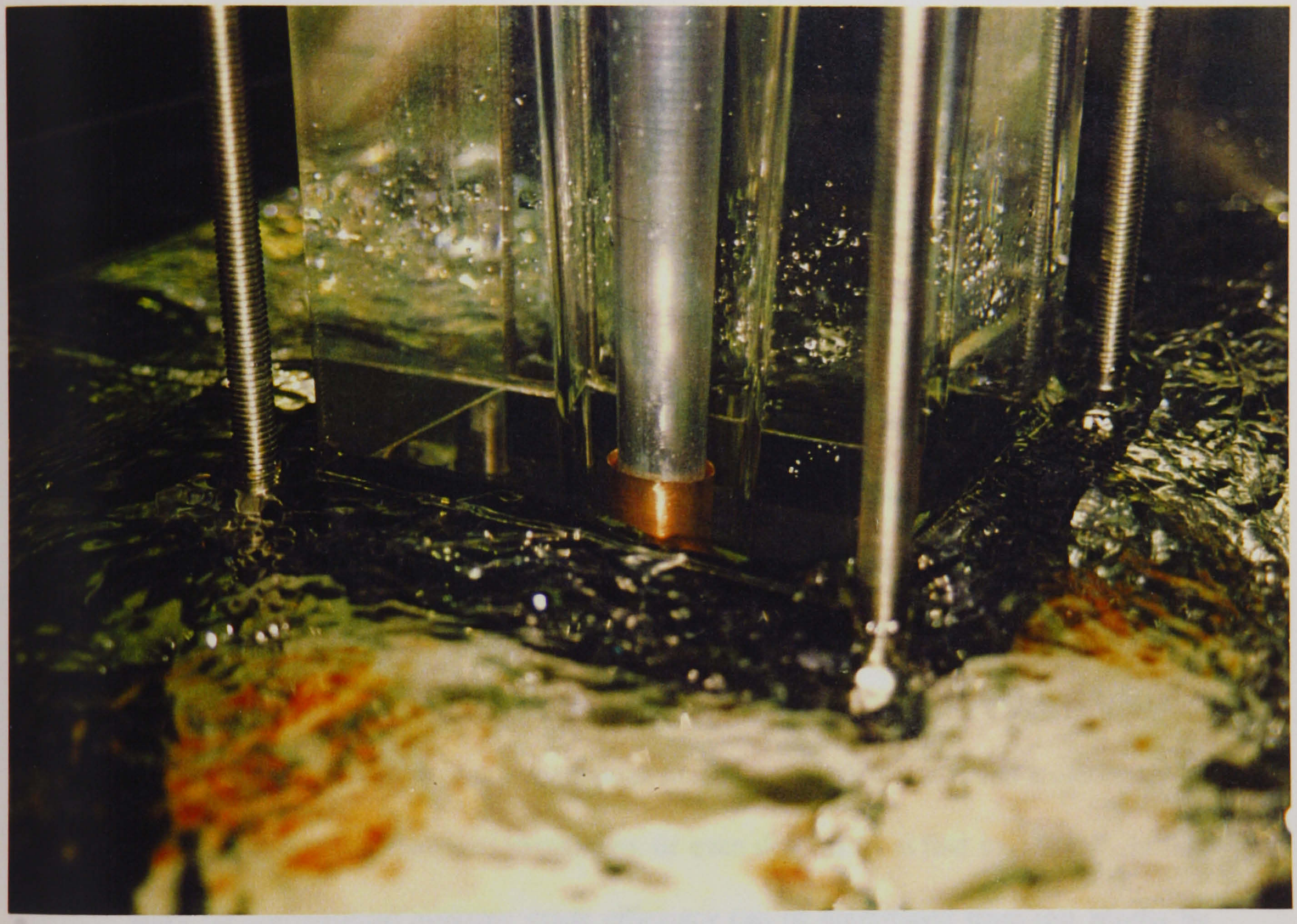

Figure 5.23. Photograph of the modified annular splitter arrangement used for the low density phase experiments in use.

which gives the corresponding size of the Eco-spheres to equivalent spherical alumina inclusions. The much higher flow of the outer annulus was too large to sieve effectively, so the separation was determined by difference.

The sample was then suspended in 210 ml of well-stirred electrolyte and analysed in a Coulter Multisizer II for a period of 60 seconds. This was sufficient time to give a good distribution of particle sizes within the samples. The use of small, 0.2g samples of Eco-spheres for the experiment was not only appropriate for the Coulter Counter measurement, but was also representative of the inclusion concentrations in steel.

5.3.4 Separation Efficiency

Classification of Solids according to size

The performance of most equipment for particle-fluid separation is highly size dependent and different sizes are separated with different efficiencies. Grade efficiency G is the efficiency corresponding to one particular particle size only. For a separator with a size dependent performance, the grade efficiency varies with particle size G(d), and a graphical representation of this is called a grade efficiency curve. Svarovsky [S7] writes, "The grade efficiency curve is a continuous function of particle size d and it can rarely be approximated by an analytical expression, or even derived from first principles". In test work on conventional cyclones grade efficiency can be determined from test results by feeding the cyclone with a material containing particles in the required size ranges. The particle size distribution of two of the three slurry streams must be known.

In common hydrocylone terminology describing classification, the ability to separate one solid from an other is referred to as sharpness of cut. A d_{50} cut would be the particle size corresponding to a 50 % chance of separation between the underflow and overflow streams, see Wills [W3]. In the separation of solids from solids, either by

particle size (classification) or by density (sorting) the effectiveness is described by the term 'sharpness of separation', the sharper the cut the steeper the grade efficiency curve.. The efficiency can also therefore be calculated by particle size analysis from two of the three slurry streams. However, difficulties occur because there are quite high errors associated with particle size measurements.

5.3.5 Error Analysis

In general, a rigorous statistical analysis [S6] has shown that the best combination of material streams to sample in the conventional cyclone is the underflow and overflow. In the solid core cyclone these two streams correspond to the inner and outer annular flows. But this choice may be outweighed by of sample collection, accessibility and flow measurement. In the present low density physical modelling experiments, it was impossible to measure the particle frequency distribution in the outer annulus. Thus it was necessary to know the particle distribution of the injected sample. Since the particle frequency distributions in the weighed out samples could never be identical, the results had therefore to rely upon an average estimate of the samples being injected at the inlet.

Grade efficiency curves are sometimes corrected to remove the effect of fine particles which simple follow the flow and are split in the same ratio as the fluid. This effect is removed in a correction of efficiency to make equipment comparisons equal. The requirement in the present measurements is to predict the quantities of different inclusion particle sizes that will remain in the melt after cycloning. Due to the core flow separation, which is inherent in the experimental method there is now flow split, absent in the real application, which needs to be taken into account. This produces a particle separation artefact which occurs purely as an effect of the flow drawn from the core flow

layer. A correction of the analysis is therefore necessary. This error is known as 'dead flux' and always occurs due to particles that do not undergo radial migration, these separate in proportion to the flow split. Following Svarovsky [S7], R_f is the ratio of the coreflow to the total throughput and the corrected grade efficiency G' Is defined as

$$G'(d) = \frac{G(d) - R_f}{1 - R_f}. \qquad 5.8$$

Particle size and size distribution of the feed solids in dense slurries can affect separation. In this experiment the concentrations of solids are so low that they might reasonably be neglected. Nevertheless, two populations with different size distributions were used as a check. Particle-particle interaction only becomes a problem in high solids concentrations where, among other effects, the apparent viscosity is increased thereby increasing the drag on the particles.

In summary, the outer annular flow rate was too large to be effectively screened, so a direct comparison between inner and outer annular particle distributions was impossible. There was a wide variation in the particle size distribution in each weighed out sample, and as size and population measurement using the Coulter Counter results in sample destruction, an approximated particle distribution of samples was used, obtained from the average of 10 samples taken from the same parent population. The initial average population distribution was then compared with that of the 10 captured particle samples. Because each test is repeated 10 times, any other random error effects will also be averaged by the analysis of the data.

5.3.6 Statistical treatment of data

Each particle size band in the ten tests was analysed using confidence intervals of 95 %. The confidence interval for a population mean is the range on either side of a

sample mean that can be predicted with a particular level of confidence. In this case it will define the range on either side of the sample mean for a given particle size band in which the loss or capture of a particular particle size can be determined with a particular confidence. The confidence interval in standard form is defined as

$$\bar{x} \pm 1.96\left(\frac{\sigma}{\sqrt{n}}\right), \qquad 5.9$$

where $\bar{x}$ will be the mean value of all the particle measurements for a given size range, σ is the standard deviation and n is the number of experiments or tests. The standard deviation of a size band is determined from the 10 measured samples.

5.3.7 Results

The measured particle distributions for the initial sample and the core flow sample for each of the two population is shown in figures 5.24 and 5.25. Eco-sphere particle sizes are given in all the figures in terms of the equivalent spherical Stokes diameter of the alumina inclusions in steel. The variation associated with particle distribution sampling and measurement is displayed as a band. This band describes a region for which there is a 95 % probability that the actual particle distributions lie within it. The two particle distribution curves for the two populations show the point where the confidence limit bands cross. The location of maximum and minimum particle size suggest the region in which the smallest particle size that has zero escape may reasonably lie, see the following table.

	Maximum	Minimum
Population 1	90 μm	115 μm
Population 2	70 μm	115 μm

The corrected grade efficiency curves for those particles that are not captured in the core flow and would consequently be lost to the melt are compared in figure 5.26. It can be seen that the magnitude and sharpness of cut compare well. The distributions predicted by Fluent (Section 4.1.5) have been mapped on to these grade efficiency curves, where a 'lost' particle is defined as one that did not touch the core at any stage in its transport. As there is no separating flow in the Fluent model, the computed grade efficiency curve needs no correction. The same particle tracking conditions as in the previous modelling (Section 4.1.5) were used for comparison but this time the physical parameters for water and Eco-spheres were used. The computed grade efficiency curve for particles lost to the melt has a sharper cut than the experimental averaged curves. Nevertheless, the predicted curve based upon the simple Fluent particle transport model lies mainly within the band of 95 % probability. The error bars are taken in this case as the 95% probability limits calculated using the difference between the captured samples and the original sample mean.

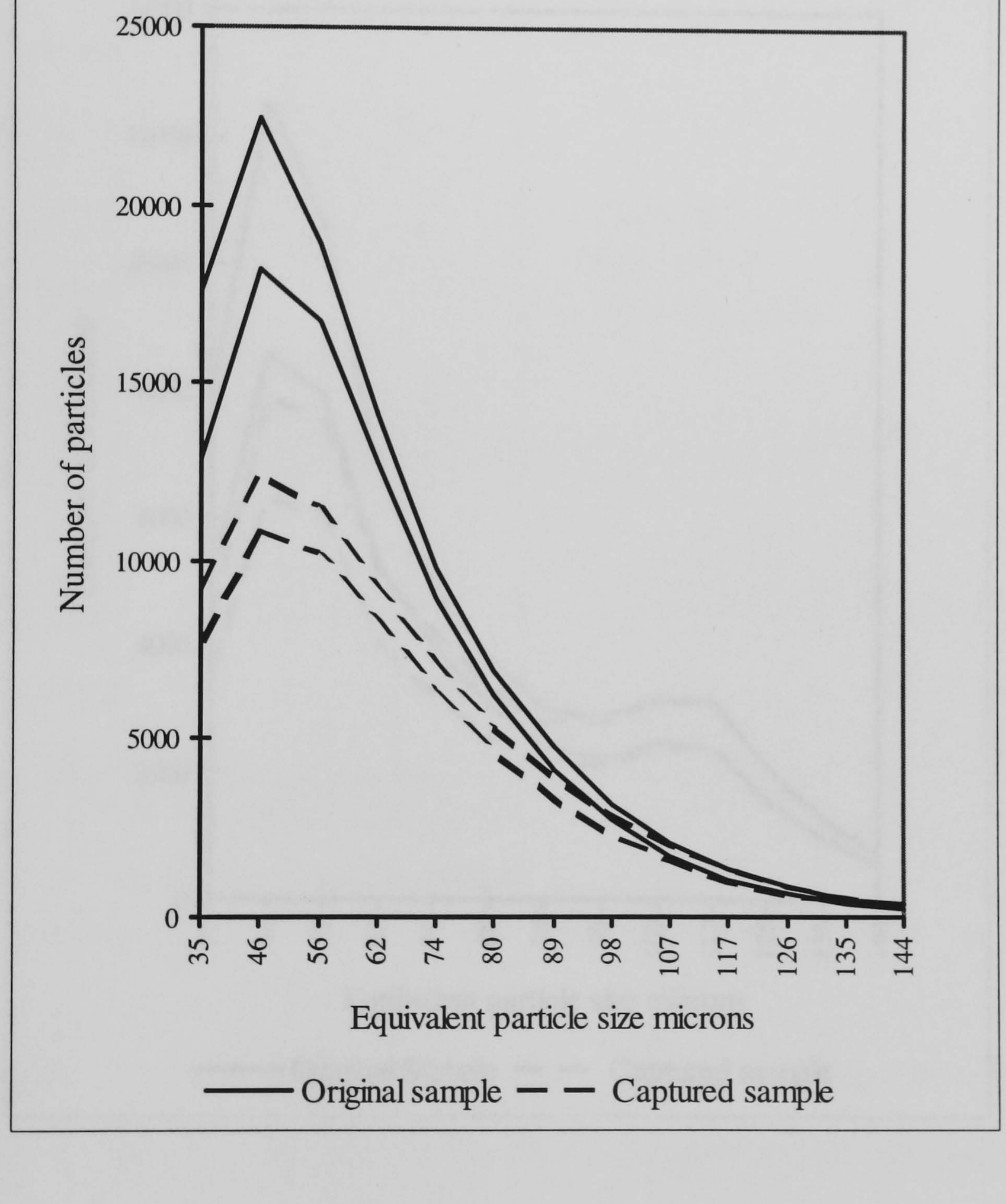

Figure 5.24. Graph showing the 95% confidence limit bands of initial and captured particles for population 1.

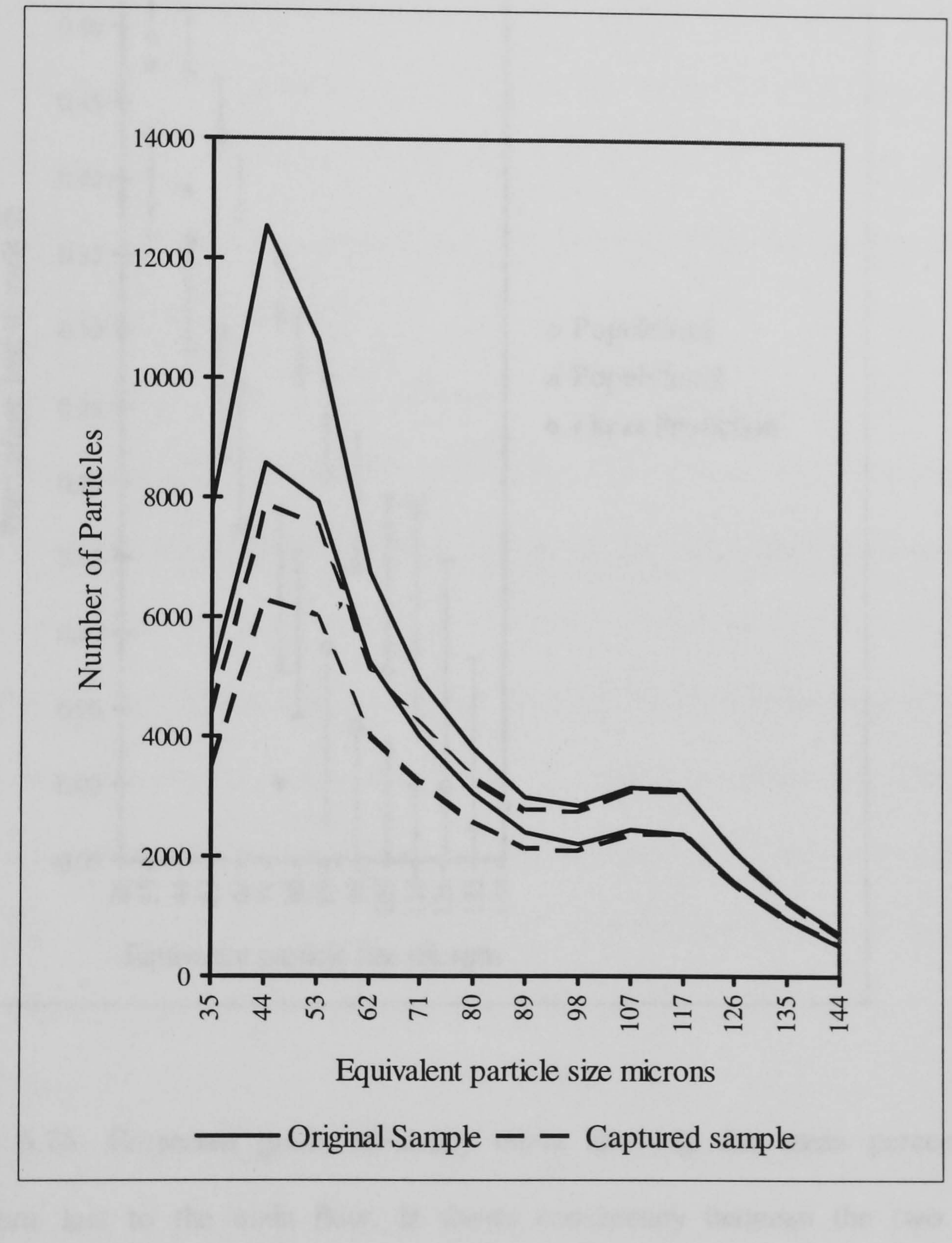

Figure 5.25. Graph showing the 95% confidence limit bands of initial and captured particles for population 2.

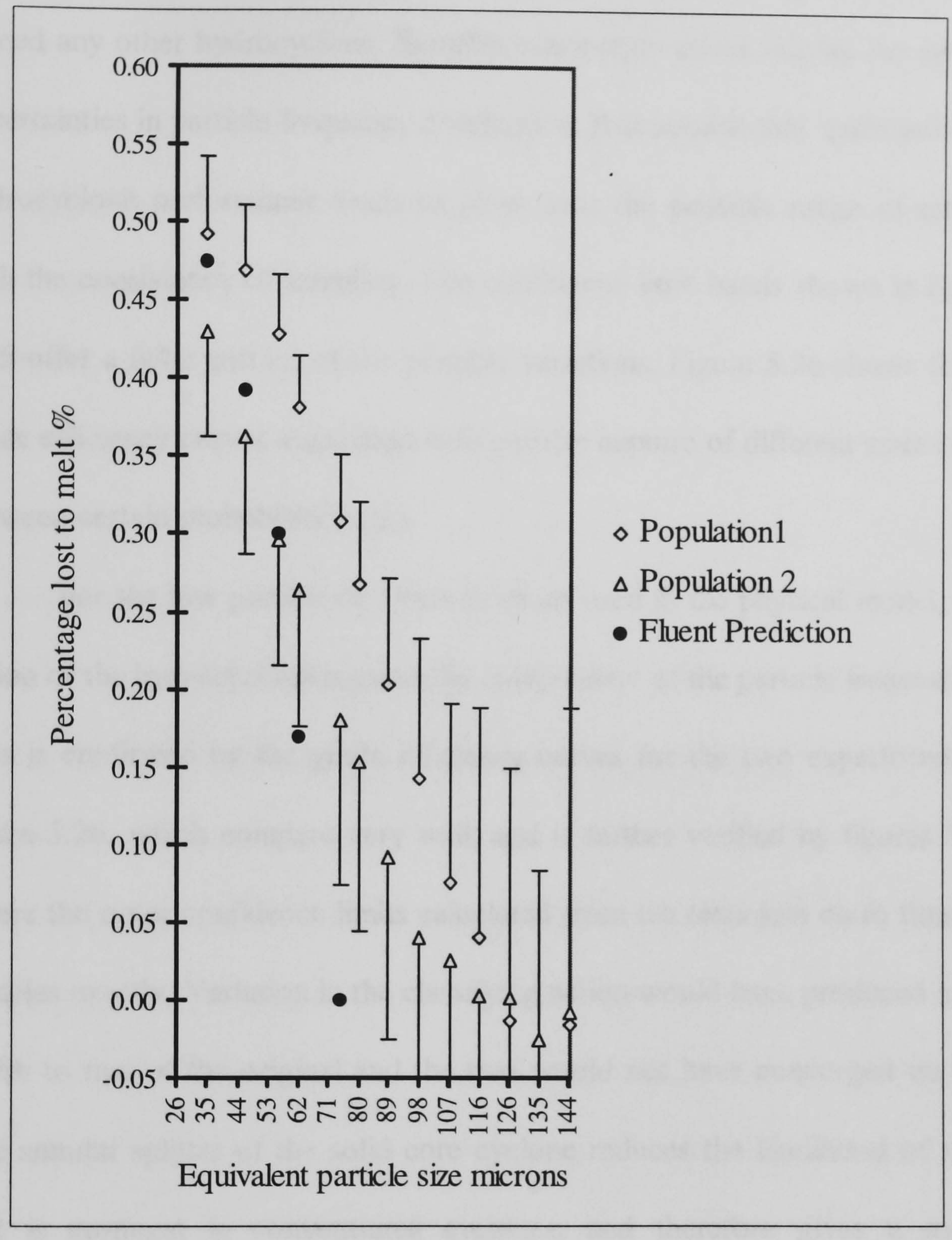

Figure 5.26. Corrected grade efficiency curve showing the mean percentages of inclusions lost to the main flow. It shows consistency between the two different populations and also the predicted values of Fluent. Error bars show the 95% certainty band either side of each population in which the mean value may lie.

5.3.8 Discussion

The study has highlighted many of the difficulties involved in the particle sampling and measurement methods used to predict the classifying action of this or indeed any other hydrocyclone. Samples taken from dense slurries are subject to similar uncertainties in particle frequency distribution. It is notable that much published work on hydrocyclone performance tends to gloss over the possible range of errors associated with the consistency of sampling. The confidence limit bands shown in figures 5.24 and 5.25 offer a fuller picture of the possible variations. Figure 5.26 shows that the average grade efficiency curves associated with particle capture of different sizes may actually lie between certain probability limits.

For the low particulate concentrations used in the physical model, the classifying action of the hydrocyclone is generally independent of the particle frequency distribution. This is confirmed by the grade efficiency curves for the two experimental populations figure 5.26, which compare very well, and is further verified by figures 5.24 and 5.25, where the outer confidence limits calculated from ten tests join on to those of the initial samples exactly. Variation in the classifying action would have produced a different band width to that of the original and the two would not have converged on to each other. The annular splitter of the solid core cyclone reduces the likelihood of short circuiting that is common in conventional cyclones, and therefore gives a more consistent classifying action.

The size and behaviour of the second phase are considered comparable with alumina inclusions in molten steel. The results show a 10x improved concentration of particulate on the cyclone core. This physical modelling validation has shown by sampling the lower density phase concentration on the core that the smallest alumina inclusion size that is potentially fully captured by this particular design lies between 70-

115μm. Though the sharpness of cut must also be taken into account, the percentage of particles smaller than this that is lost to the melt is low and comparable to a d_{50} size smaller than 35μm equivalent alumina inclusion diameter. If a core will act as a reliable capture surface, this design will act to clean molten metal. The theoretical results for the transport of Eco-spheres calculated by use of Fluent lies between or close to the calculated extremes of the probability bands from the two measured populations. This result is adequate enough to validate the use of Fluent's mean particle tracking model applied to the performance prediction of low-volume concentration in hydrocyclones. Combined with the previous visualisation study, the Fluent result is validated and this computing approach provides a suitable design tool for the solid core hydrocyclone optimisation study.

The strobe camera proved to be a cheap and effective method of measuring the velocity within the spiralling flow of the solid core annulus and was able to capture the 3-dimensional nature of the flow. This method shows the progression of the fluid stream in the flow region, in contrast to the single point achievable by LDA. In contrast to LDA, the camera could obtain simultaneous velocity measurements in the flow domain if the fluid were seeded with sufficient neutral density particles. The photographic technique provided an accurate account of the flow field, the measured velocities corresponding well with those predicted by the numerical model.

Physical modelling has shown that it is possible to produce a stable swirling flow by displacing the central air core and at the same time removing many of the inherent instabilities associated with the conventional hydrocyclone. The physical model has also shown that it is possible to transport to the central core a lower density second phase with an equivalent free settling velocity to that of alumina inclusions in steel. On reaching the core, the particulates stay in a stable layer on the core surface and are swept down

the core. By separating this core flow it was possible to predict the probable capture efficiency of the solid core cyclone applied to molten steel. The results indicate that the solid core cyclone applied to molten metal has the potential to remove a large proportion of the small alumina inclusions. The next stage is to consider the condition for a trial with molten metal and the development of a suitable refractory design.

5.4 Pilot plant design

The results of the Fluent optimisation study and the initial observations of low density dust migration in the physical model indicated potential for the cyclone method and raised the possibility of pursuing a practical design. The ultimate goal is a reliable technique for inclusion removal from steels, and this required testing under realistic conditions to demonstrate proof of principle.

It was therefore decided to undertake a design exercise for a pilot scale experiment based upon the availability of a 4 tonne supply of liquid steel from an existing pilot operation. It was not feasible at this stage to construct or run a hot pilot trial rig, but the flow performance of the proposed design was tested by a full scale water model of the pilot rig using transparent materials for the cyclone and discharge flow assembly. This enabled flow design modifications to be assessed in readiness for future hot metal experiments.

In this section the general principles and background of the proposed hot trial pilot rig and background of the proposed hot trial rig are set out and discussed. Details of the comparable water model and the experimental findings gained from it are considered and their influence upon the final design of the hot pilot plant model is explained.

5.4.1 Proposed pilot experiment with steel

Design and operating criteria for hot pilot model:

- To validate the solid core cyclone in a hot metal experiment.
- To demonstrate inclusion migration and the capture mechanism on which the study is based.
- To resolve the problems of refractory and mechanical design in a pilot study as a preliminary to application at full-scale.

On the basis of the computational studies and the experimental work to date, a plausible pilot design was developed. This was as close to the physical model as possible and within the limits of the pilot plant. Following design discussions British Steel Technical provided design drawings outlining a possible mechanical structure that was within the limits of the existing pilot plant. In addition some safety restraints were set down which also had to be conformed to. The subject of this investigation was to design the internal dimensions of the flow regions using both computer modelling and a water model mock up to test the principle.

5.4.2 Pilot plant concept

The original approach to the cyclone was based upon a maximum gravity head equal to that of a full ladle. The pilot experiments were designed to use a similar head but with a small pilot scale ladle of 4 tonnes capacity. The necessary head was achieved by attaching the solid core cyclone to a 3m down tube with a pouring trumpet by means of a crown block. The crown block could be made to incorporate more than one cyclone in a

similar way that a ring main is used for multiple hydrocyclone arrangements in the minerals processing industries. This could also provide a possible method for multiple solid core cyclone arrangements. The down tube was to be fed from the 4 ton bottom poured ladle through a stopper nozzle arrangement for flow rate adjustment. The intention was to fill the down tube to a steady height between 2-2.5 metres. The cyclone apex was arranged to run with its apex submerged by 3-4 cm in a weir box similar in design to that of the water model and discharging into a large dump dish. The cyclone and down tube dimensions were chosen to throttle the flow, thereby allowing the constant head required by the cyclone to be maintained in the down tube.

The study of the solid core cyclone so far had been somewhat idealistic. Realistically, modifications had to be made to the liquid metal model with enlarged involute entry to reduce energy loss, refractory wear and freezing up. The flow rate of the steel would still be in the region of 1 ton per minute and should have enough energy to maintain centripetal acceleration within the proposed design range. Two modified designs were proposed the dimensions are given in table 5.3. These two designs were then set up and simulated using Fluent with different inlet conditions and cyclone diameters. The designs were computed for dynamic viscosity $\mu = 5.5 \times 10^{-3}$ Pa·s and density $\rho = 7100$ kg m^{-3}. Working at a lower pressure head of 1.39×10^{5} Pa, equivalent to 2m head of steel, causes a slight decrease in capture cut off size as shown by the corresponding particle escape curve for run1 in figure 5.26. The cone length was increased to compensate by providing a little more residence time. The underflow area was also reduced throttling the flow, for better control and giving an increased residence time.

Two computer runs were made as follows:

Table 5.3

	Cyclone top dia m	Core dia m	Cylindrical length m	Cone angle deg°	Cone length m	Inlet dimensions mm	Inlet type
Run1	0.09	0.045	0.06	3.15	0.49	35x35	1/2 Involute
Run2	0.08	0.035	0.06	3,74	0.49	35x35	1/4 Involute

% of 50μm dia particles captured	Tonnes per min of steel
87.5	1.08
72.5	0.92

Run 1 is the more effective of the two designs, capturing a greater percentage of inclusions. In a conventional hydrocyclone, the sharpness of cut improves with a reduction in inlet size. The large inlet dimensions increase the volume of material passing into the narrower annulus. This produces a higher axial velocity for a similar tangential velocity, thereby reducing the residence time of the inclusions. The dimensions set by run 1 are the most efficient and therefore chosen for the preliminary experiment. A schematic design drawing figure 4.1 shows the parameters that the dimensions in table 5.3 correspond to.

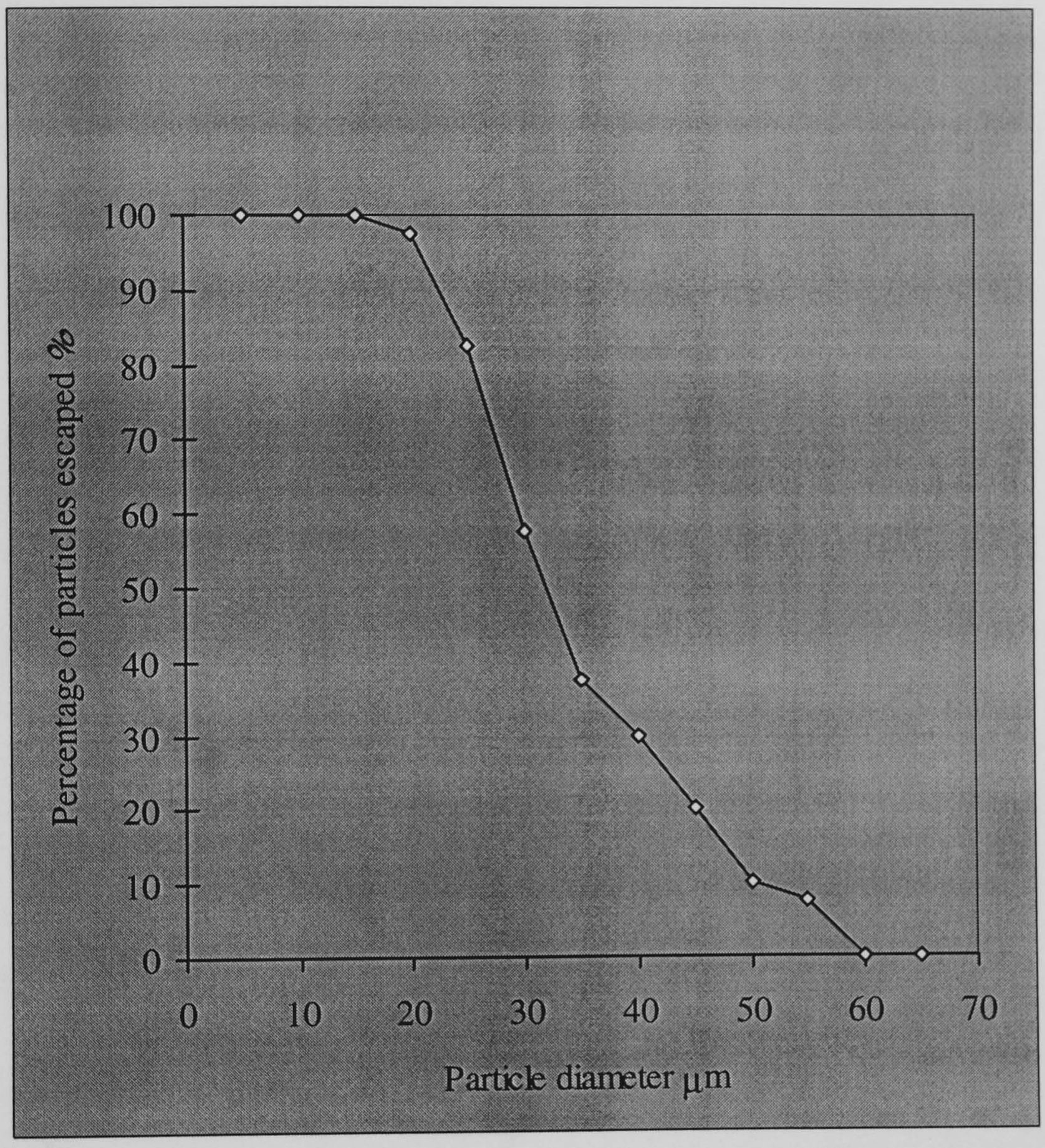

Figure 5.26. Predicted particle escape curve for hot metal experiment cyclone run 1.

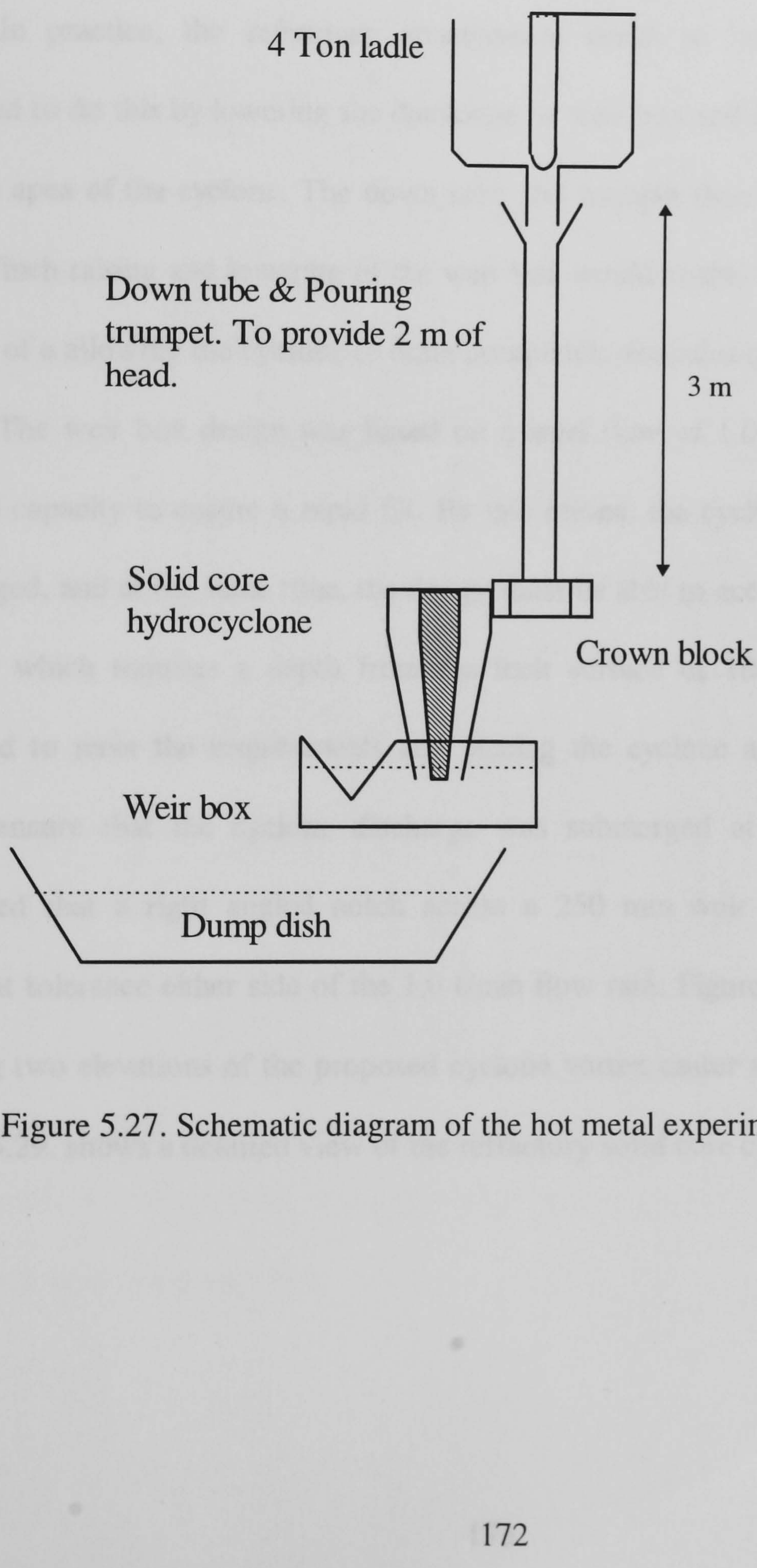

Figure 5.27. Schematic diagram of the hot metal experimental arrangement

5.4.3 Pilot plant operation

The height of the proposed assembly made it unsafe for pouring. It was decided to place the whole arrangement in a pit, taking the trumpet to floor level and thereby making teeming easier and safer. A pit location provides plenty of points to support the structure. In addition, the pit contained a rail carriage that could provide support and mobility to the apparatus. During rig operation there cannot be anyone in the pit, so sampling and adjustments must be made from outside the pit.

In practice, the refractory arrangement needs to be preheated and it was proposed to do this by lowering the discharge or weir box and inserting a pre-heat torch into the apex of the cyclone. The down tube and trumpet then act as a chimney for the heat. Winch raising and lowering of the weir box would enable the box to be lowered at the end of a allowing the cyclone to drain completely for subsequent inspection.

The weir box design was based on a steel flow of 1.0 t/min. It had to have a minimal capacity to ensure a rapid fill. By this means, the cyclone apex will be quickly submerged, and at the same time, the design must be able to accommodate an immersion sampler which requires a depth from the melt surface of 100 mm. A V-notch weir appeared to meet the requirements and placing the cyclone apex at the V tip height would ensure that the cyclone discharge was submerged at any flow rate. It was calculated that a right angled notch across a 250 mm weir would be suitable with sufficient tolerance either side of the 1.0 t/min flow rate. Figure 5.28 is a scale drawing showing two elevations of the proposed cyclone vortex caster and supporting structure.

Figure 5.29. shows a detailed view of the refractory solid core cyclone and weir box

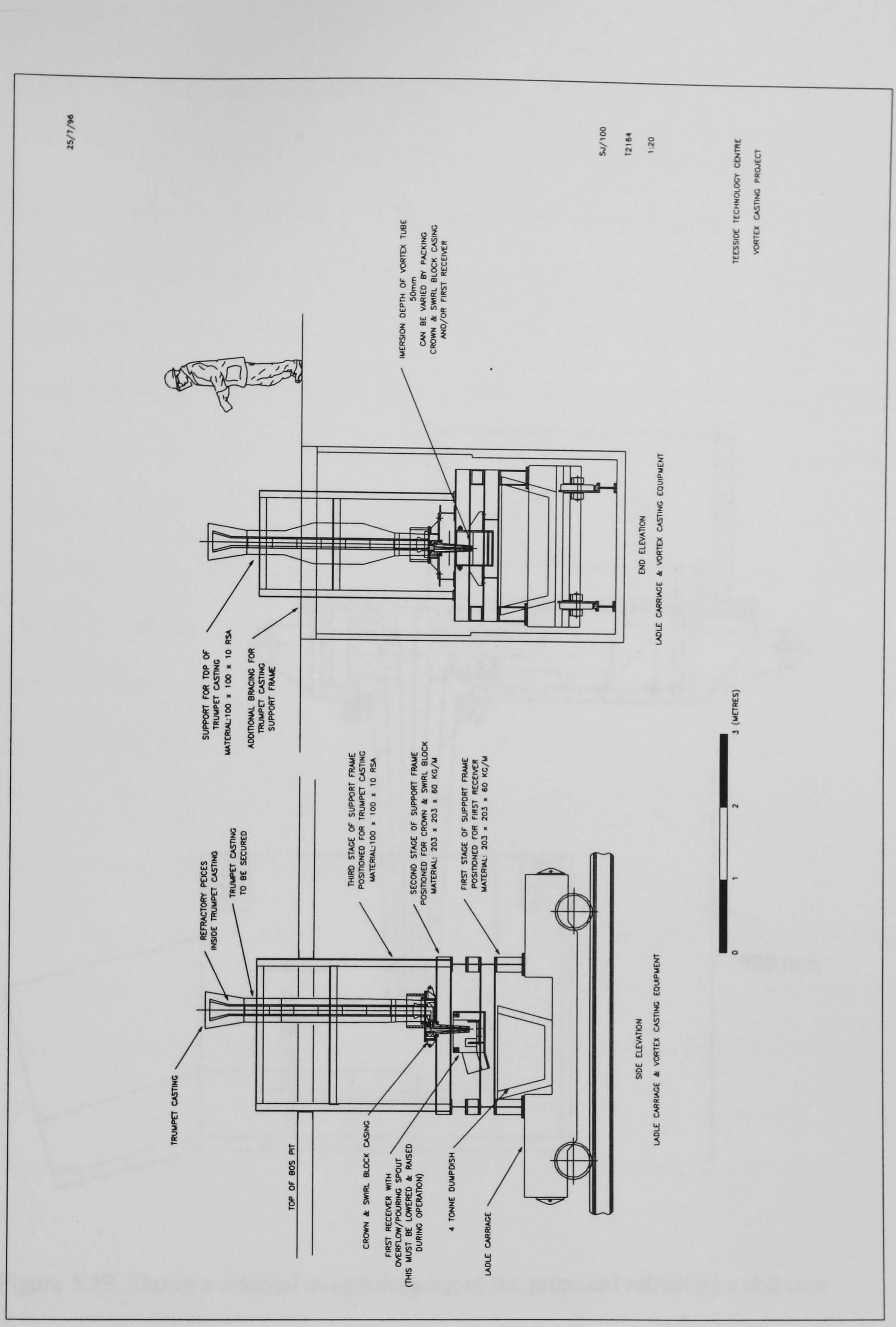

Figure 5.28. A scale drawing showing two elevations of the proposed cyclone vortex caster and supporting structure.

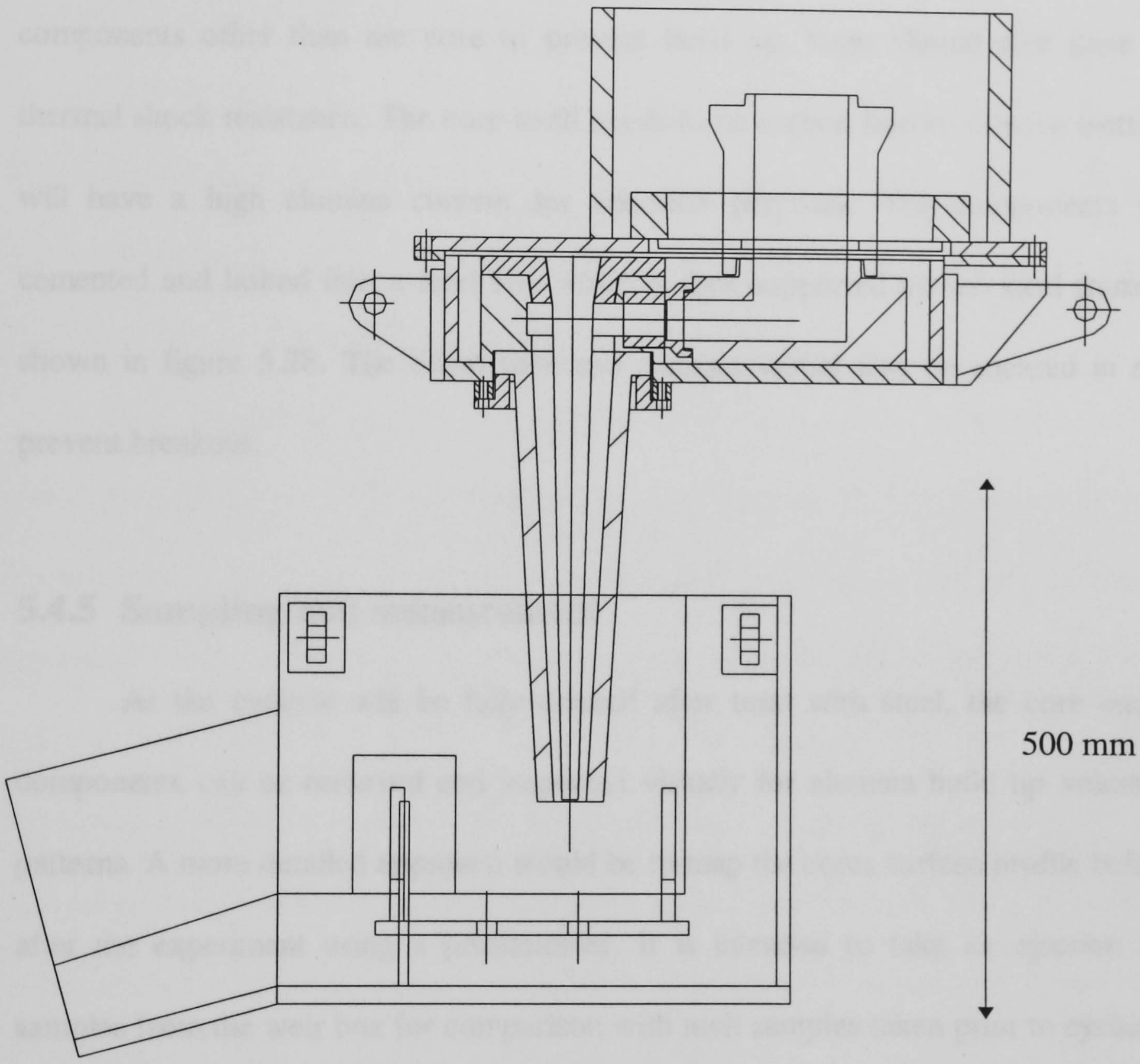

Figure 5.29. Shows a detailed design drawing of the proposed refractory solid core cyclone and weir box.

5.4.4 Materials and construction

The internal dimensions arrived at through the physical and computer modelling described earlier for the solid core hydrocyclone have been transformed into a proposed refractory design. This work is being undertaken by an outside refractory manufacturer in conjunction with the Refractory Division at British Steel Technical. The result will be a manufacturable multi-sectional arrangement. Non-wettable refractories are selected for components other than the core to prevent build up, these should also have a high thermal shock resistance. The core itself needs to be carbon free to achieve wetting and will have a high alumina content for adhesion purposes. The components will be cemented and bolted into a steel box which is then supported on the steel frame work shown in figure 5.28. The down tube and trumpet would also be encased in steel to prevent breakout.

5.4.5 Sampling and measurement

As the cyclone will be fully drained after tests with steel, the core and other components can be removed and inspected visually for alumina build up volumes and patterns. A more detailed approach would be to map the cores surface profile before and after the experiment using a profilometer. It is intended to take air ejection suction samples from the weir box for comparison with melt samples taken prior to cycloning.

5.4.6 Full scale water model of pilot experiment

Prior to finally commissioning the project it was decided to build a full scale replica to test for flow rates, filling times and any unforeseen difficulties. The replica would be run using mains water. A cyclone with the correct internal dimensions was

made from blown glass and wood. A 3 m long drainage pipe was used in place of the down tube and trumpet, with the same internal dimensions as the down tube (diameter 102 mm). The tube and cyclone were then connected using the actual ceramic crown block. A replica weir box with 90° V-notch weir was made from perspex. The weir discharged in to a 1 m^3 tank, providing adequate time for flow and splashing measurements to be made. A 10 mm bore sight tube was fasted to the drain pipe to measure the height of the water as it filled.

In addition to filling time (time to reach steady operating conditions) and flow rate measurement, air entrapment was found to be a problem during filling. Air entrainment and the subsequent scouring of the core by air bubbles in the pilot prototype could result in a failure to capture inclusions at this stage.

The conical section of the cyclone made from blown glass allowed direct observation of any entrained air bubbles that were dragged through. Figure 5.30 shows a photograph of the pre-pilot plant water model It was found that air bubbles were entrained during filling, but on submerging the water supply in the down tube, the cyclone could be made to run bubble free. See figures 5.31 and 5.32 showing photographs of entrained air bubbles on the core during start-up and a successful air free operation. A 2 m constant head of water was maintained at a flow rate 140 l/min which corresponds to the 1 t/min flow rate calculated by Fluent for an equivalent head of steel. A 3m head was also maintained at a flowrate of 210 l/min. Air entrainment during filling was estimated to persist for up to 1 minute, this representing a significant proportion of the pilot plant teeming period.

Various techniques were considered in order to minimise or eliminate air entrainment, based upon the remedy tested on the water model of initially closing the cyclone discharge to allow trumpet and down tube to fill and then releasing the flow. A

method based on blocking by fusible plates which had been used previously with down tubes in other applications was not practical here because of the necessity for pre-heat. It was finally decided that the weir box should be winched up to provide an initial seal using a ceramic fibre mat placed in the base and subsequently lowered when the down tube was full.

The water trial revealed a high level of turbulence in the weir box which could have been reduced by discharging into a larger vessel. By inserting fins into the weir box, it was possible to smooth the flow sufficiently to enable suction samples to be taken. A turbulent liquid steel flow could cause the melt to oxidise excessively giving poor sample quality. It may therefore be necessary in the prototype pilot study to shroud the weir box in argon to prevent oxidation taking place and to enable clean samples to be taken.

The pilot plant model will hopefully demonstrate the principles of the solid core cyclone idea and give further insight in order that a fully optimised design can be produced.

Figure 5.30. Pre-pilot plant water model set-up to test the operational reality of the rig design.

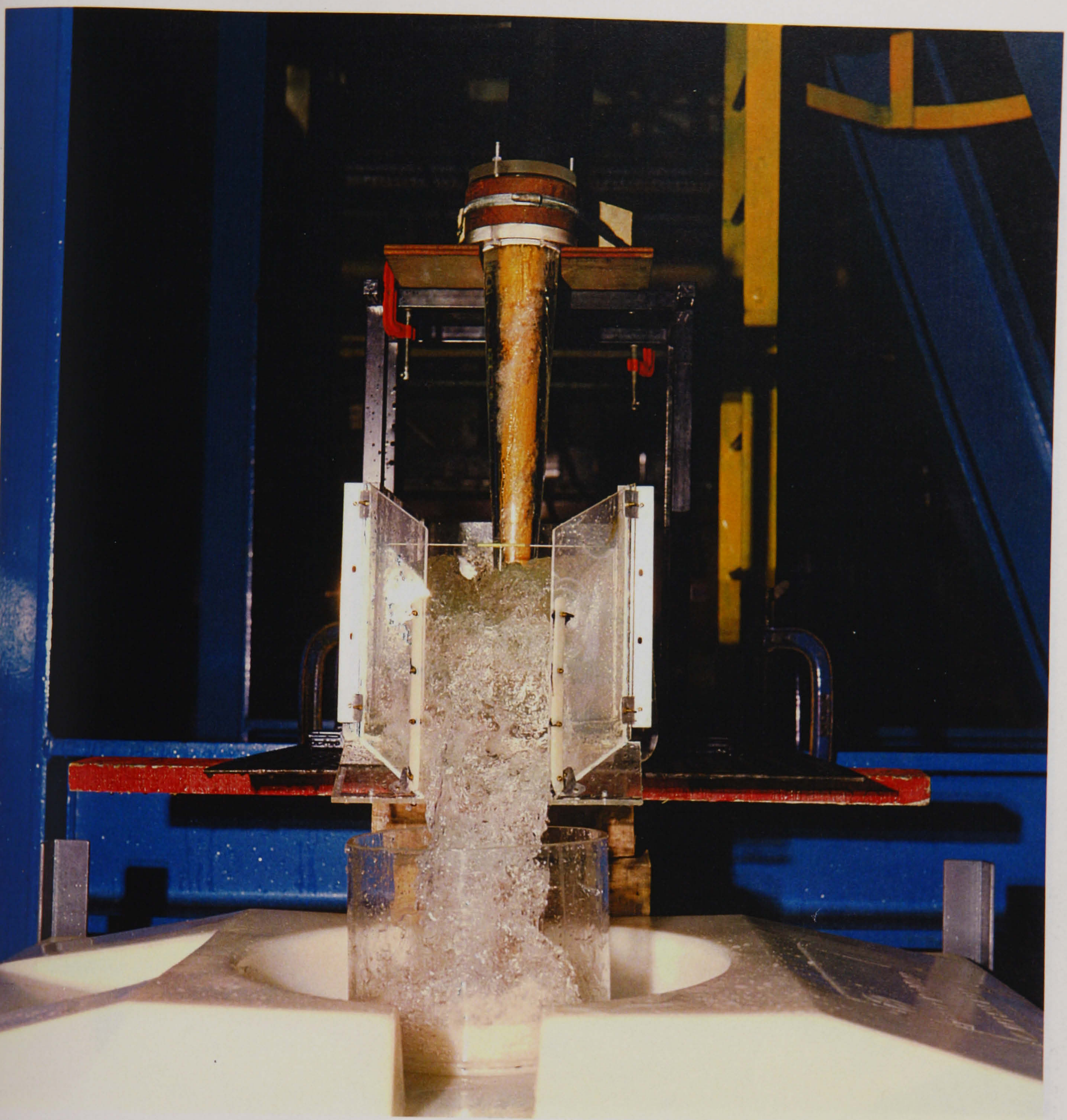

Figure 5.31. Photograph of the pre-pilot plant water model showing the unacceptable scouring of the core by air entrained during start-up.

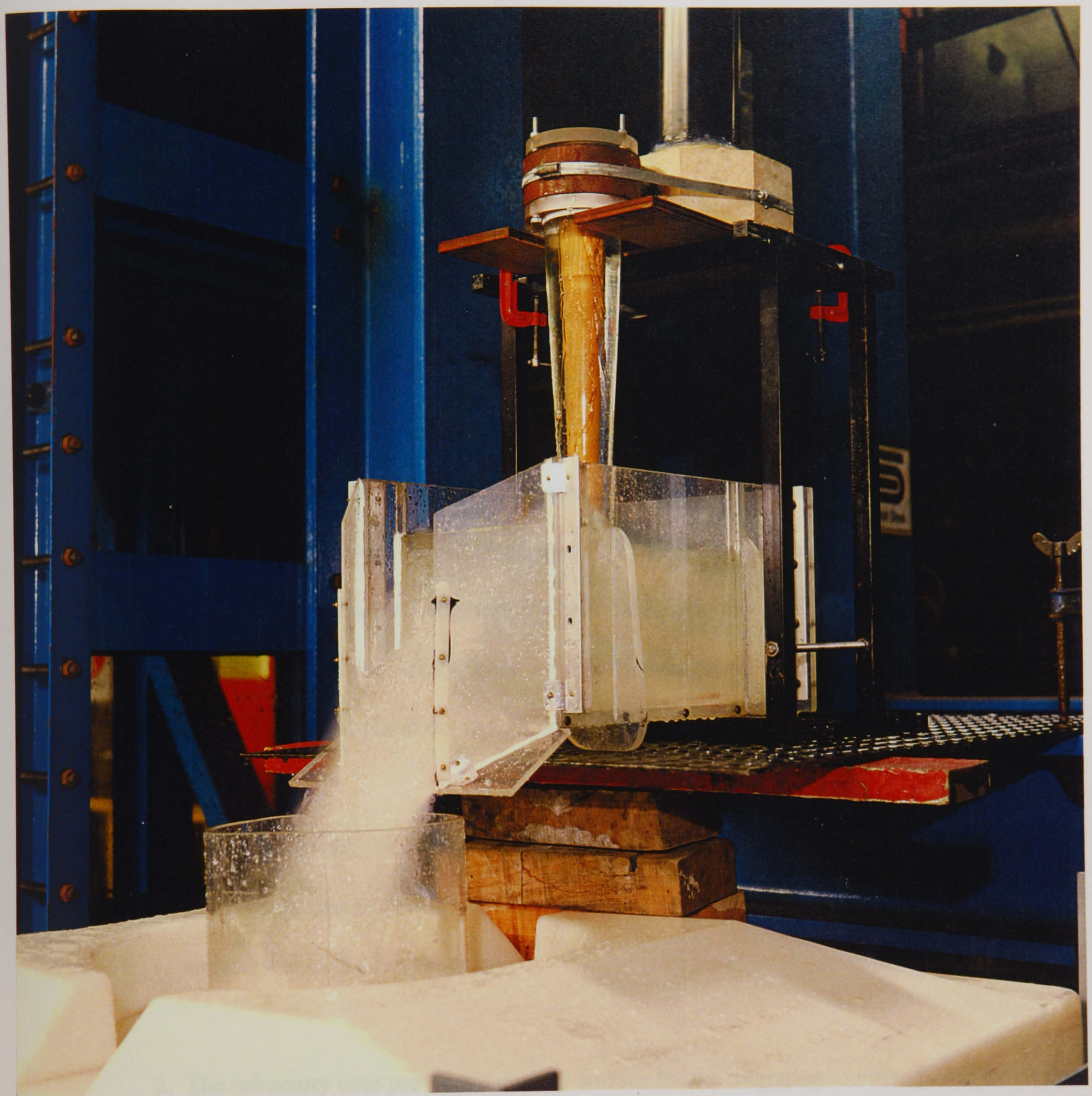

Figure 5.32. Pre-pilot water model showing successful air free operation at the specified driving head.

Chapter VI

Conclusions

A feasibility study into the removal of alumina inclusions from liquid steel based on the induced swirling flow in a cyclone has been carried out. The "clean sheet" development approach yielded a new type of hydrocyclone design. The work has examined the theoretical and physical modelling treatments that may be applied to annular confined swirling liquid flows and has accounted for their limitations and levels of success.

The new cyclone design rotates liquid steel within the confined boundaries of a tapered cylindrical annulus. A radial acceleration is imposed on the alumina inclusions due to the density difference between the solid inclusions and the liquid phase causing migration to the central sticky axial refractory solid core. The conical solid core extending along the length of the new hydrocyclone provides three main actions:

1. It displaces any air-core that may be entrained due to the radial pressure distribution that occurs in swirling flows. The pressure at the core surface should exceed that of the surroundings.

2. The refractory core provides a capture surface for the migrating alumina particles.

3. Its convex surface provides a constant stabilising effect on the swirling flow and reduces the level of turbulence.

This new hydrocyclone design is adaptable and has been shown by theoretical and physical modelling to be a potentially viable method of removing oversized alumina inclusions from liquid steel. However the (efficiency) performance that can be achieved is dependent on the dimensions and the flow rate per cyclone unit that is required and the flow conditions that can be achieved.

6.1. Theoretical modelling

The swirling flow created in a hydrocyclone is essentially very complex and therefore difficult to describe. Different theoretical modelling approaches were shown to have different levels of success. The empirical models used by early workers to characterise the velocity profiles in the conventional hydrocyclone were considered unsuitable in the light of modern analytical and numerical methods that are now available.

6.1.1 The inviscid model

An inviscid model was developed which proved successful in describing the complicated flow patterns that exist in the main flow of a conventional hydrocyclone and adequately represented the high curvature streamlines. The location of toroidal circulations can be identified but the modelling assumptions for inviscid flow mean that they can not be solved. The inviscid model represents the flow as a free vortex neglecting viscous effects near the central axis. Given these limitations it still provides a good representation of how the main flow field may change throughout the section for the imposed entry conditions and gives a good dimensionless comparison with published data for a conventional hydrocyclone.

6.1.2 Viscous models

A complicated annular vortex flow has been found in which there are both stabilising and destabilising surfaces of curvature. In a computational study using the CFD package Fluent to simulate this turbulent flow field, it was assumed that the small volume of the particulate phase had a negligible effect on the flow. Computer simulations using each of the three turbulence models available to Fluent, i.e. the k-e, renormalisation group and Reynolds stress models, have been compared with experimental results. Due to the anisotropic turbulent nature of the flow, the lower-order turbulence models were found to under predict the velocity profiles. A good comparison to measured velocity values was obtained using Fluent's higher-order Reynolds Stress turbulence model.

Fluent enabled the cyclone to be modelled in 3-Dimensions, increasing the number of variables influencing performance that could be considered in the optimisation study. The large number of conflicting dimensional considerations make the design of hydrocyclones difficult to optimise. Design and test computational studies predicted the removal of all particles larger in size than 45 μm and a high proportion of those between 25 and 40 μm for a solid core cyclone of 60 mm top diameter. The size of the cyclone matters when its application is considered even though the dimensions may not correspond to the best classifying action that can be achieved. In the initial feasibility study a compromise was made between classification efficiency and the practical throughput. The cyclone dimensions that were chosen for further investigated had a top diameter of 90 mm and corresponded to a flow rate of 1.0 ton per minute.

6.2 Physical modelling

6.2.1 velocity profiles

The strobe camera produced a scatter of velocity measurements throughout a section of the annular flow section, from this data velocity profiles were obtained. The measured velocity profiles in the annular gap in the water model matched those predicted by Fluent's Reynolds stress turbulence model. The swirling liquid behaved as a forced vortex adjacent to the core and it can therefore be concluded that the computer model based upon the RSM adequately predicts the behaviour of the fluid in the swirling annulus and thereby successfully represents the anisotropic turbulence. The predicted change from free to forced vortex flow across the annulus can be seen in the measured profiles. This consequently indicates a reduction in shearing towards the core which is favourable for alumina to stick to the core.

6.2.2 Particle migration

The low-density phase migration experiment showed that particles of equivalent Stokes velocity introduced inorder to represent alumina inclusions would migrate to the core. In experiments to measure capture efficiency these travelled down the core surface and were then stripped from it by an annular splitter at the cyclone apex. The results of CFD particle classification lay within the measured 95% confidence limits of the low-density water model, thus indicating that the solid-core cyclone design developed by use of the CFD technique would cause bulk migrations of even the smallest particle sizes to the core. Assuming that the underlying assumptions of inclussion capture on the core are correct, this initial trial design promises to clean liquid steel to a much higher degree than the existing high volume process routes.

6.3 Suggestions for further work

The principle still needs to be tested in pilot scale trials. The outcome of trials will then dictate the direction of any plant design. The current pilot plant design could feasibly be adapted for billet casting in which the down tube arrangement is used to provide a gravity head for uphill teeming. It would be necessary to examine the use of multiple cyclone units for larger scale operations to increase the throughput while maintaining the classifying action of the smaller diameter cyclone. The pilot- experiment would provide a comparison of the build-up on the core with that predicted by the model.

The study has shown that the position of particles in the inlet flow affects their chance of capture. This merits further investigation of top or inlet to improve the separation process in both the conventional and the new solid-core hydrocyclone. Published experiments on an inclined roof hydrocyclone show an improved separation efficiency in conventional gas cyclones separating a denser medium, where it appears that the flow is deflected downward to stop it recombining with the inlet flow, and thereby reducing what may be the main cause of short circuiting in the hydrocyclone. A reverse approach could be used to increase the chance of central migration in the separation of low density particles.

The use of an annular splitter to sample the flow layer at the core in the low-density phase experiments presents a potential new type of hydrocyclone classifier with many advantages in design over a conventional design of hydrocyclone separator. The core design can be modified to affect the flow profile and the flow is stabilised to a greater extent by the solid core surface than is possible with fluctuating air-core. This

type of cyclone may reduce the damaging effect of short circuiting flows associated with conventional hydrocyclones. Unidirectional discharges gives more residence time to find a radial equilibrium position before separation takes place at the apex. This may justify further design studies and an investigation of possible applications.

References

A1 Adrian, R. J., 1991, *Particle-imaging techniques for experimental fluid mechanics*, Annu. Rev. Fluid Mech., vol. 23, pp. 261-304.

A2 Arterburn, R. A., *The sizing and selection of hydrocyclones*, Krebs-Manual, California.

A3 Avérous, J., 1996, *Introduction to Direct numerical resolution in fluid dynamics and heat transfer*, CIMM. Santiago.

B1 Bahu, R. E., 1994, *Cyclone modelling*, Chem. Eng. Progress, no. 7, pp. 8-9.

B2 Batchelor, G. K., 1967, *An introduction to fluid dynamics*, Cambridge University Press, pp. 543-547.

B3 Bloor, M. I. G. and Ingham, D. B., 1973, *Theoretical investigation of the flow in a conical hydrocyclone*, Trans. Inst. Chem. Engrs, vol. 51, pp. 36-40.

B4 Bloor, M. I. G. and Ingham, D. B., 1975, *The leakage effect in the industrial cyclone*, Trans. Inst. Chem. Engrs, vol. 53, pp. 7-11.

B5 Bloor, M. I. G. and Ingham, D. B., 1987, *The flow in industrial cyclones*, J. Fluid Mech., vol. 178 pp. 507-519.

B6 Boussinesq, J., 1877, *Theorie de l écoulements tourbillonoures*, Mem. Pre. Par. Div. Sav., Paris, t-23.

B7 Bradley, D. and Pulling, D. J., 1967, *Flow patterns in the hydraulic cyclone and their interpretation in terms of performance*, Trans. Inst. Chem. Eng., vol. 37, pp. 34-45.

B8 Bradley, D., 1965, *The Hydrocyclone*, Pergamon Press, London.

B9 Bradshaw, P., Launder, B. E., and Lumley, L., 1991, *Collaborative testing of turbulence models*, J. Fluids Eng., vol. 113, p 3-4.

B10 Brayshaw, M. D., 1990, *A numerical model for the inviscid flow of a fluid in a hydrocyclone*, Int. J. Min. Proc., vol. 29, pp. 51-75.

B11 Burry, D. and Bergeles, G., 1993, *Dispersion of particles in anisotropic turbulent flows*, Int. J. Multiphase Flow, vol. 19, pp. 651-664.

C1 Chang, F. and Dhir, V. K., 1994, *Turbulent flow field in tangentially injected swirl flows in tubes*, Int. J. Heat and Fluid Flow, vol. 15, p 346-356.

C2 Chu, L. Y. and Luo, Q., 1994, *Hydrocyclone with high sharpness of separation*, Filtration and Separation, pp. 733-736.

C3 Cristinacce, M., 1992, *Developments in the production of enginnering steels*, Materials and Design, vol. 13, no. 1, pp. 33-41.

D1 Dabir, B. and Petty, C. A., 1986, *Measurements of mean velocity profiles in a hydrocyclone using laser doppler anemometry*, Chem. Eng. Commun., vol. 48, pp. 377-388.

D2 Das, A., Kinneberg, D. J., Chakraborti, N. and Miller, J. D., 1993, *Fluid motion in air sparged hydrocyclone*, Scan. J. Metall, vol. 22, pp. 254-259.

D3 Davidson, M. R., 1988, *Numerical calculations of flow in a hydrocyclone operating without an air core*, Appl. Math. Modelling, vol. 12, pp. 119-128.

D4 Davidson, M. R., 1988, *Similarity solutions for flow in Hydrocyclones*, Chem. Eng. Sci., vol. 43, no. 7, pp. 1499-1505.

D5 Doheim, M. A., Ahmed, M. N. M. and Sayed, S. A., 1995, *Hydrocyclone investigation and modelling at medium feed solids concentration of mixed minerals*, Trans. Inst. Min. Metall, vol. 104, p 37-44.

D6 Douglas, J. F. Gasiorek, J. M. and Swaffield, J. A., 1995, *Fluid Mechanics*, Wiley, London.

D7 Driessen, M. G., 1946, *The use of hydraulic cyclones as thickeners and washers in modern coal preparation*, Trans. Am. Inst. Min., vol. 177, pp. 240-261.

D8 Dyakowski, T. and Williams, R. A., 1993, *Modelling turbulent flow within a small diameter hydrocyclone*, Chem. Engng. Sci., vol. 48, pp.1143-1152.

F1 Fluent V 4.2.2, *Manual*, Fluent Europe Ltd, Sheffield.

F2 Fontein, F. J., 1961, *Separation in cyclone according to specific gravity*, Cyclones in Industry, Elsevier, ch. 10.

G1 Gibson, M. M., Jones, W. P. and Younis, B. A., 1981, *Calculation of turbulent boundary layers on curved surfaces*. Phys. Fluids, vol. 24, no. 3, pp. 386-395

G2 Gibson, M. M. and Rodi, W., 1981, *A Reynolds-stress closure model of turbulence applied to the calculation of a highly curved mixing layer*, J. Fluid Mech., vol. 103, pp. 161-182.

G3 Gladman, T., Holmes, B. and Melvor, I. D., 1971, *Effect of secondary phase particles on the mechanical properties of steel*, Production and application of clean steel, The Iron and Steel Institute, pp. 68-78.

G4 Guthrie, R. I. L.,1989, *Engineering in process metallurgy*, Oxford University Press.

H1 Hahn, B. D., 1991, *Turbo Pascal 5.5/6.0 for engineers*, NCC Blackwell.

H2 Hargreaves, J. H. and Silvester, R. S., 1990, *CFD analysis of deoiling hydrocyclone performance*, Trans. Inst. Chem. Eng., vol. 68, pp. 365-385.

H3 Hoffmann, P. H., Muck, K. C. and Bradshaw, pp., 1985, *The effect of concave surface curvature on turbulent boundary layers*, J. Fluid Mech., vol. 161, pp. 371-403.

H4 Horbach, U., Rodl, S., Abratis, H. and Hofer, F., 1995, *Flow studies on controlled tundish nozzles to prevent clogging*, Stahl und Eisen, vol. 115, pp. 71-76.

H5 Hsieh, K. T. and Rajamani, R. K., 1991, *Mathematical model of a hydrocyclone based on the physics of fluid flow*, AICHE Journal, vol. 37, pp. 735-746.

H6 Huser, A. and Biringen, S., 1993, *Direct numerical simulation of turbulent flow in a square duct*, J. Fluid Mech., vol. 257, pp. 65-95.

H7 Hutchings, B. and Iannuzzelli, R., 1987, *Benchmark problems for fluid dynamics codes*, J. Mech. Eng., vol. 106, no. 6, pp. 54-58.

H8 Hwang, C. C., Shen, H. Q., Zhu, G. and Khonsari, M. M., 1993, *On the main flow pattern in hydrocyclones*, J. Fluid Eng., vol. 115, pp. 21-25.

I8 Iida, T. and Guthrie, R. I. L., *1993,The physical properties of liquid metals*, Oxford University Press.

I9 Irani, R. I .and Callis, C. F., 1963, *Particle size: Measurement, interpretation and application*, Wiley, London.

J1 Joo, S. Han, J. W. and Guthrie, R. I. L., 1993, *Inclusion behaviour and heat transfer phenomena in steelmaking tundish operations, part 3, Applications, Computational approach to tundish design*, Metall. trans. B, vol 24, no. 5, pp. 779-778.

K1 Karanfilian, S. K. and Kotas, T. J., 1981, *Motion of a spherical particle in a liquid rotating as a solid body*, Proc. R. Soc. London, vol. 376, pp. 525-544.

K2 Kelsall, D. F., 1952, *A study of the motion of solid particles in a hydraulic cyclone*, Trans. Inst. Chem. Engrs., vol. 30, pp. 87-108.

K3 Kiessling. R. and Nerdberg, H., 1972, *Influence of inclussions on mechanical properties of steel*, Production and application of clean steel. The Iron and Steel Institute London, pp. 179-185.

K4 Kiessling, R., 1980, *Clean steel*, Metal Science.

K5 Knowles, S. R., Donald, R. W., and Feuerstein, I. A., 1973, The *velocity distribution within a hydrocyclone operating without an air core*, Can. J. Chem. Eng., vol. 51, pp. 263-271.

K6 Knowlton, 1994, *The importance of storage, transfer and collection*, Chem. Eng. Prog., April, pp. 44-45

K7 Knüpple, H., Brotzmann, K. und Förster, N. W., 1965, *Untesuchungen über oxydische verumreinigungen in aliminium berhigten, weichen stählen*, Stahl und Eisen, vol. 85, nos. 11, pp. 675-688.

K8 Kolmogrov, A. N., 1962, *A refinement of the previous hypothesis concerning the local structure of turbulence in a viscous incompressible fluid at high Reynolds numbers*, J. Fluid Mech., vol. 13, pp. 82.

K9 Kozakevitch, P. and Olette, M., 1972, *Role of surface phenomena in the mechanism of removal of solid inclusions*, Production and application of clean steel, The Iron and Steel Institute London. pp. 42-49.

K10 Kreysig, E., 1967, *Advanced engineering mathematics*, Wiley, London.

L1 Lackner, A., Paschen, P., Tatschl, R. and Pachler, K., 1995, *Numerical simulation of fluid flow in a smelting cyclone reactor*, Pyrometallurgy 95, pp. 335-346.

L2 Launder, B. E., Tselepidakis, D. P. and Younis, B. A., 1987, *A second moment closure study of rotating channel flow*, J. Fluid Mech., vol. 183, pp. 63-75.

L3 Leschziner, M. A., 1990, *Modelling engineering flows with Reynolds-stress turbulence closure*, J. Wind Eng. and Indust. Aero., vol. 35, nos. 1-3, pp. 21-47.

M1 McCoumb, W. D., 1990, *The physics of fluid turbulence*, Oxford University Press.

M2 Much, K. C., Hoffmann, P. H. and Bradshaw, P., 1985, *The effects of convex surface curvature on turbulent boundary layers*, J. Fluid Mech., vol. 161, pp. 347-369.

M3 Monredon, T. C., Hsieh, K. T. and Rajamani, R. K., 1992, *Fluid flow model of the hydrocyclone: An investigation of device dimensions*, Int. J. Min. Proc., vol. 35, pp. 65-85.

N1 Nicholson, A. and Gladman, T., 1986, *Non-metalic inclusions and developments in secondary steel making, Iron and Steel making*, vol. 13, no. 2, pp. 53-69.

N2 Nishino, K., Kasagi, N., and Hirato, M., 1989, *Three-dimensional particle tracking velocimetry based on automated digital image processing*, Trans. ASME. J. of Fluids Eng., vol. 111, pp. 384-391.

P1 Pericleous, K. A., Rhodes, N. and cuttling, G. W., 1984, *A mathematical model for predicting the flow in a hydrocyclone classifier,* Proceeding's of the Second International Conference on Hydrocyclones, Bath, United Kingdom, pp. 27-40.

P2 Pericleous, K. A. and Rhodes, N., 1986, *The hydrocyclone classifier - a numerical approach*, Int. J. Miner. Process., no. 17, pp. 23-43.

P3 Popham, A. E., 1972, *The drawings of Leonardo da Vinci*, Lowe & Brydone, London.

P4 Prandtl, L., 1925, *Bericht über untersuchungen zur ausgebildeten turbulenz*, Math und Mech., pp. 136-139.

P5 Prandtl, L., 1945, Uber ein neues Formelsystem fur die ausgebildete turbulenz, Nachrichten von der Akad., der Wissenshaft in Gottingen.

R1 Rajamani, R. K. and Devulapalli, B., 1994, *Hydrodynamic modelling of swirling flows and particle classification in large scale hydrocyclones*, KONA Powder and particle, pp. 95-100.

R2 Rajamani, R. K. and Milin, L., 1992, *Fluid flow model of the hydrocyclone for concentrated slurry classification*, Hydrocyclones: Analysis and Application: 4th Int. Conference, vol. 12, pp. 95-108.

R3 Reitema, K., 1961, *Performance & design of hydrocyclones i-iv*, Chem. Engng. Sci., vol. 15 pp. 298-325.

R4 Roldanvillasana and Dyakowski, E. J., 1993, *Design and modelling of hydrocyclones*, Minerals Eng., vol. 6, pp. 41-54.

S1 Sharif, M. A. R. and Wong, Y. K. E., 1995, *Evaluation of the performance of stress turbulence closure models in the prediction of confined swirling flows*, Computers and Fluids, vol. 24, pp.81-100.

S2 Slack, M. D. and Wraith, A. E. 1995, *Rotating field modelling for melt cleaning*, Proc. Second international Symposium on quality in non-ferrous pyrometallurgy, Vancouver August 1995. pp. 227-238.

S3 Smith, G. D., 1978, *Numerical solutions of partial differential equations, Finite Difference Methods*. Oxford University Press.

S4 Spezial, C. G., 1987, *On non-linear k-l and kε models of turbulence,* J. Fluid Mech., vol. 178, pp. 459-474.

S5 Sumner, R. J., Briens, C. L., and Bergougnou. M. A., 1987, *Study of a novel uniflow cyclone design*, Can. J. Chem. Eng., vol. 65, pp.470-475.

S6 Svarovsky, L., 1977, *Errors in measurement of efficiency of particle-fluid separators*, Powder Technology, vol. 17, pp. 139-143.

S7 Svarovsky, L., 1984, *Hydrocyclones*, Holt Rinehart and Winston, London.

S8 Szerkely, J., 1979, *Fluid flow phenomena in metals processing*, Academic Press, London.

T1 Tennekes, H. and Lumley, J.L., 1972, *A first course in turbulence*, MIT Press, London.

T2 Topping, J., 1962, *Errors of observation and their treatment*, Chapman and Hall, London.

T3 Treadgold, C.1996, Personal communication regarding wax particle modelling.

T4 Tritton, D. J., 1994, *Physical fluid dynamics*, Oxford University Press.

V1 Vetterling, W. T., 1985, *Numerical recipes in Pascal*, Cambridge University Press.

V2 Vallentine, H. R., 1959, *Applied Hydrodynamics*, Butterworths, London.

W1 Wieser, P. F., 1983, *Filtration of liquid steel*, TMS. AIME., F84-4.

W2 Williams, R. A., Dickin, F. J., Guiterrez, A., Beck, M. S., Wang, M., Ilyans. M. and Dyakowski, T., 1995, Monitoring cyclone performance using resistance tomography, Frontiers in Industrial Process Tomography, Engineering foundation, New York, pp. 261-274.

W3 Wills, B. A., 1981, *Minerals processing technology*, Pergamon Press Oxford 2nd edition.

W4 Wilson, F. G., Heeson, M. J., Nicholson, A. and Hills, A. W. D., 1987, *Effect of fluid flow characteristics on nozzle blockage in aluminium-killed steels*, Iron and Steelmaking, vol. 14, pp. 296-309.

W5 Wilson, I. R. and Addyman, A. M., 1987, *A practical introduction to Pascal - with BS 6192*, Macmillan education ltd, London.

Y1 Younis, B. A., 1995, *Models of turbulence*, An introduction to fluid dynamics, EPSRC Lecture course, Rutherford Appleton Laboratories. Ch. 10.

Y2 Yuu, S., Yasukouchi, N., Hirosawa, Y. and Jotaki, 1987, *Particle turbulent diffusion in a dust laden round jet*, AIChE., vol. 24, pp. 509-519.

Appendix I

Navier-Stokes Equations

Continuity Equation

$$\frac{\partial \rho}{\partial t}+\frac{\partial \rho v_x}{\partial x}+\frac{\partial \rho v_y}{\partial y}+\frac{\partial \rho v_z}{\partial z}=0$$

Momentum Equations

$$\frac{\partial \rho v_i}{\partial t}+v_i\frac{\partial \rho v_i}{\partial x_i}+v_j\frac{\partial \rho v_i}{\partial x_j}+v_k\frac{\partial \rho v_i}{\partial x_k}=-\frac{\partial p}{\partial x_i}+\left(\frac{\partial \tau_{ii}}{\partial x_i}+\frac{\partial \tau_{ji}}{\partial x_j}+\frac{\partial \tau_{ki}}{\partial x_k}\right)+\rho F_i$$

Energy Equation

$$\begin{aligned}\frac{\partial \rho h}{\partial t}+\frac{\partial \rho v_x h}{\partial x}+\frac{\partial \rho v_y h}{\partial y}+\frac{\partial \rho v_z h}{\partial z}=&\frac{\partial p}{\partial t}+v_x\frac{\partial p}{\partial x}+v_y\frac{\partial p}{\partial y}+v_z\frac{\partial p}{\partial z}\\&+\tau_{xx}\frac{\partial v_x}{\partial x}+\tau_{xy}\frac{\partial v_x}{\partial y}+\tau_{xz}\frac{\partial v_x}{\partial x}\\&+\tau_{yx}\frac{\partial v_y}{\partial x}+\tau_{yy}\frac{\partial v_y}{\partial y}+\tau_{yz}\frac{\partial v_y}{\partial z}\\&+\tau_{zx}\frac{\partial v_z}{\partial x}+\tau_{zy}\frac{\partial v_z}{\partial y}+\tau_{zz}\frac{\partial v_z}{\partial z}\\&+\frac{\partial}{\partial x}k\frac{\partial T}{\partial x}+\frac{\partial}{\partial y}k\frac{\partial T}{\partial y}+\frac{\partial}{\partial z}k\frac{\partial T}{\partial z}+q\end{aligned}$$

Equation of State

$$p=\rho RT$$

Constitutive Equations for a Newtonian Fluid †

$$\tau_{ii}=\lambda\left(\frac{\partial v_i}{\partial x_i}+\frac{\partial v_j}{\partial x_j}+\frac{\partial v_k}{\partial x_z}\right)+2\mu\frac{\partial v_i}{\partial x_i}$$

$$\tau_{ij}=\tau_{ji}=\mu\left(\frac{\partial v_j}{\partial x_i}+\frac{\partial v_i}{\partial x_j}\right)$$

$$\lambda=-\tfrac{2}{3}\mu \quad \ddagger$$

When both density and viscosity are constant, then the continuity equation and momentum equations (or Navier-Stokes equation) become respectively,

$$\nabla.v=0$$

and

$$\rho\frac{Dv}{Dt}=\mu\nabla^2 v-\nabla p+\rho F.$$

† For a newtonian fluid μ is observed to be independent of the rate of strain and λ is assumed to be also. In addition for a fluid of constant density ρ the continuity equation causes the term λ to drop out.

‡ This relationship is made at the cost of redefining the pressure so that it is no longer the thermodynamic pressure.

Appendix II

Inviscid 2-dimensional axisymmetric swirling flow model.

Numerical model code applied to a conventional hydrocyclone.

```
PROGRAM      HYDROCYCLONE;      {spherical co-ordinate system}
{$N+}
{$R+}

USES crt;
                {all dimensions in m}
CONST
        jmax = 30; imax = 30; thetamax = 5.7; rat = 4.0;
        U = 0.722376; V = 1.3228; holesize = 3; a = 6; cone = 0.3801;
        cyl = 0.05092; vl = 0.0304;

TYPE
        selection =
                record
                q,v    :real;
                ghost :boolean;
                end;

   grid = ARRAY [0..imax,0..jmax] OF selection;

VAR
        psi             :grid;
        i, j, iomin     :integer;
        outfile         :text;
        h, R, l, theta  :real;
        name            :string;
```

```
PROCEDURE  (Sor  var theta, R: real);

CONST
        maxits = 1000;
        eps    = 1.0e-5;

VAR
        n                                       : integer;
        resid, omega, diag, anorm, rad          : real;
        finished                                : boolean;
        Q, p, Omin, gap, x, O, z, d, total,  amin, amax  : real;


BEGIN

        p := 0.0;
        anorm := 0.0;
        clrscr;

        theta := (thetamax*(pi/180))/jmax;

        R := cone * sin( theta*jmax ) / cos ( theta * jmax );
        total := cone + cyl;
        l := R/sin(theta*jmax);
        h := total/imax;
        d := total*sin(a*theta)/cos(a*theta);
```

```
gap := sqrt(sqr(total - vl) + sqr(d));

Q := pi*U*(sqr(R)-sqr(d));

FOR j := 0 TO jmax DO BEGIN
        FOR i := 0 TO imax DO BEGIN
        psi[i,j].v     := 0.0;
        psi[i,j].q     := 0.0;
        psi[i,j].ghost := false;
        END;
END;

FOR j := 0 TO jmax DO BEGIN
psi[holesize,j].v := p + Q/(2*pi*(1+rat)) - ((Q/(2*pi*(1+rat))/ jmax)*j);
psi[holesize,j].ghost := false;
END;

FOR i := holesize TO imax DO BEGIN
psi[i,0] := psi[holesize,0];
psi[i,0].ghost := false;
END;

x := R/(imax*h);
Omin  := 1/theta*( arctan(x/sqrt(1-sqr(x))));
iOmin := trunc(Omin);

x := d/(imax*h);
amin := a {1/theta*( arctan(x/sqrt(1-sqr(x))))};

x := d/gap;
amax := 1/theta*( arctan(x/sqrt(1-sqr(x))));

FOR j := iomin DOWNTO 1 DO BEGIN
        IF j >= a
        THEN psi[imax,j].v := p + 0.5*( sqr(sin(iOmin*theta))-
        sqr(sin(j*theta)))*sqr(imax*h)*U;
        psi[imax,j].ghost := false;
         IF j < a
        THEN psi[imax,j].v := (((psi[imax,a].v - psi[imax,0].v)/a) *
        j)+psi[imax,0].v;
        psi[imax,j].ghost := false;

END;

FOR  i := trunc(l/h)+1 TO imax-1 DO BEGIN
x := R/(i*h);
O := 1/theta*(arctan(x/sqrt(1-sqr(x))));
j := trunc(O);
psi[i,j+1].ghost := true;
psi[i,j+1].q := O - j;
psi[i,j+1].v := psi[imax,iOmin].v;

END;


FOR  i := trunc(gap/h)+1 TO imax-1 DO BEGIN
x := d/(i*h);
z := 1/theta*(arctan(x/sqrt(1-sqr(x))));
j := trunc(z);
psi[i,j+1].ghost := true;
psi[i,j+1].q := z - j;
psi[i,j+1].v := psi[imax,a].v;

END;

FOR i := holesize+1 TO trunc(l/h)+1 DO BEGIN
psi[i,jmax].ghost := false;
psi[i,jmax].v := psi[imax,iOmin].v;
```

```
END;

omega := 1;
n := 1;
finished := false;


WHILE ((n < maxits) and not finished) DO BEGIN

FOR i := 0 TO imax DO BEGIN
FOR j := 0 TO jmax DO BEGIN


IF (psi[i,j].ghost = true) AND (j > amin ) AND (j < amax ) THEN
psi[i,j].v := psi[imax,a].v / psi[i,j].q - (psi[i,j-1].v*(1 -
psi[i,j].q)/psi[i,j].q);

IF (psi[i,j].ghost = true) AND (j > iomin) and (j < jmax) THEN
psi[i,j].v := psi[imax,iOmin].v / psi[i,j].q - (psi[i,j-1].v*(1 -
psi[i,j].q)/psi[i,j].q);

END;

END;

anorm := 0.0;

FOR i := holesize+1 TO imax-1 DO BEGIN
FOR j := 1 TO jmax-1 DO BEGIN
diag  := ((-2/sqr(h)) + (-2/( sqr(i*h)*sqr(theta))));
resid := +psi[i,j].v*diag
+(psi[i+1,j].v+psi[i-1,j].v)*(1/sqr(h))
+(psi[i,j+1].v+psi[i,j-1].v)*(1/(sqr(i*h)*sqr(theta)))
-(psi[i,j+1].v-psi[i,j-1].v)*(cos(j*theta)/sin(j*theta)/(2*theta*sqr(i*h)))
+(sqr(V)/U);

IF (psi[i,j].ghost = false) THEN BEGIN
anorm := anorm+abs(resid);
psi[i,j].v := psi[i,j].v - omega*resid/diag;
END;
END;
END;

gotoxy(1,23);
write(anorm);

IF (n >1) AND (anorm < eps) THEN BEGIN
writeln('finished');
finished := true;
END;

n := n + 1;
END;

END; {sor}


PROCEDURE save(VAR name:string);


VAR

        filename:string;
BEGIN


        write('enter name of data file only 6 char : ');readln(name);
```

```
filename := 'a:\data\'+name+'.dat';
ASSIGN(outfile,filename);

REWRITE(outfile);
writeln(outfile,'DATA FILE of cyclone: ',name);
writeln(outfile);
writeln(outfile,'jmax imax h thetamax U V holesize and a respectively');
writeln(outfile,jmax:2,' ',imax:2,' ',h:1:5,' ',thetamax:2,' ',rat:6);
writeln(outfile,U:3:3,' ',V:3:2,' ',holesize:2,' ',a:2);
writeln(outfile,cone:3:3,' ',cyl:2:3,' ',vl:2:3,' ',R:2:3,' ',iomin:2);
writeln(outfile,'psi');

FOR i := 0 TO imax DO BEGIN
FOR j := 0 TO jmax DO BEGIN
writeln(outfile,psi[i,j].v);
        END;
        END;
        CLOSE(outfile);

END; {save}



PROCEDURE velocity(theta,R :real; name:string );

CONST
        nos = 15;

TYPE
        gang = record
        z,c,w:real;
        end;

VAR

        vel                             :array[0..imax,0..jmax] of gang;
        uu,vv,ww,q,vw                   :real;
        dis,pos,ur,uo,rad,g,ac          :real;
        n,j,i,nmax                      :integer;
        filename        :string;

BEGIN

                FOR i := 0 TO imax DO BEGIN
                        FOR J := 0 TO jmax DO BEGIN
                        vel[i,j].z := 0;
                        vel[i,j].c := 0;
                        vel[i,j].w := 0;
                                END;
                        END;

nmax := nos;
dis := (imax-holesize)*h/nmax;
writeln('simultaneously calculating and saving velocity file ');
vw := imax*h*sin(a*theta);
filename := 'a:\data\'+name+'.vel';
ASSIGN(outfile,filename);
REWRITE(outfile);
writeln(outfile,'velocity file of cyclone: ',name);
writeln(outfile,' R, n-dis, h, thetamax jmax cone cyl');
writeln(outfile,R:2:3,' ',dis:2,' ',h:2:3,' ',thetamax:2:2,' ',cone:2:3,'
',cyl:2:3,' ',holesize:2,' ',nos:2,' ',jmax:2);
writeln(outfile,vw:2:3,' ',vl:2:3);
```

```
FOR i := holesize+1 TO imax-1 DO BEGIN
        FOR j := 1 TO jmax-1 DO BEGIN
        ur := 1/(sqr(i*h)*sin(theta*j))*((psi[i,j+1].v - psi[i,j-
        1].v)/(2*theta*180/pi));
        uo := -1/(i*h*sin(theta*j))*((psi[i+1,j].v - psi[i-
        1,j].v)/(2*h));

        vel[i,j].z := ur*cos(theta*j) - (uo*sin(theta*j));
        vel[i,j].c := ur*sin(theta*j) + (uo*cos(theta*j));
        vel[i,j].w := V / (i*h*sin(j*theta)) * (sqrt((sqr(R) -
        (2*psi[i,j].v / U))));

        END;
END;
```

```
END;
        writeln(outfile,nos:2);
CLOSE(outfile);

END;


BEGIN
        sor(theta,R);
        save(name);
        velocity(theta,R,name);
        writeln('data files saved you may hit return');
        readln
END.
```



```
FOR n := 1 to nmax DO BEGIN
        FOR j := 1 to jmax-1 DO BEGIN
        pos := (dis*n) + (holesize*h);
        g := pos / cos(j*theta);
        i := trunc(g/h);
        rad := pos * sin(theta*j)/cos(theta*j);
        q := (sqrt(sqr(rad)+sqr(pos)) - (i*h));

        IF (rad <= R) AND (i < imax) THEN BEGIN
        vv := (vel[i+1,j].c - vel[i,j].c) * q / h + vel[i,j].c;
        uu := (vel[i+1,j].z - vel[i,j].z) * q / h + vel[i,j].z;
        ww := (vel[i+1,j].w - vel[i,j].w) * q / h + vel[i,j].w;
        ac :=  sqr(ww)/rad;
        writeln(outfile,n:2,' ',rad:2:3,' ',uu:2:3,' ',vv:2:3,'
        ',ww:2:3,' ',ac:2:3);
        END;
END;
```

Appendix III

Particle Tracking velocity data at circumferential posistion 13

Height from top of cone	-230.00	(mm)
Core angle ratio	0.02557	
Photo scale factor	3.88	
Time interval	386	1/100 th sec

Original Measurements from photographs

p1x	p1y	p1z	p2x	p2y	p2z
-30.00	28.00	30.50	25.00	33.00	21.00
-20.00	27.00	35.00	30.00	28.00	26.00
-6.00	42.50	-27.50	45.00	41.00	-43.00
-22.00	28.00	-21.50	31.50	29.00	-27.00
-30.50	43.00	-48.00	11.00	50.00	-54.50
0.00	5.00	-20.00	25.00	-1.50	-39.00
-10.50	23.00	23.50	42.50	13.50	22.00
-31.00	37.00	20.00	17.00	46.00	5.50
-1.00	53.00	-44.50	41.50	50.00	-51.00
-13.00	49.00	23.50	36.00	51.50	18.50
7.00	39.50	24.00	47.50	30.00	21.50
-24.50	22.00	-52.50	31.00	22.50	-59.00
-20.00	48.50	-5.00	21.00	52.00	-22.50
-35.00	38.00	7.00	14.00	45.00	-5.00
-22.00	54.50	0.00	17.00	62.00	-12.00
-52.00	48.00	31.00	-15.00	57.50	18.00
-70.00	42.00	-22.50	-32.00	55.00	-34.50
-66.00	29.00	-52.00	-25.50	46.50	-64.50
-27.50	34.00	-57.50	20.50	40.00	-69.50
-15.00	4.00	-53.50	17.50	0.50	-66.50

Corresponding scaled cartesian locations about apex of hydrocyclone

p1x	p1y	p1z	p2x	p2y	p2z
-7.73	24.04	7.86	6.44	25.26	5.41
-5.15	23.81	9.02	7.73	24.01	6.70
-1.55	27.39	-7.09	11.60	26.90	-11.08
-5.67	23.69	-5.54	8.12	23.92	-6.96
-7.86	27.39	-12.37	2.84	29.15	-14.05
0.00	17.78	-5.15	6.44	15.98	-10.05
-2.71	22.70	6.06	10.95	20.24	5.67
-7.99	26.29	5.15	4.38	28.51	1.42
-0.26	29.99	-11.47	10.70	29.17	-13.14
-3.35	29.40	6.06	9.28	30.01	4.77
1.80	26.96	6.19	12.24	24.49	5.54
-6.31	21.94	-13.53	7.99	22.03	-15.21
-5.15	29.09	-1.29	5.41	29.87	-5.80
-9.02	26.46	1.80	3.61	28.18	-1.29
-5.67	30.67	0.00	4.38	32.52	-3.09
-13.40	29.19	7.99	-3.87	31.56	4.64
-18.04	27.30	-5.80	-8.25	30.57	-8.89
-17.01	23.75	-13.40	-6.57	28.18	-16.62
-7.09	25.00	-14.82	5.28	26.47	-17.91
-3.87	17.30	-13.79	4.51	16.31	-17.14

Equivalent cylindrical co-ordinates plan only

r1	theta	r2	theta
25.25	-0.31	26.07	0.25
24.36	-0.21	25.22	0.31
27.44	-0.06	29.30	0.41
24.36	-0.23	25.26	0.33
28.49	-0.28	29.28	0.10
17.78	0.00	17.23	0.38
22.86	-0.12	23.02	0.50
27.47	-0.30	28.85	0.15
29.99	-0.01	31.07	0.35
29.59	-0.11	31.42	0.30
27.02	0.07	27.38	0.46
22.83	-0.28	23.43	0.35
29.54	-0.18	30.36	0.18
27.95	-0.33	28.41	0.13
31.19	-0.18	32.81	0.13
32.12	-0.43	31.79	-0.12
32.72	-0.58	31.66	-0.26
29.21	-0.62	28.94	-0.23
25.99	-0.28	26.99	0.20
17.72	-0.22	16.92	0.27

Calculated tangential and axial velocities

r	z	vt	vz	helix
25.66	216.64	5.56	-0.945	9.8
24.79	217.86	5.02	-0.895	10.2
28.37	200.91	5.07	-1.542	16.9
24.81	203.75	5.38	-0.547	5.9
28.89	196.79	4.20	-0.647	8.9
17.50	202.40	2.59	-1.890	37.2
22.94	215.86	5.44	-0.149	1.6
28.16	213.29	4.86	-1.443	16.8
30.53	197.69	4.24	-0.647	8.7
30.50	215.41	4.87	-0.497	5.8
27.20	215.86	4.16	-0.249	3.5
23.13	195.63	5.61	-0.647	6.7
29.95	206.46	4.10	-1.741	23.1
28.18	210.26	4.96	-1.194	13.8
32.00	208.45	3.91	-1.194	17.1
31.96	216.31	3.81	-1.293	19.4
32.19	202.65	3.98	-1.194	17.5
29.07	194.99	4.40	-1.244	17.2
26.49	193.63	4.84	-1.194	14.0
17.32	194.54	3.27	-1.293	21.8

Appendix IV

Linear Interpolation program.

This program was developed to aid data extraction from the numerical grid used in Fluents fluid flow calculation of the flow in the hydrocyclone. The calculated data is stored at the centre of each cell in the flow domain. The alphanumeric output of the data from Fluent gives the location of the cell centres and the corresponding flow parameters at that point, i.e. velocity. There is no facility in Fluent structured to interpolate a numerical value at a point that lies between nodes. It was for this reason that the program was written. The computational blocks that make up the grid used for the flow calculation in fluent are not uniform but distort to the shape of the geometry and therefore appear skewed. If we take an axial plane through the cyclone, the grid would appear as in figure A.5.1.

The program first reads in the files containing the grid data for an axial slice of the cyclone and also a file which contains a list of all the point locations that are to be interpolated. It treats each point individually first calculating between which nodes the point lies and which sides of the given cell encompass it. The linear equation

$$a + b \cdot r_i + c \cdot x_i + d \cdot r_i \cdot x_i = v_i \qquad \text{A.5.1}$$

is used to describe all points that lie in the cell, a, b, c and d are constants r and x describe the spatial location of a point in the cell and v is a corresponding numerical value. The four unknown constants are found by solving the four simultaneous equations at the cell corners using Gausian elimination. Once the unknowns are established then the required point value can be obtained by inputting its r and x

components. The program repeats this operation for each point location in the data file.

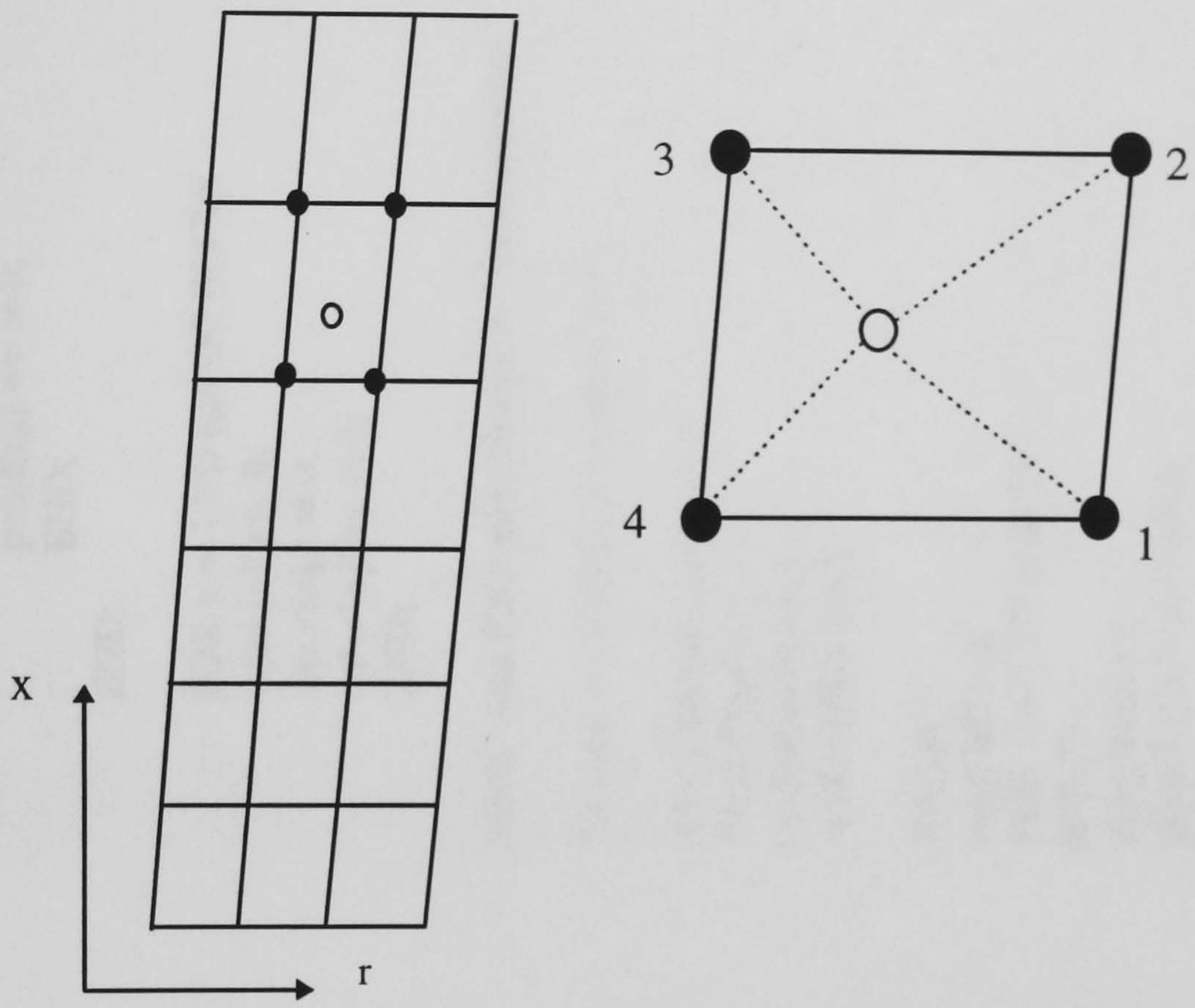

Figure A.5.1. Deformed Fluent grid showing location of an interpolation point between the nodes or cell centres at which the predicted flow values are located.

```
PROGRAM Linear_interpolation_program;

USES Wincrt;

CONST
        max = 16; jmax = 26; nos =250;

TYPE
        gang = record
        x,r,wv              :real;
                end;

        group = record
        r,z,wv              :real;
                end;

        grid =  array[0..imax,1..jmax] of gang;
        int  =  array[1..nos] of group;

VAR
        j,i,n,nosof                 :integer;
        point                       :grid;
        value                       :int;
        name,y,p                    :string;
        q                           :boolean;

PROCEDURE dataread;

VAR
        r,z,vt,any,intval   :real;
        filename            :string;
        infile                      :text;
        line                        :string;

BEGIN
```

```
        FOR i := 0 TO imax DO BEGIN
                FOR j := 1 TO jmax DO BEGIN
                point[i,j].x := 0;
                point[i,j].r := 0;
                point[i,j].wv := 0;
                END;
        END;

        FOR n := 1 TO nos DO BEGIN
        value[n].z := 0;
        value[n].r := 0;
        value[n].wv := 0;
        END;

write('enter file name xpositions: ');readln(name);

filename := 'a:\fluent\'+name+'.txt';

ASSIGN(infile,filename);
RESET(infile);
readln(infile,line);
readln(infile,line);

REPEAT
read(infile,j);
FOR  i := 1 TO imax DO
BEGIN
read(infile,any);
point[i,j].x:= any*1000;
END;
point[0,j].x  := point[1,j].x;
point[16,j].x := point[1,j].x;
UNTIL j = 1;
CLOSE(infile);
```

```
write('enter file name radial positions or Z plane: ');readln(name);

filename := 'a:\fluent\'+name+'.txt';

ASSIGN(infile,filename);
RESET(infile);
readln(infile,line);
readln(infile,line);


REPEAT
read(infile,j);
FOR  i := 1 TO imax DO
BEGIN
read(infile,any);
point[i,j].r:= -any*1000;
if (i = 16) and (point[i,j].x >= 50) then point[i,j].r := 22.5+((22.5/440)*(490-
point[i,j].x));
if (i = 16) and (point[i,j].x < 50) then point[i,j].r := 45;
END;
i := 0;
if (point[1,j].x >= 50) then point[0,j].r := 11.25+((11.25/440)*(490-point[1,j].x));
if (point[1,j].x < 50) then point[0,j].r := 22.5;
UNTIL j = 1;
CLOSE(infile);



write('enter file name w-velocities: ');readln(name);

filename := 'a:\fluent\'+name+'.txt';

ASSIGN(infile,filename);
RESET(infile);
readln(infile,line);
readln(infile,line);


REPEAT
read(infile,j);
FOR  i := 1 TO imax DO
BEGIN
read(infile,any);
point[i,j].wv:= any;
END;
UNTIL j = 1;
CLOSE(infile);



write('enter file experimental data: ');readln(name);

filename := 'a:\fluent\'+name+'.txt';

ASSIGN(infile,filename);
RESET(infile);
readln(infile,nosof);
readln(infile,line);

FOR n:=1 TO nosof DO BEGIN
readln(infile,value[n].r,value[n].z,line);
END;

CLOSE(infile);

END;

PROCEDURE interpolate;
```

```
TYPE

matrix =  array[1..5,1..4] of real;

VAR

n,x,y,k,m,e       :integer;
a,b,c,d,frac,m1,m2 :real;
augment           :matrix;

BEGIN

FOR n := 1 TO nosof DO BEGIN

j := 0;
i := 0;

REPEAT
j:=j+1;
UNTIL  point[i,j].x >= value[n].z;

REPEAT
i:= i+1 ;
UNTIL point[i,j].r >= value[n].r;

{write(n,' ',value[n].r:2:3,' ',value[n].z:2:3,' ',point[i,j].r:2:3,' ',point[i,j].x:2:3); }
m1 := (point[i,j].r-point[i,j-1].r)/(point[i,j].x-point[i,j-1].x);
m2 := (point[i-1,j].r-point[i-1,j-1].r)/(point[i-1,j].x-point[i-1,j-1].x);

{write(m1:2:3,' ',m2:2:3);readln;  }

If value[n].r - point[i,j-1].r <= (   m1 * (value[n].z - point[i,j-1].x) ) then i := i else
i:=i+1;

 If value[n].r - point[i-1,j-1].r <= ( m2 * (value[n].z - point[i-1,j-1].x) ) then i :=
i-1 else i:=i;


  FOR y := 1 TO 4 DO BEGIN

  CASE y OF
  1              :k:=i-1;
  2              : k:=i;
  3              : k:=i;
  4              :k:=i-1;
  END;

  CASE y OF
  1              : m:=j;
  2              : m:=j;
  3              :m:=j-1;
  4              :m:=j-1;
  END;


    augment[1,y] := 1;
    augment[2,y] := point[ k,m].r;
    augment[3,y] := point[ k,m].x;
    augment[4,y] := point[ k,m].r*point[k,m].x;
    augment[5,y] := point[ k,m].wv;
  { writeln(augment[1,y]:2:2,' ',augment[2,y]:2:2,' ',augment[3,y]:2:2,'
',augment[4,y]:2:2,' ',augment[5,y]:2:2);}
  END;
{   readln;}

  e := 1;
  REPEAT
     FOR y := e+1 TO 4 DO BEGIN
```

```
        CASE y OF
        2               : frac := augment[e,2]/augment[ e,e];
        3               : frac := augment[e,3]/augment[ e,e];
        4               : frac := augment[e,4]/augment[ e,e];
        END;
      FOR x := e TO 5 DO BEGIN
      augment[ x,y]:=augment[x,y]-(augment[x,e]*frac);
      {write(augment[ x,y]:2:2,' ');}
      END;
{       writeln;                }
      END;
 {      writeln;}
   e := e+1;
   UNTIL e = 4;
{    writeln;      }

    d := augment[5,4]/augment[4,4];
    c := (augment[5,3]-(augment[4,3]*d))/augment[3,3];
    b := (augment[5,2]-(augment[3,2]*c)-(augment[4,2]*d))/augment[2,2];
    a := (augment[5,1]-(augment[4,1]*d)-(augment[3,1]*c)-
(augment[2,1]*b))/augment[1,1];

    value[n].wv := a + (b*value[n].r) +  (c*value[n].z) + (d*value[n].r*value[n].z);
   { writeln(d:2:2,' ',c:2:2,' ',b:2:2,' ',a:2:2);
    writeln(value[n].r:2:2,' ',value[n].z:2:2,' ',value[n].wv:2:2);readln;}
  END;


END;

PROCEDURE save;

var
  filename :string;
  outfile  :text;

BEGIN

 write('enter file name to save as : ');readln(name);
 filename := 'a:\fluent\'+name+'.txt';
 ASSIGN(outfile,filename);

 REWRITE(outfile);


   FOR n := 1 TO  nosof DO BEGIN
     writeln(outfile,value[n].r:2:2,' ',value[n].z:2:2,'          ',value[n].wv:2:2);
   END;


 CLOSE(outfile);

END;


BEGIN

    repeat
    clrscr;
    dataread;
    write('data files all read');readln;
    interpolate;
    save;
    writeln('finished');
    readln;
    donewincrt;

    until q = false;
END.
```